Modeling and robust control approach for autonomous underwater vehicles

Rui Yang

THÈSE / UNIVERSITÉ DE BRETAGNE OCCIDENTALE
sous le sceau de l'Université Européenne de Bretagne

pour obtenir le titre de
DOCTEUR DE L'UNIVERSITÉ DE BRETAGNE OCCIDENTALE

Mention : STIC/Automatique
École Doctorale SICMA

présentée par

Rui YANG

Préparée à l'ENSTA Bretagne
Equipe OSM, Pôle STIC
et Ocean University of China
Department of Ocean Engineering

Modeling and Robust Control Approach for Autonomous Underwater Vehicles

Thèse soutenue le 26 Février 2016
devant le jury composé de:

Luc JAULIN, examinateur/president
Professeur, Université de Bretagne Occidentale, Brest, France.

Lionel LAPIERRE, rapporteur
MdC HDR, Université de Montpellier, France.

Yan ZHUANG, rapporteur
Professeur, Dalian University of Technology, China.

Philippe CHEVREL, examinateur
Professeur, Ecole des Mines de Nantes, France.

Benoit CLEMENT, encadrant
Professeur, ENSTA Bretagne, Brest, France.

Huajun LI, directeur de thèse
Professor, Ocean University of China, China.

Ali MANSOUR, directeur de thèse
Professeur, ENSTA Bretagne, Brest, France.

Modeling and Robust Control Approach for Autonomous Underwater Vehicles

by

Rui YANG

Submitted to the
Department of Ocean Engineering
STIC (École Doctorale SICMA, Automique)
in partial fulfillment of the requirements for the degree of

Doctor of Philosophy

at the

Ocean University of China
ENSTA Bretagne

February 2016

Author .....

Department of Ocean Engineering
STIC (École Doctorale SICMA, Automique)
February 26, 2016

Certified by .....

Huajun LI, Benoit CLEMENT, Ali MANSOUR, Ming LI
Professors, Thesis Supervisors

Accepted by .....

Chairman
Department Committee on Graduate Thesis

Dedicated to those who inspire my mind of freedom and independence

Modeling and Robust Control Approach for Autonomous Underwater Vehicles

by

Rui YANG

Submitted to the
Department of Ocean Engineering
STIC (École Doctorale SICMA, Automique)
on February 26, 2016, in partial fulfillment of the requirements for the degree of
Doctor of Philosophy

Abstract

Autonomous Underwater Vehicle (AUV) is a relevant technology for the sustainable use of ocean resources. AUV can be used as an important ocean observing platform to collect information on marine environmental characteristics for research and industry fields. In order to improve the observation quality and increase the navigation ability, many issues should be addressed and considered simultaneously.

Achieve necessary maneuverability depends on two key factors: an accurate hydrodynamic model and an advanced control system. However, the cost to develop an accurate hydrodynamic model, which shrinks the uncertainty intervals, is usually high. Meanwhile, when the robot geometry is complex, it becomes very difficult to identify its dynamic and hydrodynamic parameters. In addition, according to the quadratic damping factor, underwater vehicle dynamic and hydrodynamic model is nonlinear from the control point of view. Moreover, unmodeled dynamics, parameter variations and environmental disturbances create significant uncertainties among the nominal model and the reality. Sensor noise, signal delay as well as unmeasured states also affect the stability and control performance of the motion control system.

In many of our underwater competitions, it has been confirmed that the traditional Proportional-Integral-Derivative (PID) regulation is less efficient for low mass AUV. In this case, our scope is more focused on the combination of numerical modeling approaches and robust control schemes.

In this work, we proposed a model based robust motion control scheme. Without loss of generality, a robust heading controller was implemented and validated in the sea on cubic-shaped *CISCREA* AUV. The proposed solution uses cost efficient Computational Fluid Dynamic (CFD) software to predict the two hydrodynamic key parameters: The added mass matrix and the damping matrix. Four Degree of Freedom (DOF) model is built for *CISCREA* from CFD calculation. Numerical and experimental results are compared. Besides, the proposed control solution inherited the numerically obtained model from previous CFD calculation. Numerically predicted the actuator force compensates the nonlinear damping behavior result in a

linear model with uncertainties. Based on the bounded linear nominal model, we proposed H_∞ approach to handle the uncertainties, we used kalman filter to estimate unmeasured states such as angular velocity and we developed smith compensator to compensate the sensor signal delay.

The proposed robust heading control application uses only one compass as feedback sensor. This is important while AUV is working at certain depth where only magnetic sensors still work. Our robust control scheme was simulated in Matlab and validated in the sea near Brest. Simulation shows obvious advantage of the proposed robust control approach. Meanwhile, the proposed robust heading control is much faster than PID controller. The robust controller is insensitive to uncertainties and has no overshot. From both simulations and real sea experiments, we found our proposed robust control approach and the one compass heading control application are efficient for low mass and complex-shaped AUV *CISCREA*.

Thesis Supervisors: Huajun LI, Benoit CLEMENT, Ali MANSOUR, Ming LI
Title: Professors

Acknowledgments

The joint Ph.D study at ENSTA Bretagne and Ocean University of China is indeed an expectational experience in my life. During the years I have spent in France and China, I have benefited a lot from the discussions and interactions with the faculty members and the fellow students. Currently, I am delighted to share with all of you my growth about free mind and independence in the past years.

In particularly and foremost, I would like to express my greatest gratitude to my four supervisors, *Pr. Benoit CLEMENT*, *Pr. Ali MANSOUR*, *Prof. Huajun LI* and *Prof. Ming LI*, for their academic guidance and supervision. Comparing to myself four years ago, I owe all my good changes and progress to their kindly help and the important opportunities that they have offered to me. It has been a great pleasure to work and include joint papers with my supervisors. They have shown their great responsibility to help me handling the research obstacles, academic conferences and journal writings, etc. Not only as my tutors, I believe now they are all my caring friends through the years of discussions on wide range of common topics. I should mentioned that *Pr. Ali MANSOUR* and *Pr. Benoit CLEMENT* are very nice people, and they took me as family member while my stay in France. Their families delivers many great joys to my life in France. I really enjoy my days living and doing research with them in the city of Brest. *Pr. Huajun LI* is a very nice and visionary tutor. Only with his hard work to built international collaborations and interdisciplinary research, it can be convenient for me to achieve my joint study between hydrodynamics and control science both in France and China. Moreover, I want to give my thanks to *Prof. Jianguo WANG*, *Prof. Ming LI* and *Prof. Hui YU* who have been the key persons to guide me into the marine world.

I would like to give my thanks to the chairman *Prof. Luc JAULIN*, the reviewers *Prof. Lionel LAPIERRE*, *Prof. Yan Zhuang*, and the jury members of my thesis, *Prof. Philippe CHEVREL*, *Prof. Huajun LI*, *Prof. Benoit CLEMENT* and *Prof. Ali MANSOUR*. Thank you very much for your decent comments and serious work.

Here, I would like to express my great appreciation to the China Scholarship

Council for their financial supports to my study in France. It is great to make the international study and enjoy the big picture of the amazing world.

In fact, it is difficult to name all those who contributed to my Ph.D work and inspired my life, but I would like to thanks *Pr. J. M. Laurens*, *Mr. I. Probst*, *Dr. F. Le Bars* and *Mr. J. S. Zhang* for their technical supports to complete my work successfully. I am also grateful to make so many friends all around the world: *Yi Yang*, *Dongjie*, *Jie Xie*, *Liangzhang*, *Kaixiang*, *Jun Yao*, *Jianfeng*, *Jie Song*, *Saad*, *Simon*, *Guilherme*, *Dr. Mike Benjamin* and *Mr. Alon Yaari*, etc. We can not cover all here. Thank you all for the congenial time we spent together.

I would like to thank my parents for supporting my life and study in China. My special thanks to my mother who taught me to be kind and honest with all the people. I always believe that life is immense, more than we can imagine. Never give up anything, just keep going!

In the end, my sincerely gratitude to those who inspire my mind of freedom and independence!

Contents

I General Introduction **1**

1 Introduction **3**

1.1 Context and General Introduction 3

1.1.1 Underwater Vehicles Brief Review 5

1.1.2 Underwater Vehicles Applications 8

1.1.3 Research Issues of Underwater Vehicles 11

1.2 State of Art in AUV modeling and control 15

1.2.1 Modeling of Underwater Vehicles 15

1.2.2 Control of Underwater Vehicles 17

1.3 Motivation and Major Work 24

1.4 Thesis Outlines 28

1.5 Main Contributions 30

II AUV Modeling **32**

2 AUV Modeling **33**

2.1 Modeling Introduction 34

2.2 Kinematic 35

2.3 Rigid-Body Dynamic of Underwater Vehicles 37

2.4 Hydrodynamics of Underwater Vehicles 40

2.4.1 Restoring Force 41

2.4.2 Added Mass 42

2.4.3 Damping . . . 44
2.5 Environmental Disturbances . . . 46
2.6 Thruster modeling . . . 47
2.7 6 DOFs Underwater Vehicle Model . . . 48
2.8 Conclusion . . . 49

3 Numerical CISCREA AUV Model 51
3.1 Rigid-body Mass Inertia Matrix . . . 52
3.2 Added Mass Matrix . . . 56
3.2.1 WAMIT Calculating *CISCREA* Added Mass . . . 57
3.2.2 MCC Calculating CISCREA Added Mass . . . 61
3.2.3 WAMIT and MCC Added Mass Comparison . . . 63
3.3 Damping Approximation . . . 65
3.3.1 Morison Equation Analysis . . . 66
3.3.2 ANSYS-CFX Damping Analysis . . . 69
3.3.3 STAR-CCM+ Damping Analysis . . . 75
3.3.4 STAR-CCM+ Rotational Damping Analysis . . . 78
3.3.5 Damping Results Comparison . . . 81
3.4 Four CFDs model of *CISCREA* AUV . . . 83
3.5 Conclusion . . . 85

4 *CISCREA* AUV Hydrodynamic Experiment 87
4.1 Bollard Thrust . . . 88
4.2 Experiment Design . . . 93
4.3 Experiment Analysis . . . 96
4.4 Experiment Results . . . 98
4.5 Four DOFs Model of CISCREA . . . 104
4.6 Yaw Model . . . 105
4.7 Conclusion . . . 106

III AUV Control **108**

5 AUV H_∞ Controller and Simulations **109**

5.1 Robust Control Theory . . . 111

5.1.1 H_∞ Robust Analysis . . . 113

5.1.2 H_∞ Robust Design . . . 118

5.1.3 H_∞ Synthesis: Algebraic *Riccati* Equation (ARE) . . . 121

5.1.4 H_∞ Synthesis: LMI . . . 124

5.2 Control of the *CISCREA* AUV . . . 127

5.2.1 Yaw model and its linearization . . . 127

5.2.2 H_∞ control design . . . 133

5.2.3 PID control design . . . 137

5.3 *CISCREA* AUV Yaw Control Simulations . . . 138

5.3.1 H_∞ Yaw Controller . . . 139

5.3.2 PID Yaw Controller . . . 142

5.4 Simulation Results . . . 142

5.5 Conclusion . . . 145

6 Applicable H_∞ Controller at Sea **149**

6.1 *CISCREA* AUV . . . 151

6.1.1 *CISCREA* AUV Brief Introduction . . . 151

6.1.2 *CISCREA* AUV Hardware and Software . . . 153

6.2 Improved H_∞ Yaw Controller . . . 156

6.2.1 Kalman Filter Estimation . . . 158

6.2.2 Signal Delay Compensator . . . 161

6.2.3 Improved H_∞ Control Approach . . . 168

6.3 *CISCREA* AUV Sea Test . . . 171

6.3.1 Pool Test of H_∞ heading controller . . . 171

6.3.2 Sea Test of H_∞ heading controller . . . 175

6.4 AUV Virtual Simulation Program . . . 179

6.5 Conclusion . . . 180

IV General Conclusion and Perspectives **183**

7 General Conclusion and Perspectives **185**

7.1 Summary of the work 186

7.2 Future Work 189

V Appendix **190**

A AUV Modeling **191**

A.1 Euler Angles 191

A.2 Quaternion 195

A.3 Dynamics Essentials 197

A.4 Six DOFs AUV Model 198

A.5 Rigid Body Coriolis Force 199

A.6 Restoring Force 200

A.7 Added Mass Expression 201

A.8 Added Mass Coriolis Expression 202

A.9 Damping coefficients 203

B Parameter Identification **205**

B.1 PRO/E Report of *CISCREA* AUV 205

B.2 CISCREA WAMIT Configuration and Output 209

C H_∞ Control Theory Essentials **215**

C.1 Norms 215

C.2 Linear Fractional Transformation 220

D Yaw Control Experiment **221**

D.1 H_∞ Robust Control Synthesis 221

D.2 *CISCREA* AUV H_∞ Heading Controller 223

D.3 *CISCREA* AUV Control Code 224

Bibliography 228

List of Figures 241

List of Tables 248

Abbreviations 252

List of Publication 253

Résumé 255

Part I

General Introduction

fuzzy logic

Chapter 1

Introduction

Contents

1.1 Context and General Introduction 3

1.2 State of Art in AUV modeling and control 15

1.3 Motivation and Major Work 24

1.4 Thesis Outlines 28

1.5 Main Contributions 30

1.1 Context and General Introduction

The ocean covers a vast stretch of surface on the earth, around 71% according to the National Oceanic and Atmospheric Administration (NOAA) [1], it is rich in natural resources, and it is still considered to be largely unrevealed. As marine technology evolves rapidly [2], develop the sustained ability of marine activities is more important than ever before. Indeed, sustainable use of the ocean becomes a pressing problem that concerns the immediate benefits of every nation. This paper undertakes the study of modeling and control problems of AUV. In fact, AUV is currently a key technology to answer a variety of marine challenges in the sustainable use of ocean

resources and space. Nowadays, major marine activities deploy underwater vehicles, and these vehicles are widely involved in surveillance, inspection and survey missions [2, 3].

Fully explore the ocean is challenging. Every year abundant of ocean biological discoveries and marine technology innovations prove that the ocean mysteries are far beyond our imagination [4, 5, 6]. In order to improve the sustained ability of marine activities, it is required to expand both the width and depth of undersea monitoring and exploration. Actually, the ocean environment is generally harsh and complex. There is a fundamental necessity of using underwater vehicles to solve the problems such as: operating at harsh weather, limited communication bandwidth and high pressure or high temperature regions, *etc.* Meanwhile, a lot of unknown physical and ecological ocean mechanism are waiting to be revealed by mean of autonomous underwater robots [7, 8].

At the same time, modern societies face new challenges. Human civilization products are now to some extent threatens to the ocean environment. Before the great strides of industry, human and ocean relation depends on pure natural phenomena, including hurricanes, tsunami, algal bloom and offshore erosions, *etc.* However, today many industrial activities are double edge sword. They can go out of our control such as Gulf of Mexico oil spill [9], floating garbages, Fukushima nuclear accident [10, 11] and global warming, etc. The ocean is an essential part to support life on the earth, understand and protect its self-balance will save life from fatal disaster. Therefore, many countries and organizations are inspired by the past man-made accidents. They post realistic disaster scenarios to the autonomous air, land, surface and underwater robots [12, 13]. New kind of ocean safety guards are expected from potential autonomous underwater vehicle designs.

Researches on AUV show recently a large amount of alarming results. In fact, these studies prove the existence of a blank territory to improve the robustness of future AUV designs.

In this chapter, the following contents are described:

- review of underwater vehicle evolution, applications and related researches.

- the state of art in modeling and control of underwater vehicles.

- proposed algorithms and thesis organizations.

1.1.1 Underwater Vehicles Brief Review

Extending the ability of human-being to explore the ocean with man-made products date back to 1531. Indeed, two men dive into the water using *Halley's* bell as it was shown by the design of *Leonardo da Vinci* [2]. Nowadays, thousands of underwater vehicles are designed with different types for a wide range of underwater missions. A brief underwater vehicle history is described here based on the report of *Lapierre* [2] and *Caiti* [14].

Researches accelerate the steps to explore the underwater world. At the beginning, they focus on the design of Human Occupied Vehicle (HOV). In 1776, *David Brushell* designed the first submarine *Turtle* to attack surface vessels. In 1960, *Jacques Piccard* and *Lt. Don Walsh* pilot the HOV, *Trieste* of USA, reached the deepest point in the sea (10916 m *Mariana Trench*). In 2012, the *Jiao Long* HOV of China reached a depth of 7000 m near *Mariana Trench*.

To avoid HOVs accident and minimize the risk, people began to show interest in developing Unmanned Underwater Vehicle (UUV). Like HOVs, UUV designs also pass through a long history. In 1866, *Robert Whitehead* design the first torpedo in the world. In 1960s and 70s, USA and France respectively design the earliest *SPURV* (Self-Propelled Underwater Research Vehicle) and *Epaulard* UUV. Nowadays, UUV Blue fin 21 was used for MH370 blackbox searching mission.

Differences between HOV and UUV are mainly the design, the cost and the autonomy efficiency. Comparing to UUV, HOV should be designed to have critical life support systems for safety reasons. The cockpit is to some extent a high-risk and tight space for pilots. The first aim is always guaranteeing the safety of pilots, which induces very high cost to build the HOV. However, the HOV is operated by the onboard pilots, which requires less autonomy on the vehicles. Instead, the autonomy level of UUV improves rapidly, UUV currently shows more flexibility than the HOV, and a large amount of UUV designs have emerged [3]. UUVs can operate at harsh

environments 24 hours without rest (with respect to batteries capacity). There is no need to concern life support constrains. UUV related guidance, navigation, localization, motion control and intelligence researches develop rapidly. In this thesis, the focus is on UUV systems.

Autonomous ocean vehicles are of various types and mainly divided into two kind, Unmanned Surface Vehicles (USV) and UUV. For examples, there are two USVs in figures 1-1 and 1-2, respectively from Thales and Ifremer & ENSTA Bretagne.

Figure 1-1: Thales USV

Figure 1-2: Ifremer Vaimos USV

Comparing to UUV, USV has many advantages in control, localization and propulsion. Usually, USVs are exposed on the water surface. Therefore, it is convenient to receive long range wireless commands and Global Position System (GPS) signal for localization and control. Besides, USVs have many innovative designs such as Wave Glider PacX [15] and VAIMOS [16], which utilize wind or wave energy for unlimited propulsion. However, operating on the surface of the sea poses the problems of complex wind and wave coupled dynamics, unsettled weather and a lot of moving obstacles, *etc.*

UUV is generally classified into three types: Remotely Operated Vehicle (ROV), Glider and AUV. Note that, in this study we avoid the biomimetic underwater robots, as their dynamics and design characteristics are different from our work [17].

ROV is characterized by its umbilical link, and it is designed to be a human piloted vehicle for limited-space underwater intervention and survey. The most known ROVs are the *Ventana* 1850 m diving ROV of MBARI (USA), *Alvin* 4500 m ROV of WHOI (USA), *Victor 6000* ROV of Ifremer (France), *H2000* ROV of ECA Hytec company (France), *ROPOS 6000* ROV of ISE (Canada) and *Hai Long* 4500 m ROV of Shang-

hai Jiao Tong University (China). As acoustic communication technology becomes mature, some new designs of ROV require no umbilical link. For example, the *Alive* Intervention Autonomous Underwater Vehicles (IAUV), jointly developed by Ifremer and Cybernetix company, replaces the umbilical link with acoustic communications, as shown in figure 1-3. However, the *Alive* IAUV still needs wireless human control from well trained pilots. Lately, they introduced the prevalence of miniature ROV designs. Figure 1-4 shows the new design of a small-size *L2ROV* of *LIRMM* lab .

Figure 1-3: Alive Ifremer

Figure 1-4: L2ROV *LIRMM*

Glider is an important member of UUV family. It possesses the feature: propulsion power comes from the gliding process of repeated diving and surface motion. Typically, we show the *Slocum* glider in figure 1-5. As there is no requirement of onboard propulsion energy, gliders are common with a torpedo shape for long range missions. Nevertheless, gliders are not suited for a monitoring mission on a content depth, because its surge power comes from continuous diving and surface movement.

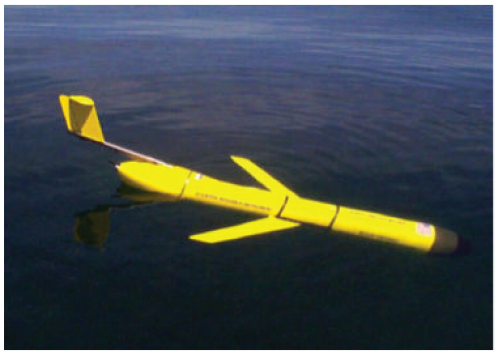

Figure 1-5: Slocum Glider

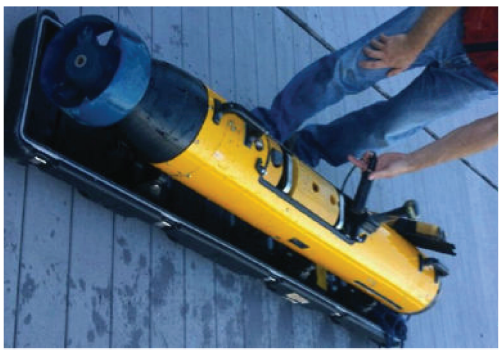

Figure 1-6: Blue Fin 9

AUV is the most common UUV. AUVs are wildly used for the autonomous missions under depth range from hundreds up to thousands meters. AUVs can fully run without human intervention for tens of hours. In figure 1-6, it is shown the *Blue Fin 9* AUV, of which its predecessor *Blue Fin 21* is deployed to find the missing blackbox of the MH370 airplane [18, 19]. Characterized by appearance and dynamic properties, AUVs can be divided into Torpedo-shaped AUV and Cubic-shaped AUV. Torpedo-shaped AUVs are distinct from cubics, and they are generally designed for long range missions. Under-actuated actuation configuration (control fins and surge propellers) determine that torpedo-shaped AUV is usually unable to hover and make a pivot steering. It is difficult for Torpedo-shaped AUV to achieve precise movement inside a small space. But there are few exceptional torpedo-shaped AUV designs which are not limited by the under-actuated issues, such as *Avalon* [20] and *Sparus II* [21] shown in figures 1-9 and 1-10. Cubic-shaped AUVs are generally fully actuated, therefore they are good at hovering, pivot steering and short range low speed missions. In figure1-7, the OCEAN Modules V8 robot has 8 thrusters, and allows 6 DOF movement. In our application, CISCREA AUV is equiped with 6 thrusters, which allows 4 DOF motion, see figure 1-8 (Two vertical thrusters are connected without differential actuation ability). Actually, hovering and pivot steering motion are critical for some specific underwater applications: undersea pipeline inspection, offshore infrastructure surveillance and large vessel maintenance. Indeed, small AUVs can be deployed to explore areas which are not accessible to HOVs and ROVs. Meanwhile, a large number of the cubic-shaped AUVs enjoy more degrees of freedom than under-actuated torpedo-shaped AUVs.

The abundant distinct designs of underwater vehicles closely rely on the requirements of its specific applications. Therefore, in the next section, we will briefly introduce the major underwater vehicle applications.

1.1.2 Underwater Vehicles Applications

Underwater vehicle (underwater robot) is a highly integrated product which involves the frontier of many high-tech research fields. Hence, the past underwater robots

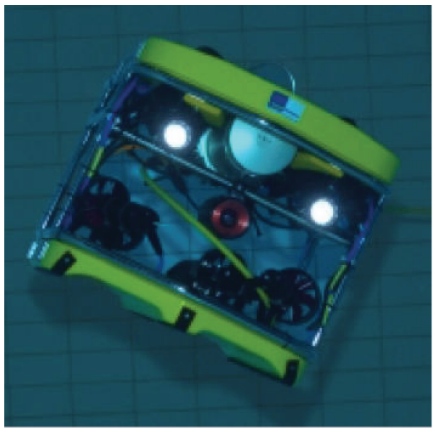

Figure 1-7: OCEAN Modules

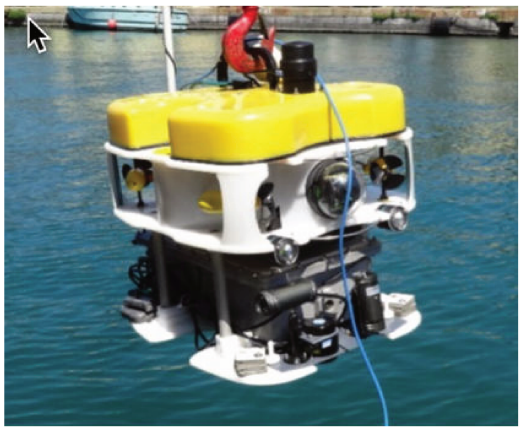

Figure 1-8: CISSAU AUV

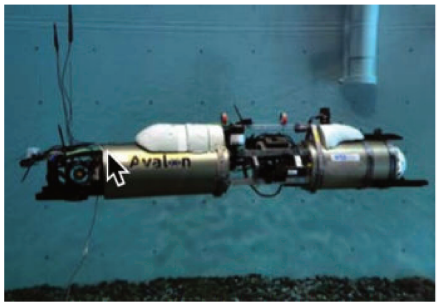

Figure 1-9: Avalon

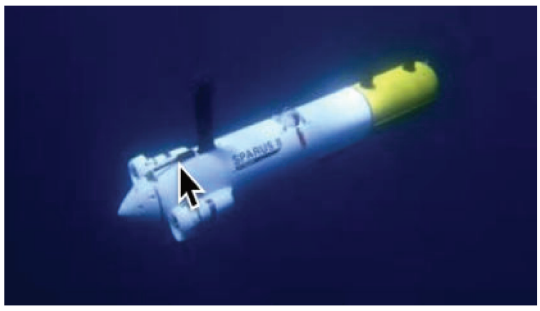

Figure 1-10: Sparus II

are expensive, and are mainly supported and operated by large military or industry organizations as well as well funded scientific institutions [2]. Accordingly, this thesis underlies an idea of developing low-cost and more accessible modeling and control algorithms for future AUV designs. AUVs are widely used for navigation charting, environmental assessment, underwater survey, monitoring and territory defense, *etc.*

For industry applications, oil and gas companies use the most underwater vehicles, as they dominate 58% of offshore marine activities [2]. Generally, there are ROVs designed for infrastructure health monitoring, telecommunication cable-laying and underwater man-made structures maintenance. Meanwhile, some AUVs are deployed for pipeline leak inspection, acoustic bathymetric detection or sediment analysis and magnetic explorations for new oilfields [22]. In this paper, the modeling and control research of CISCREA AUV is under the context of oil pipeline inspection. Among others, a huge mount of valuable minerals lies on the seabed, waiting to be collected

by autonomous robots. According to the reports [2, 3], there are an estimation of around 2000 billion tons of manganese nodules near the Hawaiian Islands. Hence, many countries such as France and Canada are inspired to develop UUVs for the emerging robot mining industries.

Military is another big buyer of underwater vehicles, and they focus on cultivating a new kind of autonomous forces by UUVs. Modern UUVs are born with good invisible properties. Instead of acting as a weapon, UUVs can save many lives in future conflicts. Some UUVs have already been used in the anti-terrorist battles [23, 24]. Meanwhile, the military UUV *Blue Fin 21* was also used in the civilian search of *MH370* airplane. As global economy boost, the future territory safety will be an essential issue of a sustainable ocean. We believe that the UUV will be an important mean to save life.

According to *Lapierre* [2], coastal activities depends on UUVs. The port security and safety burden are increasing rapidly, the monitoring and evidence gathering work will finally exceed the limit of human efficiency. The 24-hours rest-free underwater robot is indeed a good candidate as future autonomous port guards. It is important to have a tool such as UUV, that can monitor leaking vessels for environmental protection, rescue people from harsh weather or dangerous regions, and inspect automatically the sedimental condition of critical transport channels. Besides, develop the maintenance ability of UUVs for large vessels, can save currently limited dock space and docking time [25]. Wet maintenance technology is critical for large scale ports. In addition, coastal man-made structures require periodic and regular inspections. For example, European dams have to be totally checked every ten years [25]. Note that, after the Fukushima accident, people pay more attention on using autonomous underwater vehicles for missions to monitor nuclear pollution and shut down critical valves [13].

As the cost of UUV drops down, aquaculture UUV applications emerge. Indeed, there are examples using an UUV and ultra sonar to detect fishing net damages [25]. Meanwhile, biological and ecological study requires more UUVs. For example, scientists use onboard sonar to identify different fishes. UUVs are indeed important

in learning and understanding the ecological and biological mysteries of the sea.

Scientific data collection is the driving force to develop inspection UUVs. For instance, to answer the global warming phenomenon, many organizations proposed monitoring networks using multiple UUVs. The main concern is that UUVs can move like a moving buoy, from one location to another where it is needed most. Besides, it is necessary to have UUVs in many other scientific studies, such as learning the acoustic characteristics of deep water or under the arctic ice cover, collecting high temperature samples near undersea volcano, and monitoring coral reefs [26, 27].

UUVs face challenges to achieve above applications. The essential research issues are briefly listed in the next section.

1.1.3 Research Issues of Underwater Vehicles

Underwater vehicles are highly integrated. Miniature, low-cost, robust and multiple vehicle design are the current trend of new underwater vehicles. In this thesis, four levels of researches are considered to be critical to construct an efficient underwater vehicle: physical level, control level, guidance and navigation level, and mission control level.

Physical Level: the designers should have enough knowledge about the ocean environment and robotic systems, to predict precisely the physical limit of the underwater vehicle. For instance, the physical level issues include: vehicle stability analysis (naval architecture point of view), pressure container design, thruster design, hydrodynamic fairing design, embedded system, sensors integration and battery management, *etc.* Like all ordinary ocean vehicles, the ability to maintain stability without capsizing the hull is essential for underwater vehicles to handle the turbulent ocean environment. Then, it is necessary to select correct materials to prevent the corrosion of underwater vehicles. In deep water, the pressure is extremely high, the pressure container faces tons of force. Besides, collision protections are also considered to prevent data lost during unexpected collisions. For long range missions, optimizing the fairing design will obviously reduce the hydrodynamic damping drag, and extend the working range. For hovering tasks, precisely design the thrusters and

fairing structures can provide an accurate model for better hovering and pivot steering ability. As we know, sensors are the eyes of the underwater robots to explore its unknown surroundings. The sensor integration plays an important role in AUV design. New trends are to integrate more sensing devices in an even smaller space. The sensors should guarantee enough data for the underwater vehicle to make decisions by itself. Breakthroughs are expected on the above issues.

Control Level: the ocean environment is complex and full of uncertain disturbances. Therefore, the two important control level researches: modeling and control of underwater vehicles, are essential for a fully equipped underwater vehicle to achieve high quality maneuverability. Indeed, underwater vehicles with precise control algorithms would have distinct advantage in reducing the complexity of high level researches, such as localization and navigation.

Generally, an accurate hydrodynamic model of the underwater vehicle can reveal the physical details and emphasize the focus of control design [28]. The control performance can be obviously improved, as there is less parameter uncertainties in the accurate underwater vehicle model. However, the cost of current modeling methods to obtain an accurate underwater vehicle is always expensive. It is even more difficult to be accurate when the underwater vehicle has complex structures and shapes. We believe high cost is one of the major reasons, only large organizations have the modeling ability of high performance underwater vehicles.

To control the underwater vehicle is not straight forward, many issues should be addressed [29]. The hydrodynamic model of the underwater vehicle is usually nonlinear, which means traditional control algorithms are not efficient to handle the damping efforts (cross-coupling damping terms and the linear damping terms are neglected under the low speed assumption). Then, dynamic parameters have uncertainties, and they are usually different from the nominal model. For example, the mass inertia matrix will increase when payloads are added to the underwater vehicle. Unmodeled dynamics, environmental disturbance as well as obsolete components also induce modeling uncertainties. At last, sensor noise, signal transmission delay, and unmeasured states would also affect the control stability and tracking performance.

In order to build an efficient and approachable underwater vehicle control system, this thesis addresses the modeling and robust control problems simultaneously. State of art in AUV modeling and control works are described in the next section.

Guidance and Navigation Level: underwater vehicle autonomy are endeavoring to get rid of human interventions. Future UUV can analyze environmental information onboard, and make decisions by itself. To this case, the UUV autonomy requires the guidance and navigation level researches. First, localization is considered to be one of the most difficult underwater problems. It is essential for the UUV to first find its position and attitude using limited underwater information. Note that, for most of the UUV inspection data, the information is only clear and valuable if the localization information and time stamps are accurate. No straight forward and efficient solutions exist to invert realistic inspection information by inaccurate localization data. The navigation system analyzes the realtime environmental data, and optimizes reasonable path for the UUV controller to avoid obstacles. UUV guidance system will finally push the robot in the correct track.

Underwater localization is a difficult task since there exist no GPS and radio signal. Territorial methods can not be applied to underwater localization [30]. Generally, electronic magnetic compass, gyroscopic compass, fiber-optic gyro-compass, inertia navigation unit, Doppler Velocity Log (DVL), Long Base-line (LBL), and Ultra Short Base-Line (USBL) are used for underwater localization [31, 32]. Classical methods such as Dead Reckoning (DR) use initial UUV position and current acceleration information to predict locations. However, the disadvantage of DR is the error accumulates as the time passes. DR is simple and efficient for some UUV applications. For Gliders, it is possible to float to the surface, and make corrections on the DR system periodically. For some UUVs that equipped with DVL, the DR method will have an obvious performance lift [31, 33]. LBL and USBL methods depend on static reference, which limit the operating range of the UUVs in few kilometers. According to the report of *Pascoal* [34], the main work of localization is around the estimation of positions using Kalman filter (KF), Extended Kalman filter (EKF) and complementary filters. The difficulty is to obtain the nonlinear state space equation

and noise properties [35, 36, 37, 38]. Besides, localization methods using a group of AUV [31, 39] or using acoustic cooperations between ASV and UUV are also popular today [40, 13]. An important UUV localization algorithm is Simultaneous Localization and Mapping (SLAM) [41, 42]. SLAM creates and identifies the landmarks to improve its knowledge about the environment and its position. Many works exist on UUV SLAM algorithms in [43, 44, 45, 46]. Currently, navigation works are mainly mathematical optimizations, as described in [47, 48]. Navigation methods include way-point navigation, line of sight method and nonlinear guidance [49, 50], *etc.* Generally, the navigation system optimizes a group of desired way points that avoids obstacles, based on the knowledge of operating environment in advance.

Mission Control Level: the mission level concerns more about behaviors and human interaction. Construct the mission level includes: onboard mission operating system, objective laguage human interface, swarms and intelligence research, *etc.* UUV operating works can be defined into different missions, hence, many softwares are developed to manage the robot missions. For example, MOOS-IvP is one of the widely used UUV mission control system, that transfers information among operators and executive UUV hardwares. The IvP-Helm of MOOS is an optimization program based on interval programming [51]. To solve in real time, the UUV heading and speed, MOOS-IvP can achieve a frequency of 4 Hz. The *CISSAU* AUV utilizes the MOOS-IvP software as a mission control system, see Figure 6-2. Future UUV human interfaces are expected to understand the scientific or engineering language from difference professions, which will unify and ease the UUV deployment process of overall ocean observation networks. Moreover, UUVs are expected to operate in the swarm formation, which have more robustness and efficiency than a single UUV. Except our modeling and robust control work, swarm can be another important solution to increase the robustness and stability of UUVs. UUV swarms are efficient to assign optimal numbers of sensors and flexible missions, meanwhile, the failure of one or several UUVs will not affect the underwater mission.

Robustness is an essential issue for future UUV designs. This thesis focuses on the modeling and control solutions to increase UUV robustness. The state of art in

AUV modeling and control works are described in the next section.

1.2 State of Art in AUV modeling and control

Achieving good maneuverability of small AUV depends on two key factors: an accurate hydrodynamic model and an advanced control system. In [52], Yamamoto pointed out that a model-based control system is more effective if the vehicles' dynamics are modeled to some extent. Meanwhile, in [53], Ferreira *et al*. showed that an empirical linear model often fails to represent the dynamics of the AUV over a wide operating region. Indeed, obtaining hydrodynamic models of the complex-shaped cubic AUV is one of the key points for better maneuverability. In addition, inside the virtual environment engineers can replay many dynamic and hydrodynamic phenomenons with seldom limit to time, space and cost. In this section, we first introduce the current underwater modeling works.

1.2.1 Modeling of Underwater Vehicles

Actually, many methods exist to model underwater vehicles, including full-scale experiments, scaled experiments, empirical formula approximations and computational approaches.

The advantage of a full-scale experiment is high accuracy, especially, for obtaining the added mass and damping parameters. However, high cost is a fatal drawback of full-scale experiment, it requires very expensive devices, such as towing tanks. In addition, the full-scale experiment is not control oriented, which means the modeling results can not be directly used for control design. Some experimental methods without towing tanks also exist, as presented in [54, 55], and free decay approach is presented by *Ross* in [56].

Scaled experiments compromise the cost and modeling accuracy. It is less expensive than full-scale experiment, as it only implements a scaled (eg. small size) model in the hydrodynamic experiment. Generally, modeling results of scaled experiments are more reliable than empirical and computational methods. However, the accuracy

of scaled experiment is subtle due to the scale effect. A ROV modeling application using scaled experiment of free decay method is presented in [57], and its experimental results are compared with computational solutions.

Empirical formula approximation is well proved on torpedo-shaped AUVs, usually slender bodies, as mentioned in [55, 58, 28]. The advantage of this method is the simplicity in estimating slender UUV hydrodynamic parameters, which uses only an ellipsoid shape. Nonetheless, empirical formula method requires deeper knowledge and experiences to simplify the UUV into elementary components. Meanwhile, the estimation accuracy is not always reliable, because simplified geometry may neglect many details. Especially, for a complex-shaped UUV (sometimes has open-frame structure) the simplification is hard to achieve.

Depend on basic mass, momentum, and energy conservation axiom, the potential theory and finite element theory based CFD softwares are well developed. Although there is no direct solution for the *Navier-Stokes* equation [59], the computational approaches can convert a physical fluid problem into applied mathematical problem. Then, hydrodynamic phenomena or parameters can be approximated by iterative calculations. In the beginning, CFD programs were popular to analyze large marine structures and transportation vessels. Nowadays, more and more UUVs apply the CFD modeling methods.

Computational methods have many obvious advantages. Theoretically, the accuracy of CFD approximation can be infinitely small if the calculation amount is unlimited. Meanwhile, CFD is able to reveal some physical details which is difficult to observe in the experiments. In other words, using CFD can replay many invisible dynamic and hydrodynamic phenomena without any cost. More importantly, CFD requires less experiences to simplify the complex-shaped AUVs. CFD modeling complexity are lower, and this is favorable to spread miniature and low-cost AUVs. Although the CFD reliability is not as good as experimental solutions, currently, there are still reliable models obtained by mixing CFD and experimental approaches [60]. Indeed, the computational modeling approach is a potential trend for future UUV design.

As mentioned by *Newman* in [59], UUV hydrodynamic forces can be linearly superimposed. Therefore, the UUV hydrodynamic effects can be separately analyzed by different softwares. There are CFD softwares such as: WAMIT, Marine Craft Characteristics (MCC), which is created by ENSTA Bretagne and it can be downloaded at [61], SHIPMO, ANSYS-CFX, ANSYS-FLUNT, ANSYS-AQWA, STAR- CCM+ and SeaFEM. These softwares can predict hydrodynamic parameters for a complex-shaped AUV with a very low cost. In [57], it is shown the efficiency of WAMIT to predict the added mass matrix. In [62], ANSYS-CFX was employed for AUV damping analysis.

Regardless of modeling issues, the value of a UUV model depends on how robust and efficient your control scheme can adapt to the hydrodynamic model. In next section, current UUV control methods are presented.

1.2.2 Control of Underwater Vehicles

Underwater vehicles are generally designed to operate in the ocean environments. Therefore, numerous uncertainties exist, including parameter variations, nonlinear hydrodynamic damping effects, sensor transmit delays and ocean current disturbances. To solve the UUV control issues, a large amount of underwater vehicle motion control algorithms are proposed, including: classical PID control, robust control, adaptive control, sliding mode control, back-stepping control, Linear Quadratic Gaussian (LQG), predictive control, gain scheduling, fuzzy control, neural network control, and other hybrid control methods. High quality reviews of underwater vehicle control researches can be found in the works of *Yuh* [3], *Johansen* [63] and *Budiyono* [64]. An exhaustive report is given by *Maalouf* in [25], which summarizes the performance current underwater vehicle controllers.

To control an underwater vehicle is complex. The dynamic and hydrodynamic properties involves: nonlinear damping, uncertain parameters variations, environmental disturbance, sensor noise, and signal delay, *etc.* The early UUV control methods are usually simple to implement. Controllers was designed without the UUV model or assuming that the UUV model is time invariant. Linearization is generally im-

plemented assuming the equivalent linear system has the same performance as the realistic nonlinear UUV behaviors. However, the robustness was not considered in early methods, which is critical to maintain UUV stability and control performance in the presence of uncertainties. Nowadays, to achieve faster, accurate and robust control performance, it is required to address modeling and control issues simultaneously. In the following, we briefly introduce the underwater vehicle controllers by two kind: model-free and model based controllers.

PID controller and its variations are the most classical underwater vehicle control algorithms. Even today, a lot of UUVs (equipped with high precision navigation and guidance devices) still use PID controllers, as PID is less complex and simple to be implemented. For example, in [65] *MacPhail et al.* implements a PD controller on the *Autosub-1* robot. In our paper [66], the *CISSAU* AUV used PID controller for depth control in SAUCE 2014 and euRathlon 2014 competitions. *Ostafichuk* implement a hybrid PD controller on the *Dolphin* AUV in [67].

The implementation of a PID controller only depends on tuning three gains: proportional, integral, and derivative gains. Proportional gain contributes to the response speed. Integral gain attenuates the static error, which affected the tracking performance. Derivative gain can reduce overshoot while keep the response fast. PID is a model-free controller, the implementation is a process of an iterative filed tuning of the three gains. However, according to the uncertain and nonlinear behaviors of UUV, PID control is insufficient in robustness. The disadvantages of PID are:

- PID gain tuning requires intuitive experiences.
- PID control stability can be affect by uncertain disturbance.
- The gains are fixed after tuning, controller is not adaptive to unpredict changes.
- PID is inefficient to handle nonlinearity, usually nonlinearity brings in response oscillations.
- The control output is not optimal, which waste onboard energy and shorten thruster lifespan.

For specific underwater vehicle applications, there exist many improved PID controllers, which consider the nonlinearity, the wave disturbance, and the current disturbance. In [68], *Perrier et al.* proposed an improved AUV PID controller that considers nonlinearity and disturbance attenuation. *ODIN* AUV applied a PID controller which involves shallow water wave disturbance rejection [69]. *Refines et al.* designed a PID controller robot which concerns current disturbance for *Minesniper MKII* [70]. Based on the nonlinear model *Mirhosseini* builds a PID depth controller in [71]. The above PID controllers show faster response and disturbance rejection ability. However, the performance is sensitive to the specific applications, the model accuracy and disturbance characteristics. In this thesis, PID is not considered to be enough to solve the nonlinear and robust issues of underwater vehicles.

LQG is a model based Multi Input Multi Output (MIMO) optimal state feedback controller. It can be considered as the combination of Kalman filter and a linear quadratic regulator. The linear optimal controller is derived under a quadratic cost function of minimal energy consumptions as well as other performance constrains. LQG applications on underwater vehicles can be found in [72]. The advantage of LQG is the theoretically optimal and accurate control design. However, the disadvantages are, LQG is sensitive to model accuracy, meanwhile LQG is inefficient to handle nonlinearity. For example, the linearization of UUV model on equivalent point is not accurate, that makes the implementation of LQG controllers very hard.

Gain scheduling control is a model based linear feedback controller, first proposed by *Silvestre* in [73]. The objective of gain scheduling is to approximate the original nonlinear system by a group of linear systems obtained around many equilibrium points. For each linear system in the group, the control design is a regular linear feedback control problem. While operating on the plant, the group of controllers will switch among them according to the working states, i.e. equilibrium points. On each working region near the equilibrium points, gain scheduling can achieve very high performance, as if the nonlinear system is exactly the linearized system. However, the control stability and performance apparently rely on the model accuracy. The gain scheduling controller is sensitive to the uncertainties in the model and ocean

environment. UUV gain scheduling application is given in [74].

The performance of classical control methods are sensitive to the UUV model accuracy, i.e., they are inefficient to handle the model changes, such as parameter variations, external disturbances and sensor noise. In SAUC-E [12] and euRathlon [13] competition, we found PID yaw controller is less efficient than robust control method for low mass AUV. However, realistic UUVs applications face a lot of uncertainties in the complex ocean environment, and the above mentioned control methods are not robust to those uncertainties. Hence, in the early 1981, *Zames* had proposed the H_∞ control methods to solve the robust issues, guaranteeing both stability and high performance. H_∞ control method constrains the energy gains from system input to output using H_∞ norms. H_∞ theory combines the advantage of MIMO state space description and frequency domain analysis. Actually, there is a long history, people begin to notice the importantance of sensitivity, i.e., disturbance rejection, using high gain feedback control to attenuate model variation effects (Single Input Single Output (SISO)). Then, in the 60s, the state space feedback control theory made many breakthroughs, and LQG seems to be theoretically perfect. However, LQG relies on the modeling accuracy. While LQG controllers are implemented in many industrial applications, they still suffer from low robustness performance. According to *Doyle* [75], the LQG can not guarantee stability in presence of uncertainties. Note that, *Doyle et al.* made great contributions to simplify the robust controller synthesis process. They also proposed a synthesizing method using only two *Riccati* equations, which is simple and clear for spreading H_∞ robust control applications.

Robustness means the controller achieves the performance specifications as well as robust stability in presence of uncertainties. In other words, inside all robust stable solutions, the robust control design searches for the optimal controller, which satisfies the performance specifications. The robust control theory can be found in [76, 77]. In this thesis, linear H_∞ robust controller was used. Besides, there are many types of robust controllers. For instance, the H_2 and L_2 robust controllers for nonlinear system, applications are given in [78, 79]. Meanwhile, gain scheduling H_∞ methods are developed for Linear Parameter Varying (LPV) systems. Importantly,

the μ analysis of H_∞ control are used to solve the conservative issues.

There are many robust control applications on UUVs. *Pan* has implemented an indirect robust controller for depth control on the *REMSUS* AUV [80]. *Roche* designed a hierarchical H_∞ controller for depth control of *AsterX* AUV in [81], and a LPV H_∞ controller in [82]. In [83], *Clement* proposed a robust controller for the *VAIMOS* robots. Reduced order H_∞ controller for a torpedo-shaped AUV is shown successfully in [84]. The robust H_∞ yaw controller of *CISCREA* AUV can be found in [66]. Apparently, robust control methods show more robustness than other controllers. There are the advantages such as: control performance reduce the effect of model parametric uncertainty, i.e., require less expensive models; the control output is optimal, i.e., save onboard propulsion energy and expand thruster lifespan; and controllers have high-frequency noise rejection ability [85], *etc.* Nevertheless, the robust control methods have some disadvantages. First, to define the weighting functions for robust synthesis, it is necessary to have in advance the knowledge of the noise and disturbance properties, and the uncertain boundaries. Then, robust synthesis is currently a time consuming process, which is always offline. In addition, the synthesis results are sometimes high order controllers, and usually local optimal results (no guarantee for global answers).

Sliding mode control method is presented in [86]. This control algorithm specializes in handling the uncertainties and nonlinearities of control systems. The sliding surface (an equation) is a critical notion that derived based on the tracking errors. Then, the control outputs are calculated to move the system states towards the sliding surface, which keep the tracking errors to be infinitely small. Typically, there is the sliding mode control application on the *Taipan* AUV, presented by *Vaganay et al.* in [87]. Fossen also proposed an adaptive sliding mode controller in [88]. More applications can be found in [89, 90, 91]. The advantage of sliding mode is its insensitivity to model accuracy and external disturbances. In contrary, the disadvantage are the complexity in implementation and its oscillation issues on the sliding surface (chattering effect).

Backstepping control is a nonlinear control algorithm based on *Lyapunov* method,

which generates asymptotically stable controllers. It has the robustness property, as it is insensitive to the model parametric uncertainties. UUV backstepping applications can be found in [92], and the theory is described in [93, 94].

Adaptive control changes its control parameters, according to the realtime parametric variations and uncertainties of the controlled systems. The control parameters adapts to the plant base on the principle of minimizing closeloop performance evaluations. There are two kind of adaptive control methods: direct methods and indirect methods. The direct methods evaluate the controllers' parameters, and directly change the controllers using the estimated results. In contrast, indirect methods use the estimated plant parameters to calculate required controller designs. Compare to robust control, adaptive control does not need a priori information about the bounds of uncertain parameters. Adaptive control is more flexible and concerned with control law changing themselves, meanwhile, robust control is fixed and guarantees control performance of the systems inside the priori knowledge. Accordingly, adaptive controllers have the advantages of robustness, and requires little about the UUV models. However, there are the drawbacks and limitations. The control plants should not have high-frequency or high-amplitude parametric variations, as the adaptive algorithm attempts to meet the robustness specifications, the controller might not converge.

For UUV systems, the parameter variation is common, e.g., adding or remove a payload, changing working environment from fresh water to sea water, *etc.* Many adaptive control applications were shown successfully on real underwater vehicle tests. In [95] adaptive controller was used to control the diving process of UUV. In [25, 96] *Maalouf* introduced several adaptive controllers for the depth control of a mini ROV. Many other UUV adaptive control application can be found in [97, 98, 99, 88]. A clear review that summarized and compared the current UUV adaptive control applications is given by *Antonelli* in [100].

Outside the state space feedback control framework, artificial intelligence plays an important role in the control field. The ideas are to mimic either the neural structures or the evolutionary process, *etc.* There are the techniques like neural networks control, fuzzy logic control, and genetic algorithms, *etc.* Intelligent controls

can handle nonlinearity and uncertainty issues by universal approximations, however, the calculation is generally very heavy. Neural network control basically involves two steps: system identification and control. The controller iteratively learns the weightings (links between neurons) of structured neural networks from a set of input-output data pairs. It is supposed to capture the dynamics of any system. Then, the system steady state can be used to control the nonlinear plant. The UUV application of a neural network control can be found in [101, 102]. Fuzzy logic control is common for nonlinear underwater vehicle control. Rather than fixing and exact reasoning, the logics approximate the value of input and output data between complete true and complete false. UUV fuzzy logic control applications are given in [103, 104]. The genetic algorithm randomly searches the globe optimal controllers by the process of natural selections. Relevant genetic UUV control application was presented in [105].

It is obvious that the above mentioned control methods all have their advantages and their disadvantages. This makes a good reason to develop hybrid control methods, which combines the advantages of different algorithms. In [88], *Fossen* presented a hybrid adaptive sliding mode controller for UUV. In [101], a neural network control is mixed with adaptive algorithms. Other hybrid UUV control applications can be found in [106, 107].

For UUVs, it is worth to mention some other studies. For example, in [108] predictive control was used for the depth control of UUV. Like gain scheduling control, a feedback linearization method was proposed in [59, 86]. *Smallwood et al.* discussed the importance of model accuracy in the control design. Importantely, *Jaulin* had verified a robust Lyapunov controller using interval analysis algorithm on the *VAIMOS* USV [109].

In the underwater vehicle control field, a pressing need is to improve the robustness of UUV control methods. Potential trends are robust and fast controllers that can assist the pilot or autopilot with better accuracy. It is expected to see optimal propelling actions that save more battery power as well as increasing propeller lifespan. Regulated AUV motions are expected to be less complex for high level guidance, navigation and swarm research.

We presented in this section, the advantages and disadvantages of the state of art UUV modeling and control works. To summarize, we found the current underwater vehicle modeling and control issues are:

- Traditional experimental modeling methods are too expensive and empirical formulas are impractical and inaccurate.
- Robustness is critical for high performance underwater vehicle controllers, and underwater vehicles face a variety of uncertainties in real ocean environment. The effects of those uncertainties to the control performance are still to some extent not clear.

In the next section, the motivation and major works of this thesis are presented. We propose to address the modeling and control issues simultaneously, and combine computational modeling methods with H_∞ robust control algorithm to handle the nonlinearities and uncertainties.

1.3 Motivation and Major Work

In this work, we appointed the complex-shaped semi-AUV CISCREA, as shown in Figure 1-11, and characterized in Table 1.1.

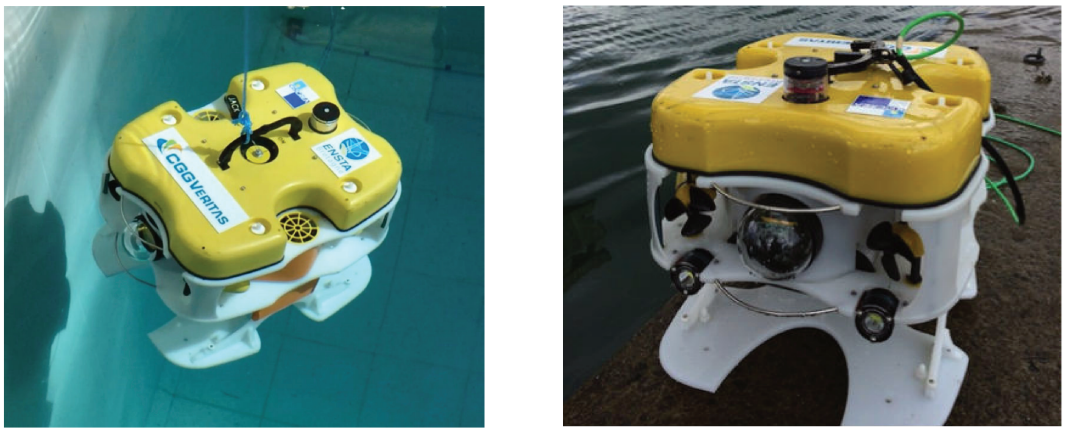

Figure 1-11: CISCREA

As it is proven before, the underwater vehicles play an important role in current marine activities. Meanwhile, the modeling and control work are essential to support

Table 1.1: CISCREA AUV Characteristics

Size	0.525m (L) 0.406m (W) 0.395m (H)
Weight in air	15.56kg (without payload and floats)
Degrees of Freedom	Surge, Sway, Heave and Yaw
Propulsion	2 vertical and 4 horizontal propellers
Speed	2 knots (Surge) &1 knot (Sway, Heave)
Depth Rating	50m
On-board Battery	2-4 hours

high level researches. Therefore, it is important to propose the method combining computational modeling and H_∞ robust control algorithms for complex-shaped underwater vehicles. It is critical to first enhance the AUVs with high performance controllers.

Using AUV, the goal of this thesis is to inspect the underwater oil pipeline leaks, meanwhile, monitor the sedimental conditions. Robustness is the first essential issue to construct this long-term running AUV monitoring networks. The control performance determine the robustness and reliability of underwater vehicles, especially, for underwater environment, the uncertainties make the control design more difficult. Hence, in order to improve the AUV maneuverability, we focus on the two critical issues: accurate model and advanced robust controller.

Although there are many modeling and control applications in the field, and some of them were verified successfully on realistic sea tests, the combination of computational modeling and robust control works are rare. In order to move the AUV design initiatives outside large organizations, i.e., to popularize the underwater vehicles to more civilian applications, we proposed a low-cost and more accessible modeling and control solution. Note that, it is always important to low the cost to build one AUV in order to create a huge network. In the following the major works and contributions of this thesis are presented.

First, according to the complex shapes of the *CISCREA* AUV and many others, we proposed the use of computational modeling methods, for the following reasons:

- Compare to the full-scale and scaled experiments, computational modeling re-

quires no experimental devices. The cost is much lower, and the modeling process is faster.

- Compare to empirical formulas, the computational modeling method is more efficient to handle complex shapes. There is no complex geometry simplification process during the modeling.

- The accuracy and reliability of computational modeling method is decent. It is generally less accurate than experimental methods, but better than the empirical formulas for complex-shaped AUVs. As H_∞ robust control is used, there is only the necessity to understand the uncertain bounds of the dynamic model rather than the exact nominal model.

- Computational modeling methods can replay many physical details, which is useful to locate the focus of control design.

- In this thesis, although the hydrodynamic experiments do not improve the modeling accuracy, instead, it guarantees the reliability of the computational results.

- The computational modeling results can be control oriented, which is convenient to build state space equations and easy to make simulations. It can greatly speed up the model analysis and even design work of high performance UUVs.

In this thesis, we build a dynamic and hydrodynamic model on *CISCREA* AUV using many computational softwares. And the CFD calculation results are compared with experimental data. The major work includes:

- Mass inertia matrix M_{RB} of *CISCREA* AUV is calculated using PRO/ENGINEER$^{\text{TM}}$.

- Added mass matrix M_A is calculated using radiation/diffraction program MCC [110] and WAMIT$^{\text{TM}}$ [61].

- Hydrodynamic programs ANSYS-CFX$^{\text{TM}}$ and STAR-CCM+$^{\text{TM}}$ are studied to predict damping behavior $D(|\nu|)$.

- The bollard thrusts of *CISCREA* AUV are measured. Several motion experiments are designed to verify the reliability of CFD results.

- Damping is found to be the major nonlinearity in the model. A model based linear compensation solution is proposed to linearize the AUV model for robust control design.

In order to handle the uncertainties, we proposed the linear H_∞ control method to guarantee the stability and achieve expected control performance. The reasons for this method are:

- Due to the modeling errors and parameter variations, there are many uncertainties in the mathematical descriptions of the UUV dynamics. Especially, the damping is theoretically hard to precisely predict. Traditional control methods are sensitive to the model accuracy, however, H_∞ robust control is efficient and insensitive to the modeling uncertainties.

- Robust control has disturbance rejection ability, which is important for the ocean environment that with unpredictable wind, wave and currents.

- Damping is the major nonlinearity in the dynamics. Linear H_∞ theory can not directly adapt to the nonlinear model. However, the robustness allows the nonlinear compensation solution, which turns the nonlinear system into a linear system with uncertainties. Although the velocity estimation of damping compensation is not accurate, there is almost no reduce of the robust control performance.

- Sensor noise rejection is important to prevent unnecessary thruster propulsions. Compare to the traditional control methods, robust control is very efficient to filter the noise with a prior knowledge.

- Signal delay effects the control stability and causes serious oscillations. By implementing the *Smith* compensation, we turn the delay problem into a negligible uncertainty that can be tackled using H_∞ control algorithm [111].

H_∞ robust control method is proposed to the control of low-mass and complex-shaped *CISCREA* AUV and others. Without lose of generality, the robust heading controller was implemented and validated in the sea. The major work include:

- A yaw model derived for robust heading control design.
- Linear compensation proposed based on CFD modeling results, which yield a linear system with uncertainties.
- Linear H_∞ controller synthesized and implemented on the *CISCREA* AUV for heading control.
- Kalman filters based on CFD model, which numerically estimates unmeasured as well as noisy states such as angular velocity.
- To handle the signal delay of the electronic compass, we proposed two delay compensation algorithms.
- Proposed yaw control experiments were implemented in the testing pool. Results are compared with PID solutions.
- We conducted several sea tests for the proposed robust yaw controller in Brest port (France) and in La Spezia port (Italy) respectively. Control performance are compared to PID controllers.

1.4 Thesis Outlines

This thesis is organized into 7 chapters. The reminder of the thesis are:

Chapter 2 AUV Modeling

The underwater vehicle modeling notions and basics are introduced in this chapter. The mathematical descriptions utilize the marine vehicle formulations that are proposed by *Fossen*. 6 DOF underwater vehicle model, and its derivative equations, and CISCREA AUV model simplifications are given in the end.

Chapter 3 Numerical CISCREA AUV Model

This chapter presents the model identification of *CISCREA* AUV. The major work is numerically calculating the dynamic and hydrodynamic parameters of: Mass inertia matrix M_{RB}, added mass matrix M_A and damping matrix $D(|\nu|)$. This chapter establishes the 4 DOF CFD model for *CISCREA* AUV. Our identification results showed that the quadratic damping is the dominant component of all damping terms, and it is the major nonlinearity in *CISCREA* model. Some elements of the added mass matrix M_A are found larger than the mass inertia matrix M_{RB} elements, which means the added mass matrix M_A is not a negligible parameter during the acceleration movement.

Chapter 4 *CISCREA* AUV Hydrodynamic Experiment

This chapter is dedicated to validate the numerical model obtained in chapter 3. Bollard thrusts of *CISCREA* propellers were measured, and real world experiments were conducted on the open-loop *CISCREA* to verify the translational and rotational damping parameters. The moving processes were captured by cameras, then analyzed for damping terms. Second order polynomial lines are implemented to approximate the relationship between damping and velocities. Finally, experimental results are compared to the CFD results.

Chapter 5 AUV H_∞ Controller and Simulations

Proposed H_∞ controller is described and simulated in chapter 5. We inherited the numerically obtained model from our previous CFD works. Numerically predicted the actuator force compensates the nonlinear damping behavior result in a linear model with uncertainties. Based on the bounded linear nominal model, we proposed H_∞ approach to handle the uncertainties. In the end, we demonstrates the Matlab simulation results of H_∞, H_∞ without linearization compensations and PID controllers.

Chapter 6 Applicable H_∞ Controller at Sea

For realistic AUV implementations, we improved the H_∞ with kalman filter to estimate unmeasured states, and we developed delay compensators to compensate the sensor delay. Finally, the proposed H_∞ were validated by *CISCREA* in the sea near Brest, and compared to PID control method.

Chapter 7 General Conclusion and Perspectives

Finally, conclusions are drawn in Chapter 7, and future directions of this thesis are given in the end.

1.5 Main Contributions

The main contributions of this thesis are the design and validation of an AUV H_∞ robust control approach using numerical hydrodynamic modeling techniques. We address the numerical AUV dynamic modeling methods and the robust control algorithms simultaneously. For any low-mass and complex-shaped AUVs, the proposed modeling and control approach is demonstrated to have sufficient modeling accuracy and efficiency as well as control robustness and performance. Comparing to PID controllers, the AUV motion control performance can be improved in face of inevitable modeling and environmental uncertainties, dynamic nonlinearities, sensor delay and unmeasured system states. A low mass and complex-shaped *CISCREA* AUV is used to validate the proposed numerical modeling and H_∞ robust control approach in real sea test. In particular, this thesis presents the following points:

- For complex-shaped and low-mass AUV, traditional modeling methods are generally insufficient to reveal the hydrodynamic characteristics. Therefore, the computational fluid dynamic method is suggested to avoid implementing hydrodynamic experiments using expensive equipments. We concluded several important AUV dynamic and hydrodynamic parameters for the AUV control design:
  - Added mass matrix M_A is calculated and compared using radiation/diffraction program WAMIT and MCC.
  - Hydrodynamic programs ANSYS-CFX and STAR-CCM+ are studied to predict damping behavior $D(|v|)$ on the surge, sway, and heave directions. Rotational damping effects are numerically built using moving reference and overset mesh techniques in STAR-CCM+.

  - Mass inertia matrix M_{RB} and the center of gravity CG are approximated using Computer Aided Design (CAD) PRO/ENGINEER (PRO/E).

  Based on these numerical estimations, a four degree-of-freedoms model is derived for the *CISCREA* AUV, which provides the foundations for the hydrodynamic experiment and control design simulations.

- A 4 DOFs (Surge, Sway, Heave, and Yaw) experiment is designed to validate the CFD models and its hydrodynamic parameters. The numerical AUV modeling method is concluded efficient for the complex-shaped underwater vehicles (Using robust control scheme). The hydrodynamic experiment confirms the damping effect is nonlinear, and it is mainly caused by the quadratic damping.

- A model based nonlinear compensated H_∞ control approach is proposed for the of *CISCREA* AUV and others to solve the following issues:

  - Dynamic and hydrodynamic parametric uncertainties.
  - External disturbance from the ocean environment and sensor noise.
  - Nonlinear damping compensation errors.

  The nonlinear damping and parametric uncertainty issues are the two critical problems that solved in the proposed approach.

- To solve the applicable issues in real sea AUV control applications, we proposed an improved nonlinear compensated H_∞ control scheme to handle the sensor delay as well as unmeasured states. The proposed approach is validated as efficient in the *CISCREA* AUV heading control simulations, pool and sea tests. The control performance of the proposed method are compared with traditional PID controllers.

Part II

AUV Modeling

Chapter 2

AUV Modeling

Contents

2.1 Modeling Introduction 34

2.2 Kinematic 35

2.3 Rigid-Body Dynamic of Underwater Vehicles 37

2.4 Hydrodynamics of Underwater Vehicles 40

2.5 Environmental Disturbances 46

2.6 Thruster modeling 47

2.7 6 DOFs Underwater Vehicle Model 48

2.8 Conclusion 49

The mathematical description of underwater vehicle dynamics is essential for the robust control design. A model is necessary to analysis the dynamic and hydrodynamic behaviors of UUVs, i.e., the interactive physics between the underwater vehicle and fluid. In addition, the UUV model provides the foundation for the efficient simulations, which verify different control schemes including PID and H_∞ robust controllers. The reminder sections describe the mathematical modeling process of *CISCREA* AUV.

2.1 Modeling Introduction

Modeling of underwater vehicles involves two parts of study: kinematics and dynamics. Kinematics describe the motion of underwater vehicles without concerning the forces and torques that act on it. That is to say, kinematics describe only the geometrical relations of underwater vehicle position, velocity and accelerations. Dynamics present the accelerating motion of the underwater vehicles, especifically, consider the forces and torques. To be accurate, the dynamic study (kinetic) is divided into classical rigid body dynamics and hydrodynamics. There are many marine vehicles modeling articles and books, and typical descriptions can be found in [59, 112, 113, 114, 115].

In this chapter, 6 DOFs underwater vehicle dynamics are represented by the marine vehicle formulation proposed by *Fossen*, in [114] and [115], using the Society of Naval Architects and Marine Engineers (SNAME) [1950] notions in [116]. For marine systems, usually two coordinate systems, Body Fixed Reference (B-frame) and North East Down Reference (NED-frame) are introduced for convenience as presented by *Fossen* in [114] and shown in Figure 2-1. Positions, angles, linear and angular velocities, force and moment definitions are defined in Tab 2.1. The position vector $\eta \in \mathbb{R}^{6\times1}$, velocity vector $\nu \in \mathbb{R}^{6\times1}$ and force and torque vector $\tau \in \mathbb{R}^{6\times1}$ are defined as equation 2.1, 2.2 and 2.3:

$$\eta = [x, y, z, \phi, \theta, \psi]^T \tag{2.1}$$

$$\nu = [u, v, w, p, q, r]^T \tag{2.2}$$

$$\tau = [X, Y, Z, K, M, N]^T \tag{2.3}$$

Here, η denotes the position and orientation of the underwater vehicles in the NED-frame, ν denotes the linear and angular velocity with coordinates definitions in the B-frame, and τ is used to describe the forces and moments acting on the vehicle in the B-frame.

Table 2.1: The notation of SNAME for marine vessels

	Positions and Angles	Linear and Angular Velocities	Forces and Moments
Coordinate	NED-frame	B-frame	B-frame
Surge	x	u	X
Sway	y	v	Y
Heave	z	w	Z
Roll	ϕ	p	K
Pitch	θ	q	M
Yaw	ψ	r	N

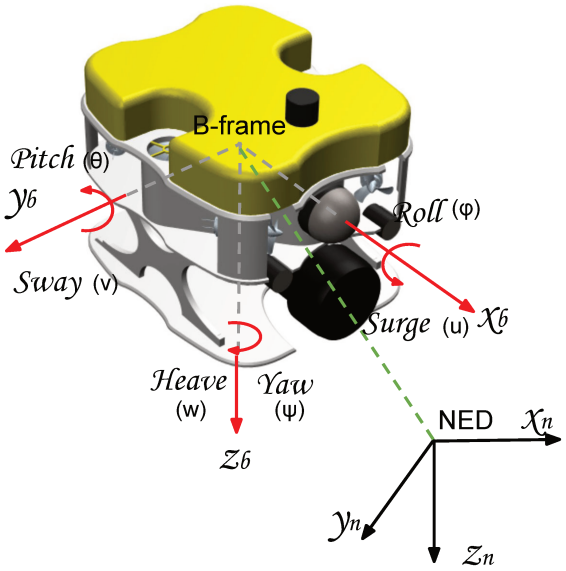

Figure 2-1: B-frame and NED-frame of Underwater Vehicles

2.2 Kinematic

As mentioned before, kinematic is the basic branch of mechanics, which treats only geometrical aspects of the underwater vehicle motions. Talking about the kinematics of marine vehicles or rigid bodies are usually in 6 degree of freedom, and the 6 different motion components are conveniently defined as: surge, sway, heave, roll, pitch and yaw. In equation 2.1 and 2.2, the first three coordinates of η and ν, i.e., vectors of $(x,\ y,\ z\ )$ and $(u,\ v,\ w)$, represent respectively the position and translational motion along each three perpendicular axes of NED-frame and B-frame, as shown in Figure

2-1. The last three coordinates of η and ν, i.e., (ϕ, θ, ψ) and (p, q, r), represent respectively the orientation and rotational motion. NED-frame is fix to an absolute location on the earth, it can be considered as the internal reference for the B-frame. The moving coordinate reference B-frame is fixed to the vehicle, which describes the relative underwater vehicle motion. B-frame origin is usually chosen to coincide with the Center of Gravity (CG) of the vehicle. To summarize, all suggest the kinematic rules are mainly the transformation relationship between the two coordinate references NED-frame and B-frame.

It is known that kinematic relation of velocity vector ν and position vector η is expressed as the vectorial equation 2.4 [114]:

$$\nu = J(\Theta)\dot{\eta} \tag{2.4}$$

where, $J(\Theta) \in \mathbb{R}^{6\times6}$, stands for a transformation matrix between B-frame and NED-frame, $\Theta = [\phi, \theta, \psi]^T$, is the vector of the euler angles on roll, pitch and yaw directions, shown in Figure 2-1.

In equation 2.4, $J(\Theta) \in \mathbb{R}^{6\times6}$ matrix relates the time derivative of underwater vehicle position and angle to the translational and rotational velocities. $J(\Theta)$ is a rotational matrix to change the basis of position vector derivative ($\dot{\eta}$) from NED-frame to B-frame (where defines the velocity vector, ν), it is a function of $\Theta = [\phi, \theta, \psi]^T$. The formulation of $J(\Theta)$ is presented as equation 2.5:

$$J(\Theta) = \begin{bmatrix} R(\Theta) & \mathbf{0}_{3\times3} \\ \mathbf{0}_{3\times3} & T(\Theta) \end{bmatrix} \tag{2.5}$$

where, $R(\Theta) \in \mathbb{R}^{3\times3}$ is the linear velocity transformation matrix, and $T(\Theta) \in \mathbb{R}^{3\times3}$ is the angular velocity transformation matrix. Assume that, $c(\cdot) = cos(\cdot), s(\cdot) = sin(\cdot)$ and $t(\cdot) = tan(\cdot)$, then, we have respectively the $R(\Theta)$ and $T(\Theta)$ definitions in

equation 2.6 and 2.7:

$$T(\Theta) = \begin{bmatrix} 1 & s\psi t\theta & c\phi t\theta \\ \mathbf{0} & c\phi & s\phi \\ \mathbf{0} & \frac{s\phi}{c\theta} & \frac{c\phi}{c\theta} \end{bmatrix} \tag{2.6}$$

$$R(\Theta) = \begin{bmatrix} c\psi c\theta & -s\psi c\phi + c\psi s\theta s\phi & s\psi s\phi + c\psi c\phi s\theta \\ s\psi c\theta & c\psi c\phi + s\phi s\theta s\psi & -c\psi s\phi + s\theta s\psi c\phi \\ -s\theta & c\theta s\phi & c\theta c\phi \end{bmatrix} \tag{2.7}$$

Note that $T(\Theta)$ is not defined at the pitch angle of $\frac{\pi}{2}$, which is called the singularity problem of euler angle representation. Consequently, there is an alternative representation of kinematic equations using quaternion. However, for most of the underwater applications such as all ASVs and our *CISCREA* AUV, it is not allowed to approach the singularity condition. Hence, the mathematical descriptions of the quaternion is only mentioned in the appendix A.2.

Depending on [114], rigid-body hydrodynamic forces and moments can be linearly superimposed. Therefore, the overall non-linear underwater model can be characterized by two parts, the rigid-body dynamic and hydrodynamic formulations (hydrostatics included). In the next section, underwater vehicle rigid-body dynamic is first introduced.

2.3 Rigid-Body Dynamic of Underwater Vehicles

Without concerning the hydrodynamics, the underwater vehicles are considered as a rigid body moving in the free space. That is to say, the underwater vehicle is rigid and 6 DOFs rigid-body dynamics obey the Newton-Euler formulation (Newton's second law) or alternatively Lagrangian Formulation (momentum and energy conservations). In this section the translational and rotational motion of underwater vehicles are derived according to classical Newtonian mechanics. The derivations of equations can be found in the appendix A.3.

It is shown that the 6 DOFs rigid-body dynamic equations of underwater vehicle

motion can be conveniently expressed as a vectorial form in equation 2.8:

$$M_{RB}\dot{\nu} + C_{RB}(\nu)\nu = \tau_{env} + \tau_{pro} \tag{2.8}$$

where, all the definitions are presented in Table 2.2

Table 2.2: Nomenclature of the notations of rigid-body dynamics

Parameter	Description
$M_{RB} \in \mathbb{R}^{6\times6}$	AUV rigid-body mass and inertia matrix
$C_{RB} \in \mathbb{R}^{6\times6}$	Rigid-body induced coriolis-centripetal matrix
$\tau_{env} \in \mathbb{R}^{6\times1}$	Environmental disturbances (wind, waves and currents)
$\tau_{pro} \in \mathbb{R}^{6\times1}$	B-frame resulting forces and torques induced by the thrusters
ν	linear and angular velocity vector

As mentioned before, underwater vehicle rigid-body dynamics are represented in 6 DOFs. Therefore, the equation 2.8 actually presented six equilibrium equations of all the forces and torques that acting on the rigid body underwater vehicle under the B-frame reference. The decomposition of equation 2.8 can be found in the Appendix A.4. The above vectorial forces and torques are considered to act on the vehicle's center of gravity, and they are balanced, including: the inertia induced force and torque vector $M_{RB}\dot{\nu}$ (Newton second law); the Coriolis force and torque vector $C_{RB}(\nu)\nu$, which is caused by the rotation of the earth; thruster propulsion τ_{pro} in 6 DOFs; and the external disturbance τ_{env} like wind, waves and currents. For most of the underwater vehicles with hard structures, rigid assumption is common and efficient, which yields a simple formulation on a single mass point and eliminates the consideration of forces acting between individual elements of mass [114]. Note that for the underwater robots with flexible structures or segments, like underwater snake robots, the dynamics are different, which is not mentioned in this thesis.

Rigid-body mass inertia matrix $M_{RB} \in \mathbb{R}^{6\times6}$ is a symmetric and positive definite matrix, which is defined in equation 2.9 and 2.10, where m is the mass, $I_{3\times3}$ is the identity matrix, and $r_G = [x_G, y_G, z_G]^T$ is the vector from O_b (origin of B-frame) to CG. If $r_G = 0$, i.e., $O_b \equiv CG$, then the matrix M_{RB} will be simplified. $S(r_g^b)$ is a

skew-symmetric matrix according to the definition 2.2 in [114]. Moreover, symmetric properties of cubic AUV, in $x = 0$ and $y = 0$ planes, can be used to simplify the inertia components to a rough diagonal form.

$$M_{RB} = M_{RB}^T = \begin{bmatrix} mI_{3\times3} & -mS(r_g^b) \\ mS(r_g^b) & I_0 \end{bmatrix} \tag{2.9}$$

$$M_{RB} = \begin{bmatrix} m & 0 & 0 & 0 & mz_G & -my_G \\ 0 & m & 0 & -mz_G & 0 & mx_G \\ 0 & 0 & m & my_G & -mx_G & 0 \\ 0 & -mz_G & my_G & I_x & -I_{xy} & -I_{xz} \\ mz_G & 0 & -mx_G & -I_{yx} & I_y & -I_{yz} \\ -my_G & mx_G & 0 & -I_{zx} & -I_{zy} & I_z \end{bmatrix} \tag{2.10}$$

Here, $I_0 = I_0^T > 0$ is the inertia matrix, which is also symmetric and positive definite [114]. The definition of I_0 are given as equation 2.11:

$$I_0 = I_0^T = \begin{bmatrix} I_x & -I_{xy} & -I_{xz} \\ -I_{yx} & -I_y & -I_{yz} \\ -I_{zx} & -I_{zy} & -I_z \end{bmatrix} \tag{2.11}$$

$C_{RB} \in \mathbb{R}^{6\times6}$ is a skew-symmetric matrix, which contributes to the centrifugal force on the rigid body. Decompose M_{RB} as equation 2.12, then, we can derived the definition of C_{RB} in equation 2.13.

$$M_{RB} = \begin{bmatrix} M_{11} & M_{12} \\ M_{21} & M_{22} \end{bmatrix} \tag{2.12}$$

$$C(v) = \begin{bmatrix} 0_{3\times3} & -S(M_{11}\nu_1 + M_{12}\nu_2) \\ -S(M_{11}\nu_1 + M_{12}\nu_2) & -S(M_{21}\nu_1 + M_{22}\nu_2) \end{bmatrix} \tag{2.13}$$

Here we know, C_{RB} depends on the mass inertia matrix M_{RB}, and the translational and rotational velocities, $\nu_1 = [u, v, w]^T$, $\nu_2 = [p, q, r]^T$, of the underwater vehicles.

Matlab function "m2c.m" is a practical way to calculate the C_{RB} using M_{RB} and ν information, which is introduced in Marine System Simulator (MSS) in [117]. In our case, C_{RB} are neglected, because the underwater vehicle speed is low enough to be considered, $C_{RB} \approx 0$.

2.4 Hydrodynamics of Underwater Vehicles

The ocean environment is complex, and the hydrodynamics play an import role in the control design of underwater vehicles. Actually, the hydrodynamic effects make the control design very difficult, which separate the underwater control design from air and land robots. In the following it is introduced the different types of hydrodynamic forces and torques that the underwater vehicles would encounter in the ocean:

- Radiation Induced Forces (neglecting second order coupling terms):
  - Added Mass due to the inertia of the surrounding fluid.
  - Hydrodynamic Damping due to energy consumption of surrounding fluid.
  - Restoring Forces due to *Archimedes* (weight and buoyancy).
- External disturbance: wind, wave and current.
- Thruster propulsions

As mentioned in [59] and [118], it is common to assume that the hydrodynamic forces and moments on a rigid body can be linearly superposed by considering two sub-problems (*Faltinsen*, 1990). Therefore, the underwater vehicle hydrodynamic force and torque vector, $\tau_{hydro} \in \mathbb{R}^{6\times1}$ can be superposed to the rigid-body dynamic equation 2.8, and as a result, derives the equation 2.14.

$$M_{RB}\dot{\nu} + C_{RB}(\nu)\nu = \tau_{env} + \tau_{hydro} + \tau_{pro} \tag{2.14}$$

It is presented in the *Fossen* marine vehicle model [114], the total acting hydrodynamic of the underwater vehicle, i.e., τ_{hydro}, can be decomposed into the sum of

sub-hydrodynamic effects in equation 2.15:

$$\tau_{hydro} = -M_A\dot{\nu} - C_A(\nu)\nu - D(|\nu|)\nu - g(\eta) \tag{2.15}$$

Here, the definitions of the various types of hydrodynamic effects in equation 2.15 are given in Table 2.3.

Table 2.3: Nomenclature of the notations of hydrodynamics

Parameter	Description
$M_A \in \mathbb{R}^{6\times6}$	Added mass matrix
$C_A \in \mathbb{R}^{6\times6}$	Added mass induced coriolis-centripetal matrix
$D(\|v\|) \in \mathbb{R}^{6\times6}$	Damping matrix
$g(\eta) \in \mathbb{R}^{6\times1}$	Restoring forces and moments vector
$\tau_{hydro} \in \mathbb{R}^{6\times1}$	Vector of hydrodynamic forces and moments
ν	linear and angular velocity vector

Actually, the hydrodynamic effects of the fluid acting on the marine structure can be divided into two kind: radiation forces and diffraction forces. For underwater water vehicles, as the vehicle size is usually small, it is common to avoid diffraction forces, and concerns mainly the radiation forces. In our case, diffraction forces of wind, wave and current effects are discussed in the reminder thesis. In the following, we first presented the three major radiation induce forces: restoring force $g(\eta)$, added mass $M_A\dot{\nu} + C_A(\nu)\nu$, and hydrodynamic damping $D(|\nu|)\nu$.

2.4.1 Restoring Force

Underwater vehicles are constrained by two hydrostatic forces: gravitational and buoyant forces, i.e, $W \in \mathbb{R}$ and $B \in \mathbb{R}$, which are called restoring forces. Generally, the floating equilibrium is achieved by W and B is equal and working on the same straight vertical line. For an underwater vehicle with neutral buoyancy, the weight W is approximately equal to the buoyancy force B (B is slightly larger). In equation 2.16, it is presented the oldest engineering result, the gravity law and *Archimedes* law.

$$W = mg, B = \rho g \nabla \tag{2.16}$$

Here, g is the gravity acceleration, ρ is the fluid density, and ∇ is the displaced fluid volume.

For the underwater vehicles, it is common to design the vehicles to be neutrally buoyant, which saves the floating energy and keep the vehicle safe from sinking. As pointed out by *Fossen*, [114], the restoring forces and moments vector $g(\eta) \in$ can be simplified into equation 2.17, if the underwater vehicle is neutrally buoyant (full definition of the restoring forces and moments vector $g(\eta)$ is given in the Appendix A.6).

In equation 2.17, $BG = [BG_x, BG_y, BG_z]^T$ is the distance from the CG to Center of Buoyancy (CB). Actually, $g(\eta)$ is a function of the vehicle's position and attitude, it decides the stability of the underwater vehicle. When the AUV is driven away from the equilibrium states under external disturbance, $g(\eta)$ can provide the torques to return to the equilibrium states. It is like a spring system, the buoyancy center CB is always higher than the center of gravity CG, which can generate a torque to oscillate back to equilibrium. For *CISCREA* AUV, CB and CG can be located using trial and error method on adding and removing the payload and floats.

$$g(\eta) = \begin{bmatrix} 0 \\ 0 \\ 0 \\ -BG_y W cos\theta cos\phi + BG_z W cos\theta sin\phi \\ -BG_z W sin\theta + BG_x W cos\theta sin\phi \\ -BG_x W cos\theta sin\phi - BG_y W sin\theta \end{bmatrix} \tag{2.17}$$

2.4.2 Added Mass

Added mass forces and moments, i.e., $\{M_A\dot{\nu} + C_A(\nu)\nu\} \in \mathbb{R}^6$, are induced by the surrounding fluid inertia. It is common to separate the added mass forces and moments in terms which belong to an added mass matrix $M_A \in \mathbb{R}^{6\times6}$ and a matrix of

hydrodynamic Coriolis terms denoted $C_A \in \mathbb{R}^{6\times6}$. The added mass matrix M_A should be understand as 'pressure-induced' virtual conception which are proportional to the acceleration $\dot{\nu}$ of the body [114]. For underwater vehicles, added mass M_A in some directions are even larger than the mass and inertias of the rigid body on the 6 DOFs. To derive the expressions for these added mass matrix, an energy approach in terms of Kirchhoff's equations will be used [114]. Alternatively, we can depict the added mass forces and moments provide the energy to make an empty space from the fluid ahead of the underwater vehicle, and fill the space by fluid in the tail of the robot, in order to make the vehicle accelerating forward. The added mass matrix M_A is defined in equation 2.18.

Generally, the added mass matrix $M_A \in \mathbb{R}^{6\times6}$ is positive definite (fully submerged), and the diagonal elements of the matrix are positive. Only in a few cases, the diagonal elements are negative, which can be found in [114]. In real fluid the 36 elements of M_A may all be distinct, and experience has shown $M_A = M_A^T$ is actually a good approximation in (*Wendel* 1956) [114]. For underwater vehicles, as the vehicle speed is very slow, the off-diagonal elements of the added mass matrix M_A induced negligible effects compared to the diagonal elements. For most practical applications, the off-diagonal elements of M_A will be small compared to the diagonal elements. Therefore, in most of the underwater vehicles, we can use the diagonal form of the added mass matrix M_A, which is described in equation 2.19.

$$M_A^{full} = -\begin{bmatrix} X_{\dot{u}} & X_{\dot{v}} & X_{\dot{w}} & X_{\dot{p}} & X_{\dot{q}} & X_{\dot{r}} \\ Y_{\dot{u}} & Y_{\dot{v}} & Y_{\dot{w}} & Y_{\dot{p}} & Y_{\dot{q}} & Y_{\dot{r}} \\ Z_{\dot{u}} & Z_{\dot{v}} & Z_{\dot{w}} & Z_{\dot{p}} & Z_{\dot{q}} & Z_{\dot{r}} \\ K_{\dot{u}} & K_{\dot{v}} & K_{\dot{w}} & K_{\dot{p}} & K_{\dot{q}} & K_{\dot{r}} \\ M_{\dot{u}} & M_{\dot{v}} & M_{\dot{w}} & M_{\dot{p}} & M_{\dot{q}} & M_{\dot{r}} \\ N_{\dot{u}} & N_{\dot{v}} & N_{\dot{w}} & N_{\dot{p}} & N_{\dot{q}} & N_{\dot{r}} \end{bmatrix} \tag{2.18}$$

$$M_A = -diag\begin{Bmatrix} X_{\dot{u}} & Y_{\dot{v}} & Z_{\dot{w}} & K_{\dot{p}} & M_{\dot{q}} & N_{\dot{r}} \end{Bmatrix} \tag{2.19}$$

The added mass matrix $M_A \in \mathbb{R}^{6\times6}$ can be derived by applying potential theory,

under the assumption of inviscid fluid, no circulation and that the body is completely submerged in an unbounded fluid [114]. Meanwhile, the M_A parameters can be numerically calculated by applying strip theory. The strip theory divides the submerged surface of the underwater vehicle into infinity strips or pieces, and sum all the hydrodynamic coefficients on each pieces together. In the next chapter, numerical softwares are introduced to calculated the added mass parameters of *CISCREA* AUV.

As mentioned before, the added mass corilois matrix $C_A(\nu) \in \mathbb{R}^{6\times6}$ can be neglected in front of $C_{RB}(\nu) \in \mathbb{R}^{6\times6}$, hence, the definitions of $C_A(\nu)$ is only mentioned in appendix A.5 in case of high speed underwater vehicle applications.

2.4.3 Damping

Hydrodynamic damping matrix, $D(|\nu|) \in \mathbb{R}^{6\times6}$, should be carefully involved in the underwater vehicle model. $D(|\nu|)$ is the parametric matrix of hydrodynamic forces and moments, $D(|\nu|)\nu \in \mathbb{R}^6$, which is a function of linear and angular velocities $\nu \in \mathbb{R}^6$. No matter from theoretically or practically point of view, the damping effects of complex shaped underwater vehicles are hard to be precisely predicted.

As described in equation (2.20), damping in the fluid consists of four parts: Potential damping $D_P(|\nu|) \in \mathbb{R}^{6\times6}$, skin friction $D_S(|\nu|) \in \mathbb{R}^{6\times6}$, wave drift damping $D_W(|\nu|) \in \mathbb{R}^{6\times6}$ and vortex shedding damping $D_M(|\nu|) \in \mathbb{R}^{6\times6}$.

$$D(|\nu|) = D_P(|\nu|) + D_S(|\nu|) + D_W(|\nu|) + D_M(|\nu|) \tag{2.20}$$

Potential damping $D_P(|\nu|) \in \mathbb{R}^{6\times6}$ is a radiation induced damping term, which is negligible comparing to the viscous damping.

Skin friction damping $D_S(|\nu|) \in \mathbb{R}^{6\times6}$ is generated by the laminar effects on the boundary layer. Generally, $D_S(|\nu|)$ is important for the low frequency motion analysis of marine vessels, and should be considered for the control design. In addition to the linear laminar effects, usually high frequency turbulence on the boundary layer contributes to the quadratic or highly nonlinear skin friction damping.

Wave drift damping $D_W(|\nu|) \in \mathbb{R}^{6\times6}$ consumes the advancing energy of the un-

derwater vehicle in the form of generating waves on the free surface. However, for underwater vehicle, the wave drift damping $D_W(|\nu|)$ is generally negligible, because the robot works underwater most of the time.

Vortex shedding damping $D_M(|\nu|) \in \mathbb{R}^{6\times6}$ assumes the fluid is viscous, and consumes the advancing energy of the constant speed underwater vehicles by inducing vortex phenomenon. According to *D'Alambert* paradox: constant speed underwater vehicle encounters no forces and torques in the non-viscous fluid. However, in viscous fluid, the vortex will consume a large part of the vehicle's energy, and induced resistance to the advancing motion of underwater vehicles. $D_M(|\nu|)$ is also considered as an important term of the *Morison* equation. In the model identification chapters, vortex shedding damping $D_M(|\nu|)$ and *Morison* equation are discussed on the *CISCREA* AUV.

As presented in [114], in real fluid the 6 DOFs damping of underwater vehicles are highly nonlinear and coupled, it is difficult to separate these effects. Therefore, the *Fossen* model assumes that high order damping effects can be neglect, and practically proposes that different damping terms contribute to either linear or quadratic damping. Then, the damping decomposition equation (2.21) is introduced,

$$D(|\nu|) = D + D_n(|\nu|) \tag{2.21}$$

where, $D \in \mathbb{R}^{6\times6}$ is the linear damping matrix and $D_n(|\nu|) \in \mathbb{R}^{6\times6}$ is a quadratic damping matrix. According to [114], if the underwater vehicle's velocities are sufficiently high D can be neglected. Otherwise, $D_n(|\nu|)$ is negligible. Assume the damping elements is not coupled, i.e., off-diagonal elements are negligible, then, the damping matrix $D(|\nu|) \in \mathbb{R}^{6\times6}$ can be simplified into a diagonal form in equation 2.22

$$\begin{aligned} D(|\nu|) = &-diag\left\{X_u \quad Y_v \quad Z_w \quad K_p \quad M_q \quad N_r\right\} \\ &-diag\left\{X_{u|u|}|u| \quad Y_{v|v|}|v| \quad Z_{w|w|}|w| \quad K_{p|p|}|p| \quad M_{q|q|}|q| \quad N_{r|r|}|r|\right\} \end{aligned} \tag{2.22}$$

2.5 Environmental Disturbances

The marine disturbances, such as the wind, waves and current contribute to the environmental disturbances $\tau_{env} \in \mathbb{R}^{6\times 1}$. Generally, environmental disturbances τ_{env} is a large part of the underwater vehicle dynamic uncertainties. It is clear that predictions of the ocean wind, wave and current can improve the AUV modeling and control design quality. Therefore, the models of environmental disturbances at real sea are discussed in [114].

Actually, the wind, wave and current of the ocean are really complex, including additive and multiplicative types of random disturbances. However, in practice a good assumption according to [114] are, the wind, wave and currents are considered to be linearly superposed for marine vehicles, which separates the effects into linear components.

First, the current plays major role and has many different types. Wind generated currents are induce by the interaction of atmosphere and ocean surface. Then, thermohaline currents are generate by the thermal and salinity balancing process of difference ocean regions. Thermohaline currents varies a lot and result in the distinct properties of currents in different ocean regions. The tidal components of the ocean circulation also induced obvious random currents, which can be up to $2-3\ m/s$ in some region. To summarize, the current disturbances must be considered in the control design of underwater vehicles.

Then, we should notice that for an underwater vehicle in deep water, wind and waves are considered to be less important than current disturbance. In contrast, for most shallow-water underwater vehicle control designs, the wind and wave effects are considered to be disturbances adding to the dynamics. Note that, wind and wave are indeed critical for the control design of shallow water underwater vehicles, such as [119]. The modeling process of ocean wind and waves can be found in [115, 114].

2.6 Thruster modeling

The dynamics properties of the underwater vehicles thrusters are highly nonlinear and complex [3]. To achieve better control performance, it is advised to get an accurate thrust model in order to adequately map the required thrust to the propeller's rotational speed [120, 25]. In order to derive an accurate thruster model, it is necessary to precisely measure the flow velocity to [25]. Currently, one of the main obstacles is there exist no efficient instruments to measure this flow velocity. Therefore, most control designs for underwater vehicles tend to neglect the thruster dynamics. It is common to treat thruster modeling errors as unknown disturbances in [25]. In this section, we will present the thruster mathematical model, more underwater vehicle thruster modeling articles can be found in [25], [114].

According to the *Fossen* model, the thruster force and torque vector $\tau_{pro} \in \mathbb{R}^6$ is a nonlinear function of the linear and angular velocity vector $\nu \in \mathbb{R}^6$, and propeller revolution vector $u \in \mathbb{R}^p (p \geqslant 6)$, which is presented in equation 2.23.

$$\tau_{pro} = b(\nu, u) \tag{2.23}$$

First, *Blanke* derives a 1st-order approximation of the induced thrust T and torque Q for a single screw propeller as equations 2.24, 2.25, and 2.26 [114].

$$T = \rho D^4 K_T(J_0)|u|u(J_0) \tag{2.24}$$

$$T(u, V_a) = T_{|u|u}|u|u + T_{|u|V_a}|u|V_a \tag{2.25}$$

$$Q(u, V_a) = Q_{|u|u}|u|u + Q_{|u|V_a}|u|V_a \tag{2.26}$$

Here , D_p denotes the propeller diameter, ρ the water density and V_a the advance speed at the propeller (speed of the water going into the propeller). J_0 is the advance number and K_T is the thrust coefficient present in equations 2.27 and 2.28

$$J_0 = \frac{V_a}{uD_p} \tag{2.27}$$

$$K_T = \alpha_1 + \alpha_2 \frac{V_a}{uD_p} \tag{2.28}$$

Although the forward and backward thrusts will be non-symmetrical, for most of the applications it is efficient to make a symmetric assumption [114]. Meanwhile, in most practical applications the bilinear model can be approximated by an affine model, that is a system which is linear in its input, as equation 2.29.

$$\tau_{pro} = Bu \tag{2.29}$$

In the reminder of this thesis, we will consider the affine model with uncertainties is enough for the following underwater vehicle robust control design.

2.7 6 DOFs Underwater Vehicle Model

In order to put forward the 6 DOFs dynamic and hydrodynamic underwater vehicle model, i.e., equations 2.14 (NED-frame) and 2.15(B-frame), in the same inertial coordinate, the previous mentioned kinematic transformation $J^{-1}(\Theta$ is used to derived equation 2.30 ($*$ stands for the variables in NED-frame):

$$M^*\ddot{\eta} + D^*(|\nu|)(\dot{\eta}) + g^*(\eta) = \tau^*_{pro} + \tau^*_{env} \tag{2.30}$$

Here, the definitions are given in the following equations 2.31, 2.32, 2.33, 2.34, 2.35, and 2.36.

$$M = M_{RB} + M_A \tag{2.31}$$

$$M^* = J^{-T}(\Theta) M J^{-1}(\Theta) \tag{2.32}$$

$$D^*(|\nu|) = J^{-T}(\Theta) D(|\nu|) J^{-1}(\Theta) \tag{2.33}$$

$$g^*(\eta) = J^{-T} g(\eta) \tag{2.34}$$

$$\tau^*_{pro} = J^{-T}\tau^*_{pro} \tag{2.35}$$

$$\tau^*_{env} = J^{-T}\tau^*_{env} \tag{2.36}$$

It should be notice that, the added mass matrix M_A and the damping matrix $D(|\nu|)$ are two major hydrodynamic components of underwater vehicles. They are generally difficult to obtain with good precision. In the next chapter, the hydrodynamic parameter identification work will focus on the identification of added mass matrix M_A and damping matrix $D(|\nu|)$.

2.8 Conclusion

In this chapter, the mathematical representation of the dynamic and hydrodynamic underwater vehicle model is given base on the *Fossen* marine vehicle formulations. First, the kinematics, i.e, the transformation rules between body-fix reference and inertial reference, are discussed. Then, the kinetics including classical rigid-body dynamic and hydrodynamic components are presented assuming all parts can be linearly superposed. Furthermore, the environmental disturbance and thruster model are given in the end. Finally, the 6 DOFs underwater vehicle model is presented in the inertial reference. To summarize all, this chapter provides the mathematical foundation for the identification and control design of underwater vehicles.

Chapter 3

Numerical CISCREA AUV Model

Contents

3.1 Rigid-body Mass Inertia Matrix 52

3.2 Added Mass Matrix 56

3.3 Damping Approximation 65

3.4 Four CFDs model of *CISCREA* AUV 83

3.5 Conclusion 85

This chapter is dedicated to describe the *CISCREA* AUV model as well as its major dynamic and hydrodynamic parameters: Mass inertia matrix M_{RB}, added mass matrix M_A and damping matrix $D(|\nu|)$. Due to the complex structure, traditional empirical formula approximation is not as efficient as it performes on the slender shaped AUVs [55]. Meanwhile, full-scale and scaled hydrodynamic experiments are generally expensive [55, 58, 28]. Therefore, to solve the modeling problems of complex-shaped underwater vehicles, we propose to numerically derive the hydrodynamic parameters using CFD software. In order to calculate each hydrodynamic parameter of the *CISCREA* AUV for the robust heading control design, the following CFD software is used in this section:

- Mass inertia matrix M_{RB} and the center of gravity CG are approximated using

CAD software PRO/E™. PRO/E™ was chosen for its convenient interface with hydrodynamic programs ANSYS-CFX™ and STAR-CCM+™, which are used for advanced hydrodynamic behavior analysis of the underwater robots. Hydrodynamic analysis applications using PRO/E™ and ANSYS-CFX™ on AUVs and ROVs can be found in [111, 121].

- Added mass matrix M_A is calculated using radiation/diffraction program MCC and WAMIT™. The approximations of *CISCREA* AUV added mass parameter given by MCC and WAMIT™ are compared. WAMIT™ is a leading commercial program in the offshore industry, this program is well proved in the hydrodynamic analysis of offshore platforms and vessels. In contrast, MCC is an open source program that is dedicated to the numerical analysis of marine objects added mass parameters.

- Hydrodynamic programs ANSYS-CFX™ and STAR-CCM+™ are studied to predict damping behavior $D(|\nu|)$ on the direction of surge, sway, and heave. Note that rotational damping effects are numerically built using moving reference and overset mesh techniques in STAR-CCM+™.

3.1 Rigid-body Mass Inertia Matrix

Due to different density components, the inertia tensor I_0 matrix (equation 3.2) and the coordinates of the center of gravity CG of *CISCREA* AUV can not be extracted using the direct calculation of equation (3.1), see [114].

$$m = \int_V \rho_m dV, \quad I = \int_V r^2 \rho_m dV \tag{3.1}$$

Here, ρ_m is the density of the related elementary volume dV, V is the total volume of the body, r is the distance between volume element dV and CG, m is the robot mass, I_0 is the inertia tensor referred to the B-frame (and its 9 elements are the moments of inertia about the three B-frame axes, for more details about the underwater vehicle rigid body derivations, please check appendix A.3).

$$I_0 = \begin{bmatrix} I_x & -I_{xy} & -I_{xz} \\ -I_{yz} & I_y & -I_{yz} \\ -I_{zx} & -I_{zy} & I_z \end{bmatrix} \tag{3.2}$$

Note that the inertia tensor I_0 matrix is a function of the CG coordinates, r and ρ_m of each dV (A.3). I_0 matrix is an important part of the mass inertia matrix M_{RB}, see equation (2.10). Correspondingly, a complex-shaped AUV has many different density components installed with different distances from the CG, these fact becames a hard problem to precisely predict the inertia tensor I_0 matrix and the mass inertia matrix M_{RB}.

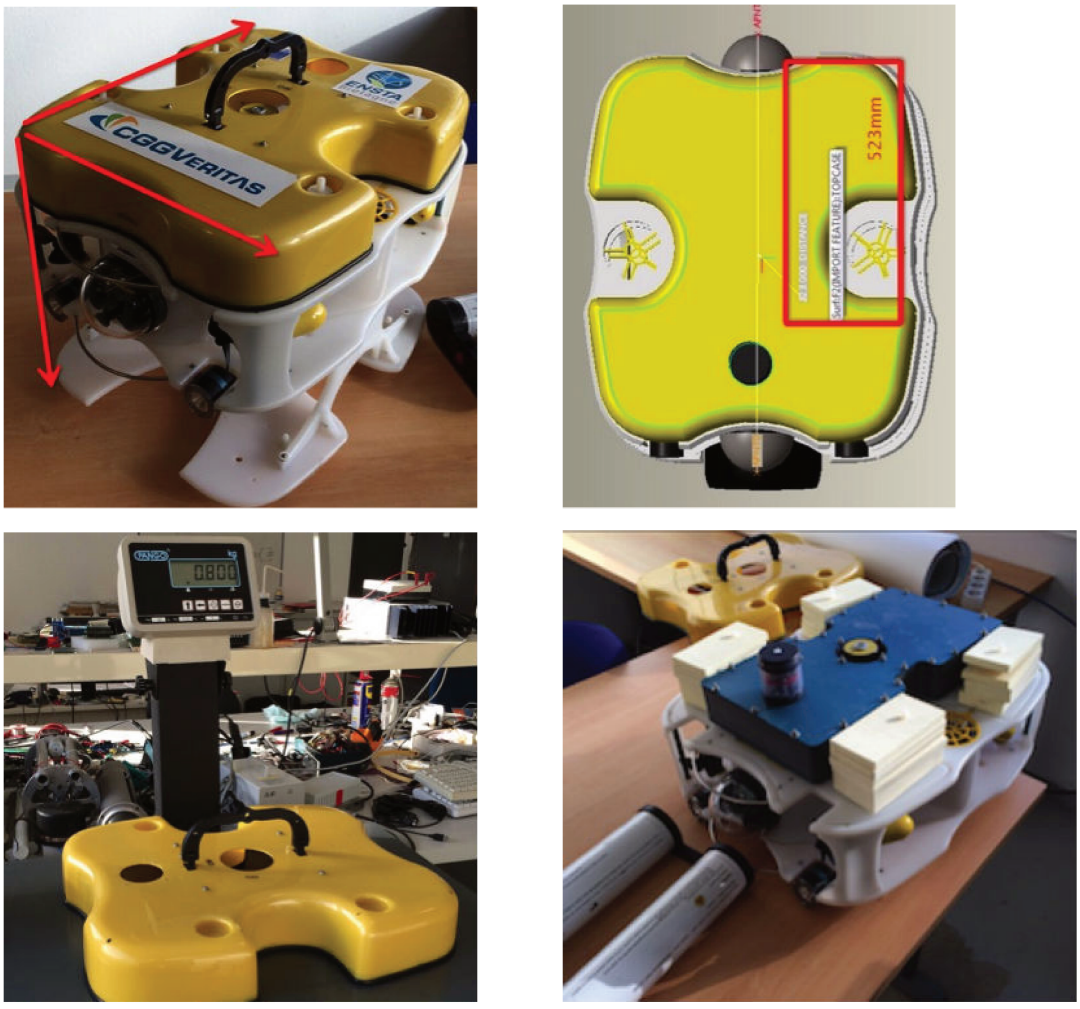

Figure 3-1: Measure the size and weight of main components on *CISCREA* AUV

In order to approximate precisely the mass inertia matrix M_{RB} of *CISCREA*,

we used the CAD software PRO/E. First, the *CISCREA* AUV is disassembled into many large pieces, and measured in size and weight, as shown in Figure 3-1. The disassembled components are assumed to have a constant density. Then, the measured data is assigned to each 3D component of a simplified underwater vehicle CAD model in PRO/E. The explode view of the 3D underwater vehicle is shown in Figure 3-2. At last, the mass inertia matrix M_{RB} and CG are numerically calculated by the PRO/E software. Note that, the *CISCREA* AUV is symmetric on surge and sway directions, therefore, the measurement errors of each component should have little effect to the M_{RB} estimation.

In Figure 3-2, the *CISCREA* AUV is disassembled or simplified into the following components: 6 propellers, the blue waterproof box of control electronics, the black waterproof tube of electronic sensors, the battery group, the LED lens, the PVC supports at the bottom, the PVC main framework and the top fairing. As the floatings and payloads are often changed for different missions, therefore, they are neglected in the estimation of M_{RB}. The mass distributions of *CISCREA* AUV are presented in table 3.1. By fixing the volumes of the components in the PRO/E configurations, hence, we evaluated the density parameters for each part in order to meet the mass results in table 3.1. Then, the software PRO/E can calculate the coordinates of gravity CG and inertia tensor I_0 matrix (the output data of PRO/E are given in appendix B.1).

Table 3.1: The mass distribution of the *CISCREA* AUV

Components	**Mass** (kg)
Battery group	3.65
Waterproof tube of electronic sensors	2.48
Top fairing	0.79
2 LED lens	0.46
PVC main framework	2.62
PVC supports at the bottom	1.63
6 propellers	0.6
Waterproof box of control electronics	3.42
Total AUV weight	15.65

In figure 3-3, the PRO/E calculations show that the CG of *CISCREA* AUV is

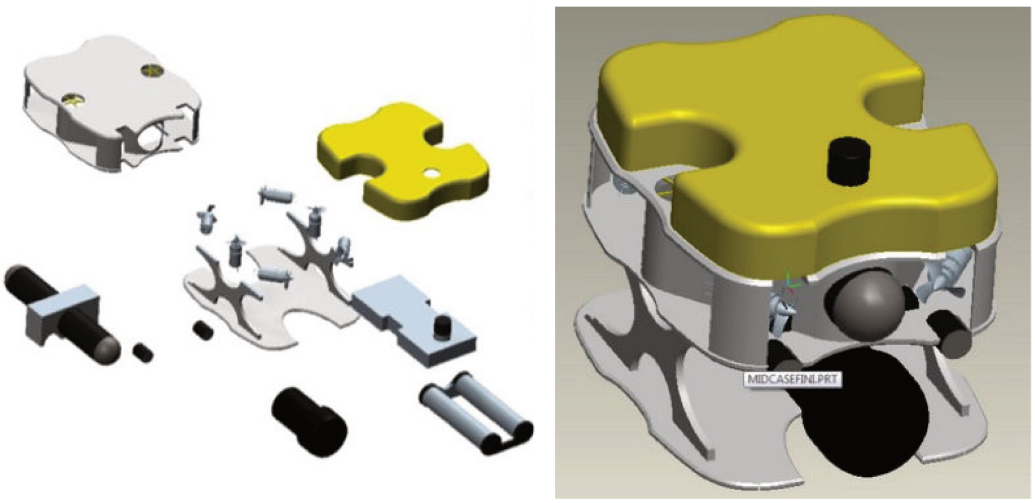

Figure 3-2: Explode View of the *CISCREA* AUV

about 223 mm from the bottom and 224 mm from the tip of the waterproof tube. Meanwhile, the inertia tensor I_0 matrix of PRO/E estimation around the CG (O_b) point is given in equation 3.3 (unit of each inertia element is $kg \cdot m^2$).

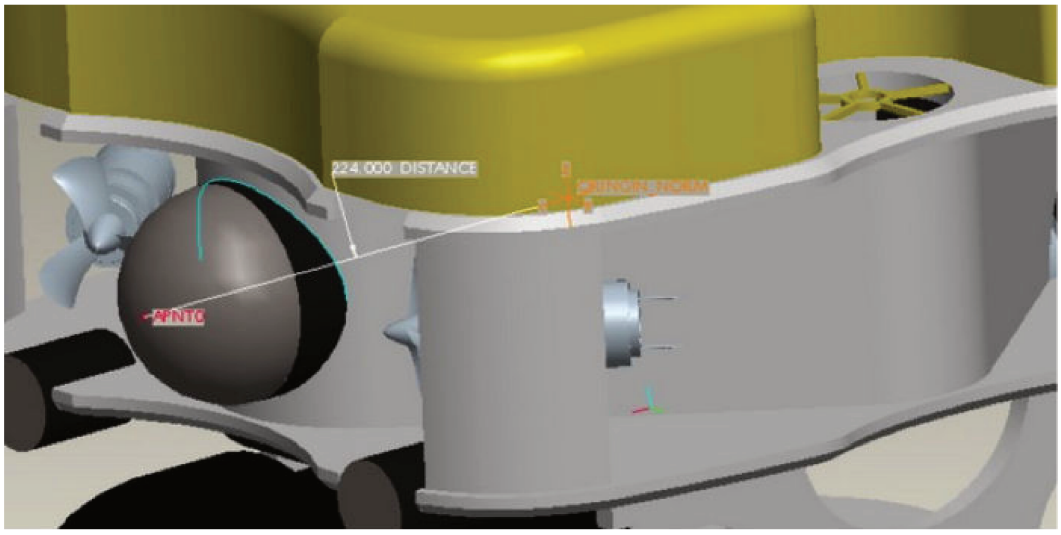

Figure 3-3: PRO/E Center of Gravity CG Estimation of the *CISCREA* AUV

$$I_0 = \begin{bmatrix} 0.2373 & 0 & 0.0029 \\ 0 & I_y & 0 \\ 0.0029 & 0 & 0.3578 \end{bmatrix} \tag{3.3}$$

According to [114], the off-diagonal elements of mass inertia matrix M_{RB} are

negligible for slow vehicles. For *CISCREA* AUV, the moving speed in any direction is less than 2 knots. Therefore, we assumed that the rotational and translational motion is not coupled (AUV has 3 planes of symmetry). To summarize, because the mass of the *CISCREA* AUV is 15.643 kg, the PRO/E approximation of mass inertia matrix M_{RB} for CISCREA around CG (O_b) is given as equation (3.4) ($Mass : kg$, $Inertia : kg \cdot m^2$).

$$M_{RB} = \begin{bmatrix} 15.643 & 0 & 0 & 0 & 0 & 0 \\ 0 & 15.643 & 0 & 0 & 0 & 0 \\ 0 & 0 & 15.643 & 0 & 0 & 0 \\ 0 & 0 & 0 & 0.2473 & 0 & 0.0029 \\ 0 & 0 & 0 & 0 & 0.3698 & 0 \\ 0 & 0 & 0 & 0.0029 & 0 & 0.3578 \end{bmatrix} \tag{3.4}$$

By neglecting the small off-diagonal inertia elements, the above matrix can be simplified to be a diagonal matrix in equation 3.5:

$$M_{RB} = diag(\begin{bmatrix} 15.643 & 15.643 & 15.643 & 0.2473 & 0.3698 & 0.3578 \end{bmatrix}) \tag{3.5}$$

3.2 Added Mass Matrix

It is mentioned in [122], that variations of underwater vehicle geometry play indeed a role on the added mass matrix $M_A \in \mathbb{R}^{6\times6}$ of the underwater vehicles. For a torpedo shaped AUV, empirical formulas prediction is validated in [55] and [28] by approximating the hull to an elementary ellipsoid or slender shape. However, the empirical formulas predicting is inaccurate for a complex-shaped AUV, such as cubic shape *CISCREA*. Note that, *CISCREA* AUV is a typical cubic shaped underwater vehicle that has various sharp and uneven outlines as well as an open framework. In order to estimated the added mass matrix M_A of *CISCREA* AUV, the computational fluid dynamic software WAMIT [110] and MCC [61] are introduced in this section.

WAMIT is a leading computational software in the offshore oil industry. It is

developed for analyzing wave interactions with offshore platforms, vessels and other structures. WAMIT utilizes the potential theory, and it calculates the fluid effects on each small panels of the structures that is divided by the strip method. WAMIT provides a variety of functions, including the functions to calculate added mass, damping and static center of gravity and buoyancy, *etc.*

MCC is developed by ENSTA Bretagne for calculating the hydrodynamic characteristics of marine objects. It uses the same strip method as WAMIT does, which slices the robot into a large amount of connected small surfaces. Each individual surface pieces are superposed to obtain the total fluid effects on the marine robot. One important focus of MCC is to calculate the added mass of submerged vehicles.

In this thesis, WAMIT and MCC results are compared in order to guarantee the reliability of the added mass matrix M_A calculations. We should mention that, WAMIT is widely used in the offshore industry applications, and it gains widespread recognition for its ability to analyze complex structures with a high degree of accuracy and efficiency. Compare to MCC, WAMIT is considered to be more reliable as it has far more successful industry applications. Therefore, the objective of MCC comparison is to verify the configurations and input files of the WAMIT calculations are correct. In the following sections, we introduce the calculation procedures of underwater vehicle added mass using WAMIT and MCC.

3.2.1 WAMIT Calculating *CISCREA* Added Mass

In this section, we introduce the basics of using WAMIT analyzing the added mass matrix M_A of the underwater vehicles, especially the *CISCREA* AUV. For reference, the WAMIT manual is given in [110], and an application approximating added mass matrix of a ROV is presented in [57]. In addition, MSS provides several Floating Production, Storage and Offloading (FPSO) applications using WAMIT in [123, 117, 124].

First, the principal input files for a WAMIT calculation are:

- Geometry Data File (.gdf): a closed surface geometry of the structure sur-

rounded by the fluid

- Potential Control File (.pot): specifies parameters including the fluid depth, wave periods, and wave heading angles for the POTEN sub-program
- Force Control File (.frc): specifies inputs regarding the body dynamics for the FORCE sub-program
- Configuration File (cfg): specifies certain options and other information used by the program
- Files list (.wam): specifies the input files to be used in the analysis
- Result file (.out): stores the analysis results

Actually, there are two options to represent the potential and geometries of the underwater vehicles to be analyzed: the high order method and low order method. The high order method allows to use B-Splines to represent the velocity potential and pressure continuously on the body surface, and to represent the geometry of the body surface in various manners. Alternatively, the low order method is less accurate than the high order method for most of applications, and it has more number of unknowns. In early WAMIT versions, the low-order method was used, where the geometric form of the submerged body surface is defined by flat quadrilateral elements, and the velocity potential or source strength solutions are assumed to be constant on each panel. As our robust control application is not sensitive to the slight compromise of added mass modeling accuracy, we chose low-order method to reduce the calculation complexity. In this thesis, MULTISURF (or Rhino 3D) was considered to represent the *CISCREA* AUV outline using the low-order method. Figure 3-4 shows the geometry of the *CISCREA* AUV represented as a set of quadrilateral surfaces, and the direction of those surfaces all pointing out of the underwater vehicle. Note that, simplification of the AUV model are important to obtain reliable results including removing sharp corners and complex curves (For example , the sharp corner between the connections of the *CISCREA* framework and supports, or the complex thruster blade geometries).

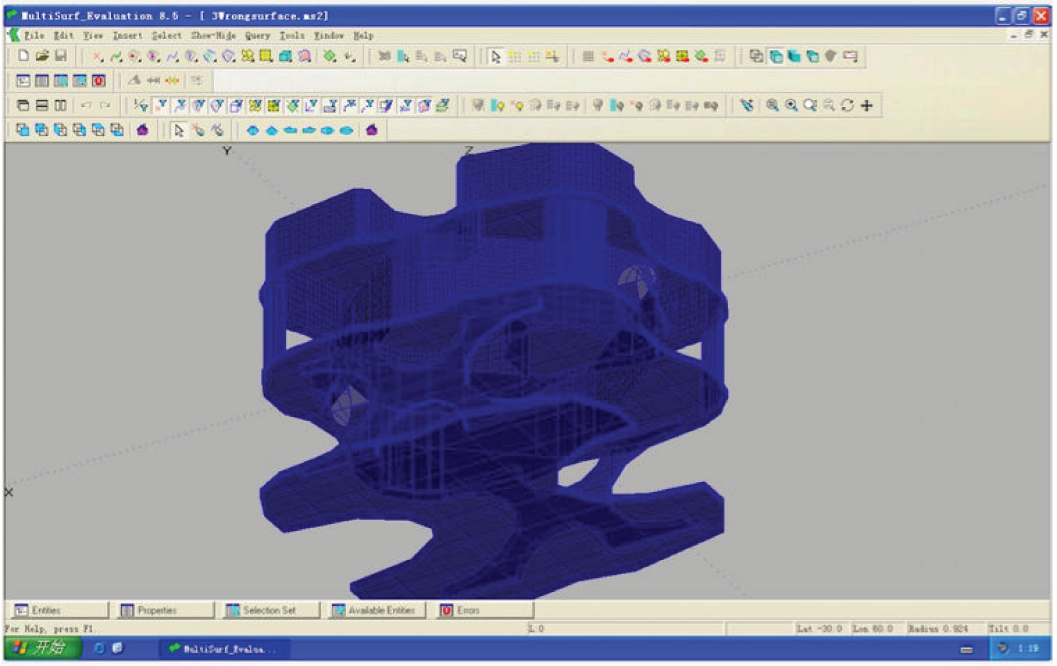

Figure 3-4: Low Order Representation of *CISCREA* AUV in MULTISURF

According to [110], WAMIT consists of two sequential subprograms, POTEN and FORCE. POTEN solves for the radiation and diffraction velocity potentials (and source strengths) on the body surface for the specified modes, frequencies and wave headings. FORCE computes global quantities including the hydrodynamic coefficients, motions, and first-order and second-order forces. Velocities and pressures on the body surface are evaluated by FORCE. The principal computational burden is in POTEN, the intermediate output data from this subprogram is saved in a binary 'P2F' file. Consequently, it is possible to make multiple runs with FORCE, varying the requested parameters to be output, without re-running POTEN in each instance. Figure 3-5 shows the working chart of the WAMIT software using two subprogram and the above mentioned input files.

Obtaining a reliable WAMIT calculation of the *CISCREA* AUV added mass matrix M_A depends on several critical issues: First, we should generate a closed surface model as the geometry input for POTEN program; then we should configure the potential control file (.pot) and force control file (.frc) with the correct physical parameters. For *CISCREA* AUV, in order to configurate the physical parameters, we

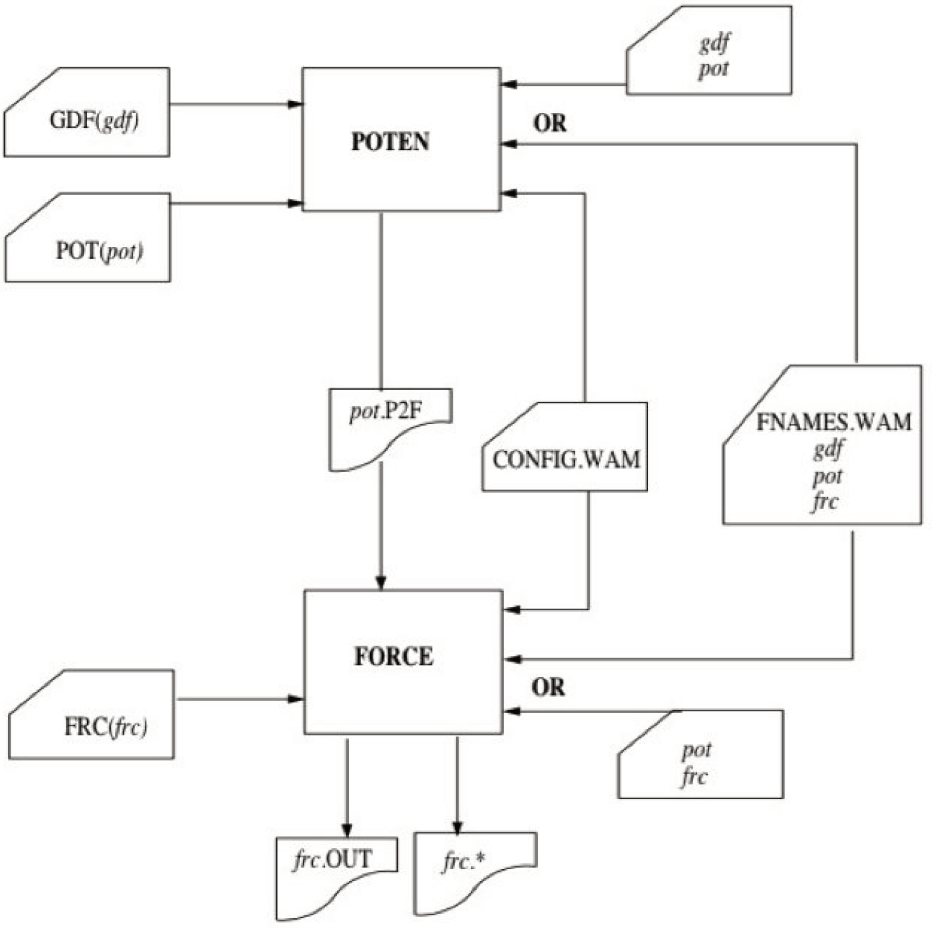

Figure 3-5: WAMIT working chart

implemented an added mass calculation in WAMIT and in MCC using a standard sphere, and we compared the outputs with the theoretical results in table 3.2 (the theoretical sphere added mass is given by $2/3\pi\rho r^3$, ρ is the density of the sphere, and r is the radius) . Apparently, the results in table 3.2 show the numerical calculation of WAMIT and MCC coincide with the theoretical added mass, which indicate the configurations reflect exactly the realistic physics. Later on, we replaced the sphere with *CISCREA* geometry file, and keep the same configuration files of the sphere calculation to the WAMIT^{TM} and MCC in order to obtain the added mass matrix M_A of *CISCREA* AUV. In [57], it was verified that the depth of the submerged vehicle plays negligible effects on the added mass results. Therefore, the depth of 10 m (regular working depth) is chosen for *CISCREA* to calculate the added mass matrix.

Table 3.2: Added Mass Results of Standard Sphere in the Surge Direction (Radius $1m$, density 1 kg/m^3, depth 10 m, Geometry: 1024 surfaces)

	Theoratical	WAMIT	MCC
Surge(kg)	2.0944	2.084236	2.106

Appendix B.2 gives the configurations and output data of the WAMIT added mass calculation for *CISCREA* AUV, including: potential control configurations (.pot), force control file (.frc), and calculation result file (.out). For the definitions of the configuration parameters, please see the WAMIT manual [110]. It is worthy mentioning that the WAMIT output file only provides the added mass coefficient result. The elements of the added mass matrix M_A can be obtained by multiplying the fluid density on the WAMIT output coefficients. The added mass calculation using WAMIT is actually an iterative process, which involves several times of model simplification and re-calculations. For instance, the damaged surface (areas not closed or covered), the inverse directions of strips or panels on the vehicle surface, and exceeding maximum strip numbers can increase the processing time and it may result in pausing or collapsing of the WAMIT program. Indeed, the calculation requires efforts and an experience to simplify the model and run the program. However, compare to experimental solutions, WAMIT definitely saves time and efforts, especially for small-size and complex shaped underwater vehicles.

3.2.2 MCC Calculating CISCREA Added Mass

MCC software is introduced in [61]. To calculate the added mass matrix M_A of the underwater vehicles, MCC requires a closed surface model to be striped. Like WAMIT, the model simplification is important to guarantee the quality of calculation accuracy. For MCC, the widely used CFD mesh tool GAMBIT is utilized to generate the strips or panels of the underwater vehicles. Note that, during the mesh procedure in GAMBIT software, the mesh representations need to be transformed and saved to the neutral format. The neutral format is adapted to MCC as well as other hydrodynamic programs that have no special geometric representation standards.

The neutral format is generally represented as the neutral (.neu) geometry files, i.e. the surfaces are represented by squares or triangles that are connected each other. For example, the neutral representation of *CISCREA* AUV with few strips is presented in figure 3-6.

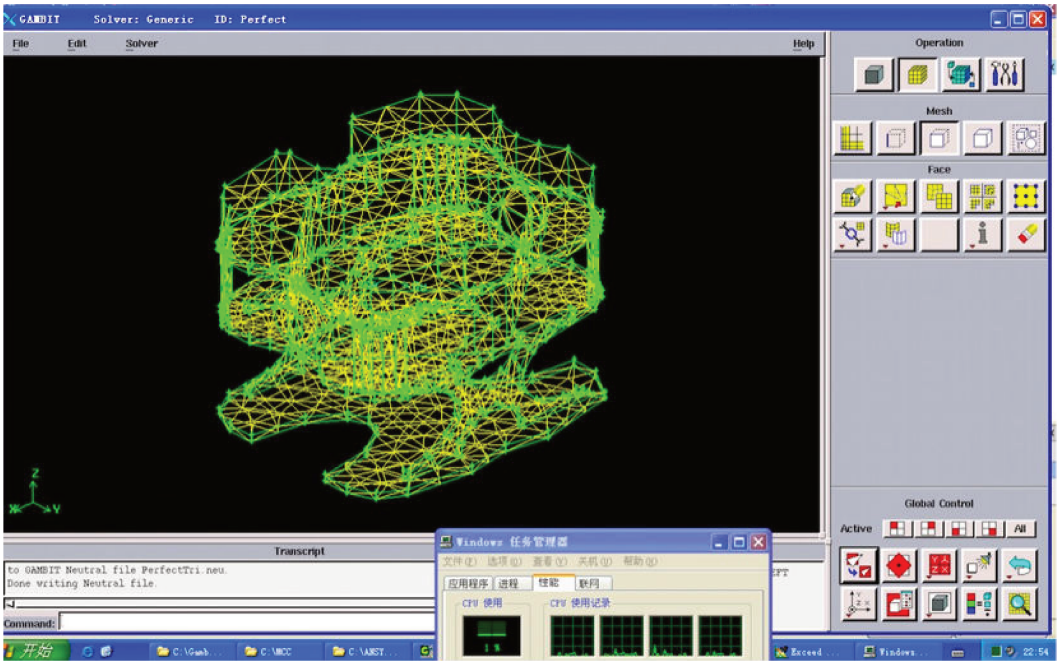

Figure 3-6: Neutral representation of *CISCREA* AUV in GAMBIT

As WAMIT software, the added mass calculation using MCC is also an iterative process. The simplification of the closed surface model is critical to run smoothly the program and to obtain a reliable result. Especially, choosing the number of strips indeed affects the final added mass matrix result. For example, in meshing the surface of *CISCREA* AUV with fewer strips, the GAMBIT software pauses and informs that it is impossible to close the vehicle surface. On the contrary, to mesh the surface of *CISCREA* AUV with a large amount of strips yields a fine and smooth surface model, however, the MCC generally collapses due to exceed of the computational power. Even though MCC can give a result after a long calculation, the accumulation of errors effects the final result which becomes inaccurate. Therefore, it is suggested to choose the number of strips using the method of bisection, and implement many calculations until the result converges to a constant. Otherwise, the direction of the

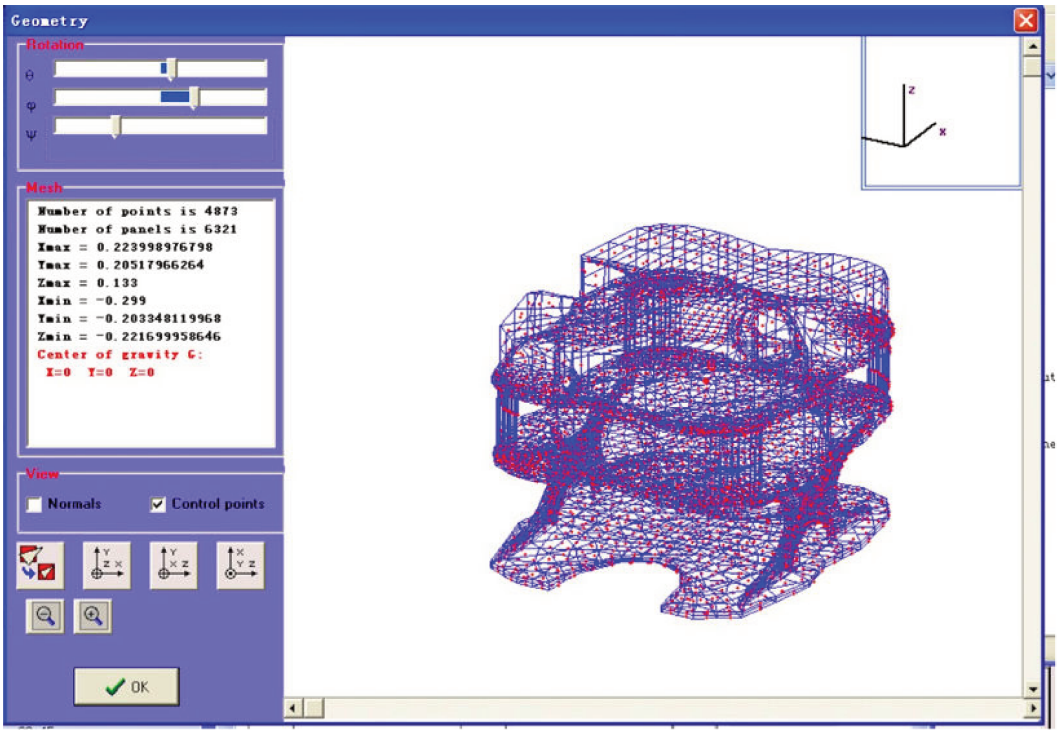

Figure 3-7: Neutral representation of *CISCREA* AUV in MCC

strips or panels are also important, as inverse directions may cause the stop of the program. In figure 3-7, the closed-surface model of *CISCREA* AUV is presented using MCC. The added mass matrix M_A results of *CISCREA* AUV from WAMIT and MCC are compared in the next section.

3.2.3 WAMIT and MCC Added Mass Comparison

In equation 3.6, M_{A1} is the added mass matrix of *CISCREA* AUV calculated using radiation/diffraction program WAMIT$^{\text{TM}}$($Mass : kg, Inertia : kg \cdot m^2$).

$$M_{A1} = \begin{bmatrix} 11.985 & -0.091 & -0.105 & 0.039 & 0.308 & 0.012 \\ 0.149 & 20.261 & -0.147 & 0.085 & -0.013 & -0.758 \\ 0.111 & -0.129 & 67.141 & -0.033 & 2.530 & 0.064 \\ 0.122 & 0.319 & -0.056 & 0.385 & 0.003 & -0.011 \\ 0.407 & -0.001 & 2.543 & -0.002 & 0.791 & 0.002 \\ -0.003 & -0.758 & 0.064 & -0.003 & 0.004 & 0.138 \end{bmatrix} \tag{3.6}$$

In equation 3.7, M_{A2} is the added mass matrix of *CISCREA* AUV calculated using fluid program MCC ($Mass : kg, Inertia : kg \cdot m^2$).

$$M_{A2} = \begin{bmatrix} 11.8 & 4.08 & 9.41 & 0.326 & 0.349 & -0.267 \\ 4.53 & 17.9 & -10.3 & 0.492 & -0.913 & 0.233 \\ 8.6 & -12.3 & 52.7 & -2.88 & -7.94 & 1.49 \\ 0.256 & 0.676 & -2.74 & 0.91 & 0.573 & 0.0087 \\ -0.067 & -0.628 & -9.17 & 0.655 & 1.54 & 0.04 \\ -0.184 & 0.162 & 1.29 & -0.0289 & -0.0252 & 0.0854 \end{bmatrix} \tag{3.7}$$

According to [114], the off-diagonal elements of the added mass matrix M_A are also negligible for slow vehicle. For *CISCREA* AUV, the moving speed in all the directions are less than 2 knots, which is considered to be slow. Hence, by neglecting small off-diagonal elements, the above matrices can be simplified into diagonal matrices respectively in equation 3.8, 3.9. The coupling between translational and rational directions are assumed to be negligible.

$$M_{A1} = diag(\begin{bmatrix} 11.99 & 20.26 & 67.14 & 0.385 & 0.791 & 0.138 \end{bmatrix}) \tag{3.8}$$

$$M_{A2} = diag(\begin{bmatrix} 11.80 & 17.90 & 52.70 & 0.910 & 1.540 & 0.086 \end{bmatrix}) \tag{3.9}$$

Apparently, the added mass prediction from WAMIT^{TM} coincides with MCC to some extent. This result confirms the efficiency of WAMIT^{TM} and the possibility of MCC to calculate the added mass matrix for complex-shaped underwater vehicles. In next chapter, the numerical added mass results are validated in moving experiments. Furthermore, for robust control scheme, the numerical calculation errors of WAMIT and MCC added mass results can be considered to be mass-inertia uncertainties.

We should mention that, the added mass matrix M_A has indeed an important hydrodynamic effect for the control design. As it is obviously shown the added mass elements of *CISCREA* AUV on the surge, sway and heave directions are respectively 11.985 kg, 20.261 kg, and 67.141 kg, some of them are even larger than the mass

of the AUV 15.643 kg. Similar conclusion can be yielded for the inertia parameters. This indicate the added mass effect can not be ignored during the AUV accelerating process.

3.3 Damping Approximation

As mentioned in chapter 2, in real fluid the 6 CFD damping $D(|\nu|) \in \mathbb{R}^{6\times6}$ of underwater vehicles are highly nonlinear and coupled, it is difficult to separate the contributed effects. Especially, different damping terms contribute to either linear or quadratic damping in the *Fossen* damping formula (equation 2.21). Either practically or theoretically, it is very hard to precisely approximate the 6 CFD damping effects for complex-shaped underwater vehicles. However, it is critical to study and estimate the accurate damping matrix $D(|\nu|)$ in order to improve the maneuverability as well as the navigation or localization abilities of advanced underwater vehicles.

Therefore, in this section computational fluid dynamic software ANSYS-CFX and STAR-CCM+$^{\text{TM}}$ are introduced to estimate the damping matrix $D(|\nu|)$ for the complex-shaped *CISCREA* AUV. We proposed two CFD software in order to improve the reliability of the numerical CFD results. Configuration errors can be avoid from the numerical calculations stage, that provides more confidence to conduct a realistic hydrodynamic and control experiment.

Among the damping analysis methods that mentioned in chapter 2, we select numerical solutions, i.e. the CFD software ANSYS-CFX and STAR-CCM+ for underwater vehicle damping analysis for the following reasons:

- *CISCREA* AUV has complex-shaped outlines as well as an open frame structure. Empirical formulas are inefficient and inaccurate to estimate the damping matrix $D(|\nu|)$ for *CISCREA* AUV, as it requires complex model simplifications that may effect the estimation accuracy.

- Full-scale and scaled experiments are expensive, and they are usually one-shoot results. Comparing to the CFD software, which allows easily the modifications

of the physical details, the experiment efficiency is not flexible for low-cost and small-size underwater vehicles.

- Although the damping analysis accuracy of CFD software is not as high as the experimental hydrodynamic results, generally the CFD solutions are sufficient for control design using a robust control scheme. Actually, the robust control scheme requires only the uncertain boundaries instead of an accurate damping result.

In the following, the damping analysis work of *CISCREA* AUV are divided into five parts:

- Morison equation is introduced to identify the main contribution from linear and quadratic damping effects of the underwater vehicles.
- ANSYS-CFX is used to approximate the relationship among damping forces and vehicle velocities on the translational directions of surge, sway and heave.
- STAR-CCM+$^{\text{TM}}$ are used to estimate the relationship among damping forces and vehicle velocities on the translational directions of surge, sway and heave.
- The rotational damping effect on the AUV yaw direction is analyzed by the moving reference technique of STAR-CCM+ [125], which is relatively simple and efficient to simulate.
- Finally, the numerical damping estimation $D(|\nu|)$ of *CISCREA* AUV using ANSYS-CFX and STAR-CCM+ are compared.

3.3.1 Morison Equation Analysis

As mentioned in previous chapters, four elements contribute to the damping matrix $D(|\nu|)$ of the marine vehicles: the potential damping $D_P(|\nu|)$; skin friction damping $D_S(|\nu|)$; waves drift damping $D_W(|\nu|)$; vortex shedding damping $D_M(|\nu|)$. Generally, they can be linearly superposed, see equation 3.10:

$$D(|\nu|) = D_P(|\nu|) + D_S(|\nu|) + D_W(|\nu|) + D_M(|\nu|) \tag{3.10}$$

Three of the four damping elements contribute to the viscous damping $D_v(|\nu|)$ given by equation 3.11:

$$D_v(|\nu|) = D_S(|\nu|) + D_W(|\nu|) + D_M(|\nu|) \tag{3.11}$$

According to [114], viscous damping $D_v(|\nu|)$ dominates the damping effects of marine vehicles, while on the contrary potential damping $D_P(|\nu|)$ is comparably small and negligible. In addition, as waves are assumed to act on surface vehicles, and AUVs are considered to work at certain depth, therefore, waves drift damping $D_W(|\nu|)$ is also negligible for *CISCREA*. Reminder the robust control scheme to the *CISCREA* AUV, $D_P(|\nu|)$ and $D_W(|\nu|)$ can be considered as additive uncertainties for the control design. To summarize, the skin friction damping $D_S(|\nu|)$ and vortex shedding damping $D_M(|\nu|)$ are the only effective parameters.

According to *Fossen*'s damping model (see equation 3.12), it is assumed that high order damping effects can be neglected, and low order damping effects are not coupled.

$$D(|\nu|) = D + D_n(|\nu|) \tag{3.12}$$

Here, $D \in \mathbb{R}^{6\times6}$ is the linear damping matrix and $D_n(|\nu|) \in \mathbb{R}^{6\times6}$ is the quadratic damping matrix, defined as follows:

$$D(|\nu|) = \begin{bmatrix} |\nu|^T D_1 \\ |\nu|^T D_2 \\ |\nu|^T D_3 \\ |\nu|^T D_4 \\ |\nu|^T D_5 \\ |\nu|^T D_6 \end{bmatrix} \tag{3.13}$$

Here, velocity vector is defined as $|\nu|^T = [|u|, |v|, |w|, |p|, |q|, |r|]$, and damping matrix

are decomposed into $D_i \in \mathbb{R}^{6\times6}$. According to [114], if the underwater vehicle's velocities are sufficiently high the D can be neglected. Otherwise, $D_n(|\nu|)$ is negligible.

For AUV modeling and control design, the critical issue is that both skin friction damping $D_S(|\nu|)$ and vortex shedding damping $D_M(|\nu|)$ contribute to the linear and quadratic damping matrix simultaneously. In this case, it is difficult to identify the dominate effect. Therefore, we used *Morison* formula to roughly determine the damping behaviors of *CISCREA* AUV. *Morison* damping formula $f(U)$ is presented in equation 3.14 [126]:

$$f(U) = -\frac{1}{2}\rho_d C_D(R_n) A U|U| \tag{3.14}$$

Here, U is the vehicle velocity, ρ_d is the fluid density, A is the cross-sectional area projected on the fluid and $C_D(R_n)$ is the damping coefficient, which is a function of *Reynolds* number R_n.

$$R_n = \frac{\rho_d U D_{CL}}{\nu_{is}} \tag{3.15}$$

where ν_{is} is the fluid viscosity and D_{CL} is the characteristic length, which is the lenth of the object that the flow is going through or around. Generally, $C_D(R_n)$ of spheres and cylinders are obtained by experiments of various moving velocities and data fitting.

In our application, the fluid is considered to be sea water, therefore, its ν_{is} is $1.56 \times 10^{-6} kg/(s \cdot m)$ at 5°C and salinity 3.5%, density $\rho_d = 1023 kg/m^3$ [114]. CISCREA generally operates at a speed U range from 0 to $1 m/s$ (0 to 2 knots) in any translational direction. Meanwhile, the robot characteristic length is approximately 0.5 m. In this case, the R_n of CISCREA is generally around 10^8 to 10^9. According [126], in the standard damping experiments of spheres and cylinders, there should be a distinct switch between the laminar and the turbulent flows when the *Reynolds* number is between 10^5 to 10^6, i.e. the critical area, and damping coefficient $C_D(R_n)$ becomes instable (damping coefficient $C_D(R_n)$ chart with respect to R_n is given in appendix A.9). On the contrary, the damping coefficient $C_D(R_n)$ converges to a constant value, when the *Reynolds* number is much higher than 10^6 or far from the critical area. In our case, we can assume the *CISCREA* AUV as a cylinder shape of

$0.5m$ radius. Then, the damping coefficient $C_D(R_n)$ of the underwater vehicle can be approximated by a constant C_D. In this case, the damping effect $f(U)$ becomes quadratic with respect to the vehicle velocity U, see equation (3.16).

$$f(U) = -\frac{1}{2}\rho_d C_D A U|U| \tag{3.16}$$

Theoretically, we can predict that the nonlinear quadratic damping $D_n(|\nu|)$ should dominate the damping matrix $D(|\nu|)$ of the *CISCREA* AUV. However, the *Morison* equation can not give accurate damping estimations, as the *CISCREA* AUV has complex-shaped structures and open framework. Therefore, in the following sections CFD software ANSYS-CFX and STAR-CCM+ are considered to calculate more precise and quantitive damping effects.

3.3.2 ANSYS-CFX Damping Analysis

The damping analysis of underwater vehicles using ANSYS-CFX CFD software can be divided into five steps:

- Create the simplified 3D model of the underwater vehicle as well as the water tank for hydrodynamic analysis
- Mesh the water tank and the underwater vehicle for the FEM (Finite Element Method) calculation
- Set the boundary and stop conditions for the FEM calculation
- Execute iterative FEM calculations until the convergence
- Post-process the FEM data to obtain the concerned hydrodynamic parameters

First, simplify the closed surface 3D underwater vehicle model is essential for the CFD analysis. As shown in figure 3-8, the *CISCREA* AUV has a complex shape. For instance, the thrusters, LED lens, battery group, and the recovery handle are neglected in the CFD damping analysis. Usually, the geometrical details are removed

for damping analysis, otherwise, they will induce more difficulties for the mesh and calculations procedures. Especially, the sharp corners can dramatically effect the mesh quality of the boundary layer, which is critical for the damping analysis accuracy. Therefore, the *CISCREA* AUV model is simplified as a single solid body with the main geometrical features.

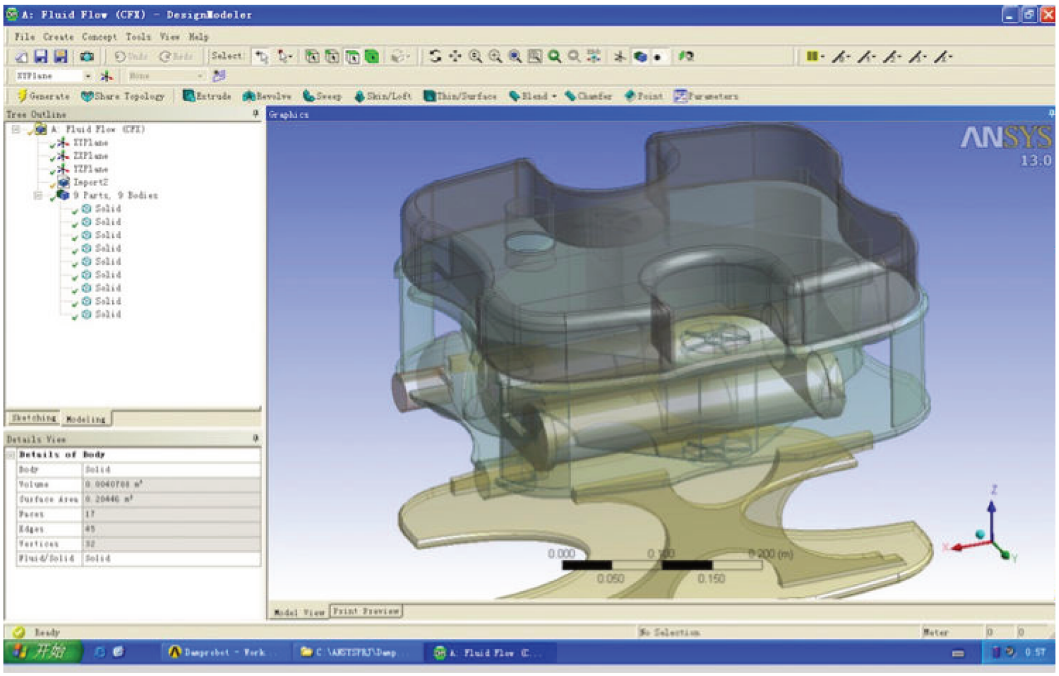

Figure 3-8: *CISCREA* AUV in ANSYS

Generally, the underwater vehicle is always moving, and the water is relatively static. The underwater vehicle velocity with reference to the static fluid environment is considered to be the vehicle speed. However, the reference is inversed in the ANSYS-CFX damping analysis. As the damping effect is only a function of the relative speed between the AUV and the fluid, and in order to optimize the calculation burden, the underwater vehicle is fixed in the water tank as shown in figure 3-9. The fluid is injected into the water tank from a constant speed boundary, and flows out of the tank at the zero pressure boundary.

Note that, either in CFD or experiments, it is impossible to simulate the fluid environment of infinite size. Therefore, the water tank is selected to be 10.5 m for length, 4.5 m for width and 4.5 m for height, which is much larger than the size of

the AUV.

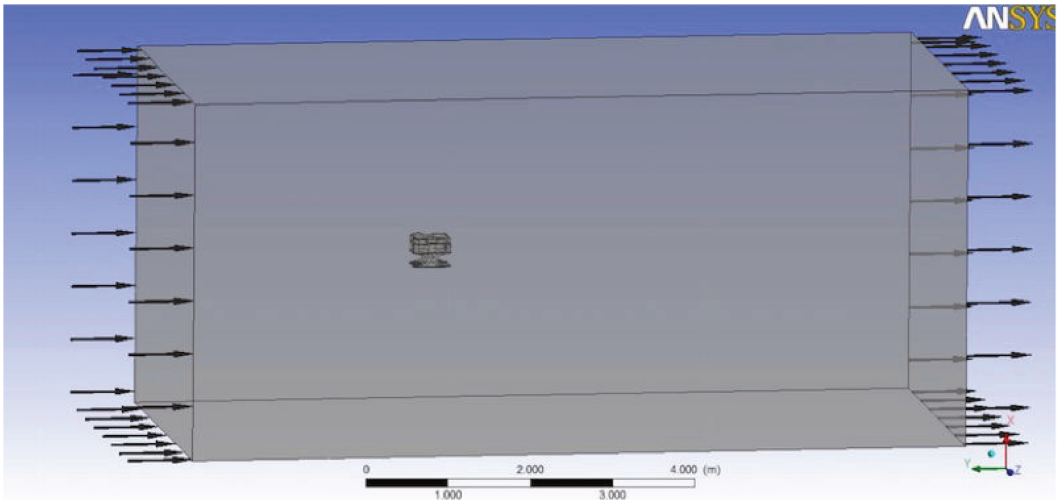

Figure 3-9: *CISCREA* AUV in ANSYS, constant speed boundary is on the left side with arrows pointing inside the water tank, and zero pressure boundary is on right side with arrows pointing out

For *CISCREA* AUV, the fluid moves in the water tank with the speed ranges from 0 to $0.5m/s$ on surge, sway and heave directions to simulate the realistic vehicle speed.

The incremental speed interval is selected to be 0.1 m/s. Correspondingly, five rounds of damping calculations are implemented on each translational direction. In order to achieve accurate damping estimation, a smaller speed interval should be chosen. However, limited by the computational power (the time cost of the current damping analysis is generally very high), it is impossible to reach an extremely small speed interval for the CFD damping analysis.

The meshing work plays an important role in the CFD damping analysis. The quantity and quality of the underwater vehicle meshes impact respectively the calculation speed and the accuracy of the damping estimation. First, increasing the number of meshes can efficiently improve the damping estimation quality, however, on the contrary the extra meshes would increase the calculation burden. Especially, for an underwater vehicle with complex-shaped outline, such as *CISCREA* AUV, the excessive meshing accuracy would cause difficulties in the automatic meshing process, and hence reduce the modeling efficiency. In this thesis, we propose the robust

control scheme for the underwater vehicles control design, which is not sensitive to the modeling accuracy. For *CISCREA* AUV, around 0.6 million meshes are used for the damping analysis on surge, sway, and heave directions, as shown in figure 3-10. Second, the meshing quality is critical for the CFD damping analysis of underwater vehicles. Meshing quality decides if the physical phenomena can be reflected in the damping calculation. The *Reynolds* number R_n for the *CISCREA* AUV is very large, around 10^8 to 10^9. Therefore, the turbulence flows should be the dominant damping effects for *CISCREA* AUV. In order to reflect the realistic turbulence phenomena in the CFD damping estimation, it is necessary to build very fine meshes in the critical areas such as boundary layer, which should guarantee the mesh length is generally less than the turbulence size. Note that, the prism layer meshing is important to obtain the fluid damping behaviors. On the contrary, to reduce the calculation burden, the meshes in the insensitive area is configured with gradually increased mesh size. We should mention that the mesh size should increase gradually, otherwise, the physical details in the smaller-size meshes can not transfer to the larger meshes outside the critical areas.

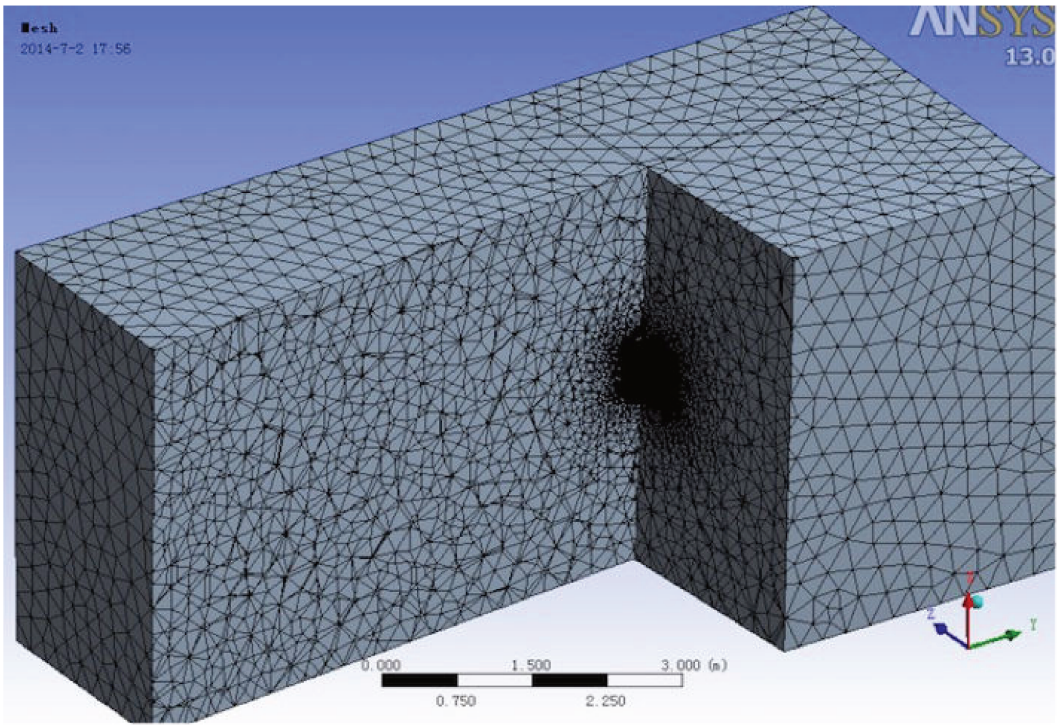

Figure 3-10: The Mesh of *CISCREA* AUV in ANSYS

Setting the boundary conditions is essential for the damping analysis. For *CISCREA* AUV, the turbulence model is chosen as the $k-\omega$ SST (Shear Stress Transport) equations, which represents the separation phenomena on the boundary layer from laminar to turbulence flows [57]. Then, the water tank boundary is chosen to be free slip wall that reduces the space constrains as much as possible. Furthermore, the submerged surface of the *CISCREA* AUV is considered as non-slip wall having roughness parameters using PVC materials. The fluid injection speed varies from 0 to 0.5 m/s, and the turbulence intensity coefficient of the inlet fluid boundary is set to 1%. The outlet fluid boundary is configured to be a static pressure 0 Pa.

Actually, the initial conditions do not effect the convergence of the CFD calculation, but they impact on convergence speed. In order to speed up the damping calculation, the initial fluid speed are usually given equal to the speed at the inlet fluid boundary.

The convergence criterions and time step are used to determine the solver stop behaviors. For *CISCREA* AUV, the convergence criterion is set to be 10^{-4}. To achieve different accuracy specifications, more sophisticated configurations can be found in [57]. To summarize, the configurations or parameters that used in ANSYS-CFX are presented in Tab 3.3.

Table 3.3: Configurations of ANSYS-CFX

Parameter	ANSYS-CFX Configurations
Tank	10.5m (L) 4.5m (W) 4.5m (H)
Fluid	steady
Density	$\rho = 1023kg/m^3$
Viscosity	$1.56 \times 10^{-6}kg/(s \cdot m)$
Turbulence	1% at inlet boundary, (k-ω)
Mesh	588221 elements for heave (around for surge and sway)
Convergence	10^{-4}
Roughness	PVC 0.0015 - 0.007 (mm)

The post-process stage of ANSYS-CFX analyzes the CFD data, and yields some information: the damping forces and moments, the velocities, and the pressures, *etc.* Figure 3-11 presents the stream-line view of the fluid velocities surround the

CISCREA AUV.

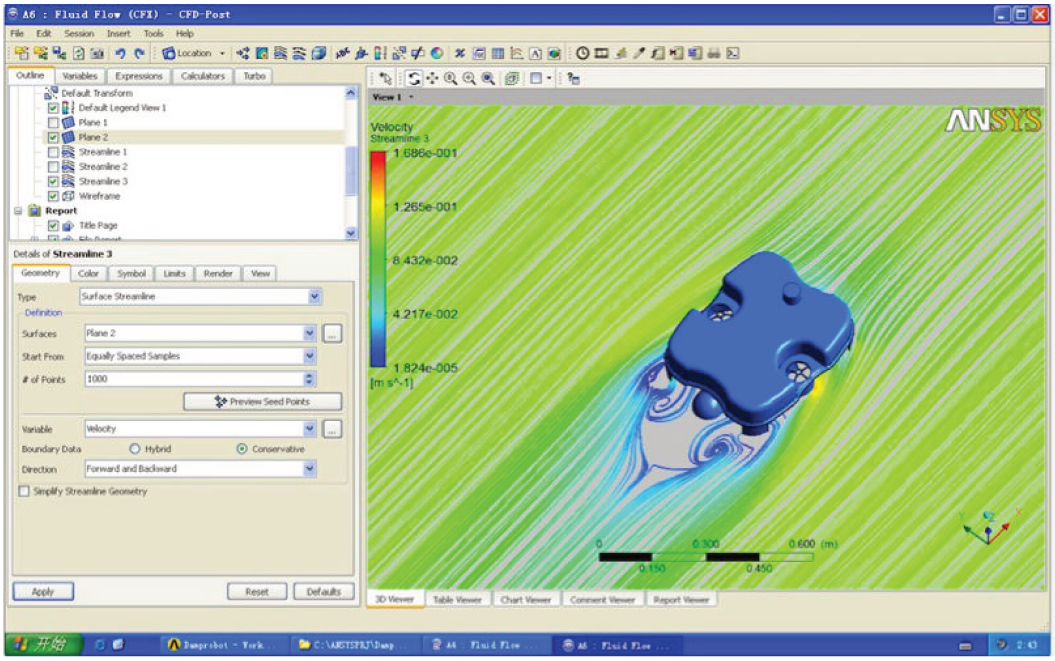

Figure 3-11: Streamline View of *CISCREA* AUV in ANSYS Surge Damping Analysis

In table 3.4, it is presented the ANSYS-CFX estimation of damping forces on the *CISCREA* AUV in presence of the fluid velocity range from 0 to 0.5 m/s. The damping matrix $D(|\nu|)$ parameters are given in surge, sway and heave directions.

Table 3.4: Damping Forces of *CISCREA* AUV at Different Velocities

ANSYS-CFX	0.1m/s	0.2m/s	0.3m/s	0.4m/s	0.5m/s
Surge (N)	0.287	1.146	2.577	4.579	7.222
Sway (N)	0.537	2.14	4.815	8.561	13.382
Heave (N)	0.51	3.319	7.47	13.28	20.751

In the following section, the ANSYS-CFX damping estimation results are compared with the STAR-CCM+ solutions. Note that, the CFD software ANSYS-CFX can only estimates the damping forces on the translational directions. However, the damping matrix $D(|\nu|)$ is consisted by translational damping forces as well as rotational damping torques. Therefore, in the next section, the CFD software STAR-CCM+ are introduced to identify both the translational damping forces and rotational damping torques.

3.3.3 STAR-CCM+ Damping Analysis

STAR-CCM+ employs the same five step of the analysis procedure as ANSYS-CFX, including: creating the simplified AUV damping model; mesh the water tank and the underwater vehicles; set boundary conditions; execute iterative calculation; and post-process the CFD data.

In the STAR-CCM+, the damping analysis of *CISCREA* AUV is done using: an underwater vehicle simplified model, in order to guarantee the CFD estimation reliability, and to verify the independence of the damping analysis and the water tank size. For this reason, we set a water tank with different size compared to the one used in ANSYS-CFX, 9 m length, 4 m width, 4 m height. Figure 3-12 shows the *CISCREA* AUV fixed in there water tank for the damping analysis of sway direction.

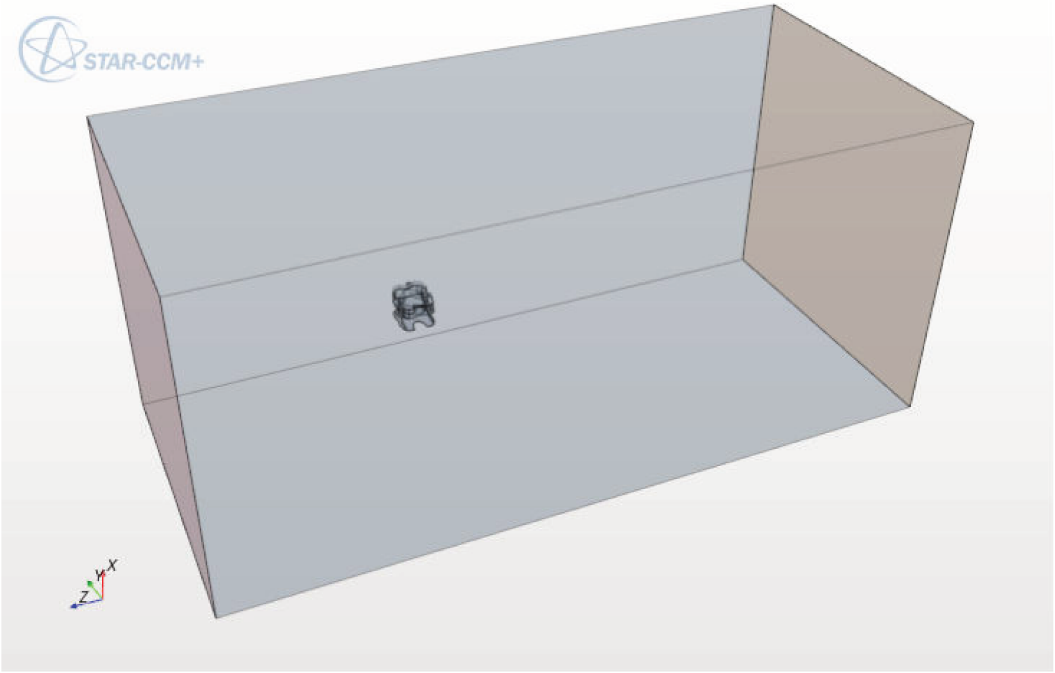

Figure 3-12: *CISCREA* AUV fixed in Star-ccm+ for Heave Damping Analysis

In STAR-CCM+ around 3 million meshes are employed for the damping estimation of *CISCREA* AUV in surge, sway and heave directions. Figure 3-13 demonstrates the meshing procedure for damping analysis of surge direction. In STAR-CCM+, prism layer is well considered to involve the boundary layer physics, as shown in fig-

ure 3-14. The fine meshes near the underwater vehicle submerged surface are expect to simulate the turbulence phenomena. However, a more strict convergence condition is given using 10^{-5} (100 iteration).

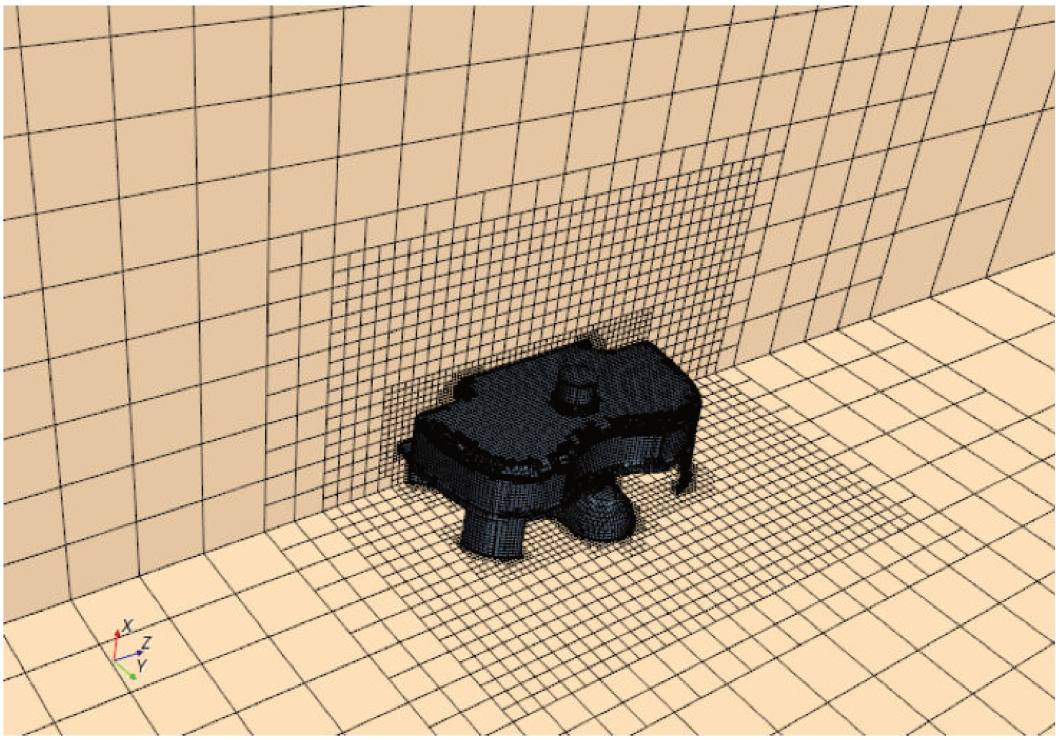

Figure 3-13: Star-ccm+ Meshing Result of *CISCREA* AUV for Surge Damping Analysis

The CFD configurations of STAR-CCM+ for *CISCREA* AUV damping analysis are presented in table 3.5. According to the working speed of *CISCREA* AUV, the fluid velocities are defined range from 0 to 5 m/s in surge, sway, and heave directions. The incremental speed interval is chosen to be 0.1 m/s, which yields five rounds of calculations for each translational direction.

Correspondingly, the damping forces estimated using STAR-CCM+ are given in table 3.6. In surge, sway and heave directions, the damping forces are calculated according to a variety of vehicle speeds. The translational damping forces estimated using STAR-CCM+ are compared with the ones obtained by using ANSYS-CFX in the next section.

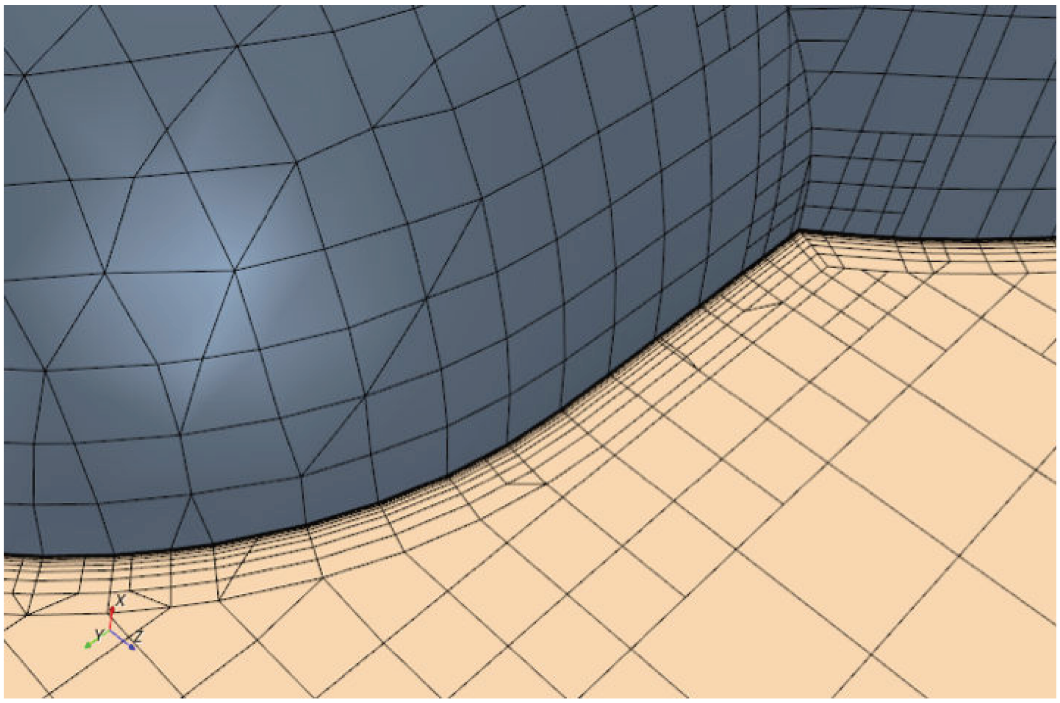

Figure 3-14: Star-ccm+ Prsim Layer Meshing Result of *CISCREA* AUV

Table 3.5: Configurations of STAR-CCM+ Estimating the Damping Effects of *CISCREA* AUV

Parameter	STAR-CCM+ Configuration
Tank	9m (L) 4m (W) 4m (H)
Fluid	steady
Density	$\rho = 1023kg/m^3$
Viscosity	$1.56 \times 10^{-6} kg/(s \cdot m)$
Turbulence	1% at inlet boundary, (k-ω)
Mesh	3002121 faces for sway (around for surge and heave)
Convergence	100 steps ($< 10^{-5}$)
Roughness	Wall

Table 3.6: Damping Forces and Moments of *CISCREA* AUV at Different Velocities

STAR-CCM+	0.1m/s	0.2m/s	0.3m/s	0.4m/s	0.5m/s
Surge (N)	0.273	1.06	2.39	4.253	6.539
Sway (N)	0.5077	2.011	4.4531	8.0222	12.2759
Heave (N)	0.8393	3.298	7.43	12.974	20.745

3.3.4 STAR-CCM+ Rotational Damping Analysis

In [29], both ANSYS-CFX and STAR-CCM+ are employed to calculate translational damping coefficients for the damping matrix $D(|\nu|)$ in surge, sway and heave directions. The rotational damping coefficients are not approximated using CFD solutions, as it is generally hard to predict precisely the damping effects of roll, pitch, and yaw directions.

For rotational motions, the CFD calculation are considered to be difficult, and inappropriate for damping analysis of underwater vehicles. *Floc'h* in [127] shows that the re-mesh calculation is too expensive even for 2D rotational simulation. Each calculation cycle requires more than 24 hours to be done. In this thesis, we use the move reference technique of STAR-CCM+ to approximate the rotational damping of *CISCREA* AUV [111, 125]. The idea is to estimate rotational damping torque and angular velocity relationships with less expensive calculation.

In STAR-CCM+, three ways exist to analyze rotational motion [128, 125]:

- Moving reference method
- DFBI (Dynamic Fluid Body Interaction) or similarly rotation motion method
- Overset mesh method

Moving reference approach converts an unsteady motion problem into a steady-state problem by imposing a moving frame on a static mesh. In this case, steady fluid is available to solve fast the rotational problems. Rotation motion or DFBI involves actual displacement of regions. Moving regions and static regions exchange physics among contacting interfaces. Overset mesh method applies real time displacement between background mesh and overlap mesh. It is a recent mesh technique widely implemented on the complex motion analysis applications in free space. In every calculation iteration, overset mesh interacts with background mesh through overset boundaries. The last two methods bind to implicit unsteady fluid, and calculation load is generally heavier than in the moving reference method. Therefore, in our work, moving reference method is selected for rotational damping simulation. To achieve

better CFD results, overset mesh solution is also considered. A streamline plot of moving reference method and static overset mesh results are shown in figure 3-25.

Due to the thrusters design, the *CISCREA* AUV only have 4 degree-of-freedoms, and the roll and pitch directions are self-balancing. Therefore, the rotational damping analysis of *CISCREA* AUV $D(|\nu|)$ is dedicated to the torque and angular velocity relationship of the yaw direction.

As previously mentioned, the simplified *CISCREA* AUV model is fixed in the cylindrical (yaw) water tanks, as shown in figure 3-15. The damping effect is approximated by moving references or overset mesh techniques.

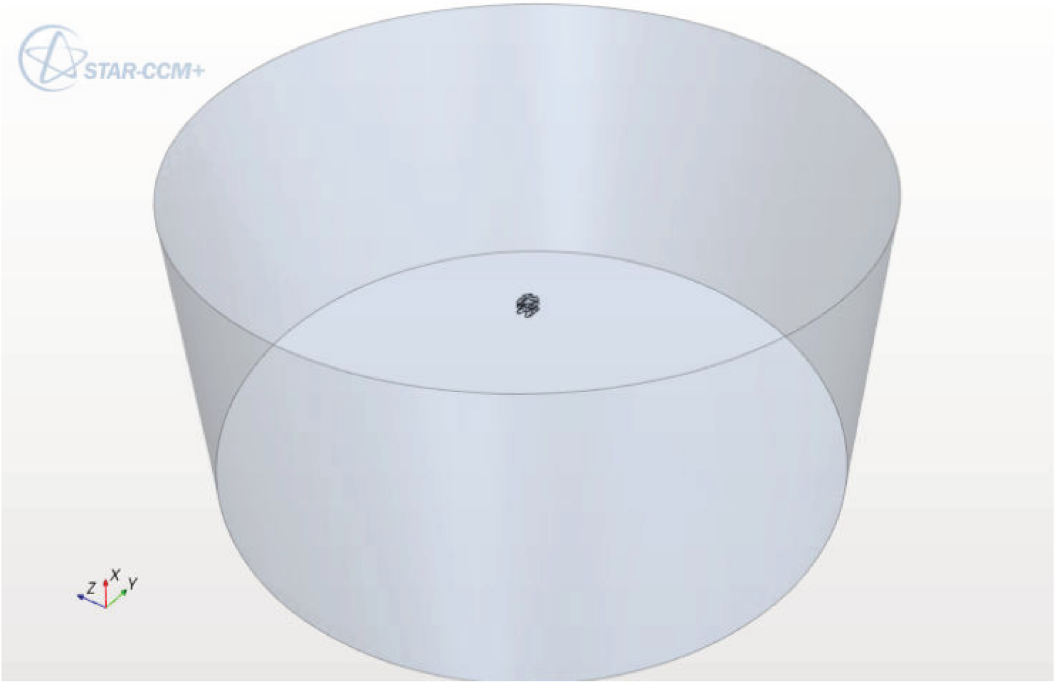

Figure 3-15: *CISCREA* AUV Fixed in the Cylinder Tank

In figure 3-16, around 1million meshes are implemented to present the cylinder water tank and underwater vehicles for rotational damping estimation in yaw direction.

The rotational speed of *CISCREA* AUV varies from 0 to 5 rad/s, and the incremental speed interval is chosen to be 0.5 rad/s. Consequently, five operating modes of different rational speed are calculated. In table 3.7, the damping analysis configurations are presented.

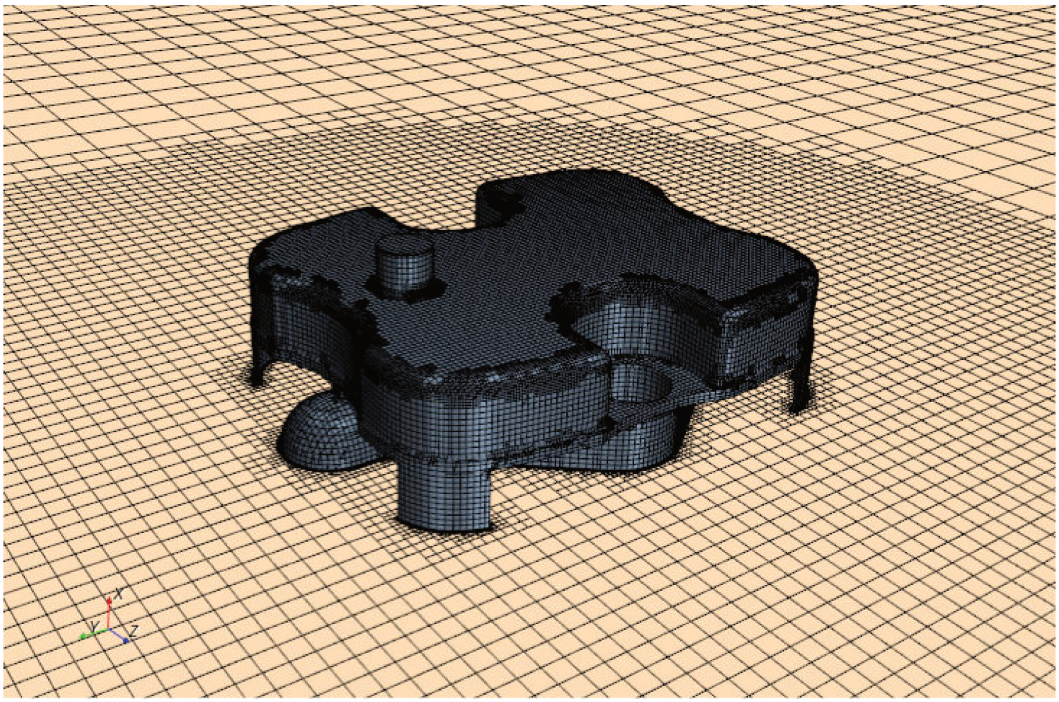

Figure 3-16: Meshing Result of *CISCREA* AUV for Rotational Damping Analysis (STAR-CCM+)

Table 3.7: Configurations of STAR-CCM+ estimating the rotational damping effects of *CISCREA* AUV

Parameter	STAR-CCM+ Configuration
Cylinder	8m(H) 8m(radius)
Fluid	steady
Density	$\rho = 1023kg/m^3$
Viscosity	$1.56 \times 10^{-6}kg/(s \cdot m)$
Turbulence	1% at inlet boundary, (k-ω)
Mesh	1002637 cells (Yaw)
Convergence	100 steps ($< 10^{-5}$)
Roughness	Wall

The yaw damping relationship of moments and angular velocities are given in table 3.8, these data are estimated using STAR-CCM+. Note that, the ANSYS-CFX is not capable to provide the rotational damping estimations. Therefore, in the next chapter real world experiments have been conducted on the open-loop *CISCREA* AUV to verify the STAR-CCM+ rotational damping parameters.

Table 3.8: Damping moments of *CISCREA* AUV at different Velocities

CCM+ (rad/s)	0.5	1	1.5	2	2.5	3	3.5	4
Yaw $(N \cdot m)$	0.038	0.149	0.338	0.593	0.932	1.33	1.792	2.381

3.3.5 Damping Results Comparison

In this section, the numerical damping estimation results of ANSYS-CFX and STAR-CCM+ are compared, in three directions: surge, sway and yaw.

According to the calculated CFD damping force and moment, second order polynomial lines are implemented to approximate the relationship between the damping force and moment and the velocities. The polynomial approximation lines are given in figure 3-17, meanwhile, the polynomials are given in table 3.9.

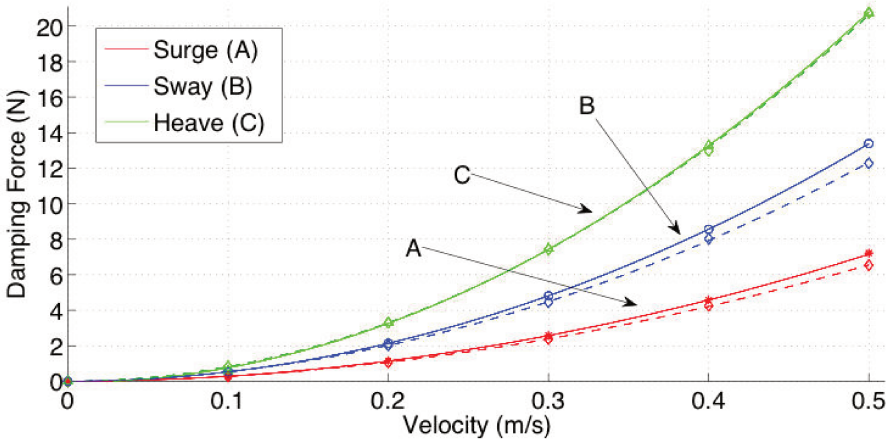

Figure 3-17: Damping force and velocity of *CISCREA* AUV (CFX: solid line, STAR-CCM+: dash line)

Table 3.9: CFD results curve fitting

	CFX & RMSE		STAR-CCM+ & RMSE	
Surge	$y = 28.6x^2 + 0.0089x$	0.01773	$y = 25.75x^2 + 0.2406x$	0.02294
Sway	$y = 53.52x^2$	0.00188	$y = 48.39x^2 + 0.4512x$	0.0595
Heave	$y = 83.42x^2$	0.103	$y = 82.44x^2$	0.1144
Yaw	-	-	$y = 0.1479x^2 + 0.001328x$	0.009881

It can be concluded from the damping comparisons of ANSYS-CFX and STAR-CCM+ that the estimation results of the two solutions coincide with each other.

Therefore, the CFD software are considered as a reliable solution to obtain the hydrodynamic damping parameters of complex-shaped underwater vehicles. Especially, for the robust control scheme, CFD estimations can be more efficient, as it allows to compromise accuracy to some extent.

On the contrary, we should mention that the objective to employ CFD damping analysis is to obtain the major damping properties of the complex-shaped underwater vehicles. The modeling errors can be treated as uncertainties in the robust control design. Achieving more accuracy is still considered to be difficult, hence during the CFD damping estimation, we compromise the accuracy with less (decent) number of meshes to reduce the calculation time. Figure 3-18, 3-19, 3-20, 3-21, 3-22, 3-23, 3-24 , 3-25 present the streamline view of *CISCREA* AUV under different operating modes. To validate the overset mesh method for the rotational damping analysis applications, we compare its results to the moving reference technique at an angular velocity of 4 rad/s. The comparison shows the approximated damping forces obtained respectively by the overset mesh method and the moving reference technique are 2.515 $N \cdot m$ and 2.381 $N \cdot m$. Our results show that quadratic damping components dominate the damping effects, and the linear damping component is negligible, as expected according to the *Morison* equation.

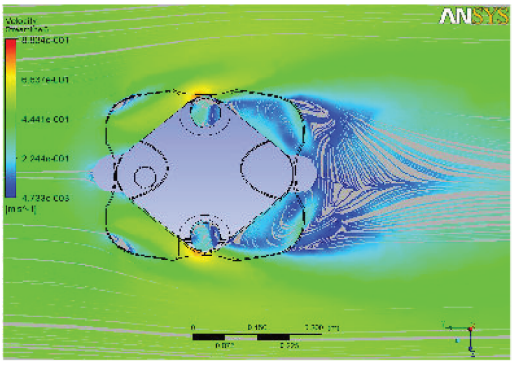

Figure 3-18: CISCREA Surge 0.5m/s (CFX)

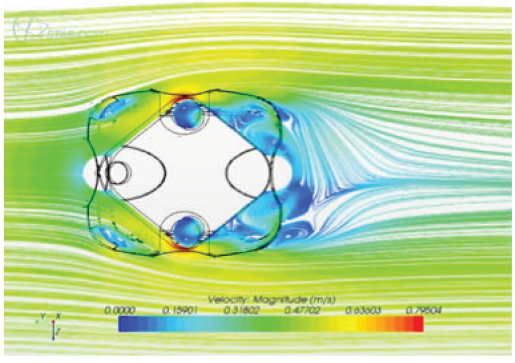

Figure 3-19: CISCREA Surge 0.5m/s (CCM+)

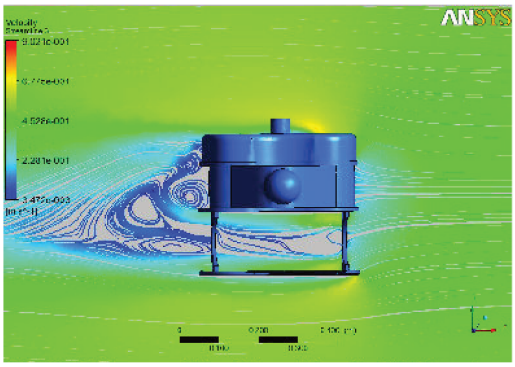

Figure 3-20: CISCREA Sway 0.5m/s (CFX)

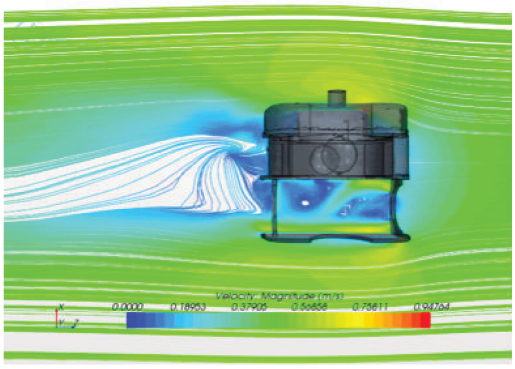

Figure 3-21: CISCREA Sway 0.5m/s (CCM+)

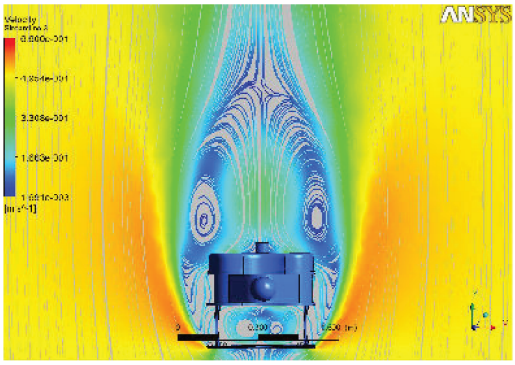

Figure 3-22: CISCREA Heave 0.5m/s (CCM+)

Figure 3-23: CISCREA Heave 0.5m/s (CCM+)

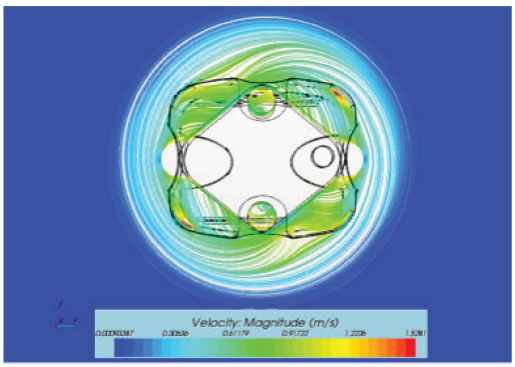

Figure 3-24: Moving Reference Rotation (2.381 $N \cdot m$)

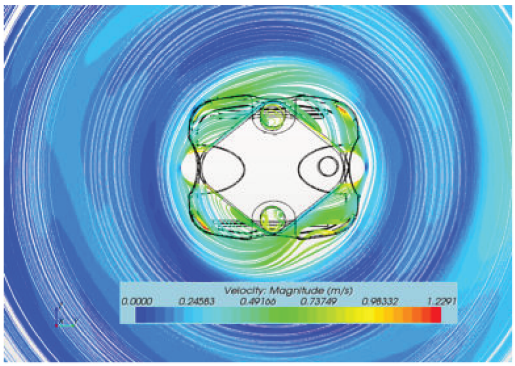

Figure 3-25: Overset Mesh Method (2.515 $N \cdot m$)

3.4 Four CFDs model of *CISCREA* AUV

In this section, the four degree-of-freedoms underwater vehicle model as well as its dynamic and hydrodynamic parameters are presented for the *CISCREA* AUV, which

involves the translational and rotational motions in the surge, sway, heave and yaw directions.

First, the 4 CFDs *CISCREA* AUV model is given in equation 3.17.

$$(M_{RB} + M_A)\dot{\nu} + D(|\nu|)\nu + g(\eta) = \tau_{env} + \tau_{pro} \tag{3.17}$$

Here, the mass inertia matrix M_{RB} is approximated by the CAD software PRO/E, as shown in equation 3.18 (mass: kg, moment of inertia: $kg \cdot m^2$).

$$M_{RB} = \begin{bmatrix} 15.643 & 0 & 0 & 0 \\ 0 & 15.643 & 0 & 0 \\ 0 & 0 & 15.643 & 0 \\ 0 & 0 & 0 & 0.3578 \end{bmatrix} \tag{3.18}$$

Added mass matrix M_A of *CISCREA* AUV is represented by the WAMIT estimation results:

$$M_A = \begin{bmatrix} 11.985 & -0.091 & -0.105 & 0.012 \\ 0.149 & 20.261 & -0.147 & -0.758 \\ 0.111 & -0.129 & 67.141 & 0.064 \\ -0.003 & -0.758 & 0.064 & 0.138 \end{bmatrix} \tag{3.19}$$

The damping matrix $D(|\nu|)$ of *CISCREA* AUV is estimated using the STAR-CCM + (equation 3.20):

$$
\begin{aligned}
D(|\nu|) &= D + D_n(|\nu|) \\
&= \begin{bmatrix} 0.2406 & 0 & 0 & 0 \\ 0 & 0.4512 & 0 & 0 \\ 0 & 0 & 0 & 0 \\ 0 & 0 & 0 & 0.0013 \end{bmatrix} \\
&+ diag\{|\nu|\}^T \begin{bmatrix} 25.75 & 0 & 0 & 0 \\ 0 & 48.39 & 0 & 0 \\ 0 & 0 & 82.440 & 0 \\ 0 & 0 & 0 & 0.1479 \end{bmatrix}
\end{aligned} \tag{3.20}
$$

The propulsion τ_{pro} forces and torques of the *CISCREA* AUV of equation 3.17 will be given in the hydrodynamic experiment in next chapter. The environmental disturbances τ_{env} are considered as uncertainties in the robust control design. In addition, since *CISCREA* AUV only has four degree-of-freedoms, i.e. the pitch and roll stability is guaranteed by the structural design of vehicle's gravity and buoyancy, instead of the control propulsions. Therefore, the restoring force $g(\eta)$ can be neglected for the *CISCREA* AUV robust control design.

3.5 Conclusion

In this chapter, we employed a variety of numerical methods and software to identify *CISCREA* AUV's major dynamic and hydrodynamic parameters: mass inertia matrix M_{RB}, added mass matrix M_A and damping matrix $D(|\nu|)$. Based on the estimation or calculation of numerical parameters, a four degree-of-freedoms model is derived for the *CISCREA* AUV, which provides the foundations for the hydrodynamic experiment and control design simulations.

In our numerical analysis of *CISCREA* AUV added mass matrix M_A, the WAMIT and MCC results show that the mass and inertia elements of the added mass matrix M_A are even larger than those in the mass inertia matrix M_{RB}. These results indicate

that the added mass matrix M_A is indeed an important hydrodynamic effects for the control design. The damping analysis of the *CISCREA* AUV damping matrix $D(|\nu|)$ shows that the quadratic damping components dominates the damping effects, and the linear damping component is negligible. Numerical results confirm the perdition of *Morison* equation. We can conclude that the quadratic damping is the major non-linearity in the underwater vehicle dynamics, which should be carefully considered to prevent control response oscillations. In order to verify the above mentioned conclusions, real world experiments have been conducted on the open-loop *CISCREA* AUV. These results are given in the following chapter.

Chapter 4

CISCREA AUV Hydrodynamic Experiment

Contents

4.1 Bollard Thrust 88

4.2 Experiment Design 93

4.3 Experiment Analysis 96

4.4 Experiment Results 98

4.5 Four DOFs Model of CISCREA 104

4.6 Yaw Model 105

4.7 Conclusion 106

In order to evaluate the numerical model as well as its dynamic and hydrodynamic parameters obtained in Chapter 3, real world experiments about the translational and rotational motion characteristics have been conducted on the open-loop *CISCREA* AUV [60, 29].

As it is mentioned before, numerical calculation and simulations are insufficient comparing to a real-world hydrodynamic experiment. To completely validate the ef-

ficiency of the numerical model (the computational hydrodynamic approximations), an independent experimental comparison is indeed required. It is necessary to implement hydrodynamic experiments in terms of the need for the following robust control design, and the experimental results should provide the nonlinearity and uncertainty information or properties of the *CISCREA* AUV. The main concern of this chapter is to validate the numerical estimations, i.e., the major hydrodynamic characteristics: the added mass and the damping effects of the *CISCREA* AUV in the surge, sway, heave and yaw directions.

Note that the main objective of our study consists in the use of robust control method to reduce the control sensitivity about the hydrodynamic modeling accuracy. Therefore, this chapter is dedicated to validate the numerical models required for the CFD software of complex-shaped underwater vehicles. Actually, the experimental results in this chapter is not capable to improve the modeling accuracy. To our perspective, the numerical estimation of the dynamic and hydrodynamic parameters should only describe approximately the dynamic behavior as well as uncertainty boundaries. Our goals are to avoid implementing hydrodynamic experiments using expensive equipments.

4.1 Bollard Thrust

In this part, we measured the bollard thrusts and torques of the *CISCREA* propellers.

According to Figure 4-1, the *CISCREA* AUV has six fixed thrusters four of them are installed in the horizontal plane, and they have a 30° angle align to the AUV center line. The other two vertical thrusters are on each side of the AUV body to control uniquely the heave motion.

Typically, the four horizontal thrusters simultaneously generate the force and torque vectors on the AUV body, which results in the movement on surge, sway and yaw directions. However, the two vertical thrusters of the *CISCREA* AUV can only rotate in the same direction to control the heave motion. The power and control signal of the vertical thrusters were designed to be connected, which limit the control

ability of *CISCREA* AUV on the roll direction motion. Besides, there is no propulsion configurations on *CISCREA* AUV for the pitch direction motion. In this case, it is necessary to design and distribute the buoyancy center and gravity center appropriately to satisfy the self-balancing stability on pitch and roll motions by mean of a strong restoring force.

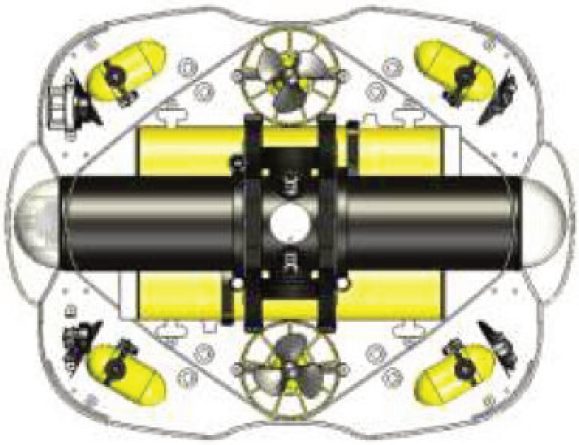

Figure 4-1: Propulsion Configuration of the *CISCREA* AUV

As shown in Figure 4-2, a dynamometer of SHIPMO (accuracy of 0.01 N) was introduced in the measurements of AUV bollard thrust force and torques. In this study, the major measurements include the following terms:

- Surge forces from the two front horizontal propellers (4 propellers can be too strong to maintain direction)
- Sway forces from the four horizontal propellers(2 propellers are too week to reach desired speed)
- Heave force from the two vertical propellers
- Yaw torque from the four horizontal propellers.

Note that, the propulsion control signal, i.e., Pulse Width Modulation (PWM) signal in the *CISCREA* AUV software has a range from 0 to 127. In order to deal with the dead-zone of the propellers, we tuned each propeller by add compensations

to the control signal. After the compensation, this PWM signal should be linear with the propulsion forces and torques. The thrust force varing from 0 to 30 (PWM signal) is too small to be accurately measured by the dynamometer. Meanwhile, a maximum propulsion should be avoided for long term operating. Hence, we selects the PWM signals range between 30 to 120.

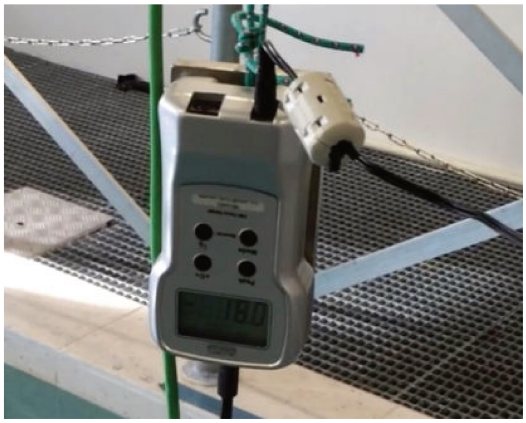

Figure 4-2: Force measurement using a dynamometer with an accuracy of 0.01 N

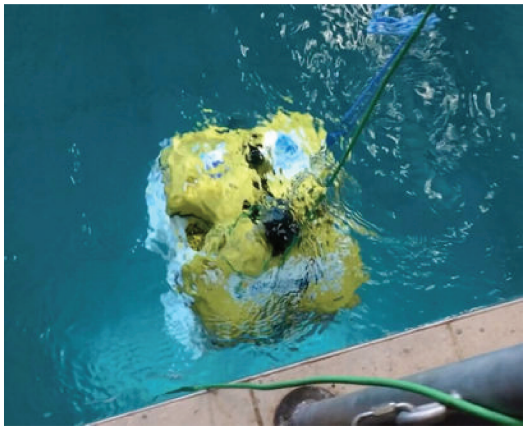

Figure 4-3: Measurement of the vertical propeller bollard thrust on *CISCREA* AUV

First, the bollard thrust measurement of the two vertical propellers is shown in Figure 4-3. In order to keep the *CISCREA* AUV steady during the measurement process, we fastened a heavy weight about half a meter beneath the AUV body to keep the gravity center in a low postion. The force values are shown in Table 4.1.

Table 4.1: Bollard thrust measurement results, Heave direction using 2 vertical propellers

PWM	30	40	50	60	70	80	90	100	110	120
Force (N)	1.3	2.0	3.1	4.1	5.1	6.8	8.3	9.2	9.9	11.3

Table 4.2: Bollard thrust measurement results, Surge direction using 2 front horizontal propellers

PWM	30	40	50	60	70	80	90	100	110	120
Force (N)	1.4	2.0	2.8	3.4	3.9	4.7	5.2	6.2	6.9	7.5

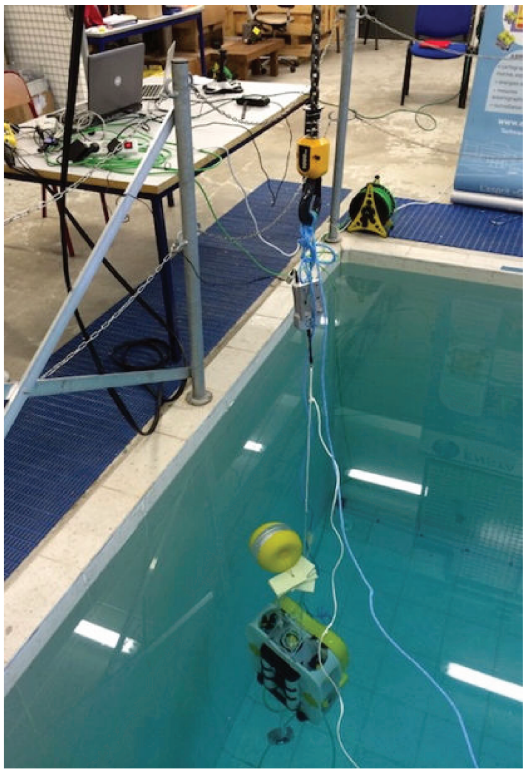

Figure 4-4: Bollard thrust measurement of the horizontal propellers

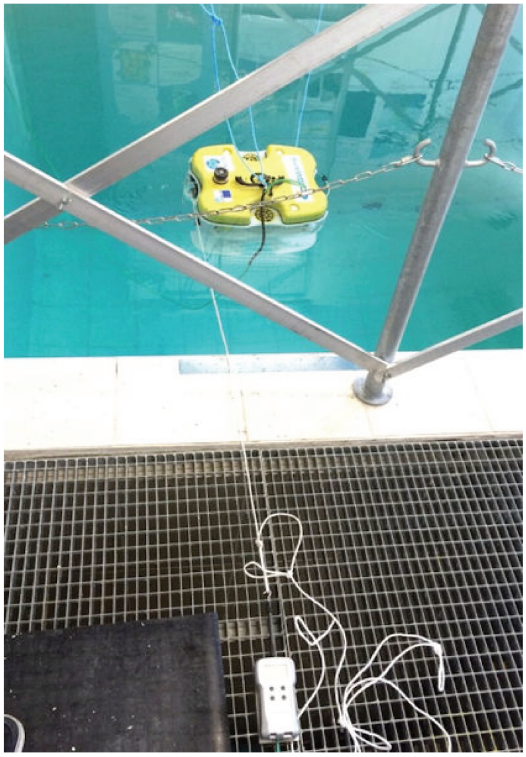

Figure 4-5: Torque measurement

Table 4.3: Bollard thrust measurement results, Sway direction using 4 horizontal propellers

PWM	30	40	50	60	70	80	90	100	110	120
Force (N)	1.9	3.0	4.2	5.4	6.2	7.6	8.9	9.9	11.0	12.3

Table 4.4: Bollard thrust measurement results, Torque on yaw direction using 4 horizontal propellers, around the center of the AUV body

PWM	30	40	50	60	70	80	90	100	110	120
Torque ($N \cdot m$)	1.9	3.0	4.2	5.4	6.2	7.6	8.9	9.9	11.0	12.3

To measure the horizontal bollard thrust in the vertical direction using the dynamometer, we used a heavy weight and some floating parts to flip by 90° the attitude of the *CISCREA* AUV, as shown in Figure 4-4. In this case, the bottom frame of the AUV is removed and the propulsion force can act on the same direction as gravity and buoyancy forces. The AUV body is steady during the measurement process,

since the gravity center is much lower than the buoyancy center. Any small error of perpendicular propulsion (perpendicular to the gravity direction) can be restrained by a strong restoring force.

For the surge motion, the two front horizontal propellers are used, see Table 4.2. In the contrary, as the horizontal propellers have a 30° angle to the center line of the *CISCREA* AUV body, the propulsion force in the sway direction becomes smaller than the one in the surge direction. Therefore, we activated the four horizontal propellers together for the sway motion. The bollard thrusts results for the sway direction are given in Table 4.3. The torque measurement of the yaw rotation is shown in Figure 4-5, and the torque results using the four propellers are given in Table 4.4.

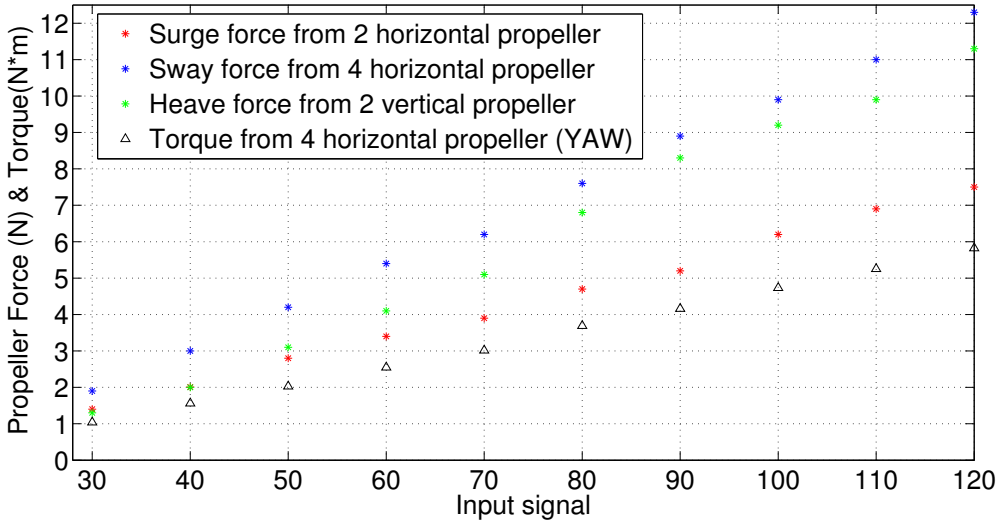

Figure 4-6: Measurements of propulsion forces and torques of the *CISCREA* AUV

AUV bollard thrust data are shown in Figure 4-6. It is seen clearly that the PWM signal is approximately linear to the AUV bollard thrust forces and torques. According to a previous propulsion model [99], the AUV motion can affect the speed of the fluid that injected into the propellers, which results in some reduction of the AUV propulsion efficiency. As we use the robust control scheme in the following chapters, the modeling assumption or the measurement errors of bollard thrusts can be considered as adding uncertainties for the robust controller. Therefore, we have made the following assumptions for the research:

- There is no propulsion efficiency reduction of the AUV in a moving fluid environment.
- The effect of the propulsion difference between the propeller blade clockwise and courter-clockwise rotation is neglected.
- The *CISCREA* AUV PWM signal is linear to the propulsion force, which is acting in realtime without any delay.

4.2 Experiment Design

During the experiment, the open-loop *CISCREA* AUV is driven in the surge, sway, heave or yaw directions in the pool with setting propeller PWM values, related to known propulsion forces or torques measured in the bollard thrust section. Then, the AUV motions were captured by several cameras, both on top of the pool ceiling and underwater. The AUV motion video may derive the hydrodynamic characteristics during the analysis of each video-frame. Finally, the experimental hydrodynamic results (include added mass and damping properties) should be compared to the computational *CISCREA* model calculated in chapter 3.

As shown in Figures 4-7, 4-8, 4-9, 4-10, the bollard thrust measurement data (Figure 4-6) is used to drive the *CISCREA* AUV moving in 4 DOFs in the pool. The size of the pool is $4m$ (length) $\times$ 4 m (width) $\times$ 3.5 m (height). A 15-fps camera is installed on top of the pool on the laboratory wall, to capture the AUV motion in surge, sway and yaw directions. Meanwhile, a 25-fps camera is used and installed underwater to capture the AUV heave motion. For the surge and sway directions, the *CISCREA* AUV is driven in the pool from one end to another using a constant propulsion force. For the heave direction, the *CISCREA* AUV is driven by the constant vertical propulsion force moving downward in the pool from the top to the bottom. For the yaw rotation, the *CISCREA* is spinning and accelerating by a constant propulsion torque until it reaches a constant angular velocity.

Actually, the experimental goal of this part is to build a map relating different

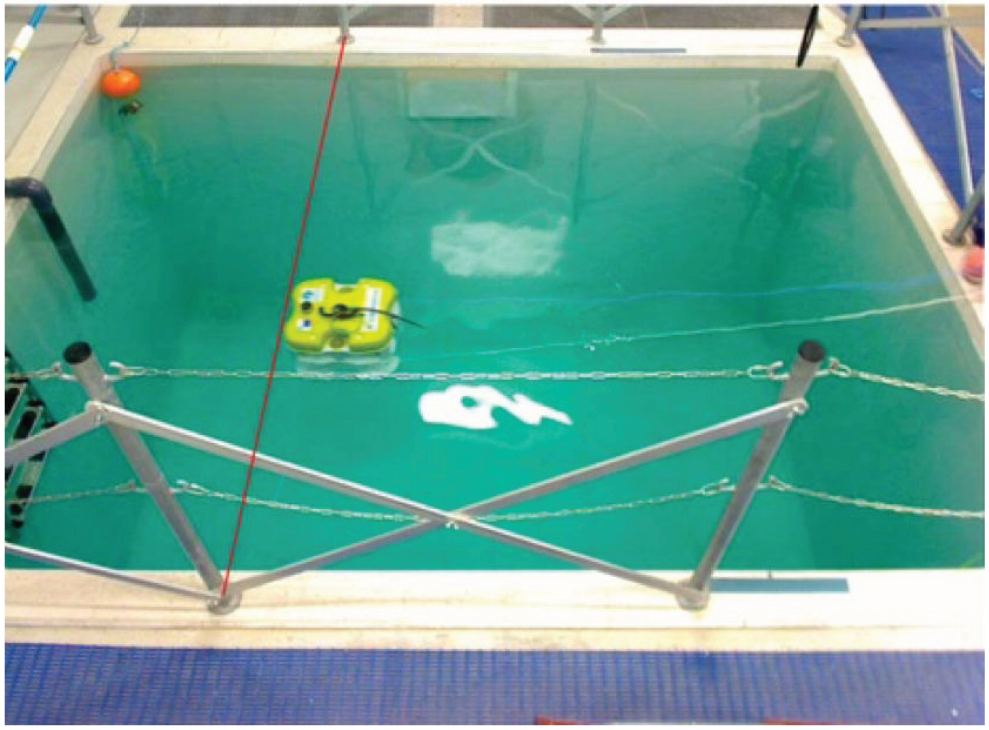

Figure 4-7: *CISCREA* AUV captured by a camera moving in the surge direction

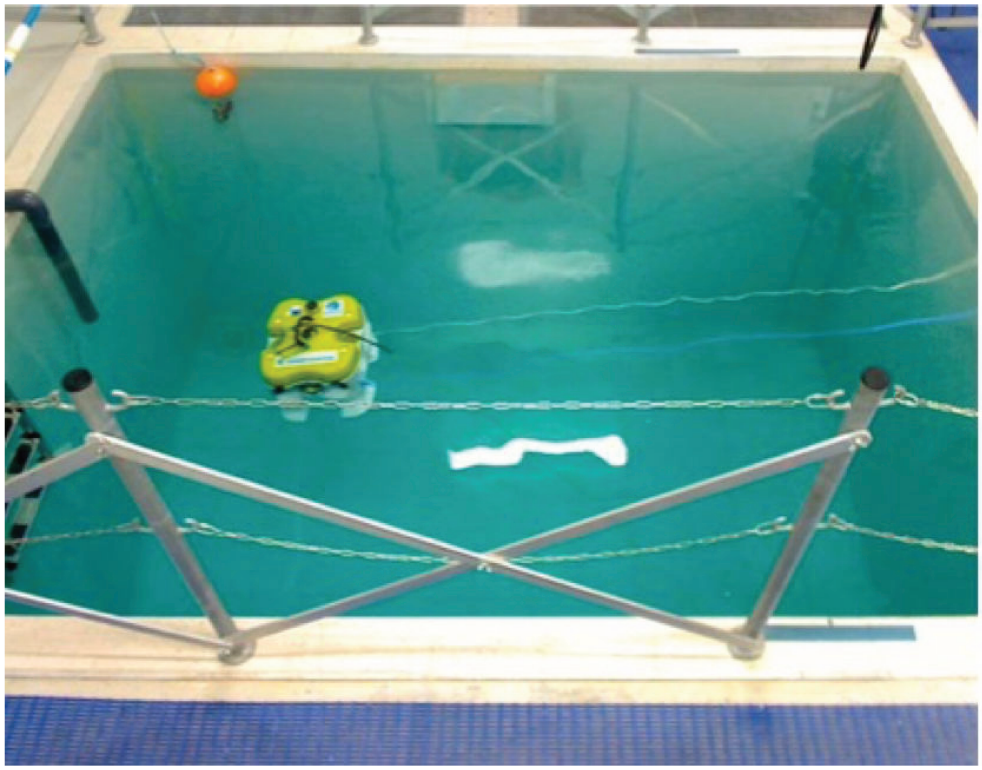

Figure 4-8: *CISCREA* AUV captured by a camera moving in the sway direction

Figure 4-9: *CISCREA* AUV captured by an underwater camera moving in the heave direction

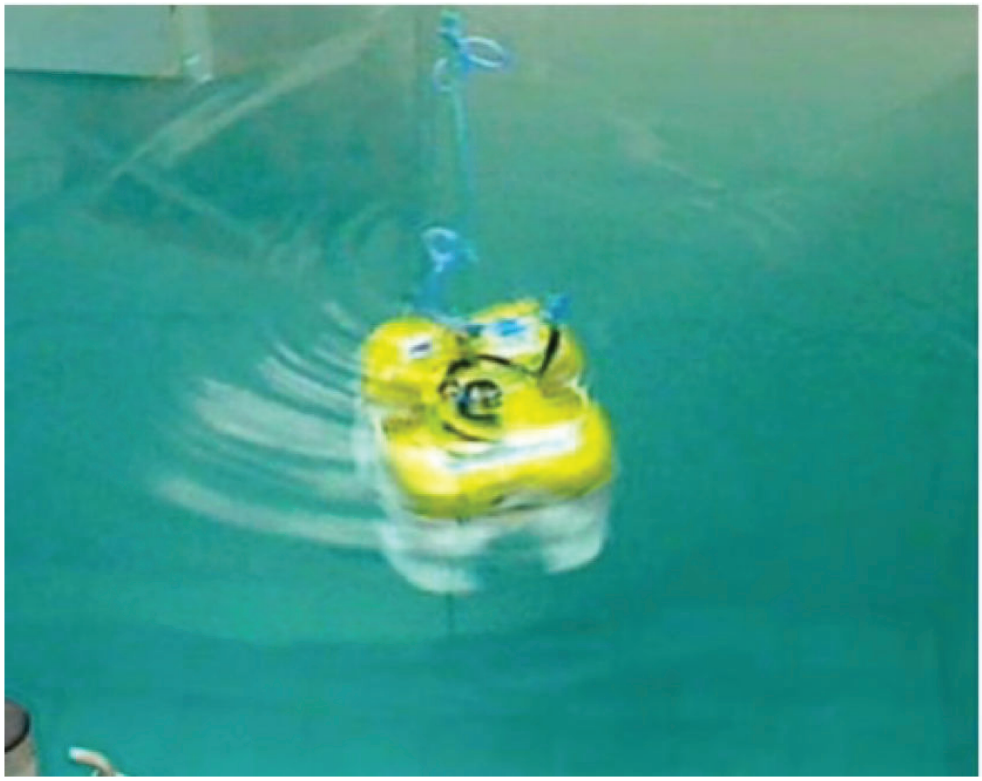

Figure 4-10: *CISCREA* AUV captured by a camera moving in the yaw direction

AUV damping forces or torques to their corresponding converged AUV velocities or angular velocities. Then, the experimental results can be compared to the computational damping and velocity relationship calculated in chapter 3. By neglecting the uncertainty or the disturbance, the AUV added mass force or torque is only active in the acceleration process. For a a constant speed AUV the added mass becomes zero, and the primary hydrodynamic effect affects merely the damping force or torque. As the *CISCREA* AUV is driven by many constant propulsion forces and torques during the experiment, the AUV would accelerate and finally reaches its steady regime speed, namely the equilibrium condition when the damping force or torque is equivalent to the propulsion force or torque. Note that, this propulsion force or torque, equivalent to the damping force or torque, is known from the bollard thrust measurement in previous section. In additional, the motion video provides the velocities and angular velocities information corresponding to each propulsion configuration. In practice, the velocity or angular velocity are derived from the AUV position or angle in each video frame. As mentioned before, the propulsion force, the pool size and the time hitting the wall or single rotational lap are known. Therefore, the expected experimental damping and velocity map can be approximated using the bollard thrust and video velocity data.

4.3 Experiment Analysis

In order to validate the experiment designed in previous parts, it is necessary to verify two issues for the comparison of computational and experimental AUV hydrodynamic parameters:

- Is the pool large enough for the AUV to reach the equilibrium condition, i.e., accelerate to the converged constant velocity?
- How to measure or derive the final converged speed of the AUV from the captured video frames?

First, let us simply assume that the *CISCREA* AUV has a linear dynamic equation

4.1:

$$(M_{RB} + M_A)\ddot{x} + D_L\dot{x} = \tau_m \tag{4.1}$$

where D_L is the unknown linear damping vector (coefficients), τ_m is the propulsion force or the torque vector, x is the position and angle vector of the *CISCREA* AUV, and M_{RB} and M_A are defined in chapter 2.

By only considering the surge direction, and the initial conditions and 4 necessary assumptions can be described as follows:

- The rigid body mass in the surge direction of M_{RB} of the *CISCREA* AUV is 15.643 kg (See chapter 3).
- The added mass in the surge direction of M_A of the *CISCREA* AUV is 11.985 kg (Calculated using WAMIT, see chapter 3).
- Initial AUV velocity in all translational directions are 0 m/s (surge, sway, heave). During the experiment, the only speed considered is related to the surge motion.
- Initial position is 0 m (surge direction).

As a result of those modeling information, the unknown linear damping coefficient in the surge direction of D_L can be calculated, since the start and end moment of the AUV surging in the pool are known from the video, and the distance traveled in the experiment is equal to the pool length 4 m minus the AUV size 0.525 m. Note that, as the surge motion is approximated by linear dynamics, it can provide information as the estimation of the steady speed for further purposes.

In Figure 4-11, the surge motion is approximated using 10 data points of the bollard thrust measurements, using equation 4.1. It is clear in Figure 4-11 the *CISCREA* AUV can converge to steady speeds (or equilibrium velocities) after nearly 10 s with all possible surge propulsions configurations. The convergence in Figure 4-11 indicates that the pool size is large enough for the *CISCREA* AUV to reach a constant speed, and the average speed can be measured after a specific time. For example, the average surge speed is measured after the red mark which is shown in Figure 4-7.

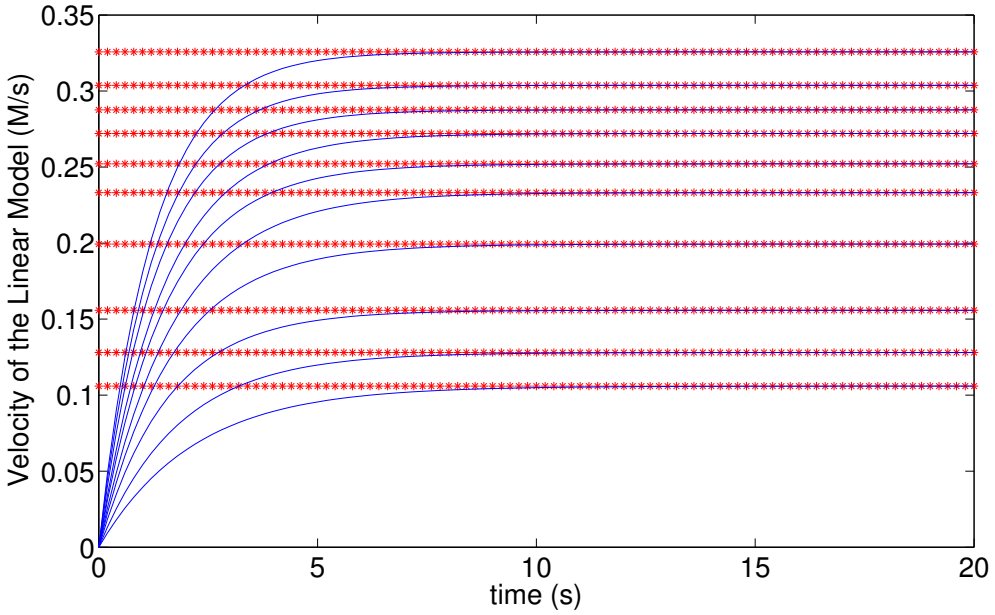

Figure 4-11: Convergence of velocities after 10s for 10 constant bollard force points

In additional, the converged speed, derived from the video with the aid of the linear dynamic equation 4.1, can also provide an estimation of the final velocity while the final speed is impossible to be measured using regular average speed method.

Similar conclusions can be draw for the sway, heave and yaw directions. The equilibrium speeds are estimated from the video related to the damping forces and torques (equal to the bollard thrust). We should mention that, the average speed (converged) are measured from the video for *CISCREA* AUV's surge, sway and yaw motion. The speed approximation of equation (4.1) is used to represent the converge speed for the heave motion. We used the heave approximation instead of the average speed method because the distance for calculating average speed is hardly identified on our underwater camera.

4.4 Experiment Results

From the hydrodynamic experiment of the *CISCREA* AUV, we get 40 discrete data points representing the following damping and velocity relationships in surge, sway, heave and yaw, in addition, we implement 4 second order polynomial approximation

curves to compare the hydrodynamic charateristics:

- Surge: experimental damping and velocity relationship are given in Table 4.5, and its comparison to the ANSYS-CFX and STAR-CCM+ approximation is shown in Figure 4-12. Note that an average nominal model is proposed for further robust control design.

- Sway and Heave: experimental results are given respectively in Table 4.6 and 4.7, and its comparisons to ANSYS-CFX and STAR-CCM+ results are shown in Figure 4-13 and 4-14.

- Yaw: experimental results are given in Table 4.8, and its comparison to STAR-CCM+ results is shown in Figure 4-15. As mentioned in Chapter 3, only STAR-CCM+ provides the numerical damping estimation for the yaw rotation.

Table 4.5: Surge direction using 2 front horizontal propellers

Force (N)	1.4	2.0	2.8	3.4	3.9	4.7	5.2	6.2	6.9	7.5
Speed (m/s)	0.11	0.15	0.18	0.23	0.25	0.27	0.30	0.35	0.36	0.40

Table 4.6: Sway direction using 4 horizontal propellers

Force (N)	1.9	3.0	4.2	5.4	6.2	7.6	8.9	9.9	11.0	12.3
Speed (m/s)	0.13	0.16	0.20	0.22	0.25	0.28	0.30	0.32	0.35	0.39

Table 4.7: Heave direction using 2 vertical propellers

Force (N)	1.3	2.0	3.1	4.1	5.1	6.8	8.3	9.2	9.9	11.3
Speed (m/s)	0.12	0.18	0.21	0.26	0.28	0.31	0.32	0.33	0.35	0.39

Table 4.8: Yaw direction rotation both clockwise (CW) and counter-clockwise (CCW) using 4 horizontal propellers, around the center of the AUV body

Torque $(N \cdot m)$	2.0	3.0	3.9	4.9	5.8	7.1	8.0	9.1	10.1	11.2
CW (rad/s)	1.57	1.99	2.33	2.69	3.00	3.24	3.38	3.61	3.83	3.98
CCW (rad/s)	1.54	1.90	2.29	2.62	2.93	3.18	3.44	3.63	3.79	3.95

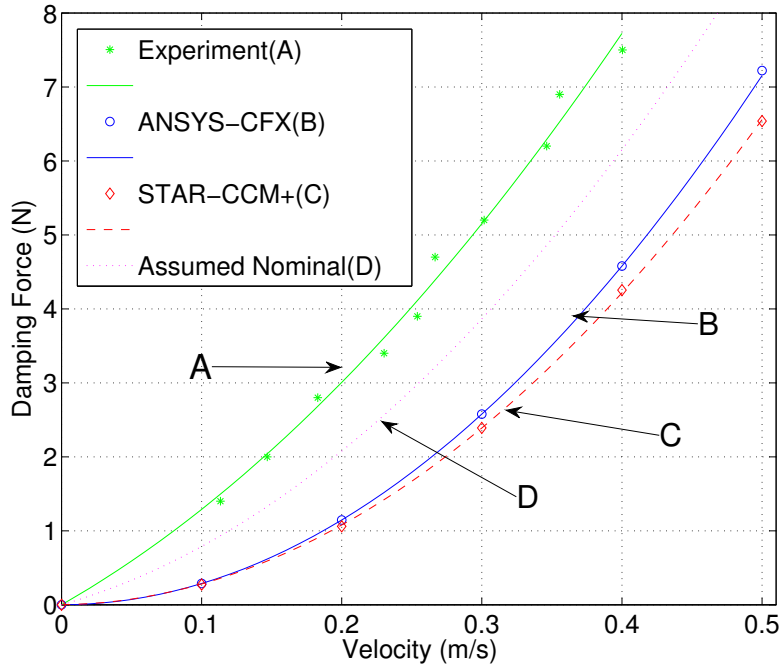

Figure 4-12: Experimental and computational comparison of damping and velocity relationship in the surge direction of the *CISCREA* AUV

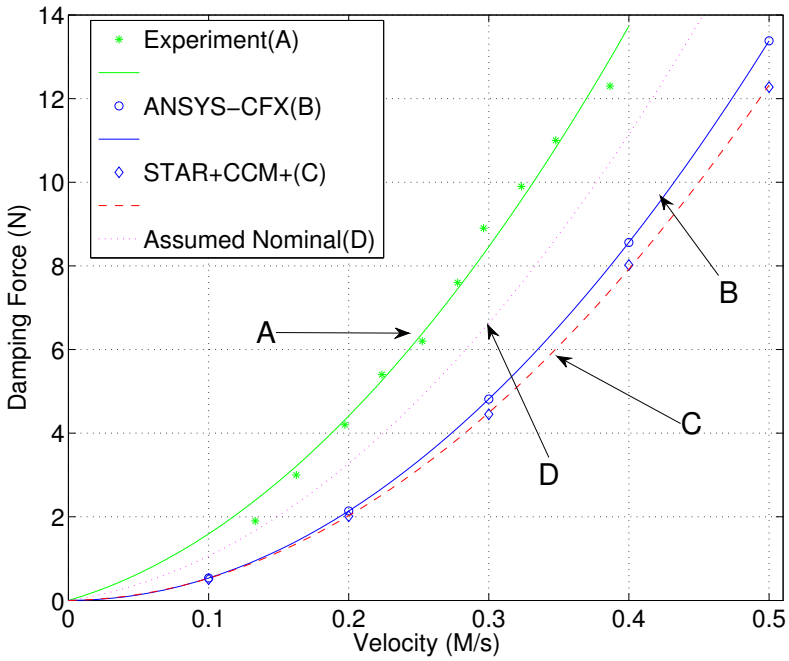

Figure 4-13: Experimental and computational comparison of damping and velocity relationship in the sway direction of the *CISCREA* AUV

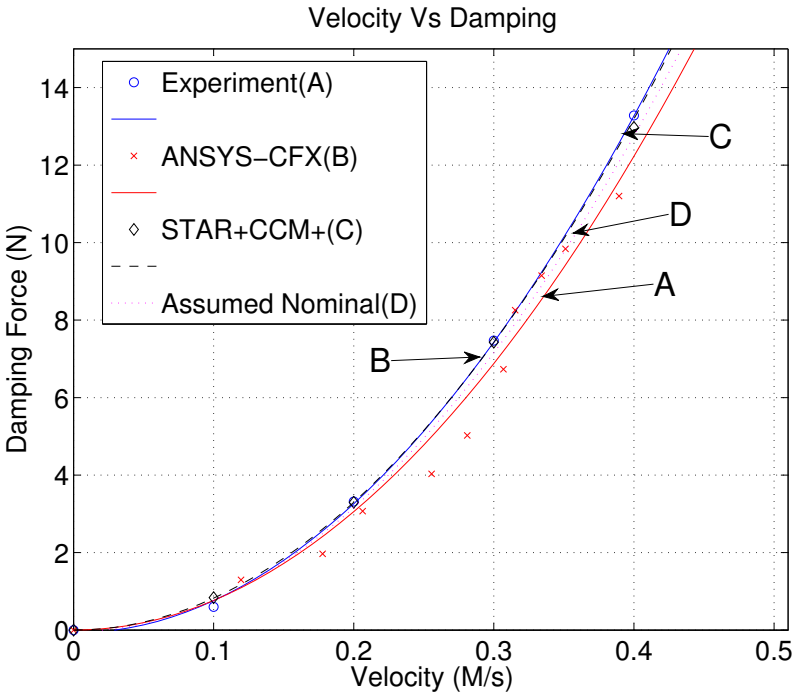

Figure 4-14: Experimental and computational comparison of damping and velocity relationship in the heave direction of the *CISCREA* AUV

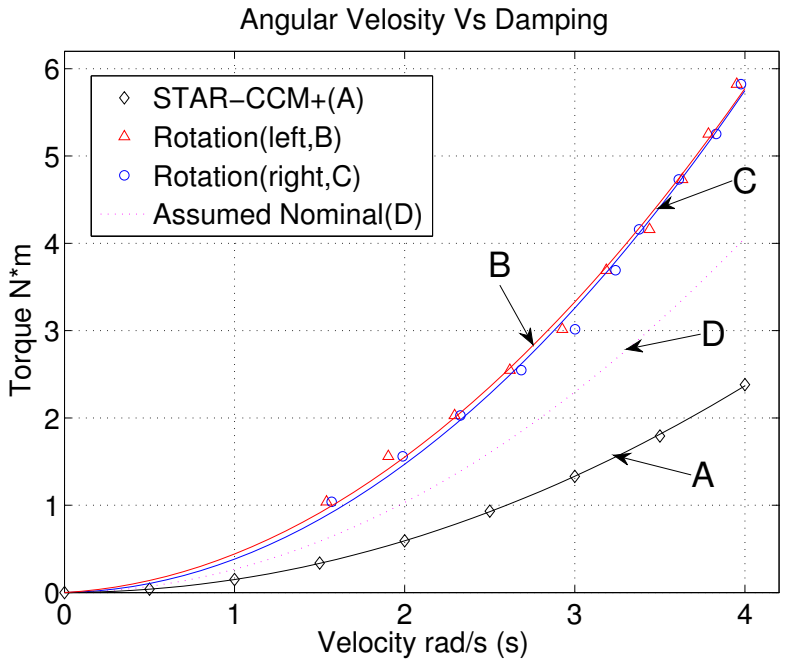

Figure 4-15: Experimental and computational comparison of damping and velocity relationship in the yaw direction of the *CISCREA* AUV

Table 4.9: Experimental results of curves fitting (x: velocity m/s or angular velocity rad/s, y: propulsion force N or torque $N \cdot m$, CW: clockwise, CCW: Counter-clockwise)

	Experiment & RMSE	
Surge	$y = 21.4x^2 + 10.75x$	0.214
Sway	$y = 61.39x^2 + 9.775x$	0.3817
Heave(dive)	$y = 83.42x^2$	0.5924
Yaw(CW)	$y = 0.3513x^2 + 0.0321x$	0.119
Yaw(CCW)	$y = 0.3338x^2 + 0.1081x$	0.117

Table 4.10: STAR-CCM+ results curve fitting (x: velocity m/s or angular velocity rad/s, y: propulsion force N or torque $N \cdot m$)

	Experiment & RMSE	
Surge	$y = 25.75x^2 + 0.2406x$	0.02294
Sway	$y = 48.39x^2 + 0.4512x$	0.0595
Heave(dive)	$y = 82.44x^2$	0.1144
Yaw	$y = 0.1479x^2 + 0.001328x$	0.009881

Table 4.11: ANSYS-CFX results curve fitting (x: velocity m/s or angular velocity rad/s, y: propulsion force N or torque $N \cdot m$)

	Experiment & RMSE	
Surge	$y = 28.6x^2 + 0.0089x$	0.0177
Sway	$y = 53.52x^2$	0.0018
Heave(dive)	$y = 83.42x^2$	0.103

Table 4.12: Assumed nominal model (x: velocity m/s or angular velocity rad/s, y: propulsion force N or torque $N \cdot m$)

Surge	$y = 25x^2 + 5.379x$
Sway	$y = 57.48x^2 + 4.88x$
Heave(dive)	$y = 80.37x^2$
Yaw(left)	$y = 0.2496x^2 + 0.021x$

The second order polynomial approximation of the experimental damping and velocity relationship is given in Table 4.9, while the polynomial approximation of the computational STAR-CCM+ and ANSYS-CFX results are shown respectively in Table 4.10 and 4.11.

Finally, we can conclude from the comparison of the experimental and the computational hydrodynamic results that:

- According to Figures 4-12, 4-13, 4-14, 4-15, the numerical models in Chapter 3 give the principal hydrodynamic characteristics of the complex-shaped *CIS-CREA* AUV. It is efficient to provide approximately the major hydrodynamic information such as damping, added mass, and uncertain boundaries for the robust controller synthesize.

- Although the numerical modeling accuracy is not considered to be very high, for example to be used for precise physical phenomena analysis, the modeling errors can be assigned as the uncertainties in further robust control loop.

- The gap in Figures 4-12 and 4-13, are mainly caused by the drag of the cables and ropes, which are playing opposite efforts in Figure 4-14. In addition, moving fluid causes the decrease of the propulsion also contributes to some experiment error ([114]).

- Rotational damping results of the STAR-CCM+ and experiment are compared in Figure 4-15. Obviously, there is a considerable difference between the two results. However, the numerical model is still validated, and considered to be enough for the robust controller in real sea test. In the next chapter, we introduce an improved robust control scheme to handle this difference. An efficient robust controller is synthesized based on the numerical hydrodynamic model. Form the practical view, the rotational CFD results can be improved by more intensive calculations or simulations, which is out of our scope.

Considering propulsion decrease and rope drag, etc., real AUV hydrodynamic damping should be smaller than the experimental results. Therefore, we proposed an ideal nominal models for the robust control design by taking average of the CFD and experimental results. The nominal model is shown in Table 4.12 representing the 4DOFs hydrodynamics.

4.5 Four DOFs Model of CISCREA

Considering the experimental hydrodynamic results and the proposed nominal model, a 4 DOFs AUV model as well as its dynamic and hydrodynamic parameters are presented for the *CISCREA* AUV (equation 4.2):

$$(M_{RB} + M_A)\dot{\nu} + D(|\nu|)\nu + g(\eta) = \tau_{env} + \tau_{pro} \tag{4.2}$$

Here, the mass inertia matrix M_{RB} is approximated by the CAD software PRO/E, as shown in equation 4.3 (mass: kg, moment of inertia: $kg \cdot m^2$).

$$M_{RB} = \begin{bmatrix} 15.643 & 0 & 0 & 0 \\ 0 & 15.643 & 0 & 0 \\ 0 & 0 & 15.643 & 0 \\ 0 & 0 & 0 & 0.3578 \end{bmatrix} \tag{4.3}$$

Added mass matrix M_A of *CISCREA* AUV is estimated by WAMIT software:

$$M_A = \begin{bmatrix} 11.985 & -0.091 & -0.105 & 0.012 \\ 0.149 & 20.261 & -0.147 & -0.758 \\ 0.111 & -0.129 & 67.141 & 0.064 \\ -0.003 & -0.758 & 0.064 & 0.138 \end{bmatrix} \tag{4.4}$$

The nominal damping matrix $D(|\nu|)$ (equation 4.5) of the *CISCREA* AUV is replaced by the average of the ANSYS-CFX, STAR-CCM + (equation 3.20) and experimental results:

$$
\begin{aligned}
D(|\nu|) &= D + D_n(|\nu|) \\
&= \begin{bmatrix} 5.379 & 0 & 0 & 0 \\ 0 & 4.88 & 0 & 0 \\ 0 & 0 & 0 & 0 \\ 0 & 0 & 0 & 0.021 \end{bmatrix} + \\
&\quad diag\{|\nu|\}^T \begin{bmatrix} 25 & 0 & 0 & 0 \\ 0 & 48.39 & 0 & 0 \\ 0 & 0 & 82.440 & 0 \\ 0 & 0 & 0 & 0.1479 \end{bmatrix}
\end{aligned} \tag{4.5}
$$

4.6 Yaw Model

Without lose of generality, a yaw model is derived in this section for the robust heading control design of the next chapter. Actually, the goal of our work is to validate the method that combines an improved robust control scheme with the numerical dynamic and hydrodynamic AUV models. Therefore, we only demonstrate the robust controller in the yaw direction to keep a simple and small problem that can prove our approach. Although the robust control scheme is a MIMO control method, it does not prevent the validated SISO robust yaw control (heading control) algorithm extending to 6 DOFs.

Moreover, the heading control problem is one of the most important or critical issues for the hovering underwater vehicles. It is the foundation for the hovering AUVs to achieve fast, accurate and stable control performance, which increase their maneuverabilities to enter complex space, observe precise underwater targets, and make accurate survey or operating actions. For example in SAUCE competition [12], the AUVs are required to monitor and take precise pictures of a man-made underwater structure from fixed distances and attitudes. In this case, the key issue to accomplish the task is to install a precise controller that can handle the environmental and modeling uncertainties as well as the hydrodynamic nonlinearities.

As mentioned before, the pitch and roll directions of the *CISCREA* AUV are stable and self-balanced by the restoring force. Therefore, the attitude of *CISCREA* AUV is assumed to be always vertical, which neglecting buoyancy and gravity effects. The rotational model can then be simplified as follows (equation (4.6)):

$$(I_{YRB} + I_{YA})\ddot{x}_r + D_{YN}|\dot{x}|\dot{x} + D_{YL}\dot{x}_r = \tau_i \tag{4.6}$$

Definitions and parametric values, such as inertia and damping coefficients, are listed in Table 4.13.

Table 4.13: Rotational model notions of yaw direction

Parameter	Description	Value
I_{YRB}	Rigid-body inertia	$0.3578kg \cdot m^2$
I_{YA}	Added mass inertia	$0.138kg \cdot m^2$
D_{YN}	Nominal quadratic damping factors	Ideal 0.2496
D_{YL}	Nominal linear damping factors	Ideal 0.021
$\dot{x}_r$	Angular Velocity	0 to 4rad/s
τ_i	Torque input	0 to $6N \cdot m$

It is clear from equation 4.6, the *CISCREA* AUV yaw model is nonlinear, and the quadratic damping effect plays a major role in the hydrodynamic nonlinearity. Notice that, all the parameters have uncertainties, as they are either measured or numerically calculated. There also exit many un-modeled physics in the real ocean environment. In the following chapters, those uncertainties will be carefully discussed and treated using H_∞ control method.

4.7 Conclusion

In chapter 4, we designed a 4 DOFs (Surge, Sway, Heave, and Yaw) experiment to validate the CFD models and its hydrodynamic parameters that obtained in Chapter 3. Conclusion can be made according the experimental results: the numerical AUV modeling method (Chapter 3) is concluded sufficient for the complex-shaped underwater vehicles under the scope using the robust control scheme.

During the experiment, the bollard thrust of *CISCREA* AUV propellers are measured and studied. The results show an approximately linear propulsion behavior, and lead to the assumption of a linear propulsion model (with uncertainties) for further robust control synthesis.

With the aid of the linear dynamic approximation (equation 4.1), we verified the pool size is large enough for the *CISCREA* AUV to reach a constant speed, and the experiment provides the specific position region to measure the average speed to represent the converged AUV velocity.

Finally, 4 DOFs (Surge, Sway, Heave, and Yaw) damping and velocity relationships were derived from the recorded videos. Second order polynomial curves are implemented to approximate damping and velocity results, in addition, they are compared to CFD results from ANSYS-CFX and STAR-CCM+. The comparison shows the hydrodynamic damping is nonlinear, and mainly consisted of or caused by the quadratic damping. This nonlinear damping issue is essential and critical for the further control design.

Part III

AUV Control

Chapter 5

AUV H_∞ Controller and Simulations

Contents

5.1 Robust Control Theory 111

5.2 Control of the *CISCREA* AUV 127

5.3 *CISCREA* AUV Yaw Control Simulations 138

5.4 Simulation Results 142

5.5 Conclusion 145

AUV is not a new invention now, but the world is making ever-greater demands of intelligent, agile and reliable AUV or swarm of AUVs to work in deep water for long periods. The underwater space is a complex, un-modeled or even unknown environment. Therefore, AUV robustness becomes one of the key challenges for long term working AUVs in the presence of uncertainties. Currently, the AUV controller is a hot issue [81, 84, 111], and its robustness is important for high performance AUVs. In fact, the robust control schemes for AUVs should be stable with not only one specific AUV dynamic and hydrodynamic model, it should handles at any time a group of models which represent any changing behaviors or parameters with the real ocean environment.

In reality, the uncertainties are ubiquitous for any controlled plant. In addition,

they are inevitable in the ocean environment, and they introduce difficulties in the AUV controller design, such as: unpredictable wind, wave, current, turbulence or obstacles. Generally, an automatic system consists of two parts: the controller part and the controlled plant. Control schemes can modify the controller part and change the closed-loop behavior. However, it can be very difficult to accurately estimate the parameters or dynamics of the controlled plants or models in real time. In addition, it is hard for traditional controllers to handle those unknown uncertainties. Concerning the uncertainties in the real ocean environment, many mathematically perfect AUV control solutions can be less efficient, and sometime the controller can be unstable and damage the AUV.

A robust AUV requires a motion controller that can achieve both the control performance and the closed-loop stability in the presence of ocean uncertainties. Actually, the H_∞ control theory handles the uncertainty issues using H_∞ norms in the frequency domain [77, 76]. Recently, the H_∞ control method has been adopted more frequently in marine activities.

Consider the robust control problems of the *CISCREA* AUV, several issues matters [129]:

- Parametric uncertainties and un-modeled dynamics in the AUV models
- Quadratic damping effects
- External disturbance as well as sensors' noise

As mentioned in Chapter 1, most of traditional control schemes can not prevent the inefficiency of the control performance as well as the stability reduction in the presence of dynamic uncertainties. Meanwhile, the few nonlinear control schemes are generally complex and limited to specific assumptions. Therefore, we proposed a simple AUV linear H_∞ control scheme. The proposed robust control approach inherited a numerical model from previous CFD works [129]. Numerically predicted the actuator force compensates the nonlinear damping behavior, thereby results in a linear AUV model with uncertainties. Based on the bounded linear nominal model,

the classical H_∞ approach [76] was used to handle the uncertainties raising from the modeling and compensating process, etc. A linear AUV behavior can be derived, which is critical and convenient for both control design and navigation improvement.

Deep inside the ocean, the earth magnetic signal is one of the merely existing information that tells the heading of robots with very good cost efficiency. It is important the AUV can control its heading using only one magnetic compass as feedback sensor. Without lose of generality, a robust heading controller using the proposed linear H_∞ approach was implemented and simulated for the *CISCREA* AUV. Simulation results provided, mainly including: proposed model based H_∞ approach, classical H_∞ approach without nonlinearity compensation, and classical PID control scheme.

5.1 Robust Control Theory

The robust controller handles the uncertainty issues by building the nominal model based closed-loop feedback control, and it satisfies for every plant belonging to the uncertainty model set, two conditions:

- Robust stability,
- Robust performance.

The robust control can be related to two problems: robust analysis and robust synthesize problems. The analysis problem pushes the controller to satisfy the desired properties for all admissible noises, disturbances, and model uncertainties. The synthesis problem designs a controller satisfying the desired properties for admissible noises, disturbances, and model uncertainties [77, 76]. A standard H_∞ problem is shown in Figure 5-1. The AUV dynamic and hydrodynamic models, uncertainties and disturbances, the weighting functions are all describe in a Linear Fractional Transformation (LFT) form, representing as the generalized system G, robust controller K and the uncertainties block Δ.

In historical reviews of robust control theory [130, 76, 77, 131], *Zames et al.* introduced the first robust control breakthrough in early 1980s [132, 133]. They considered

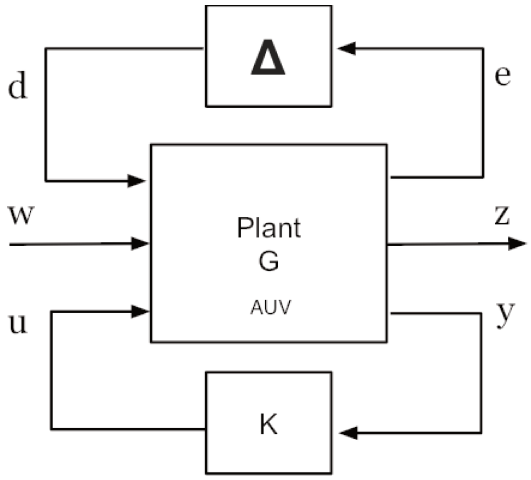

Figure 5-1: Robust control design diagram, where G matrix is the controlled plant, Δ matrix block describes the uncertainties, K matrix is the controller, d, w, u are elements of input vectors, e, z, y consist of output vectors.

the sensitivity issue raised by the uncertainties, and solved the optimal controller for a SISO system, which forms the foundation of the H_∞ optimal theory. *Doyle* also changed the control research direction by his pioneering work on the robustness of LQG control systems [75], and he built the subsequent μ-synthesis/analysis paradigm. The authors of [134, 135, 136, 137] proposed the multivariable H_∞ theories that extend the complex theoretical H_∞ scope to MIMO systems. Later on, *Doyle et al.* validated the H_∞ synthesis method using only two *Riccati* equations [138], to reduce the computational burden and optimization complexity of H_∞ synthesis. The theoretical frame-work of the H_∞ robust control theory took shape in the 1980s, and a lot of engineering applications were matured in the 1990s. In the last few decades, many related theories and algorithms, such as the Linear Matrix Inequality (LMI) method for synthesis, algorithms for low-order controllers, have been tackled and form the state of art for H_∞ robust control theory. Currently, there are still new trend to solve the suboptimal issues for future H_∞ theory.

H_∞ theory has shown its efficiency to handle uncertainties for the Linear Time Invariant (LTI) Systems. In addition, H_∞ control theory consists of two problems: the robust analysis and robust synthesis. Therefore, in the following section, we would introduce the theory for our proposed robust control algorithm (a LTI H_∞ approach)

for the nonlinear AUV plant in face of uncertainties. The complete robust control theory can be found in [76, 77, 131], and the mathematical conceptions used in our approach are described in the Appendix C.

5.1.1 H_∞ Robust Analysis

In this part, the H_∞ criteria for robust stability and the robust performance that can handle the uncertainties in control design are discussed. The unstructured uncertainties are considered as generic errors in all robust control designs.

Generally, the uncertainties of the controlled plant can be classified into two categories: internal dynamic perturbations and external disturbances. The internal dynamic perturbations represent the discrepancy between the mathematical model and the actual dynamic, including the parametric uncertainties, un-modeling dynamics, neglected nonlinearity, etc. In contrast, the external disturbances refer to environmental input and output disturbances, including unspecified currents or obstacle effects, sensor or actuator noise, etc. Hence, it is quite complex to built a model representing the reality. Traditional control schemes handle the uncertainties by assuming that the real uncertainties are instant disturbances added to the initial states of the nominal model. The nominal model is the single physical description trusted in the traditional control designs. Using the stability margin analysis based on the nominal model, the traditional controller considers a stable closed-loop system as the real plant. However, in reality the practical uncertainties are far different from assumptions, and the control stability can not be guaranteed. The response of the single model might not match the varying true plant. Therefore, a set of models is a minimum requirement to describe model dynamics in reality. Besides the stability issue, the performance reduction causing by the uncertainties are unmeasured in the traditional control designs. Note that, the robust performance analysis is inevitable in the real world control applications, and this is another important reason to introduce the robust control algorithms. In conclusion, it is essential to bring in the uncertainty descriptions and their relevant analysis method.

In general, the actual controlled-plant G can be described into different compo-

nents, where G_0 denotes the nominal model of the physical system, and ΔG the perturbations associated with the nominal model. In case of a LTI system of G, the uncertainties ΔG are characterized by: unstructured uncertainties (the uncertain block is represented by an unknown transfer matrix [76, 77]) and structured uncertainties (i.e., parametric uncertainties, whose behavior can be written in to a fix order model by a LFT form [77]). By considering the controlled plant G as a LTI system, we can derive the state space representation of the structured uncertainties, in equation 5.1, and unstructured uncertainties by equation 5.2.

$$\begin{bmatrix} \dot{x} \\ y \end{bmatrix} = \begin{bmatrix} A(\theta) & B(\theta) \\ C(\theta) & D(\theta) \end{bmatrix} \begin{bmatrix} x \\ u \end{bmatrix} \tag{5.1}$$

$$\begin{bmatrix} \dot{x} \\ y \end{bmatrix} = \begin{bmatrix} A + \Delta A & B + \Delta B \\ C + \Delta C & D + \Delta D \end{bmatrix} \begin{bmatrix} x \\ u \end{bmatrix} \tag{5.2}$$

In equation 5.1, $x \in \mathbb{R}^n$ denotes the states of the system, $u \in \mathbb{R}^m$ is the input vector, $y \in \mathbb{R}^p$ is the output vector, $\theta \in \mathbb{R}^s$ is the vector of the uncertain parameters, $A(\theta) \in \mathbb{R}^{n \times n}$, $B(\theta) \in \mathbb{R}^{n \times m}$, $C(\theta) \in \mathbb{R}^{p \times n}$, $D(\theta) \in \mathbb{R}^{p \times m}$ are the system matrices $(n, m, p, s \in \mathbb{R})$. Meanwhile, in equation 5.2, ΔA, ΔB, ΔC, ΔD are the unstructured perturbations in form of unknown matrices. The key issue is to make robust analysis (stability anlaysis) under small gain theorem [76] with different types of uncertainties.

In fact, there are various types of uncertainties, including: additive or multiplicative uncertainties, and inverse perturbations, etc. [76].

Generally, it is difficult or impossible to get an exact frequency response or a high accuracy *Laplace* transfer function approximation of uncertainty characteristics in $\Delta G(s)$. Therefore, a bounding method using a less complex weighting functions $W(s)$ that covers $\Delta G(s)$ (covers the group of the uncertainty characteristics) is introduced in equation 5.3 (SISO system for example).

$$\delta_{max}(\Delta G(j\omega)) \leqslant |W(j\omega)|, \quad \forall \omega \in \mathbb{R} \tag{5.3}$$

Here, $\delta_{max}(\cdot)$ is the maximum singular value of the uncertainties, ω stands for fre-

quency variable, $\Delta G(\cdot)$ represents perturbations, $W(\cdot)$ is the weightings. The exact perturbations $\Delta G(j\omega)$ is bounded inside the set of models described by the weighting functions $W(s)$ (upper boundary) using H_∞ norms inequality (or the peak singular value inequality). Note that, the guidelines for the selection of the weighting functions $W(s)$ are a key open challenge in the robust control design. The inefficient of the weighting functions describing the uncertainties might cause conservative controllers or invalidated control results for real world controlled plants. If the weighting functions are close to the exact true plant, the synthesized robust controller can be less conservative, more accurate and efficient.

There are several methods proposed to estimate the weighting functions for regular robust control design, such as the system identification method which implements the experimental frequency response tests, the empirical formula approximation method which recreates the model characteristics based on low-level physical principals, etc. According to *Zhou* [76]: "In many occasions, the weights are chosen purely as a design parameter without any physical basis, so these weights may be treated as tuning parameters chosen by the designer to achieve the best compromise between the conflicting objectives". Given a specific weighting function $W(s)$, the stability tests in face of various type of uncertainties is actually of central importance before all the robust control design process. Here, the small gain theorem [77, 76] is introduced as the foundation to achieve the stability tests.

Small Gain Theorem [77]: if there is an unknown bounded unstructured perturbation $\Delta(s)$, $||\Delta(s)||_\infty < 1$, i.e., $\Delta(s) \in H_\infty$, and a stable nominal controlled plant $G_0(s)$, the closed-loop feedback system is robust stable if and only if there is a controller $K(s)$ stabilizes the nominal model $G_0(s)$ and the condition $||\{G_0(s), K(s)\}||_\infty < 1$ holds (equation 5.4, 5.5). Here, the $\{G_0(s), K(s)\}$ is the closed-loop nominal system.

$$||\Delta K(I + G_0K)^{-1}||_\infty < 1 \tag{5.4}$$

$$||K(I + G_0K)^{-1}\Delta||_\infty < 1 \tag{5.5}$$

By another word, the robust controller internally stabilizes every plant belonging to

the set of models bounded by the weightings when the above H_∞ norm inequality stands. Depend on different types of uncertainties, some important closed-loop robust stable conditions are summarized in table 5.1.

Table 5.1: Robust stable conditions under different types of uncertainties, given by the small gain theorem

Uncertainty type	Uncertainty Boundary	Robust Stable Condition
Multiplicative uncertainty $(I+\Delta)G_0$	$\|\|\Delta(j\omega)\|\|_\infty < w_k(j\omega)$	$\|\|w_kT\|\|_\infty \leqslant 1$
Inverse multiplicative uncertainty $(I+\Delta)^{-1}G_0$	$\|\|\Delta(j\omega)\|\|_\infty < w_{mo}(j\omega)$	$\|\|w_{mo}TS\|\|_\infty \leqslant 1$
Additive uncertainty $(G_0+\Delta)$	$\|\|\Delta(j\omega)\|\|_\infty < w_a(j\omega)$	$\|\|w_aKS\|\|_\infty \leqslant 1$
Inverse additive uncertainty $G_0(I+\Delta G_0)^{-1}$	$\|\|\Delta(j\omega)\|\|_\infty < w_{mi}(j\omega)$	$\|\|w_{mi}SG_0\|\|_\infty \leqslant 1$

Here, w_k, w_a, w_{mi}, w_{mo} are the prior knowledge of weightings or replacement of original uncertainties about the upper bound as mentioned in equation 5.3. $T(s)$ stands for the sensitivity function, and $S(s)$ denotes the complementary sensitivity function:

$$T(s) = (I + G_0K)^{-1} \tag{5.6}$$

$$S(s) = G_0K(I + G_0K)^{-1} \tag{5.7}$$

Consider a system as described in figure 5-1, if a bounded $\Delta(j\omega)$ exists and has $||\Delta(j\omega)||_\infty < 1$, then, the robust stability is equivalent to the internally stability of the closed-loop system $(G_0(s), K(s))$, and the closed-loop transfer function $T_{rw}(s) = \zeta\{G_0(s), K(s)\}$ ($\zeta\{\cdot\}$ is a transfer function), from the perturbation input w (see figure 5-1) to the evaluation output z, satisfies $||T_{rw}||_\infty < 1$. In the contrary, if the closed-loop system $\{G_0(s), K(s)\}$ is internal stable and $||T_{rw}||_\infty < 1$ stands, then, for any stable $\Delta(s)$ connected to the system, that has $||\Delta(s)||_\infty < 1$ robust stability stands.

The second important issue of robust control design is the robust performance represented by H_∞ norms. According to [77]: "the H_∞ design and relevant approaches

first formulate the stability as well as performance design specifications as a robust stabilization problem and then solve the robust stabilization problem to find a controller". For a regular closed-loop robust control system in figure 5-1, whose inputs and outputs are energy bounded, it is generally required the following performance specifications:

- tracking performance, $min||(I + G_0K)^{-1}||_\infty$.
- disturbance attenuation, $min||(I + G_0K)^{-1}||_\infty$ (same as above).
- noise rejection, $min|| - (I + G_0K)^{-1}G_0K||_\infty$.
- energy consumption, $min||K(I + G_0K)^{-1}||_\infty$.

For the robust performance analysis, the weighting functions as well as its formulation of H_∞ problems are also of central importance to achieve desired objectives about the control performance. The weighting selections are actually the active engineering tuning to reject unwanted dynamics and perturbations. Let a SISO system as in equation 5.8:

$$y_1(s) = H(s)u_1(s) \tag{5.8}$$

where, $u_1(s) \in \mathbb{C}$ denotes the system input, $y_1(s) \in \mathbb{C}$ the system output, and $H(s)$ is a stable close loop transfer function of the SISO system. Then, the H_∞ norm of the transfer function from input to output are given in equation 5.9:

$$||H(s)||_\infty = sup_{||u_1||_2 \neq 0} \frac{||y_1||_2}{||u_1||_2} = sup_\omega |H(j\omega)| \tag{5.9}$$

Here, the norm $||H(s)||_\infty$ can be considered as an energy amplifier from the input to the output under certain frequency. Define a constant $\gamma > 0$ as the expected energy gain for the closed-loop system $H(s)$ that confined the effect of the input signal to the output behavior, then we have:

$$||H(s)||_\infty < \gamma \tag{5.10}$$

Let $d(s)$ be a disturbance, whose frequency response can be covered by a weighting function $W(s)$ (gain upper boundary):

$$|d(j\omega)| < |W(j\omega)|, \quad \forall\omega \in \mathbb{R} \tag{5.11}$$

Meanwhile, if the following H_∞ norm inequality stands:

$$||H(s)W(s)||_\infty < \gamma \tag{5.12}$$

then, the energy reflection of the disturbance $d(s)$ through the closed-loop system $H(s)$ to the output becomes less than γ, namely, the restrain of the disturbance $d(s)$ in the robust system $H(s)$ is capable to achieve the range of γ.

5.1.2 H_∞ Robust Design

The robust control design is to find a stable controller that simultaneously achieves the robust stability and certain robust performance in the face of uncertainties. As a result, the H_∞ optimization methods are proposed and validated as efficient tools in the last decades, to solve the robust control design problem for LTI system.

As mentioned in the robust stability theorem, a MIMO system as shown in figure 5-1, engineering selected weightings can generally guarantee a stable bounded form of $\Delta(j\omega)$ (i.e. $||\Delta(j\omega)||_\infty < 1$), then, the robust control design problem of G is equivalent to the H_∞ design problem on the weighted nominal model G_0 without concerning the perturbation block $\Delta(s)$. Therefore, the LFT representation of the robust system is given in equation 5.13:

$$\begin{bmatrix} z \\ y \end{bmatrix} = G(s) \begin{bmatrix} w \\ u \end{bmatrix} = \begin{bmatrix} G_{11}(s) & G_{12}(s) \\ G_{21}(s) & G_{22}(s) \end{bmatrix} \begin{bmatrix} w \\ u \end{bmatrix} \tag{5.13}$$

and the controller $K(s)$ is given in equation 5.14:

$$u = K(s)y \tag{5.14}$$

We summaries the definitions in figure 5-1 as follows:

- $\Delta(s)$ denotes the perturbation set, which is the mathematical approximation of the uncertainties and disturbances.

- $K(s)$ stands for the robust controller, which is yielded from the H_∞ optimization.

- $G(s)$ is the generalized model, which consists of the nominal model G_0 as well as the weighting functions that guarantees the stability and performance constrains.

- u is the control signal representing the control command that is given to the generalized plant $G(s)$.

- y is the output signal representing the dynamic data of $G(s)$ that is obtained by the feedback sensors.

- w represents the external uncertainty, including disturbance, noise, etc.

- z is the error signal which evaluates the closed-loop signal attenuation performance about the uncertaintys or disturbances.

As shown in equation 5.13, the generalized system $G(s)$ is generally described by the LFT form with several block matrices ($G_{11}(s)$, $G_{12}(s)$, $G_{21}(s)$, $G_{22}(s)$). The closed-loop transfer function $T_{rw}(s) = \zeta\{G_0(s), K(s)\}$ relates the external uncertainty w (input) to the error signal z:

$$T_{rw}(s) = G_{11}(s) + G_{12}(s)K(s)[I - G_{22}(s)K(s)]^{-1}G_{21}(s) \tag{5.15}$$

Moreover, the state space representation of the generalized model $G(s)$ and the robust controller $K(s)$ are respectively shown in equations 5.16 and 5.17:

$$
\begin{aligned}
G(s) &= \begin{bmatrix} G_{11}(s) & G_{12}(s) \\ G_{21}(s) & G_{22}(s) \end{bmatrix} = D_G + C_G(sI - A_G)^{-1}B_G \\
&= \begin{bmatrix} D_{11} & D_{12} \\ D_{21} & D_{22} \end{bmatrix} + \begin{bmatrix} C_1 \\ C_2 \end{bmatrix} (sI - A)^{-1} \begin{bmatrix} B_1 & B_2 \end{bmatrix}
\end{aligned} \tag{5.16}
$$

$$
K(s) = D_K + C_K(sI - A_K)^{-1}B_K \tag{5.17}
$$

where, the A_G, A_K, B_G, B_K, C_G, C_K, D_G and D_K are appropriately dimensioned real constant matrices.

Thereby, the state space realization of the closed-loop transfer function $T_{rw}(s)$ can be given by the following equations:

$$
\zeta(G, K) = D_{BF} + C_{BF}(sI - A_{BF})^{-1}B_{BF} \tag{5.18}
$$

$$
A_{BF} = \begin{bmatrix} A + B_2(I - D_K D_{22})^{-1} D_K C_2 & B_2(I - D_K D_{22})^{-1} C_K \\ B_K(I - D_{22} D_K)^{-1} C_2 & A_K + B_K(I - D_{22} D_K)^{-1} D_{22} C_K \end{bmatrix} \tag{5.19}
$$

$$
B_{BF} = \begin{bmatrix} B_1 + B_2(I - D_K D_{22})^{-1} D_K D_{21} \\ B_K(I - D_{22} D_K)^{-1} D_{21} \end{bmatrix} \tag{5.20}
$$

$$
C_{BF} = \begin{bmatrix} C_1 + D_{12}(I - D_K D_{22})^{-1} D_K C_2 & D_{12}(I - D_K D_{22})^{-1} C_K \end{bmatrix} \tag{5.21}
$$

$$
D_{BF} = \begin{bmatrix} D_{11} + D_{12}(I - D_K D_{22})^{-1} D_K D_{21} \end{bmatrix} \tag{5.22}
$$

According to the stability theorem [139], the closed-loop transfer function $T_{rw}(s)$ is internally stable if all the poles of the system matrix A_{BF} are on the left panel of

the s surface, i.e., all the eigenvalues satisfy $Re(\lambda_i(A_{BF})) < 0$. As a matter of fact, it is not suitable to use analytic formula to derive robust control solutions for MIMO systems. Therefore, the robust design goals are to optimize a stable control result, i.e., finding a stabilizing controller with the performance limited to a given positive number $\gamma > 0$ (the expected energy gain from the input signal w to the error signal z). By taking the tracking performance of the closed-loop robust system for example, the performance constrain can be presented by:

$$||T_{rw}||_\infty < \gamma \tag{5.23}$$

In fact, the synthesis objective for good tracking performance is to minimize the constrain value γ which results in better disturbance attenuation. The optimal goal can be achieved by guaranteeing the stability of the closed-loop transfer function T_{rw}. In this case, the above robust design problem becomes a H_∞ optimization problem. Given an initial value $\gamma > 0$, then, gradually decreases the γ and tests the stability condition until it reaches a minimum value, this is to say the optimal gain γ_{opt}. Theoretically, the robust performance is satisfied as a result of disturbance attenuation under the minimum transfer amplification.

The robust control design is actually a constrained optimization problem. The H_∞ robust synthesis solves the optimal controller by recursive calculations. According to [77], the solution to the optimization problem is not unique except in the scalar case. During the past decades, many algorithms are developed to solve the H_∞ optimization problems. In the following part, we would introduce two important methods for robust control systhesis: ARE and LMI [140], [141].

5.1.3 H_∞ Synthesis: ARE

"Lyapunov eqautions are most useful in system analysis while AREs are most useful in control system synthesis." said *Zhou* in [76]. For H_∞ synthesis, *Doyle* first proposed the two ARE synthesis method in 1980s [138].

Let the state-space description of the generalized system $G(s)$ in equation 5.24:

$$\begin{bmatrix} \dot{x} \\ z \\ y \end{bmatrix} = \begin{bmatrix} A & B_1 & B_2 \\ C_1 & D_{11} & D_{12} \\ C_2 & D_{21} & D_{22} \end{bmatrix} \begin{bmatrix} x \\ w \\ u \end{bmatrix} \tag{5.24}$$

where $x \in \mathbb{R}^n$ is the state vector, $u \in \mathbb{R}^{m_2}$ is the control input vector, $y \in \mathbb{R}^{p_2}$ is the measurement vector, $w \in \mathbb{R}^{m_1}$ stands for the disturbance input vector, $z \in \mathbb{R}^{p_1}$ denotes the error evaluation output vector, $D_{12} \in \mathbb{R}^{p_1 \times m_2}$, $D_{21} \in \mathbb{R}^{p_2 \times m_1}$, with $p_1 \geqslant m_2$, and $p_2 \leqslant m_1$. In practical applications, D_{22} is generally zero.

According to *Glover* and *Doyle* [77], the necessary and sufficient conditions for the existence of a H_∞ suboptimal solution are obtained under the following assumptions (solvability conditions).

- (A, B_2) is stabilisable and (C_2, A) is detectable.
- $\begin{bmatrix} A - j\omega I & B_2 \\ C_1 & D_{12} \end{bmatrix}$ has full column rank for all $\omega \in \mathbb{R}$.
- $\begin{bmatrix} A - j\omega I & B_2 \\ C_2 & D_{21} \end{bmatrix}$ has full row rank for all $\omega \in \mathbb{R}$.
- $D_{12} = \begin{bmatrix} 0 & I \end{bmatrix}$, $D_{21} = \begin{bmatrix} 0 \\ I \end{bmatrix}$

Consider the two following *Riccati* equations:

$$\begin{aligned} (A - BR^{-1}D_{1\cdot}^T C_1)^T X + X(A - BR^{-1}D_{1\cdot}^T C_1) - XBR^{-1}B^T X \\ + C_1^T (I - D_{1\cdot} R^{-1} D_{1\cdot}^T) C_1 = 0 \end{aligned} \tag{5.25}$$

$$\begin{aligned} (A - B_1 D_{\cdot 1}^T \widetilde{R}^{-1} C) Y + Y(A - B_1 D_{\cdot 1}^T \widetilde{R}^{-1} C)^T - YC^T \widetilde{R}^{-1} CY \\ + B_1 (I - D_{\cdot 1}^T \widetilde{R}^{-1} D_{\cdot 1}) B_1^T = 0 \end{aligned} \tag{5.26}$$

where,

$$R = D_{1\cdot}{}^T D_{1\cdot} - \begin{bmatrix} -\gamma^2 I & 0 \\ 0 & 0 \end{bmatrix}, D_{1\cdot} = [D_{11}, D_{12}] \tag{5.27}$$

$$\widetilde{R} = D_{\cdot 1} D_{\cdot 1}^T - \begin{bmatrix} -\gamma^2 I & 0 \\ 0 & 0 \end{bmatrix}, D_{\cdot 1} = \begin{bmatrix} D_{11} \\ D_{21} \end{bmatrix} \tag{5.28}$$

Partition $D_{11} = \begin{bmatrix} D_{1111} & D_{1112} \\ D_{1121} & D_{1122} \end{bmatrix}$, where D_{1122} has m_2 rows and p_2 columns.

Let us suppose that the generalized plant G satisfies the above four assumptions, then, there exists an internal stabilizing controller $K(s)$ such that

$$||T_{rw}(s) = \zeta\{G(s), K(s)\}||_\infty < \gamma$$

if and only if :

- $\gamma > max(\overline{\delta}[D_{1111}, D_{1112}], \overline{\delta}[D_{1111}{}^T, D_{1121}{}^T])$ ($\overline{\delta}(\cdot)$ is the singular value)
- the two *Riccati* equations 5.25 and 5.26 respectively have a stable solution X and Y.
- the *Riccati* equations 5.25 has a positive semidefinite solution $X \geqslant 0$ that guarantee a stable matrix $(A - BR^{-1}D_{1\cdot}^T C_1 - BR^{-1}B^T X)$.
- the *Riccati* equation 5.26 has a positive semidefinite solution $Y \geqslant 0$ that guarantee a stable matrix $(A - B_1 D_{\cdot 1}^T \widetilde{R}^{-1} C - Y C^T \widetilde{R}^{-1} C)$.e
- $\rho(XY) < \gamma^2$ ($\rho(\cdot)$ denotes the spectral radius)

The existence of the solutions to a H_∞ problem depends on the selected constant $\gamma > 0$. Limited to the structure and performance requirements, the control system can not achieve an arbitrary small γ, and for some small γ, the H_∞ problem might not be feasible.

Generally, the control performance is better if the γ value remains small. Therefore, the control design process is the γ bisection as well as its robust test until γ reaches the smallest feasible value. For the H_∞ problem of robust control synthesis, the ARE method executes the following steps (dichotomic procedure):

1. Initial: select a sufficient large γ_{max} that guarantees the H_∞ problem is admissible, meanwhile, chose a sufficient small γ_{min} that makes the H_∞ problem infeasible. Select a small enough $\Delta\gamma_s$ value to stop the optimization process.

2. Iterative: calculate the expected energy gain γ for the incoming robust test, i.e., the feasible conditions for AREs.

$$\gamma = \frac{\gamma_{min} + \gamma_{max}}{2} \tag{5.29}$$

3. Check: if the H_∞ problem with expected γ has solutions (i.e. AREs are feasible), then updates $\gamma_{max} = \gamma$, if not update $\gamma_{min} = \gamma$.

4. Stop: check if stop criteria $\gamma_{max} - \gamma_{min} < \Delta\gamma_s$ is satisfied, then stop the optimization process, if not turn to step 2 for further calculations.

Using the ARE robust control synthesis method, the H_∞ problem or the generalized plant $G(s)$ should first meet the four constrain assumptions. Meanwhile, the optimization calculation depends on the empirical selection of energy gains γ_{min} and γ_{max}. When the control plant is complex and the parameters are not well known, the AREs solution might consume a lot of time to be optimized, and feasible solutions are not guaranteed.

5.1.4 H_∞ Synthesis: LMI

In the past decades, LMI theory was validated as an efficient convex algorithm to solve H_∞ problems for LTI systems [142, 141]. Typical LMI method is flexible in choosing the performance specifications as it provides better solvability conditions, i.e., it requires less assumptions than the *Riccati* method. A richer body of controlled-plants can be treated using LMI method. LMI algorithms also allows to directly minimize γ in order to find the best upper bound [141]. In fact, the LMI approach turns the H_∞-norm constrains into linear matrix inequalities (LMI problems). Thereby, the H_∞ synthesis problems can be solved with matured mathematical LMI tools.

In the following, we would introduce the derivation of the H_∞ problems using LMI techniques.

The generalized plant $G(s)$ and its minimal state-space realization is presented in equation 5.30:

$$G(s) = D_{SG} + C_{SG}(sI - A_{SG})^{-1}B_{SG} \tag{5.30}$$

where, the A_SG, B_SG, C_SG and D_SG are appropriately dimensioned real constant matrices.

According to the LMI theory, if $\gamma > 0$ and matrix A_{SG} is stable and of minimal realization, there is $||G||_\infty < \gamma$ if and only if, there exists a positive definite matrix $X > 0$ satisfying:

$$\begin{bmatrix} A^TX + XA & XB & C^T \\ B^TX & -\gamma I & D^T \\ C & D & -\gamma I \end{bmatrix} < 0 \tag{5.31}$$

The H_∞ control problem is transformed into a standard LMI problem in equation 5.31. The above lemma is considered as the foundation of the LMI method, its proof can be found in [143].

To solve a robust controller $K(s)$ using the LMI theory, there is the following lemma: If the generalized system $G(s)$ satisfies the assumption ((A, B_2) is stabilisable and (C_2, A) detectable), there exists a stable controller $K(s)$ and its closed-loop system has $||T_{rw}||_\infty < \gamma$, if and only if, the following LMIs has a symmetric solution matrix $X > 0$ and $Y > 0$:

$$\begin{bmatrix} N_X^T & \\ & I_{n_w} \end{bmatrix} \begin{bmatrix} AX + XA^T & XC_1^T & B_1 \\ C_1X & -\gamma I & D_{11} \\ B_1^T & D_{11}^T & -\gamma I \end{bmatrix} \begin{bmatrix} N_X^T & \\ & I_{n_w} \end{bmatrix} < 0 \tag{5.32}$$

$$\begin{bmatrix} N_Y^T & \\ & I_{n_z} \end{bmatrix} \begin{bmatrix} YA + A^TY & YB_1^T & C_1^T \\ B_1^TY & -\gamma I & D_{11}^T \\ C_1 & D_{11} & -\gamma I \end{bmatrix} \begin{bmatrix} N_Y^T & \\ & I_{n_z} \end{bmatrix} < 0 \tag{5.33}$$

$$\begin{bmatrix} X & I \\ I & Y \end{bmatrix} \leqslant 0, \quad \begin{bmatrix} X & I \\ I & Y \end{bmatrix} \geqslant n + n_k \tag{5.34}$$

In equations 5.32∼5.34, n and n_k respectively, represent the dimension of the generalized system and the robust controller. Matrix definitions are given as : $N_X = [C_1, D_{21}]$, $N_Y = [B_2^T, D_{12}^T]$.

Note that, in the LMI method the solvability condition, (A, B_2) is stabilisable and (C_2, A) detectable, is the only requirement. The performance specifications can be chosen with more flexibility, and the dimension of the control input, disturbance input, evaluation and control outputs can be arbitrary.

The technical steps to solve a H_∞ controller using LMI methods are given as follows:

1. Solve the LMIs of equation 5.32 and 5.33, to get the symmetric solutions $X > 0$ and $Y > 0$.

2. Find the matrix F such as $FF^T = Y - X^{-1}$

3. Let

$$P = \begin{bmatrix} Y & F \\ F^T & I \end{bmatrix} \tag{5.35}$$

and then move P into equation 5.36 and 5.37 ($*$ denotes the matrix of any values that fits the size),

$$\begin{bmatrix} Q & E^T \\ F & * \end{bmatrix} = \begin{bmatrix} \overline{A}^T P + P\overline{A} & P\overline{B}_1 & \overline{C}_1^T & P\overline{B}_2 \\ \overline{B}_1^T P & -\gamma I & \overline{D}_{11}^T & 0 \\ \overline{C}_1 & \overline{D}_{11} & -\gamma I & \overline{D}_{12} \\ \overline{C}_2 & \overline{D}_{21} & 0 & * \end{bmatrix} \tag{5.36}$$

$$Q + E^T \Theta F + F^T \Theta E < 0 \tag{5.37}$$

4. A parametric matrix Θ can be found, and its state space realization consists of the elements of the robust controller $K(s)$.

$$\Theta = \begin{bmatrix} D_K & C_K \\ B_K & A_K \end{bmatrix} \tag{5.38}$$

In practice, the robust control toolbox in Matlab software provides two H_∞ controller synthesis algorithms: *Riccati* method and LMI method, and its relevent applications can be found in [77].

5.2 Control of the *CISCREA* AUV

Without lose of generality, H_∞ control approach is prensented and adapted to the *CISCREA* AUV for a heading control. A major problem is that the yaw model is nonlinear with serious uncertainties. In reality, the AUVs nonlinearity and uncertainty issues are mainly caused by: nonlinear damping effects, changing parameters, unmodelled dynamics, external disturbances, sensor noise, etc. Therefore, we propose a framework to change the nonlinear yaw model to a linear system with uncertainties based on previous CFD modeling work. By then, we can solve a H_∞ controller for the linear system. At the end, the simulation results of the H_∞ control and the classical PID control schemes are compared.

5.2.1 Yaw model and its linearization

In order to validate the proposed H_∞ robust control approach, and reduce the complexity to implement the controller, we abstract the yaw model from the full dimensional *CISCREA* AUV dynamics. In fact, previous dynamic and hydrodynamic modeling work is control-oriented, and it brings a lot of convenient benefits. For example, it is possible to build model based Kalman filters for unobservable states that faces considerable noise [144]. Otherwise, the dynamic and hydrodynamic information can be used to design the Smith compensators in order to handle the signal

delay and its response oscillation consequence [145].

Most importantly, in this part, we propose a method to deal with system nonlinearities for robust control scheme. We discuss the AUV nonlinear dynamic problem without concern of parametric uncertainties, such as inertia, added mass and damping coefficient errors. As found in Chapter 3 and 4, damping is a major nonlinear component in an underwater vehicle hydrodynamic model. Therefore, we propose to compensate nonlinear behaviors by creating a linear behavior. The compensation error is assigned to be an extra uncertainty beside parametric uncertainties.

The reason to introduce such a linearization method is that most of the control theories assume the controlled-plant as a linear time invariant system [144]. The major H_∞ control methods are developed on linear theories. Only in some specific linearizable assumptions, a few nonlinear systems can be treated using linear methods [144]. Generally, the control performance are dramatically reduced to directly fit a linear H_∞ controller on the nonlinear AUV dynamics, such as *CISCREA* AUV. The linearization of the yaw model is critical and essential for the robust control design of underwater vehicles. Generally, there are several essential linearization methods to implement linear control algorithms on the nonlinear control applications:

- Equilibrium approximation: First, formulate the nonlinear dynamic model of the nonlinear system according to the physical knowledge or input-output data analysis. Thereby, the engineers determine the steady-state operating point or a group of operating points about which to linearize. Derivations are made about the operating points to obtain an approximate linear model. The equilibrium approximation has one disadvantage. The states of the closed-loop system should be near the operating pionts, otherwise, the controller can be invalid.

- Perturbation method: Using H_∞ control scheme, the nonlinear damping effect can be directly defined as a parametric uncertainty adding to the linear behaviors. Describe the whole nonlinearity into the uncertainty set Δ, the H_∞ synthesis can yield a stable control system with some compromise to the performance conservation.

- Nonlinear compensation method: The nonlinear damping behaviors are estimated using numerical physics on CFD software. The CFD modeling estimation results are used to create an artificial linear AUV dynamic behavior as the robust control nominal model. The CFD model guides the AUV actuators to execute the compensations about damping forces and torques on real world AUV dynamics. Obviously, comparing to the perturbation method the damping compensations errors are generally small. Small linearization errors leads to small uncertainty set Δ. Therefore, H_∞ synthesis are finally implemented based on small Δ to obtain a stable robust controller with less compromise on performance conservation.

In chapter 4, we abstract the nonlinear yaw model from the 4 DOFs *CISCREA* AUV dynamics for further H_∞ research. For the convenience of model linearization, we present the yaw model again in equation 5.39 (neglecting buoyancy and gravity). Relevent linearization variable definitions are given in table 5.2. The three mentioned linearization methods will be compared in the following.

$$(I_{YRB} + I_{YA})\ddot{x}_r + D_{YN}|\dot{x}_r|\dot{x}_r + D_{YL}\dot{x}_r = \tau_i \tag{5.39}$$

Table 5.2: Rotational model notions of yaw direction

Parameter	Description	Value
I_{YRB}	Rigid-body inertia	$0.3578kg \cdot m^2$
I_{YA}	Added mass inertia	$0.138kg \cdot m^2$
D_{YN}	Nominal quadratic damping factors	Ideal 0.2496
D_{YL}	Nominal linear damping factors	Ideal 0.021
$\dot{x}_r$	Angular velocity	0 to 4rad/s
τ_i	Torque input	0 to $6N \cdot m$
τ_com	Compensation torque	0 to $6N \cdot m$
$\dot{x}_{r0}$	Steady-state operating point (Equilibrium velocity)	0 to 4rad/s
D_{YND}	CFD quadratic damping factors	0.1479
D_{YLD}	CFD linear damping factors	0.0013
D_{YLA}	Artificial linear factors	<thrust limit (select 1.2)

For traditional AUV applications, the equilibrium approximation method is usu-

ally the first option for model linearization. Assume the steady-state angular velocity of the AUV is $\dot{x}_{r0}$, thereby, the linearization about equilibrium point results in equation 5.40.

$$(I_{YRB} + I_{YA})\ddot{x}_r + (D_{YL} + 2D_{YN}|\dot{x}_{r0}|)\dot{x}_r - D_{YN}|\dot{x}_{r0}|\dot{x}_r = \tau_i \tag{5.40}$$

Generally, the equilibrium state of a regular system is either zero or a constant value. Unfortunately, the equilibrium state of the AUV (angular velocity) is not steady and varies in a wide range from 0 rad/s to 4 rad/s. A real dynamic system does not stay around the equilibrium point as supposed. As a result, the control performance is significantly disturbed.

The second perturbation method is more straight forward, as shown in equation 5.41:

$$(I_{YRB} + I_{YA})\ddot{x}_r + (D_{YN}|\dot{x}_r| + D_{YL})\dot{x}_r = \tau_i \tag{5.41}$$

Nonlinear damping coefficient $D_{YN}|\dot{x}_r|$ is supposed to be an uncertainty adding to the linear coefficient D_{YL}. As found in previous modeling work, the nonlinear quadratic damping component dominates the damping effect, and the linear damping is comparably negligible. In this case, there is a large error about the damping model using the linear nominal that derived with only the linear damping coefficient D_{YL}. The synthesized H_∞ controller can be seriously conservative by assuming nonlinear damping is an uncertainty.

To the last, the proposed linearization approach uses nonlinear CFD yaw model as feedback to real world propellers, see Figure 5-2. The main idea is to compensate the original nonlinear behavior, and creates a rough artificial linear damping behavior as robust control nominal.

According to the suggested nonlinear compensation methods of linearization, the compensation propulsion is derived in equation 5.42.

$$\tau_{com} = (D_{YLA} - D_{YLD} - D_{YND}|\dot{x}_r|)\dot{x}_r \tag{5.42}$$

The compensation parameters above are all figured by the damping study of the *CIS-CREA* AUV, such as ANSYS-CFX, STAR-CCM+ and experimental results. D_{YLA} is the artificial linear factor after the nonlinear damping compensation. D_{YLD} and D_{YND} are respectively the CFD estimations of linear and nonlinear damping coefficients that calculated by ANSYS-CFX or STAR-CCM+ . Note that, the linear factor D_{YLA} can be chosen by the engineers with principles to minimize the total compensation propulsions (errors of compensation). Meanwhile, the D_{YLA} selection is limited to the thruster capability. The objective of the nonlinear compensation is to avoid the control propulsion waste and remains small performance conservation. After the nonlinear compensation, the AUV nominal linear model for robust design is given in equation 5.43:

$$(I_{YRB} + I_{YA})\ddot{x}_r + (D_{YLA} + (D_{YN}|\dot{x}_{r0}| - D_{YND}|\dot{x}_r| + D_{YL} - D_{YLD}))\dot{x}_r = \tau_i \quad (5.43)$$

The term δ in equation 5.44, represents the error between numerical AUV model and the AUV dynamic in reality. Generally, this error δ is considered as an uncertainty

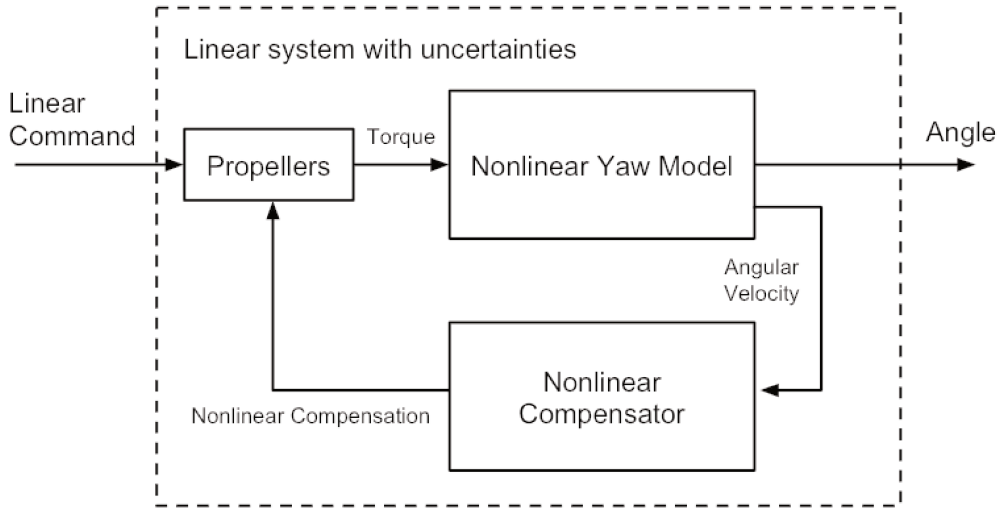

Figure 5-2: Nonlinear damping compensation

added on the artificial linear factor D_{YLA}, and it remains small.

$$\delta = D_{YN}|\dot{x}_{r0}| - D_{YND}|\dot{x}_r| + D_{YL} - D_{YLD} \tag{5.44}$$

To validate the nonlinear compensation method, we can consider the yaw model in chapter 4 is an ideal model that has no errors comparing to the reality. Calculate δ using the following parameters,

$$\begin{aligned} &\dot{x}_r \in [-4, 4] rad/s; \quad D_{YLA} = 1.8; \quad D_{YN} = 0.2496; \\ &D_{YL} = 0.021; \quad D_{YND} = 0.1479; \quad D_{YLD} = 0.0013; \end{aligned} \tag{5.45}$$

then, we can result in that D_{YLA} only has the dynamic uncertainty of 23.7%. In additional, we can derive the linear nominal model for robust control design in equation 5.46:

$$(I_{YRB} + I_{YA})\ddot{x}_r + (D_{YLA} + \delta)\dot{x}_r = \tau_i; \quad \delta \in [-0.4265, 0.4265] \tag{5.46}$$

Table 5.3: Linear Damping Uncertainty Margin

Methods	Nominal Linear Factor	Uncertainty Margin
Compensation	D_{YLA}:1.8 (for instance)	D_{YLA} : $[1.3735, 2.2265], 23.7\%$

In previous hydrodynamic study, we concluded that only in the yaw direction numerical damping results has the worst error comparing to the experimental one, see figure 4-15. The surge, sway and heave directions have better numerical results, which means the yaw model is the most difficult one for robust control deign. Considering the nominal models derived by nonlinear compensation, the worst case of the parametrical uncertainty that adding to the linear factor D_{YLA} is only 23.7%. The proposed model, equation 5.46, is therefore a linear system with uncertainties. However, in the following H_∞ robust control design the parametric uncertainty boundary is generally

selected higher than $40\% > 23.7\%$, i.e., the linearized model with uncertainties is well bounded and is feasible for further H_∞ robust control design.

5.2.2 H_∞ control design

The H_∞ control theory achieves the advantage of robustness and MIMO control characteristics by combining frequency domain techniques and the state space feedback theory. Both the robust stability and robust performance can be simultaneously achieved after founding such a fix controller using optimizing algorithms. For the MIMO AUV control problem, robust control theory can result in accurate control performance in face of many bounded uncertainties. Therefore, for the AUVs control problem, the H_∞ controller is proposed to solve the following issues:

- Dynamic and hydrodynamic parametric uncertainties.
- Nonlinear damping compensation errors.
- External disturbance from the ocean environment and sensor noise.

Based on the linearized yaw model that derived from the nonlinear damping compensation, a H_∞ control scheme is proposed for the heading control of the *CISCREA* AUV, see figure 5-3. The thruster compensates the nonlinear damping behavior by calculating its propulsion value using equation 5.42 and the AUV angular velocity $\dot{x}_r$. From the controller perspective, the compensated AUV controlled-plant is a first order linear system with minor uncertainties. As a result of the improved linear AUV dynamic behavior, the robust issues can be conveniently solved by essential H_∞ controllers. Although, for few AUVs, the angular velocity $\dot{x}_r$ is not measured or indirectly sensed, the proposed modeling based robust control scheme could easily solve the detection issue by building Kalman filters. This technique of estimating unmeasured states would be introduced in the next chapter for real world AUV robust control in the sea.

Generally, the nominal model is derived from the LFT technique, which separates uncertainties into an individual block [76]. Denotes the *CISCREA* AUV yaw model,

equation 5.46, into the LFT form, and represents the uncertainties into the set Δ (inertia variations and damping compensation errors, etc.). Then, the generalized controlled-plant is given by equation 5.24, where,

$x \in \mathbb{R}^n$ is the states vector, representing the yaw angular velocity $\dot{x}_r$ and yaw angle x_r of the *CISCREA* AUV;

$u \in \mathbb{R}^{m2}$ denotes the control input, indicating the thruster torque τ_i that acts on the yaw motion of the *CISCREA* AUV;

$y \in \mathbb{R}^{p2}$ represents the system output, which is in fact the yaw angle x_r that measured by the electronic magnetic compass of the *CISCREA* AUV;

$w \in \mathbb{R}^{m1}$ is the external input vector;

$z \in \mathbb{R}^{p1}$ is the error evaluation vector, and $D_{12} \in R^{p1 \times m2}$, $D_{21} \in R^{p2 \times m1}$.

Finding appropriate weighting functions is critical and difficult. According to the H_∞ theory, the robust design process is to find a feedback controller K, such that the closed-loop system remains stable and achieves certain performance criteria in the presence of uncertainties [76, 77]. Generally, cost functions (weighting functions) for

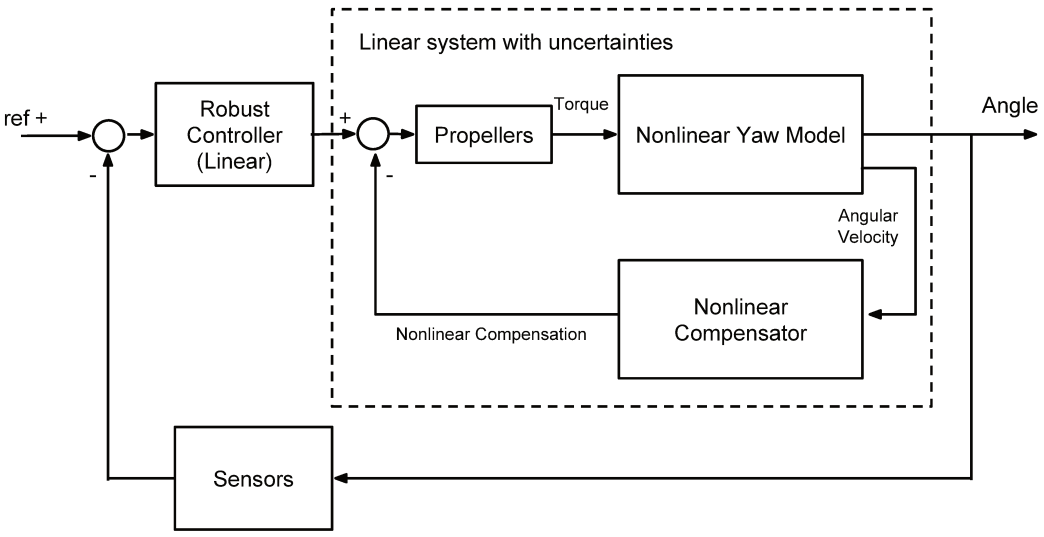

Figure 5-3: Robust controller & Nominal model of damping compensation

finding such a K are represented by H_∞ norms of the closed-loop transfer functions from w to z, see equation 5.47.

$$\min_{K\,stable} \left\| \begin{matrix} W_p(I+G_0K)^{-1} \\ W_e(I+G_0K)^{-1} \\ W_uK(I+G_0K)^{-1} \end{matrix} \right\|_\infty < \gamma \tag{5.47}$$

Here, K is the robust controller in figure 5-3, G_0 is the above obtained linear nominal yaw model from LFT interpretation, W_e, W_u, and W_p are the weighting functions. In addition, $S(s)$, and $T_k(s)$ and $T(s)$ stand for different types of sensitivity functions:

$$S(s) = G_0K(I+G_0K)^{-1} \tag{5.48}$$

$$T_k(s) = K(I+G_0K)^{-1} \tag{5.49}$$

$$T(s) = (I+G_0K)^{-1} \tag{5.50}$$

In general, weighting functions as well as relevant sensitivity functions would be used in the minimization to meet the design specifications.

In H_∞ control design, the weighting functions are introduced for setting control specifications. Generally, it is difficult to get the accurate frequency characteristics of external input signal. In addition, the real signal characteristics generally have complex transfer function representations for the control design. Therefore, the weighting functions, which have simple transfer representations, are proposed as upper bound constrains that cover original signals, see figure 5-4. All the weighting functions W_e, W_u, and W_p are connected to the generalized control plant G_0. The weighting function W_p represents the frequency characteristics of the external disturbance. Usually, it is used to describe output disturbance rejection ability. Without W_p, the generalized system (only has W_e and W_u) is actually a classical H_∞ synthesis problem. Satisfying the above norm inequality (equation 5.47), indicates that the closed-loop system indeed reduces the disturbance effects to a prescribed level.

As we mentioned, finding appropriate weighting functions is critical and difficult, trials are necessary for a successful robust control design. Generally, it is important to take care of the controller performances such as response speed, disturbance attenuation, overshooting, etc. For the yaw control application of the *CISCREA* AUV, we choose a structure with three weighting functions to describe our performance goals, see figure 5-4. W_e, W_u, and W_p are interpreted as following:

- W_p can restrict the disturbance in output signal w, and it can be regarded as a generator characterizing all relevant disturbances [77]. The closed-loop is filtered, and only effective information is allowed to pass through. W_p can have the same specification as W_e, but with different objectives.

- W_e is chosen as a reference tracking error specification, in order to reduce the tracking errors between system output and desired reference. W_e and W_p work on the same closed-loop transfer function.

- W_u represents the input disturbance rejection capability. It restrains the signal effect from control input signal u to the output w.

During the H_∞ synthesis, weighting functions are generally stable and of minimum phase. In our case of AUV control, W_e, W_u, and W_p are given in the forms of second

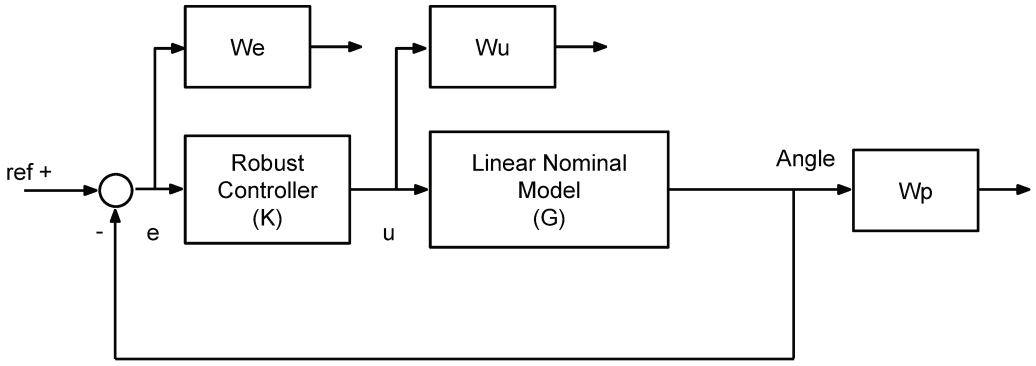

Figure 5-4: H_∞ control design with weighting functions connected

order transfer functions [77]:

$$W_p(s) = Gp\frac{s^2 + p_{n1}s + p_{n2}}{s^2 + p_{d1}s + p_{d2}} \tag{5.51}$$

$$W_e(s) = Ge\frac{s + e_{n1}}{s + e_{d1}} \tag{5.52}$$

$$W_u(s) = Gu \tag{5.53}$$

where, Gp, Ge, Gu, p_{n1}, p_{n2}, p_{d1}, p_{d2}, e_{n1} and e_{d1} are the constant parameters to be configured.

The above H_∞ control design can be concluded as three parts.

1. The energy gain of the concerned closed-loop is restrained in a specific H_∞ norm inequality, which are generally the performance goal interpretation.

2. Finding a controller K such that the H_∞ norm inequality is satisfied after defining relevant weighting functions (or to say the description set of signal characteristics).

3. To solve the H_∞ problem, one can use the *Riccati* method or Linear Matrix Inequality (LMI) approach [76, 77] to implement the mathematical optimization calculation. It was mentioned before, we prefer to choose LMI approach, since it requires less initial conditions [77].

5.2.3 PID control design

In order to validate the H_∞ AUV controller, we compare the H_∞ controller with the widely used PID control method. In this part, some essentials of PID control algorithms are introduced.

The PID control method can be given by the following equations:

$$u(t) = K_p e(t) + K_i \int_0^t e(t)dt + K_d \dot{e}(t) \tag{5.54}$$

$$e(t) = r(t) - y(t) \tag{5.55}$$

where, $e(t)$ is the error signal between the system output $y(t)$ and the reference input $r(t)$, $u(t)$ stands for the control input, K_p, K_i, and K_d denote the coefficients for the proportional, integral, and derivative terms. The PID controller can achieve the desired set-point by minimizing the error $e(t)$. Generally, the PID controller calculates the control adjustment based on the existing error $e(t)$ and PID coefficients K_p, K_i, and K_d. As the PID controller only depends on the system output measurement, and no model is required, therefore, it is broadly applicable. However, tuning the three PID coefficients are critical, but empirically relies on the system response (overshoots, steady-state error, or response oscillation). The tuning of the PID controller can not guarantee an optimal control or even stability. During the PID tuning process, there are the following physical characteristics:

- K_p represents the error adjustment ability, it determines the response speed and the control stability.

- K_i reduces the steady-state error, it accumulates the past errors over time, and bring in sufficient control to reduces any small error.

- K_d prevents the overshoot and oscillations of the control output, it predicts the future error and reduces redundant control.

Currently, PID control is still widely used in most of AUV control applications. Meanwhile, there are new trends of advanced PID control methods to optimize the PID tuning process [146]. In the following simulations, we introduce the PID control design for the *CISCREA* AUV.

5.3 *CISCREA* AUV Yaw Control Simulations

In this part, the yaw control simulations as well as the design details of the H_∞ and PID controller are presented.

5.3.1 H_∞ Yaw Controller

For the convenience, the compensated linear yaw model of the *CISCREA* AUV is given again in equation 5.56:

$$(I_{YRB} + I_{YA} + \delta_1)\ddot{x}_r + (D_{YLA} + \delta_2)\dot{x}_r = \tau_i \tag{5.56}$$

where, δ_1 and δ_2 respectively represent the uncertainties adding to the inertia $I_{YRB} + I_{YA}$ and compensated damping coefficient D_{YLA}.

As mentioned in the modeling work, the major uncertainties of the *CISCREA* AUV dynamics mainly consists of three parts:

- I_{YRB}: The inertia of the AUV rigid body, estimated by PRO/E software.
- I_{YA}: The added mass inertia of the AUV, calculated by the fluid dynamic program WAMIT.
- D_{YLA}: The artificial linear damping coefficient is compensated using the numerical damping coefficients (D_{YN}, D_{YL}) of ANSYS-CFX and StarCCM+ calculations.

In the H_∞ yaw control simulation, the inertia $I_{YRB} + I_{YA}$ are considered to be two varying parameters, which have a total 30% of variations. In the contrary, linear damping coefficient D_{YLA} is bounded by the variation limit of 40%. As we know from the H_∞ control design analysis, the D_{YLA} uncertainty boundary $40\% > 23.7\%$ is sufficiently large to guarantee the control performance goals. In fact, in face of the parametric uncertainties, we consider that AUV dynamics belonging to an uncertain systems family on the bode plots, see figure 5-5.

During the *CISCREA* AUV H_∞ synthesis, weighting function are tuned by many trials, and its results are given in the following equations:

$$W_p(s) = 0.95\frac{s^2 + 1.8s + 10}{s^2 + 8s + 0.01} \tag{5.57}$$

$$W_e(s) = 0.5\frac{s + 0.92}{s + 0.0046} \tag{5.58}$$

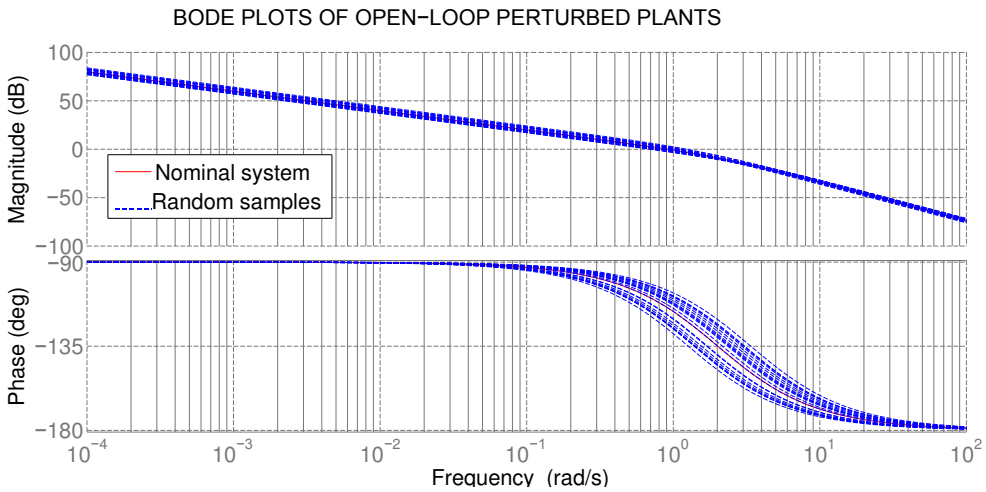

Figure 5-5: Bode Plot of Open-loop Perturbed Plants

$$W_u(s) = 0.01 \tag{5.59}$$

$W_u(s)$ is selected to be a very small scalar ($Gu = 0.01$) for simply disturbance rejection. $W_e(s)$ and $W_p(s)$ are chosen carefully considering that: the tracking error should be less than $< 1\%$; fast control response time (around $2 \sim 3$ seconds); the robust margins, etc. The principal of weighting function selections are given in [77, 76].

For the *CISCREA* AUV yaw controller, we execute the H_∞ synthesis using the LMI method. Figure 5-6, shows that the found feedback controller K (five states, one input and one output) satisfies the H_∞ norm inequality with $\gamma = 1.075$. Closed-loop sensitivity functions ($S(s)$, $T(s)$) are well covered by the inverse of chosen weightings $1/W_p(s)$, $1/W_e(s)$, $1/W_u(s)$. The output log files are of the H_∞ synthesis process are given in the Appendix D.1.

The H_∞ yaw robust controller is finally implemented on the embedded system of the *CISCREA* AUV, and it runs with the frequency of 10Hz. Therefore, the discrete state space realization of the H_∞ *CISCREA* yaw controller $K(z)$ is given in equation 5.60 $\sim$ 5.64. The continuous state space realization of the H_∞ *CISCREA* yaw controller $K(z)$ is given in the Appendix D.2.

$$K(z) = D_{ZK} + C_{ZK}(zI - A_{ZK})^{-1}B_{ZK} \tag{5.60}$$

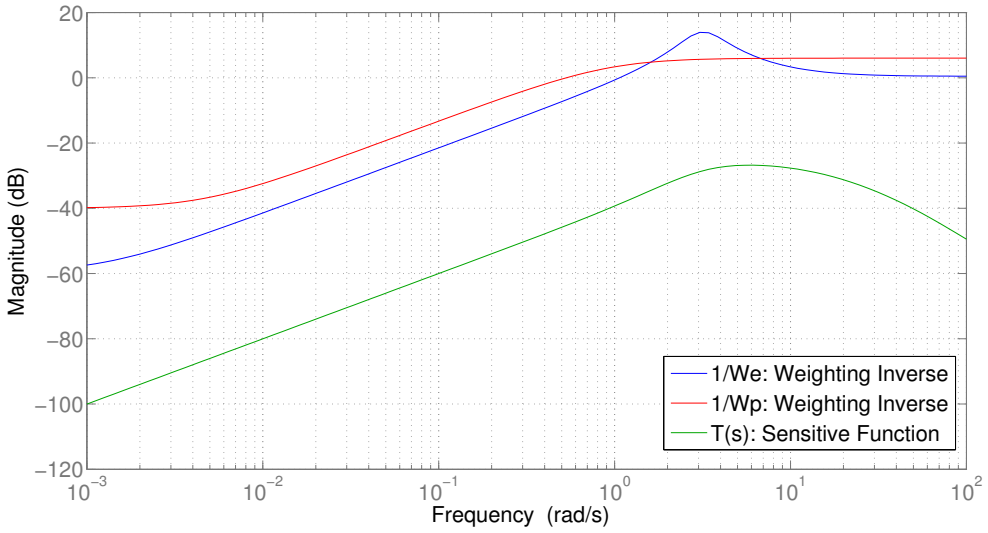

Figure 5-6: Complementary sensitivity function T(s) is well covered by the inverse of weighting functions $1/W_p(s)$, $1/W_e(s)$

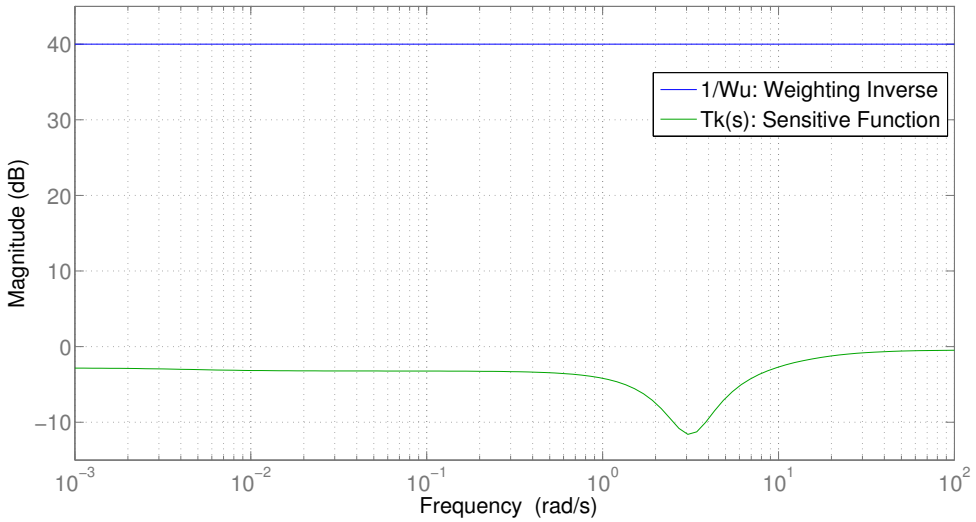

Figure 5-7: Sensitivity function $T_k(s)$ is well covered by the inverse of weighting functions $1/W_u(s)$

$$A_{ZK} = \begin{bmatrix} 0.1973 & 1.5954 & 4.498 & -3.7178 & -0.3001 \\ -0.0062 & 0.7597 & -0.6852 & -0.5474 & -0.0451 \\ 0.0146 & -0.1709 & 0.5505 & 0.0406 & -0.0156 \\ -0.0015 & -0.0363 & -0.0211 & 0.3053 & 0.0297 \\ 0.0003 & 0.0003 & 0.0002 & 0.0277 & 0.9984 \end{bmatrix} \tag{5.61}$$

$$B_{ZK} = \begin{bmatrix} 0.2731 \\ -0.0179 \\ 0.2065 \\ 0.1106 \\ 0.0005 \end{bmatrix} \tag{5.62}$$

$$C_{ZK} = \begin{bmatrix} -16.0063 & 58.3996 & 178.6582 & -258.9466 & 16.8046 \end{bmatrix} \tag{5.63}$$

$$D_{ZK} = 0 \tag{5.64}$$

5.3.2 PID Yaw Controller

Based on the designed control performance Matlab provides an interface to automatically tune the PID parameters. Hence, we obtained an original PID controller . The automatic PID results with the considerations of the overshoot, response speed, and etc. Finally, the PID three parameters for *CISCREA* AUV yaw control are obatined:

$$K_p = 16, \quad K_i = 0.1, \quad K_d = 10 \tag{5.65}$$

5.4 Simulation Results

In order to validate the H_∞ AUV control approach, we proposed a yaw control simulation of step response on the *CISCREA* AUV. The *CISCREA* AUV is ordered to rotate from 1.8 *rad* to 4.8 *rad*. In order to compare different scenarios, the many simulations are implemented including: control of nominal yaw model, the yaw model with parametric variation, and the yaw model with disturbance.

In figure 5-8, step responses of three scenarios are represented: PID control, damping compensated H_∞ approach and H_∞ control. From the simulation comparison, we can conclude that the compensated H_∞ controller handles the nonlinearity with the fastest response. Compensated H_∞ controller has no overshot or oscillations during

the rotation process. The tracking error achieves the specification less than 1%. The response speed is inside the performance design goal of $2s$. The compensated H_∞ control output has no overshoot. In the contrary, PID controller is less efficient, it has obvious overshoot and slow step response speed. The proposed compensated H_∞ AUV control approach can be several times faster than the transitional PID controller. In addition, the energy waste on inefficient thrust using the PID controller are seldom seen on the compensated H_∞ controller. Note that, the H_∞ control has no damping compensation, and it connects directly on the nonlinear yaw model. The results show that the H_∞ control is also less efficient to handle the AUV hydrodynamic nonlinearity, clear oscillations can be found in the control output.

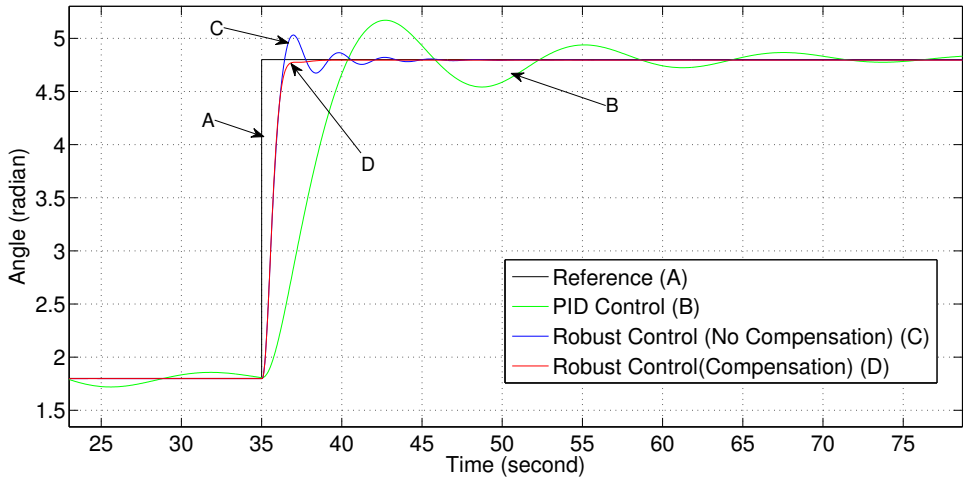

Figure 5-8: Step Response of three scenarios: PID control, damping compensated H_∞ approach and H_∞ control

During the design process, 30% of inertia variations are chosen as the uncertain boundary for $I_{YRB} + I_{YA}$. Therefore, in figures 5-8 and 5-9, we respectively demonstrate the robust performance of our controller handling the nominal yaw model and the yaw model with 30% inertia variations. The control output, i.e., the AUV thruster torque of three different types of controllers are given in the subplot of figures 5-8 and 5-9. As it is shown clearly, in face of the inertia variations (to the worst case), the proposed H_∞ AUV control approach achieved all the designed performances. The response speed is inside $2s$, tracking error less than 1%, and there is no obvious os-

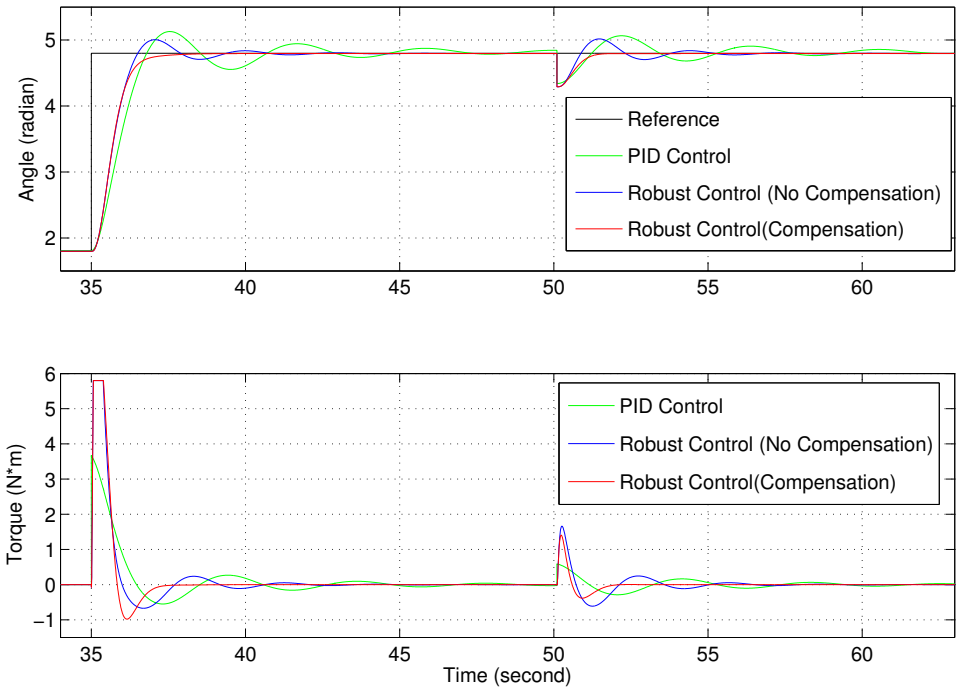

Figure 5-9: Step Response and Propeller Output on Nominal Yaw Model

cillations during the motion. In the contrary, the PID controller and the H_∞ control are all sensitive to the parametric changes such as the inertia variations. Performance decrease can be clearly seen from the comparison with the nominal model scenarios. The response speed becomes slow, and control response oscillation is more serious for both the PID controller and the H_∞ control algorithm. In conclusion, the proposed H_∞ AUV control approach is insensitive to the inertia variations within 30%. This result indicates, the compensated H_∞ AUV control approach is robust to the WAMIT and MCC estimation errors.

To emphasize the speed and robustness of our approach, we inject a small disturbance of 0.5 rad on the output at 50s. Both figure 5-7 and figure 5-8 demonstrate our compensated H_∞ AUV controller is capable to handle the disturbance efficiently. In the simulation, the compensated H_∞ AUV controller is stable, fast in response, and robust to the uncertainties and disturbances.

Note that, the compensated H_∞ AUV control simulations consider the following

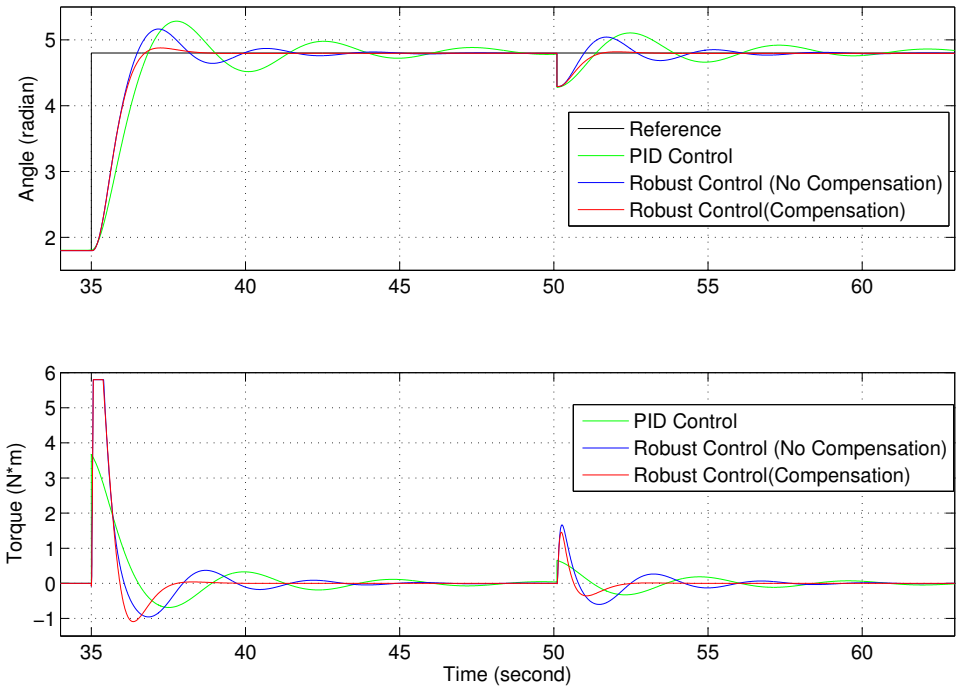

Figure 5-10: Step Response and Propeller Output with 30% of inertia variation

assumptions: there is no delay in the sensor measurements, and the yaw angular velocity $\dot{x}_r$ is accurately measured for linear compensation. However, in real AUV control applications, such as the *CISCREA* AUV, the vehicle might not be equipped with sensors to detect the yaw angular velocity $\dot{x}_r$. Meanwhile, the electronic magnetic compass output has an obvious 0.5s delay in measuring yaw angles. In the next chapter, we will propose to use CFD model based Kalman filters, numerically estimating unmeasured as well as noisy states. In addition, model based compensation algorithms are recommended to deal with the sensor delay.

5.5 Conclusion

In this chapter, the nonlinear compensated H_∞ control approach as well as its heading control simulations are introduced for the *CISCREA* AUV and others. Nonlinear damping and parametric uncertainties are the two critical problems that are solved

in the proposed approach. We propose the framework in figure 5-3 to change the nonlinear yaw model to a linear system with uncertainties based on previous CFD modeling work. By then, we can solve a H_∞ controller for the linear system.

In details, the proposed linearization approach uses nonlinear CFD yaw model as feedback to real world propellers. The AUV propellers compensate the original nonlinear damping behavior, and create a rough artificial linear damping behavior as robust control nominal. From the controller perspective, the compensated AUV controlled-plant is a first order linear system with minor uncertainties. Linear H_∞ control theory are introduced to solve the minor uncertainty control problems, including parametric variations, damping compensation errors, modeling errors, external disturbance, etc. Comparing the step response simulation results, the proposed nonlinear compensated H_∞ control approach can achieve fast response speed ($2s < 15s$), better tracking errors ($< 1\%$), and no overshoot transition. Both the PID and H_∞ control approach fails to maintain good performance in handling the nonlinearity and uncertainty problems. The following conclusions can be observed based on our simulations:

- The proposed nonlinear compensated H_∞ control approach is robust stable.
- The proposed nonlinear compensated H_∞ control approach has the fastest response speed, and it is several times faster than the PID control method.
- The control commands of the proposed H_∞ approach is optimal, seldom energy waste can be found in the propulsions. Compared to PID controllers, this is critical to save battery and thruster life.
- The proposed H_∞ approach can achieve the performances (response speed in $2s$, tracking errors $< 1\%$) in face of parametric variations such as substantial inertia change.
- The proposed H_∞ approach is insensitive to the hydrodynamic estimation errors, which is important to make the numerical modeling solutions more ap-

plicable. The added mass estimation using WAMIT, and damping estimations using ANSYS-CFX and STAR-CCM+ is more reliable in the H_∞ approach.

- Nonlinear damping issues are solved using the numerical damping estimations. The overshoot and oscillations on regular H_∞ control method is eliminated.

In this chapter, the focus is to validate the proposed H_∞ approach in simulations. Therefore, the yaw angular velocity $\dot{x}_r$ is assumed to be accurately measured, and there is no delay in the sensors. However, in real AUV applications the above assumptions can't be satisfied. Several model based complementary techniques are essential to generate an applicable H_∞ approach for real AUV control applications. Hence, in the next chapter, the CFD model based Kalman filters as well as delay compensation algorithms are recommended to deal with the further control problems. A fully applicable nonlinear compensated H_∞ control approach is introduced for the robust control of classic AUVs.

Chapter 6

Applicable H_∞ Controller at Sea

Contents

6.1 *CISCREA* AUV 151

6.2 Improved H_∞ Yaw Controller 156

6.3 *CISCREA* AUV Sea Test 171

6.4 AUV Virtual Simulation Program 179

6.5 Conclusion 180

In the previous chapter, an AUV hydrodynamic model based on H_∞ control approach is proposed to solve the nonlinearity and uncertainty issues. The proposed nonlinear compensated H_∞ control approach is validated as an ideal method in the *CISCREA* AUV heading control simulations. Comparing to the other controllers, it has the advantages, such as:

- The H_∞ controller effectively eliminates the nonlinear quadratic damping caused control overshoot and oscillations.

- The controller can be insensitive to the disturbances and hydrodynamic modeling errors. In fact, the numerical fluid modeling results from the WAMIT,

ANSYS-CFX and STAR-CCM+ software are directly applicable for the H_∞ control approach.

- Comparing to the traditional PID controller, the H_∞ control approach is several times faster (can be more than 10 times faster).
- The H_∞ control commands are generally optimal (or suboptimal), which reduces the energy waste on inefficient propulsions and battery consumptions.
- The H_∞ controller is comparably accurate, and it can have a steady-state error less than 1% in the *CISCREA* AUV heading control application.

However, in real AUV control applications, the theoretical H_∞ control approach is insufficient, and it can possibly failed. For example, in the *CISCREA* AUV heading control simulations, the theoretical H_∞ control approach assumes the yaw angular velocity $\dot{x}_r$ is accurately or sufficiently measured to calculate the critical nonlinear damping compensations. Meanwhile, the yaw angle x_r measurements are assumed to be adequate to complete the feedback control loop. In addition, there should be no delay in the AUV yaw angle x_r measurements. Unfortunately, in the *CISCREA* AUV heading control sea test, neither of the above assumptions are satisfied. The low configuration *CISCREA* AUV only provides an electronic magnetic compass that measures the yaw angle x_r with considerable delay of $0.5s$. The yaw angular velocity $\dot{x}_r$ is not measured. In general AUV tasks, such a magnetic compass is only capable to distinguish very rough AUV directions such as north or south. To solve the applicable issues in *CISCREA* AUV heading control application, we proposed an improved nonlinear compensated H_∞ control scheme. Our solution can be implemented using numerical modifications, and no hardware or device upgrades are required. The improved H_∞ controller integrates three components:

- As mentioned in the previous chapter, a model based H_∞ controller handles the nonlinearity and uncertainty issues with the aid of numerical CFD modeling compensation and the robust control design on the linearized system in face of minor uncertainties.

- The Kalman filter estimates the yaw angular velocity $\dot{x}_r$ for nonlinear quadratic damping compensation. The numerical estimation avoids the need to add expensive sensors.

- The model based delay compensator eliminates the stability lost and oscillations in the feedback control performance.

The sections are organized as follows: The *CISCREA* underwater vehicle is first introduced. After, the improved H_∞ control algorithm is presented. Then, H_∞ control design as well as its simulations are given. Finally, the improved H_∞ controller are validated in *CISCREA* AUV heading control experiments in the lab pool and sea. The experimental heading control results are compared with PID controllers. For the convenience of control simulations and vehicle display, a 3D virtual environment is created for future physical analysis of the *CISCREA* AUV.

6.1 *CISCREA* AUV

We demonstrate throught our works that the improved H_∞ control approach is applicable for the real sea environment with several *CISCREA* underwater vehicles, see figure 6-1. These vehicles are manufactured by the CISCREA company [147], and the heading control experiments are mainly implemented in the Lab-STICC (CNRS 6285 laboratory, OSM team, ENSTA Bretagne [148]) in France.

6.1.1 *CISCREA* AUV Brief Introduction

As shows in figure 6-1, the *CISCREA* AUV has two working modes: ROV and AUV modes. While in the ROV mode, the cable is only used as an information channel to transmit control signals and video data, etc. The *CISCREA* AUV has independent onboard battery supply for electronic devices and thruster propulsions. There is no power supply go through the communication cable, and this feature allows the *CISCREA* ROV to be a ready-to-use as an AUV. During the H_∞ control experiment, the cable disturbances to the AUV dynamics are considered as negligible and bounded

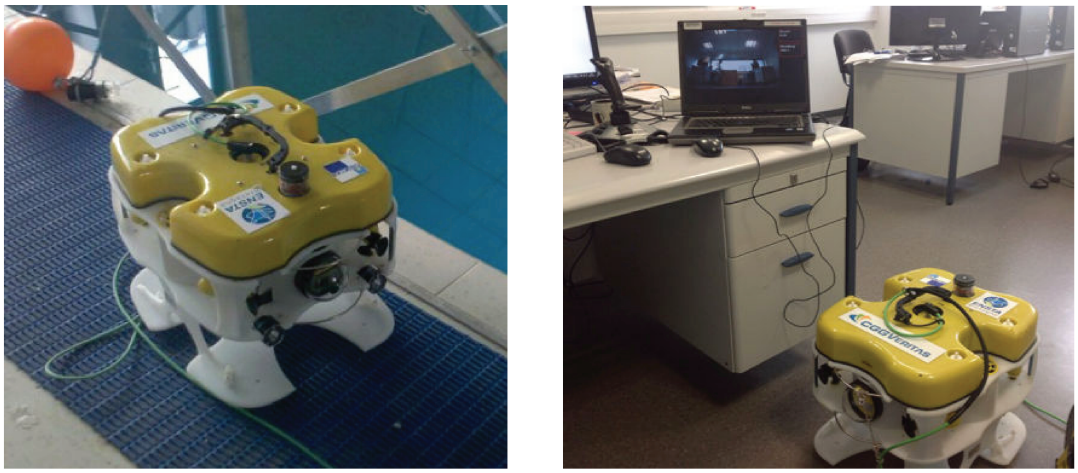

Figure 6-1: *CISCREA* semi-AUV can work in the ROV mode with connected communication cable, or it can work in an AUV mode with autonomous devices.

within uncertainty closed set. In order to fulfill some autonomous underwater tasks, the *CISCREA* AUV is upgrade to the *CISSAU* robot, see figure 6-2. The *CISSAU* robot is generally an improved AUV with more autonomous navigation and sensing devices.

The major characteristics of the *CISCREA* AUV are given as follows:

- The *CISCREA* AUV weight in air is $16kg$ ($29kg$ for the *CISSAU* robot).
- The *CISCREA* AUV has an open-frame design, and it is a collision-proof structure. The major sizes are: 0.525 m in length, 0.406 m in width, 0.395 m in height.
- The AUV surfaces are consisted of corrosion proof materials, including: PVC, PE, PMMA, ABS, and anodized aluminum tube.
- The shell of the *CISCREA* has a rough fluid dynamic design.
- Six thrusters are equipped with the *CISCREA* AUV to have 4 DOFs: surge, sway, heave and yaw directions.
- The maximum depth is $50m$, and the maximum speed is 2 *knots*.
- Battery generally last for $2 \sim 4$ hours with normal mission.

The *CISCREA* AUV is flexible and small. It is a hovering underwater robot suitable for object identification and pipeline surveillance missions, etc. For example, in the SAUCE competition [12], the *CISSAU* AUV is deployed for target identification missions. In the ROV mode, we found a router in the competition port after its lost one year before, see figure 6-3. Figure 6-4 shows the mission of euRatholon competition [13] to turn the valves using the underwater vehicles. The big picture behind the task is a real scenario of the fukushima nuclear accident, and one of the hardest challenge is the AUV motion control problem. As the *CISCREA* AUV is small, complex-shaped and requires accurate maneuverability, its dynamic control is indeed critical and far more difficult than the other AUVs.

6.1.2 *CISCREA* AUV Hardware and Software

The major hardware components of the *CISCREA* AUV are listed as follows:

- Battery package: 48 NiMH units, and each charge provides the energy of 24 Ah at 9.6 V (AUV battery at 12 V).
- Thrusters: 4 horizontal vector propellers, and 2 vertical propellers.
- Wide-angle underwater camera: support 530 line PAL signal, normally has the sensitivity of $0.3Lux/F1.2$, and in Feel Up mode of $0.002Lux$.
- The camera has vertical $\pm 40°$ of turning freedom, and it is equipped with two 5 W LED lens, 440 $Lumen$.
- Depth meter: Maximum depth is about 100 m. Resolution is 1 cm, and the accuracy is 10 cm.
- Electronic magnetic compass: Resolution is 1°, and its accuracy is 1.5°.
- Communication cable: 6.2 mm in diameter, and 80 m in length, weight is 0.052 kg/m.
- Computational units: $FOX\ G20$, Armadeus APF27_DEV (Core frequency: 400Mhz).

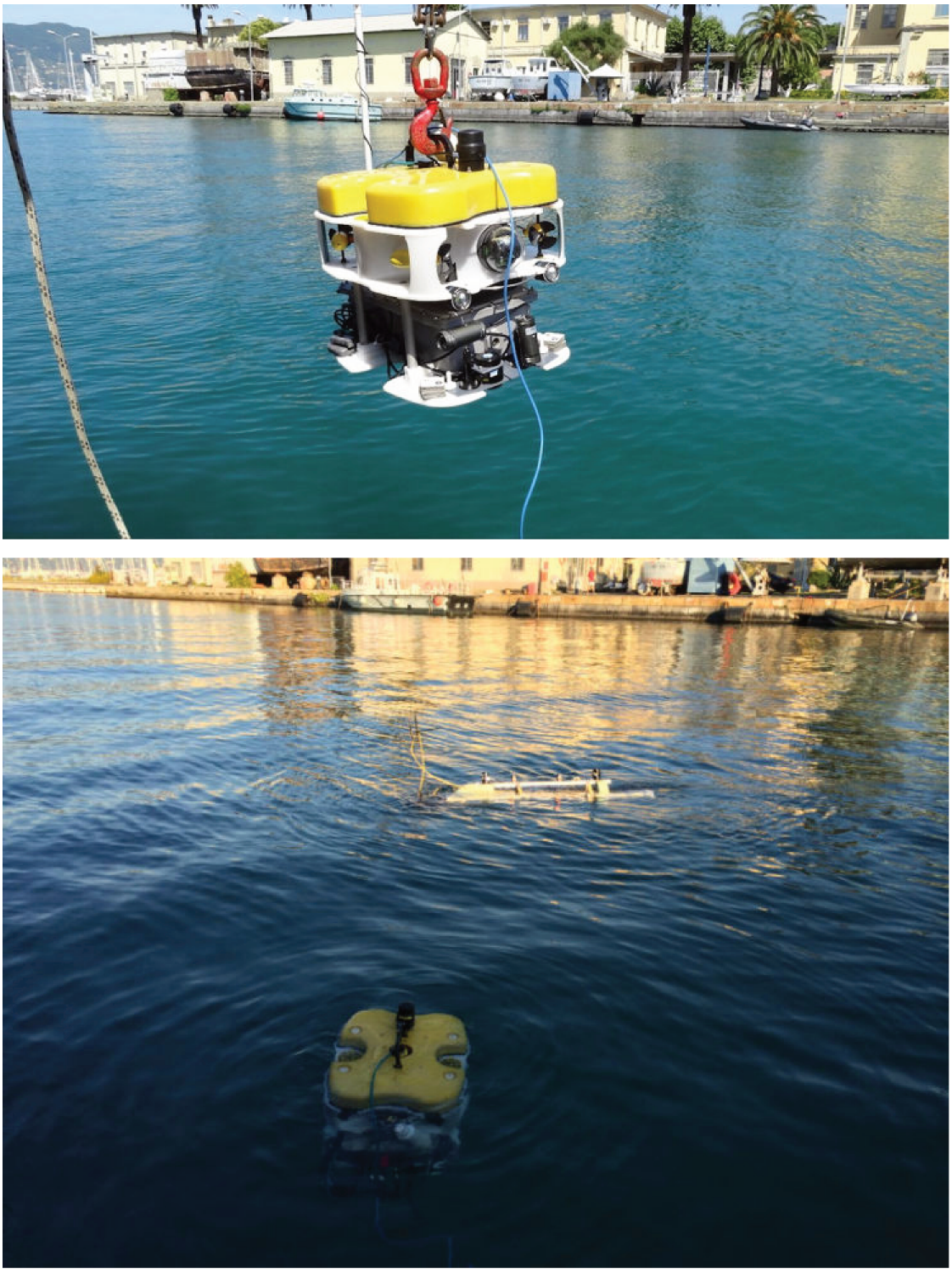

Figure 6-2: An improved AUV version of the *CISCREA* robot that equipped with fully autonomous sensors, such as sonar, underwater cameras, INS/electro-gyros, depth meter and other self-navigate and control unit

Figure 6-3: *CISCREA* AUV founds the router on the bottom of shallow water one year after its lost.

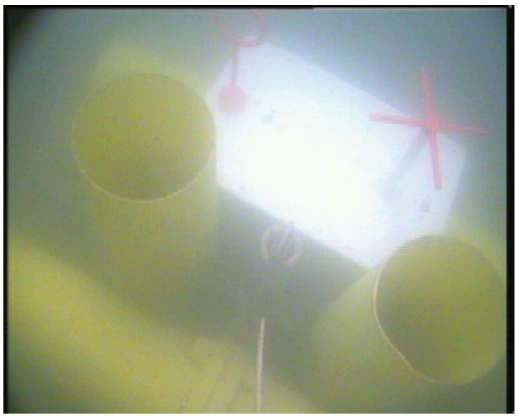

Figure 6-4: *CISCREA* AUV discovers the underwater structures and its valve and o-ring for autonomous manipulations.

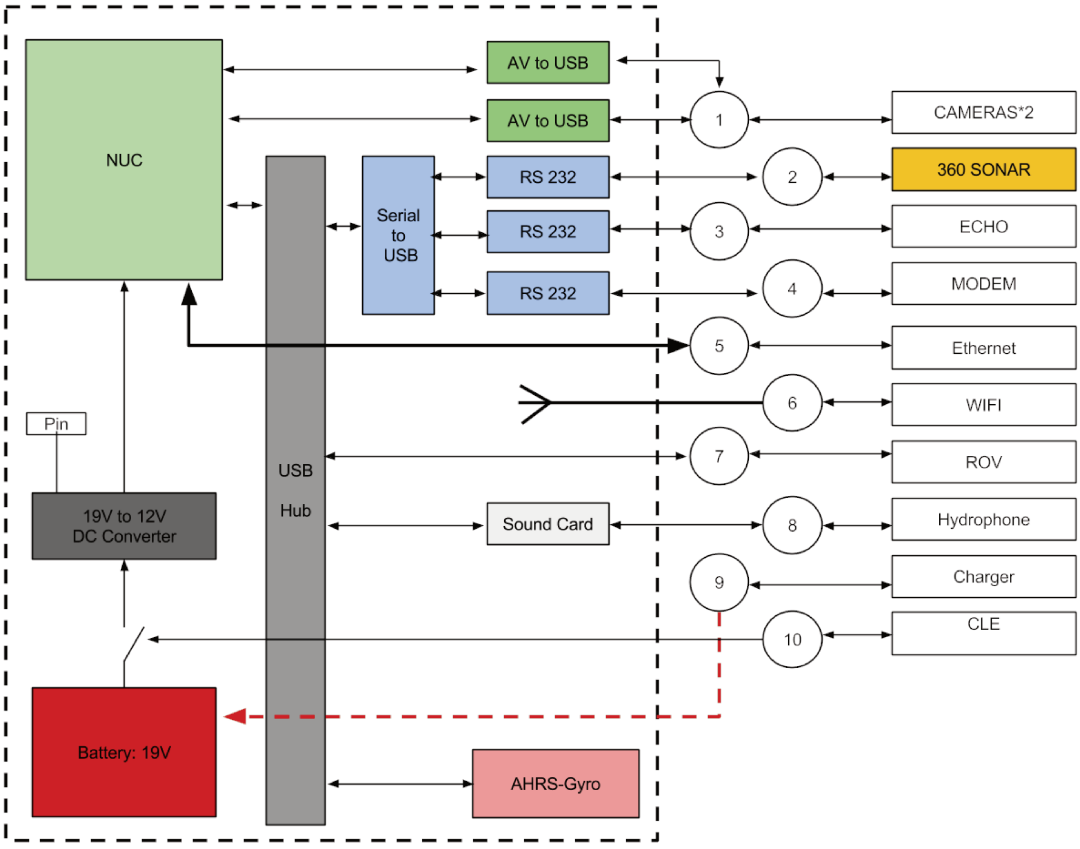

Figure 6-5: The hardware hierarchy diagram of the *CISCREA* AUV

Beside the compact instruments, the *CISCREA* AUV are usually equipped with

the following sensors:

- Underwater acoustic modem: Tritech Micron Acoustic.
- Sonar: Tritech MiniKing sonar (range 100m, waterproof 1000m).
- Hydrophone: Aquarian Audio H2a-XLR.
- INS: AHRS gyro (9 axes).
- Surface sensor: power wifi($1km$), GPS.

The diagram of the hardware and software hierarchies of the *CISCREA* AUV is given in figure 6-5. The *CISSAU* robot uses MOOS-IvP [51] as its top-level mission control software. The MOOS-IvP software can be divided into the MOOS, a mission oriented operating system with a tailorable topology, and the IvP core, a multi-objective optimization program for intelligent AUV behaviors. For the *CISSAU* robot, each program of control (acoustic communication, navigation, guidance, and behavior) can be package and joint into the MOOS-IvP framework. For the *CISCREA* AUV, a python shell is also available. For the convenience, the python version of the H_∞ heading control code is given in appendix D.3.

6.2 Improved H_∞ Yaw Controller

In order to solve the applicable issues of the *CISCREA* AUV heading control application, we design an improved H_∞ control approach in figure 6-6. The new design is fully numerical and solves the *CISCREA* AUV heading control problem using only one magnetic compass as feedback sensor. Note that, in deep ocean, the earth magnetic signal is one of the merely existing information about the heading of the robot with a very good cost efficiency. Therefore, the H_∞ heading control application can show obviously the benefits to address AUV modeling and control issues simultaneously.

Two components play the important role in the improved H_∞ approach: the Kalman fitler and delay compensator. As the dynamic and hydrodynamic model of

the *CISCREA* AUV is roughly obtained through the previous numerical or experimental modeling work, the Kalman filter can be conveniently constructed. First, the Kalman filter estimates the critical damping compensation information, the yaw angular velocity $\dot{x}_r$. Then, the Kalman filter is used to attenuate the sensor noise such as the yaw angle x_r noise induced by the low-price magnetic compass. The errors of the Kalman filter estimations can cause some damping compensation errors. However, benefits from the H_∞ algorithms, the above errors can be treated as some minor bounded uncertainties in the robust control design. Since there exists an obvious sensor delay using the magnetic compass measuring the yaw angle, x_r, the delay compensating algorithms are used. The delay compensating errors are also characterized by minor bounded uncertainties during the robust control design.

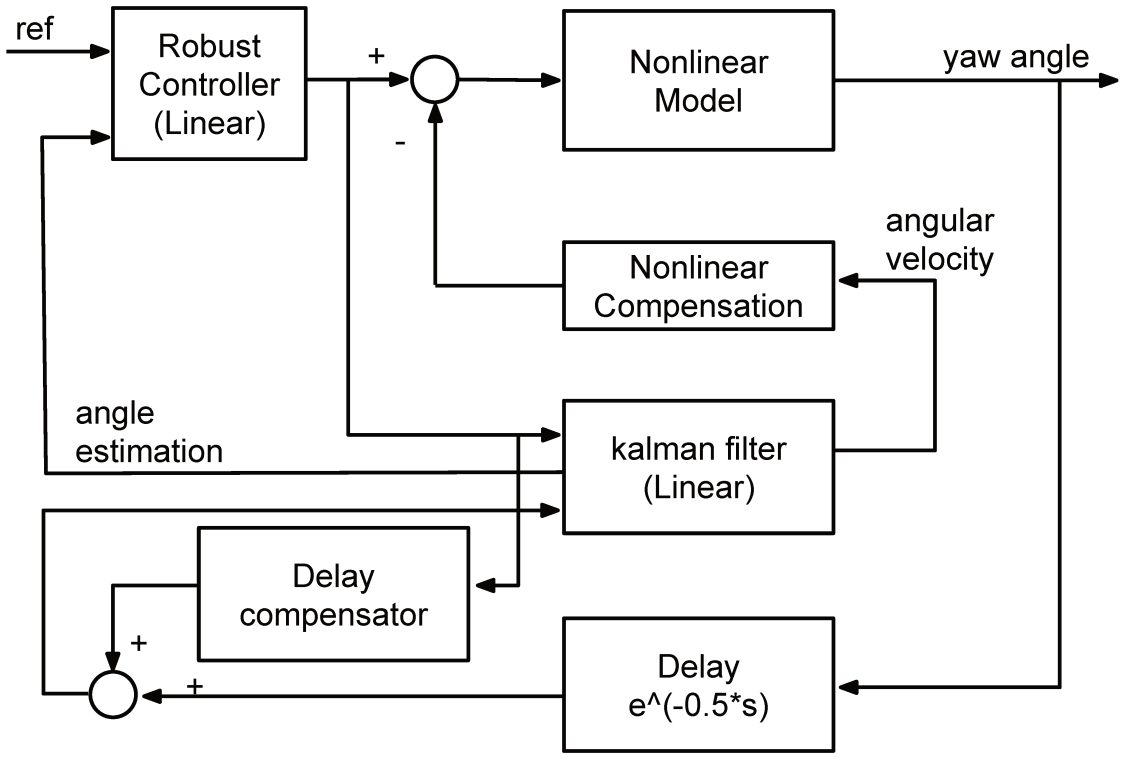

Figure 6-6: The improved compensated H_∞ control approach for the *CISCREA* AUV and other AUVs. Only one magnetic compass is used as the feedback sensor. The H_∞ controller, nonlinear compensator, delay compensator, and Kalman filter are all numerical calculations.

6.2.1 Kalman Filter Estimation

The main application of the Kalman filters is to estimate the noisy states when the noise has known probability characteristics. This Kalman technique is widely used for linear system in the space, military and robotic areas. In case of nonlinear systems, the extended Kalman filters are presented. For the Kalman filter, there are only two input information: noisy measurements come from sensors and the inaccurate model prediction. The Kalman filter estimates the most possible state under an optimal noise principle.

Let us consider the discrete system described in equation 6.1:

$$\begin{cases} x_{k+1} = A_k x_k + B_k u_k + \alpha_k \\ y_k = C_k x_k + \beta_k \end{cases} \tag{6.1}$$

where, x_k is the state vector, u_k is the control input vector, y_k is the system output vector, α_k and β_k respectively denote the known independent white noises with known Probability Density Function (PDF).

Then, define the following equations 6.2 $\sim$ 6.4:

$$E(\upsilon|l) = E(\upsilon|y_0 \cdots y_l) \tag{6.2}$$

$$\widehat{x}_{k|l} = E(x_k|l) \tag{6.3}$$

$$\Gamma_{k|l} = E(\widetilde{x}_k \widetilde{x}_k^T|l) \tag{6.4}$$

According to the Kalman theory [35], Prediction and Update process are two critical steps for the Kalman filter, see figure 6-7. In each clock period interval, the Kalman filter iteratively executes two steps using the following equations:

$$\widehat{x}_{k+1|k} = A_k \widehat{x}_{k|k} + B_k u_k \tag{6.5}$$

$$\Gamma_{k+1|k} = A_k \Gamma_{k|k} A_k^T + \Gamma_{\alpha_k} \tag{6.6}$$

$$\widehat{x}_{k|k} = \widehat{x}_{k|k-1} + K_k \widehat{y}_k \tag{6.7}$$

$$\Gamma_{k|k} = (I - K_k C_k)\Gamma_{k|k-1} \tag{6.8}$$

$$\widehat{y}_k = y_k - C_k \widehat{x}_{k|k-1} \tag{6.9}$$

$$S_k = C_k \Gamma_{k|k-1} C_k^T + \Gamma_{\beta_k} \tag{6.10}$$

$$K_k = \Gamma_{k|k-1} C_k^T S_k^{-1} \tag{6.11}$$

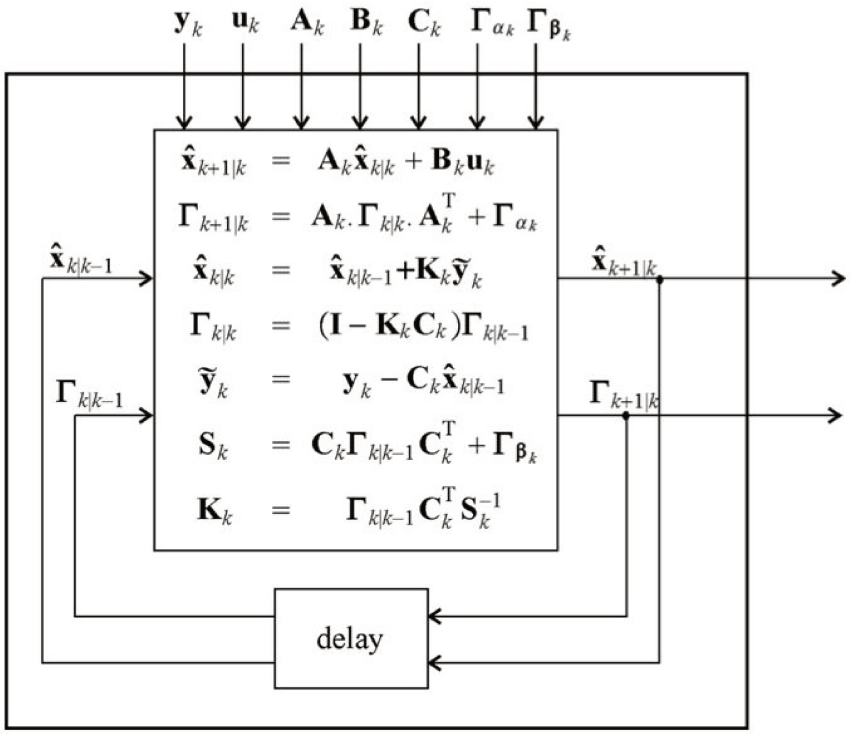

Figure 6-7: Kalman filter

From a robust controller perspective, the nonlinear damping compensated *CIS-CREA* AUV model is a linear system with minor uncertainties, see equation 6.12. Therefore, the Kalman filter assumes the nonlinear damping compensation has no error, and it takes the compensated linear dynamics according to its prediction model.

$$(I_{YRB} + I_{YA} + \delta_1)\ddot{x}_r + (D_{YLA} + \delta_2)\dot{x}_r = \tau_i \tag{6.12}$$

According to the compensated linear dynamics (equation 6.12) as well as its previous modeling results, the 10 Hz discrete state space realization of the compensated *CISCREA* AUV yaw dynamics are given as follows:

$$G(z) = D_{ZG} + C_{ZG}(zI - A_{ZG})^{-1}B_{ZG} \tag{6.13}$$

$$A_{ZG} = \begin{bmatrix} 0.8174 & 0 \\ 0.0906 & 1 \end{bmatrix} \tag{6.14}$$

$$B_{ZG} = \begin{bmatrix} 0.1826 \\ 0.0094 \end{bmatrix} \tag{6.15}$$

$$C_{ZG} = \begin{bmatrix} 0 & 1 \end{bmatrix} \tag{6.16}$$

Furthermore, the covariance matrices are chosen to be: $Q = 1$ and $R = 1$ (magnetic compass sensor). Thereby, the 10 Hz discrete state space realization of the Kalman filter are derived by equation 6.17 $\sim$ 6.21:

$$K_a(z) = D_{ZKA} + C_{ZKA}(zI - A_{ZKA})^{-1}B_{ZKA} \tag{6.17}$$

$$A_{ZKA} = \begin{bmatrix} 0.8174 & -0.027 \\ 0.0906 & 0.9175 \end{bmatrix} \tag{6.18}$$

$$B_{ZKA} = \begin{bmatrix} 0.1826 & 0.027 \\ 0.0094 & 0.0825 \end{bmatrix} \tag{6.19}$$

$$C_{ZKA} = \begin{bmatrix} 0 & 0.9205 \\ 1 & -0.0331 \\ 0 & 0.9205 \end{bmatrix} \tag{6.20}$$

$$D_{ZKA} = \begin{bmatrix} 0 & 0.0795 \\ 0 & 0.0331 \\ 0 & 0.0795 \end{bmatrix} \tag{6.21}$$

In summary, the Kalman fitler estimates the unmeasured states such as the *CISCREA* AUV yaw angular velocity $\dot{x}_r$, and its yaw angle x_r from the noisy magnetic compass signal. The Kalman estimation of yaw angular velocity $\dot{x}_r$ provides essential input to realize necessary damping compensations of the proposed H_∞ approach. In fact, the estimation errors of the yaw angular velocity indeed results in damping compensation errors. However, it can be considered as a minor parametric uncertainty during the H_∞ control design. Besides, the Kalman estimation of yaw angular x_r eliminates some of the sensor noise, and it provides a clear yaw angle information for the H_∞ feedback control.

Without considering signal delay, a yaw control simulation is implemented adding the Kalman filter to the compensated H_∞ control approach, see figure 6-8. The improved H_∞ control approach with Kalman filter aiding is validated in the simulations. The unmeasured and noisy states in the AUV dynamics can be efficiently estimated using the linear compensated model based Kalman filters.

6.2.2 Signal Delay Compensator

Signal delay is an ubiquitous phenomenon for every sensor. However, excessive signal delay can result in control performance reduction and stability lost in regular model based control algorithms. See figure 6-9, the previous Kalman filter aided H_∞ control approach fails to achieve the desired control performance in the *CISCREA* AUV heading control pool test. There are obvious control response oscillations comparing to the simulation expectations in figure 6-8.

In figure 6-9, at the beginning of step jump (around $24s$), the magnetic compass measurements of the AUV yaw angle shows a delay of $0.5s$ comparing to the Kalman yaw angle estimations. Normally, there is no delay in the Kalman yaw angle estimations. The Kalman prediction model is theoretically derived from the numerical

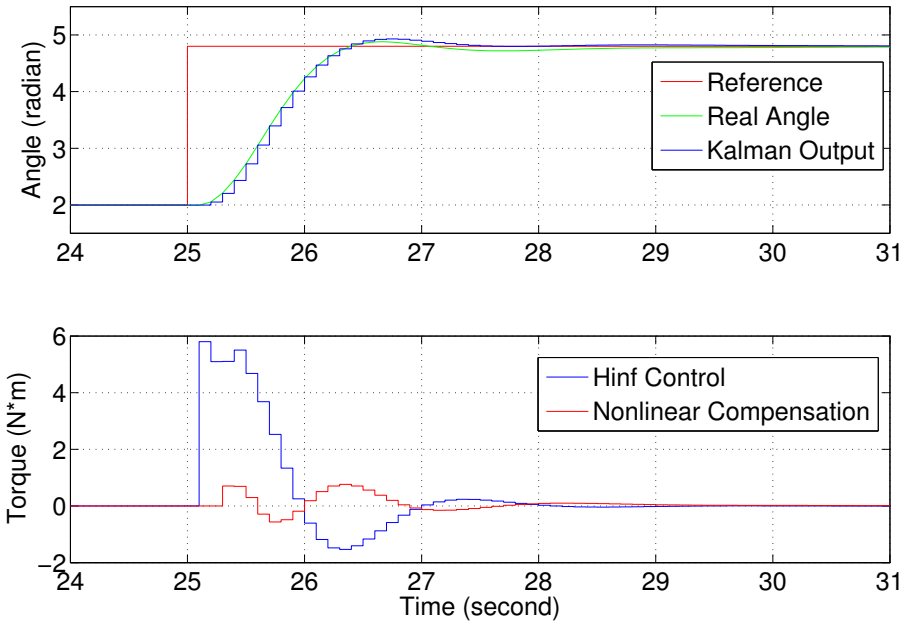

Figure 6-8: H_∞ heading control of the *CISCREA* AUV with the aid of Kalman filter that estimates the angular velocity $\dot{x}_r$. The above subplot shows the yaw angle control step response, and the down one shows the thruster propulsions.

.

calculations. Therefore, it can be concluded that the onboard electronic magnetic compass of the *CISCREA* AUV should have the signal transmission delay of around $0.5 \sim 1s$. With the aid of measuring devices, it can be proved the magnetic compass indeed suffers from a signal delay issue. A simulation is designed to reveal the signal delay issues of the *CISCREA* AUV. In our simulations, a feedback signal delay of $0.5s$ is added to the yaw angle measurements. The similar signal delay caused control oscillations is found in figure 6-10 (comparing to figure 6-9).

As a result of the signal delay issues, it is essential to design the delay compensators in the following. The compensating method for signal delay should be the second critical issue to extend our proposed H_∞ control approach to real AUV control applications in the sea. In fact, delay control system is actually a very large research branch in the control theory. There are many delay control design algorithms and techniques presented in *Zhong*'s book [145]. However, our research focus is AUV modeling and control study, hence, the delay control algorithms are out of the

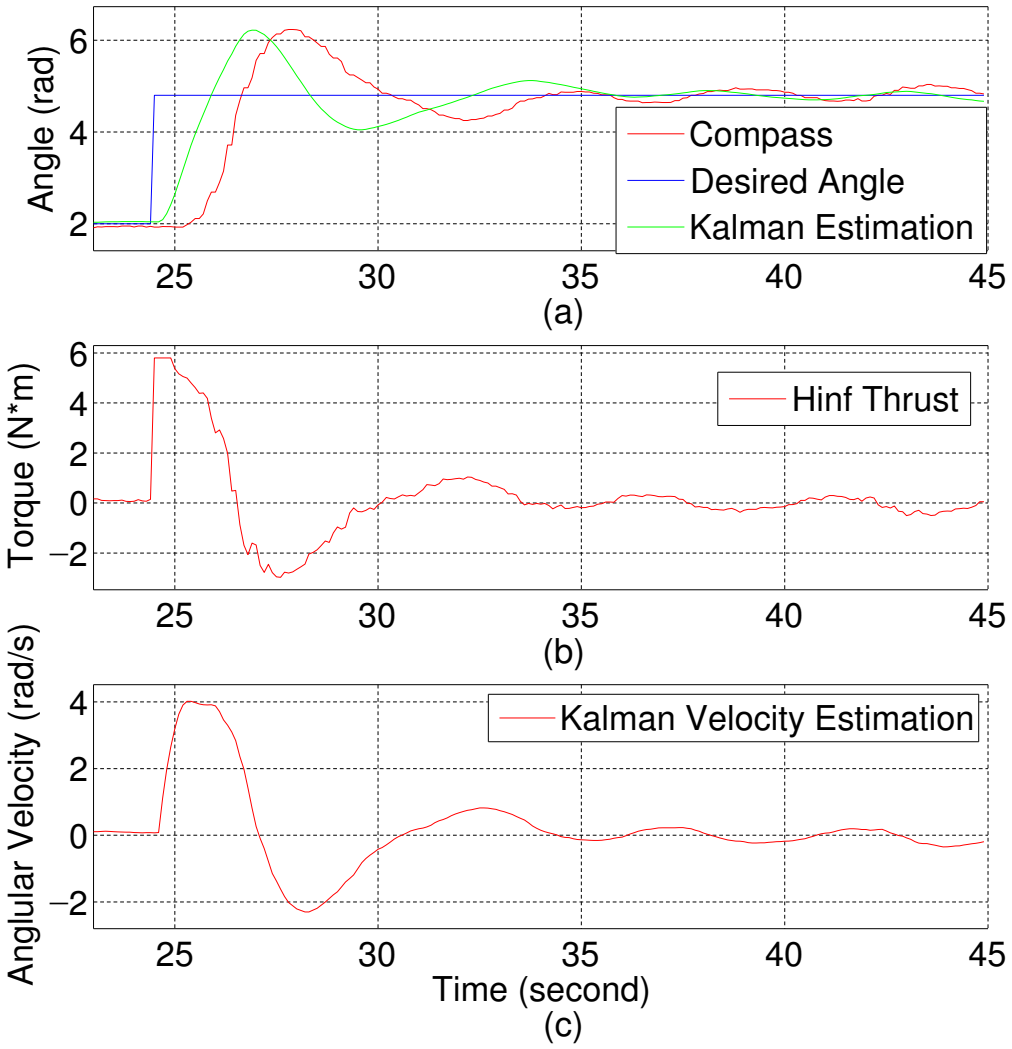

Figure 6-9: Sensor signal transmission delay issue (magnetic compass) and its oscillation consequences about the H_∞ heading control during the water tank experiment of the *CISCREA* AUV. Subplot (a) shows the yaw angle control step response, subplot (b) shows the thruster propulsions, and subplot (c) shows the Kalman angular velocity estimations. A clear time delay of 0.5s can be seen between the yaw angle Kalman estimation and the magnetic compass measurements.

scope of this chapter. Moreover, normal AUVs are generally equipped with sufficient sensors, and they are usually fast enough to avoid delay issues. The reason we choose the electronic magnetic compass as feedback sensor is to push the experiment to the worst limit and show the adequacy of the H_∞ approach (implement fully numerical control using only one compass for heading control). To keep our approach bright,

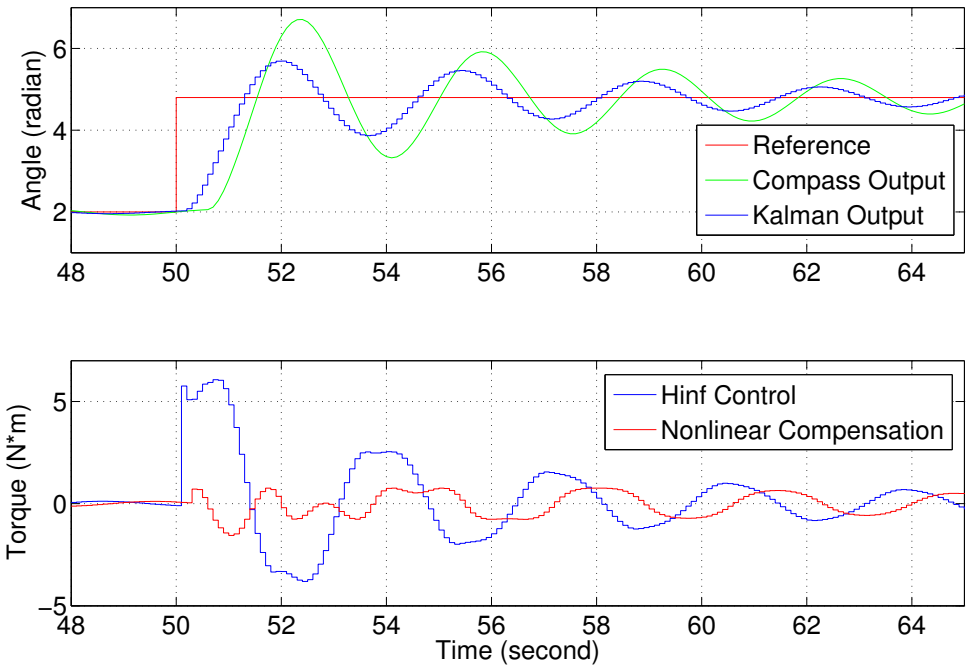

Figure 6-10: The simulation result of the *CISCREA* AUV H_∞ heading control method in face of a virtually adding delay of 0.5 s on the magnetic compass sensor. The above subplot shows the yaw angle control step response, the down one shows the thruster propulsions. A similar oscillation pattern can be drawn comparing to the *CISCREA* AUV heading control pool test.

only basic Smith predicting method and a Kalman velocity compensating method is introduced as engineering solutions to improve our H_∞ control approach in face of sensor delay.

The Smith predictor was first introduced in 1950s [145], and its main idea is to design a controller that keeps the closed-loop system in form of $\frac{C(s)G(s)}{1+C(s)G(s)}e^{-\tau s}$, as a result, a delay-free model $G(s)$ can be equivalently seen from the controller perspective, see figure 6-11. The Smith predictor turns the delay system $G(s)e^{-\tau s}$ control design problem to a regular control design for $G(s)$ without concerning delay effect. The closed-loop system should be $\frac{C(s)G(s)}{1+C(s)G(s)}e^{-\tau s}$. Adding the Smith compensator to the *CISCREA* AUV H_∞ approach, the AUV delay issues can be conveniently solved. The delay compensating errors between the Smith predition model $G_0(s)$ and the real system $G(s)$ can be assumed as a minor uncertainty in the H_∞ control scheme.

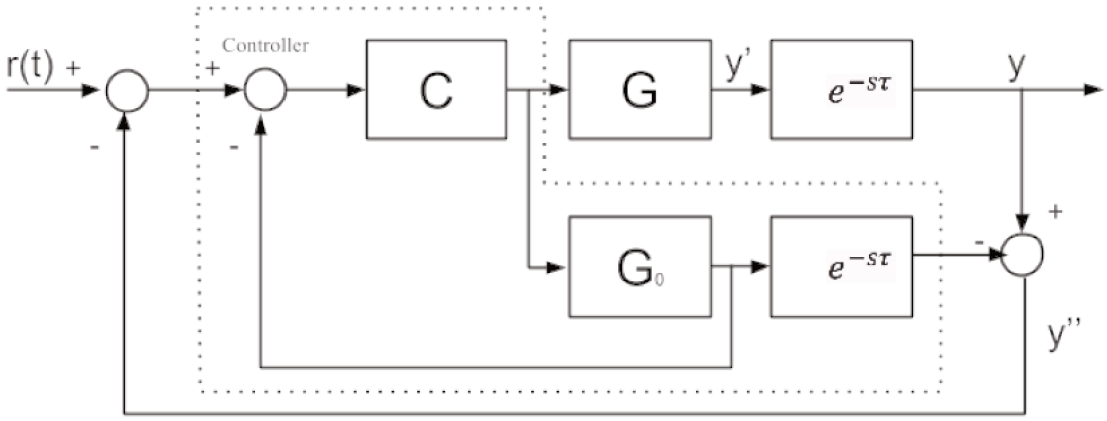

Figure 6-11: Diagram of the Smith compensating technique

Consider the system in figure 6-11, the stable transfer function $P(s)$ is derived to feedback to the controller $C(s)$ (guarantee the $e^{-\tau s}$ is equivalently outside the control loop), see equation 6.22:

$$P(s) = G_0(s)(1 - e^{-s\tau}) \tag{6.22}$$

According to the physical explanation of the Smith compensator, after adding transfer function $P(s)$ to $C(s)$, the input signal of $C(s)$ becomes equal to the output $y_1(t)$ of the delay-free system $G_0(s)$ ($G_0(s)$ is the model approximation of real plant $G(s)$). In summary, the Smith predictor attempts to estimate the current delay-free output $y_2(t)$ from the model $G_0(s)$ prediction $y_1(t)$ and the delay sensor output $y(t)$. If the model $G_0(s)$ is equal to the real system $G(s)$, then, the control design of $C(s)$ can totally ignore the delay $e^{-\tau s}$, and designs directly on $G(s)$.

To deal with the compass delay issue in the *CISCREA* AUV heading control application, a Smith compensator is designed and implemented. According to the compensated linear AUV model in equation 6.12 $G_0(s)$ and the signal delay interval of $0.5s$, the Smith compensator is derived in equation 6.23:

$$P(s) = G_0(s) - G_0(s)e^{-0.5s} \tag{6.23}$$

$$G_0(s) = \frac{2.0158}{s^2 + 2.0158s} \tag{6.24}$$

Note that, the prediction model $G_0(s)$ uses the linear nominal model of the H_∞ controller. The nonlinear damping compensation should have some errors, hence, there are indeed some errors between $G_0(s)$ and $G(s)$. As a result, the delay compensation also has minor errors. However, the above errors caused effect can be largely handled using the H_∞ control design. In order to validate the fully improved H_∞ algorithm, the step response simulation was implemented first, see figure 6-12. In summary, the unmeasured and noisy states are estimated by the model based Kalman filter, meanwhile the Smith compensator compensates the $0.5s$ delay of the magnetic compass. The H_∞ controller inherits from our previous design to eliminate the uncertainty and nonlinearity issues. It is shown, the fully improved H_∞ algorithm is efficient to solve the AUV heading control issues.

In order to facilitate the delay compensating method without using a model, we proposed an engineering solution to compensate the compass sensor delay using the Kalman estimation of the angular velocity $\dot{x}_r$. The Kalman delay compensating method assumes a robust controller to handle the compensating errors (such as H_∞ controller). As mentioned before, the idea of Smith predictor is to estimate current delay free output $y_2(t)$ from the delay sensor output $y(t) = y_1(t - \tau) + \delta$ (δ is a small modeling error, τ is the delay interval) and the model output prediction $y_1(t) = F^{-1}[G_0(s)u(s)]$. A model based compensation value $F^{-1}[P(s)u(s)]$ is calculated and add to the delay sensor signal $y(t)$.

$$y_2(t) = F^{-1}[P(s)u(s)] + y(t) = F^{-1}[P(s)u(s)] + y_1(t - \tau) + \delta \tag{6.25}$$

Here, $P(s)$ is the compensator given in equation 6.22, and $G_0(s)$ is the prediction model, $u(s)$ stands for the control input. In equation 6.25, a physical model is always required to implement such delay compensations.

In the contrary, the *CISCREA* AUV heading control uses H_∞ controllers, the output estimation $y_2(t)$ allows minor errors. The model based compensation $F^{-1}[P(s)u(s)]$

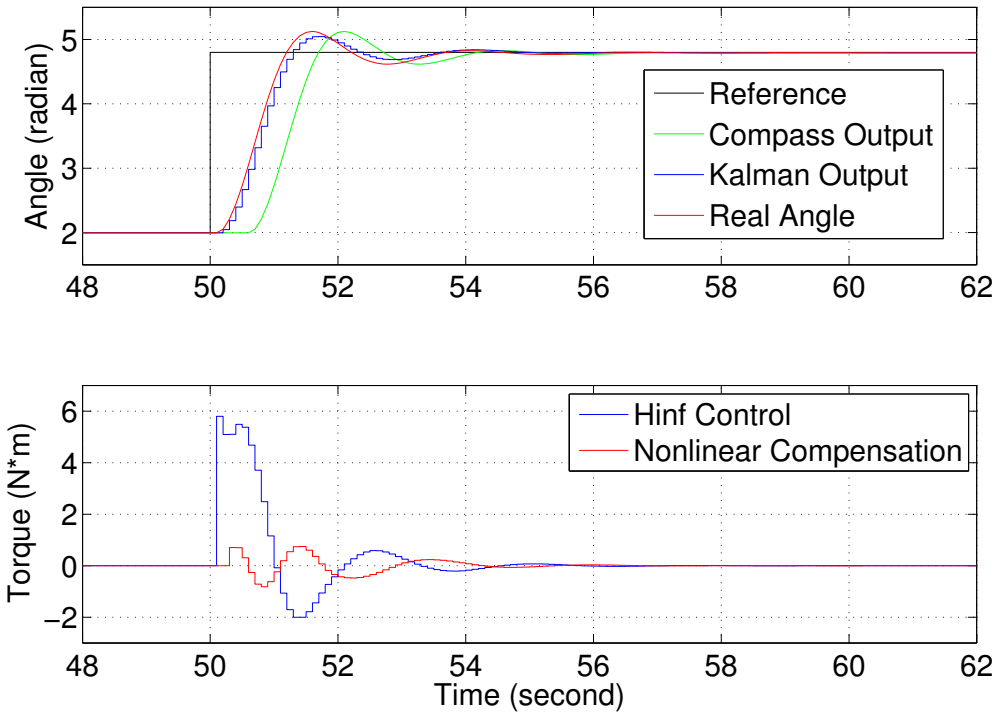

Figure 6-12: The simulation result of the improved *CISCREA* H_∞ heading controller (Smith Compensation). The above subplot shows the yaw angle control step response, the down one shows the thruster propulsions. Both Kalman filter and Smith compensators are used to eliminate the applicable issue for the original H_∞ control design.

is relevant to a function of the AUV angular velocity $\dot{x}_r$, see equation 6.26. Moreover, we can simply assume that the approximation function $f(\dot{x}_r)$ is proportional to the AUV angular velocity $\dot{x}_r$, see equation 6.27.

$$y_2(t) = F^{-1}[P(s)u(s)] + y(t) = f(\dot{x}_r) + y(t) \tag{6.26}$$

$$y_2(t) = f(\dot{x}_r) + y(t) = K\dot{x}_r + y(t), \quad K > 0 \tag{6.27}$$

Thereby, the delay compensation becomes a problem to find such a constant K, that roughly compensates the sensor delay. The compensating errors are handled in the H_∞ control design. In the delay compensating simulations, we tuned a $K =$

0.57 to provide a good compensation to the compass sensor delay, and the control performance is sufficient, see figure 6-13.

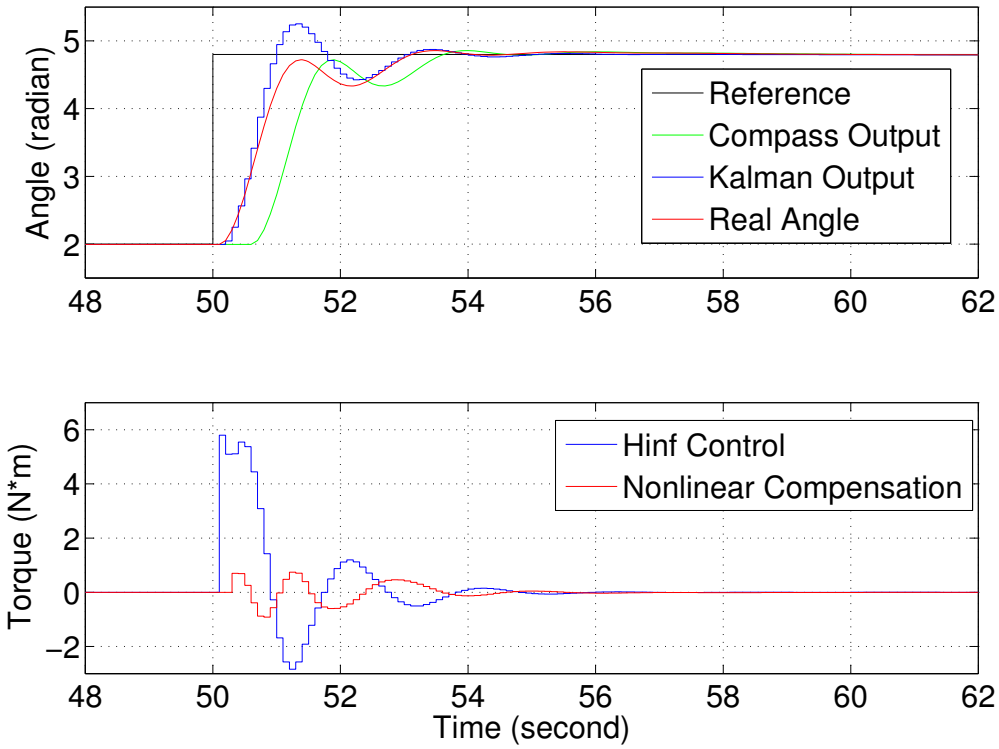

Figure 6-13: The simulation result of the improved *CISCREA* H_∞ heading controller (Kalman Compensation). The above subplot shows the yaw angle control step response, the down one shows the thruster propulsions.

6.2.3 Improved H_∞ Control Approach

This section summarizes the entire improved H_∞ control approach for the *CISCREA* AUV heading control application.

According to the nonlinear yaw model of the *CISCREA* AUV in equation 6.28:

$$(I_{YRB} + I_{YA})\ddot{x}_r + D_{YN}|\dot{x}_r|\dot{x}_r + D_{YL}\dot{x}_r = \tau_i \tag{6.28}$$

The nonlinear quadratic damping compensation method is proposed. The improved H_∞ control approach calculates the compensating torques based on equation 6.29,

and sends the results to the AUV propellors:

$$\tau_{com} = (D_{YLA} - D_{YLD} - D_{YND}|\dot{x}_r|)\dot{x}_r \tag{6.29}$$

The nonlinear compensation results in a linear AUV dynamic with minor uncertainties, see equation 6.30:

$$(I_{YRB} + I_{YA} + \delta_1)\ddot{x}_r + (D_{YLA} + \delta_2)\dot{x}_r = \tau_i \tag{6.30}$$

Based on the derived LTI AUV model, the H_∞ controller is synthesized, its $10Hz$ discrete state-space realization $K(z)$ is given in equations 6.31 $\sim$ 6.34:

$$K(z) = D_{ZK} + C_{ZK}(zI - A_{ZK})^{-1}B_{ZK} \tag{6.31}$$

$$A_{ZK} = \begin{bmatrix} 0.1973 & 1.5954 & 4.498 & -3.7178 & -0.3001 \\ -0.0062 & 0.7597 & -0.6852 & -0.5474 & -0.0451 \\ 0.0146 & -0.1709 & 0.5505 & 0.0406 & -0.0156 \\ -0.0015 & -0.0363 & -0.0211 & 0.3053 & 0.0297 \\ 0.0003 & 0.0003 & 0.0002 & 0.0277 & 0.9984 \end{bmatrix} \tag{6.32}$$

$$B_{ZK} = \begin{bmatrix} 0.2731 \\ -0.0179 \\ 0.2065 \\ 0.1106 \\ 0.0005 \end{bmatrix} \tag{6.33}$$

$$C_{ZK} = \begin{bmatrix} -16.0063 & 58.3996 & 178.6582 & -258.9466 & 16.8046 \end{bmatrix} \tag{6.34}$$

For the applicable reasons, a Kalman filter is designed to estimate unmeasured AUV angular velocity $\dot{x}_r$ and noisy yaw angle x_r. The $10Hz$ discrete state space

realization of the Kalman filter is given in equations 6.35 $\sim$ 6.39:

$$K_a(z) = D_{ZKA} + C_{ZKA}(zI - A_{ZKA})^{-1}B_{ZKA} \tag{6.35}$$

$$A_{ZKA} = \begin{bmatrix} 0.8174 & -0.027 \\ 0.0906 & 0.9175 \end{bmatrix} \tag{6.36}$$

$$B_{ZKA} = \begin{bmatrix} 0.1826 & 0.027 \\ 0.0094 & 0.0825 \end{bmatrix} \tag{6.37}$$

$$C_{ZKA} = \begin{bmatrix} 0 & 0.9205 \\ 1 & -0.0331 \\ 0 & 0.9205 \end{bmatrix} \tag{6.38}$$

$$D_{ZKA} = \begin{bmatrix} 0 & 0.0795 \\ 0 & 0.0331 \\ 0 & 0.0795 \end{bmatrix} \tag{6.39}$$

At last, the Smith predictor is used to compensate magnetic sensor delay, see equations 6.40 and 6.41:

$$P(s) = G_0(s) - G_0(s)e^{-0.5s} \tag{6.40}$$

$$G_0(s) = \frac{2.0158}{s^2 + 2.0158s} \tag{6.41}$$

In figure 6-6, three important components consist of the improved applicable H_∞ control approach: the compensated H_∞ controller to handle uncertainty and nonlinearity, the Kalman filter for state estimations, and the delay compensator to eliminate oscillations. The proposed H_∞ control approach only uses one magnetic compass as a feedback sensor in deep sea AUV heading control. The rest of the control scheme is fully numerical program that derived or designed according to the CFD modeling results, the H_∞ control algorithm, Kalman filter technique, and delay control theory.

The AUV heading control simulations proved that the improved applicable H_∞ control approach is robust stable, fast response, and accurate. Note that, the above H_∞ control approach is initially proposed for AUV 6 DOFs control, the robust features are expected to be validated in further control research on coupled 6 DOFs dynamics. In order to validate the improved H_∞ control approach in real sea environment, several experiments are implemented in the following.

6.3 *CISCREA* AUV Sea Test

Two scenarios are proposed for the *CISCREA* AUV heading control experiments:

- H_∞ heading control pool test in the laboratory of ENSTA Bretagne.
- H_∞ heading control sea test near the Brest harbor, France.

Classical PID control method is tested for control performance comparisons.

6.3.1 Pool Test of H_∞ heading controller

The pool is located at ENSTA Bretagne (CNRS 6285) for underwater testing, with an area of 16 m^2 and a depth of $3.5m$, see figure 6-14. As the concrete wall is built with some metal supports that impact the magnetic compass, therefore, the AUV was maintained in the center of the pool during the underwater test.

During the pool test, two control methods are used in the heading control experiments: classical PID control method, and improved H_∞ control approach. The PID as well as the H_∞ controller python code can be found in the appendix D.3. The experimental results of the PID heading control method are shown in figure 6-15. The results show that the PID controller is slow in step response, and rotating from 2 rad to 4.8 rad can take around 15 s. The yaw rotating step response shows that the PID controller has obvious overshoot, and the rotation motion is abnormal with sawtooth in face of the external environment disturbance and sensor noise. The PID control command has clear oscillations, and the reason can be the noise of the magnetic compass measurements. In fact, the AUV propellers lifespan is dramatically decreased as

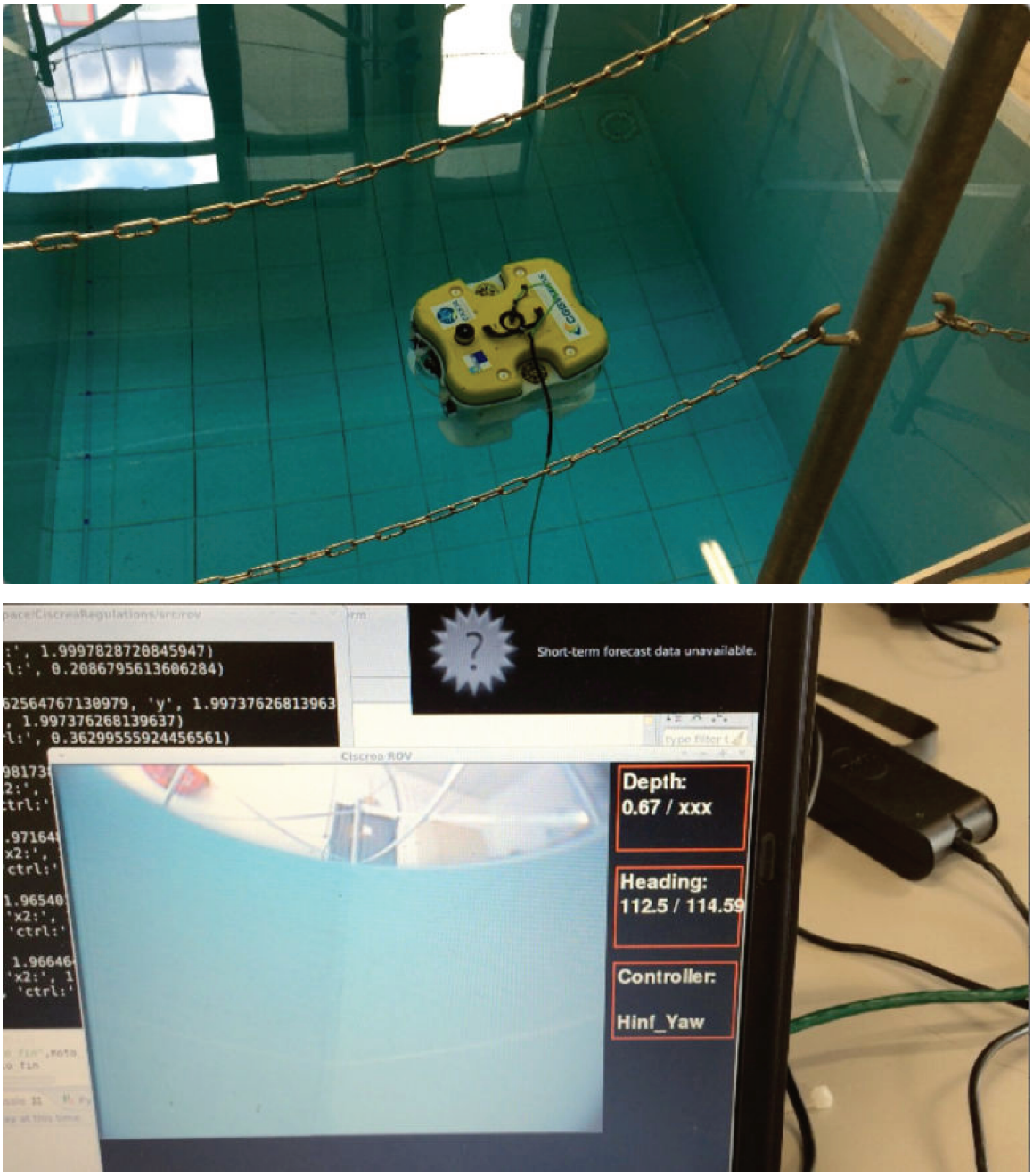

Figure 6-14: The pool experiment of the fully compensated H_∞ heading control approach as well as other control methods on the *CISCREA* AUV. The above subplot shows the *CISCREA* AUV rotating around the yaw axis in the testing pool, and the one below shows the real-time control monitor of the AUV camera and control parameters, such as the yaw angle.

a result of redundant propulsions and vibrations. Note that, the magnetic compass signal transmission delay also contributes to the control oscillation. However, it is

difficult to notice this delay issue immediately without a model analysis or essential sensor check.

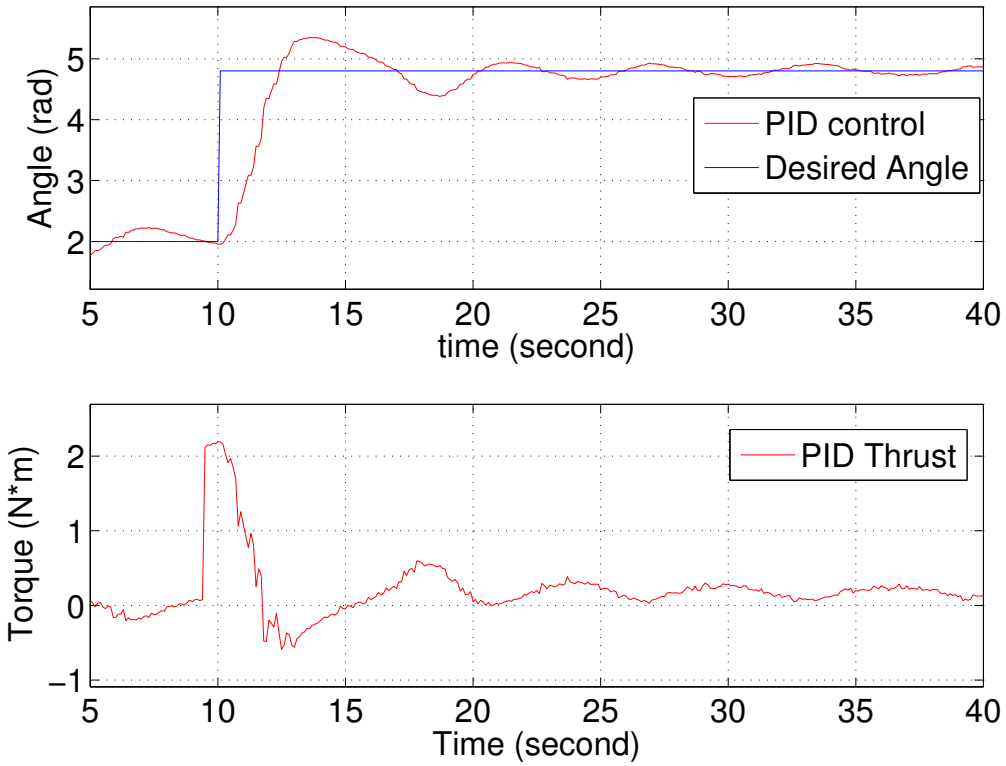

Figure 6-15: Experimental heading control results of the *CISCREA* AUV using the PID control approach in the water pool of ENSTA Bretagne laboratory (CNRS 6285), the subplots respectively show the robot yaw angle and control output propulsions

In the contrary, the improved H_∞ control approach is implemented and validated to be efficient in the AUV heading control pool test, see figure 6-16. The experimental results demonstrate that the improved H_∞ control approach achieved the robust design performances as it was shown in simulations. First, the H_∞ control approach has a fast response speed, to rotate from 2 rad to 4.8 rad only need 2$\sim$3 s (the response speed specification of the robust synthesis is 2 s). The H_∞ control approach is several times faster than the traditional PID control method. Comparing to the PID AUV heading controller, the H_∞ control approach has no overshoot, and the tracking accuracy is obviously improved. In figure 6-16, the unmeasured AUV angular velocity $\dot{x}_r$ is clearly estimated by the designed Kalman filter. Therefore, corresponding

nonlinearity compensator can efficiently eliminate the nonlinear quadratic damping to result in the linear AUV dynamics with minor uncertainties. In addition, the AUV yaw angle x_r is well filtered by the Kalman design. From the controller perspective, the smooth yaw angle measurements bring in the benefit of notable noise attenuation on the magnetic compass output. Correspondingly, the optimal and smooth control command can extend the AUV propeller lifespan and dramatically reduce the battery consumption. Comparing to the PID control method, the H_∞ control approach is indeed optimal, and the efficiency of propulsion utilization and battery consumption is dramatically improved.

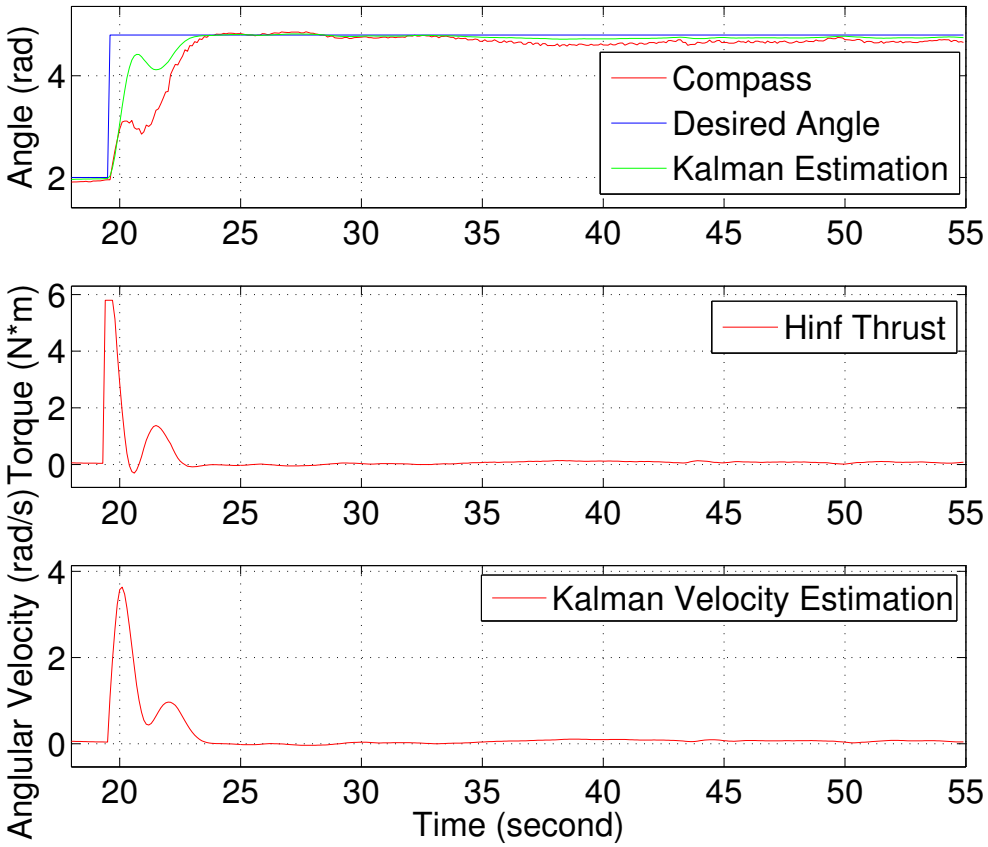

Figure 6-16: Experimental heading control results of the *CISCREA* AUV using the proposed fully compensated H_∞ control approach in the water pool of ENSTA Bretagne laboratory (CNRS 6285) , the subplots show the robot yaw angle, the control output propulsions, and the Kalman estimation of the yaw angular velocity $\dot{x}_r$

6.3.2 Sea Test of H_∞ heading controller

Several sea tests are implemented with the *CISCREA* AUV to validate the proposed H_∞ control approach. These sea tests have been took place near the Brest harbour (France) in Apr. 2014, and the CMRE base in La Spezia (Italy) in Oct. 2014 during the SAUCE and euRathlon competitions[12, 13]. For the convenience, the Brest harbor sea test is presented in this section using two control methods, see figure 6-17:

- Classical PID heading control method.
- Improved nonlinear compensated H_∞ control approach.

Figure 6-17: The sea experiment of the fully compensated H_∞ heading control approach as well as other control methods on the *CISCREA* AUV near the Brest harbour, France.

The real sea environment is different and more complex than the laboratory conditions. From the exterior perspective, more external disturbances are induced to the

AUV control system, such as the water density and temperature change, the salinity variations, unpredictable wind, wave and currents, etc. From the interior perspective, the AUV control changes include:

- In each sea test, the payload of the *CISCREA* AUV is different with the AUV buoyancy adjustment.
- During the missions, there are possible AUV propeller damage or malfunction in face of underwater algae, etc.
- The transport, re-assembly and deploy of the AUV to the sea sometimes cause propeller and sensor damage or malfunctions.
- The propulsion capability and hydrodynamic characteristic should be slightly different between sea water and fresh water.
- Complex sea environment can cause more disturbances to the AUV sensors.
- The most importantly, the battery power drop is a critical uncertainty in the control of underwater vehicles.

In summary, the AUV can be less efficient in the sea if the controller can not adapt to the above uncertainties. Therefore, it is important to design and validate the improved H_∞ control approach for the AUV control applications in the sea.

The sea experiment results of the PID heading control method are shown in figure 6-18. The results show that the PID controller is slow in step response, and it can hardly converge to the desired reference angle (takes around 15 s). Similar to the pool test results, the PID controller has obvious overshoot, and the control commands mix a lot of sawtooth in face of the external environment disturbance and sensor noise. Note that, as many physical parameters change in the sea environments, and more unpredictable disturbances are induced, therefore, the un-robust fixed PID controllers can not adapt to the new environment, and it shows irregular control commands and behaviors comparing the pool test. Different types of oscillations can be seen on the control output, i.e., the sea environment indeed brings in more disturbance and

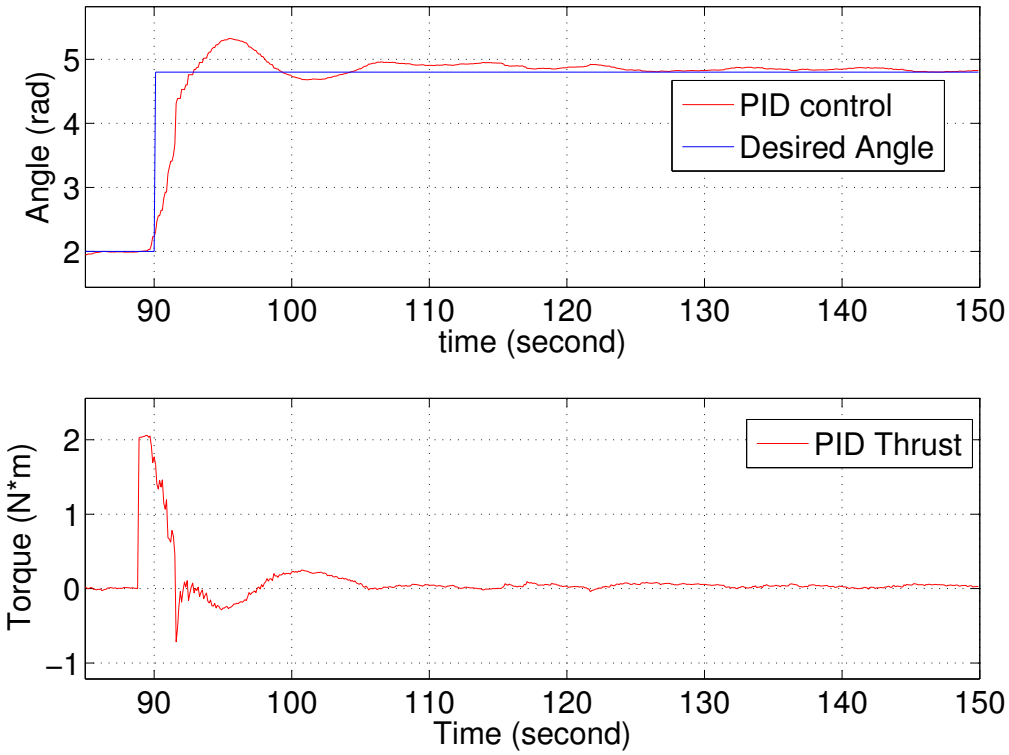

Figure 6-18: Experimental heading control results of the *CISCREA* AUV using the PID control approach near Brest harbour, France. The subplots respectively show the robot yaw angle and control output propulsions.

uncertainties to the AUV control problem. In this case, no matter a good PID control performance is tuned in the laboratory conditions, it might fail in the changing sea environment. The robust and adaptive ability is essential for high precision AUV control in the real sea.

The sea test results of the improved H_∞ approach is shown in figure 6-19. In order to emphasis the robust ability of the improved H_∞ control approach, the experimental heading control results in figure 6-19 extract the time slot while the *CISCREA* AUV is at low battery power. First, the H_∞ control approach is still faster than PID response speed, rotating from 2 rad to 4.8 rad only needs 5∼8 s in face of obvious battery power drop. Comparing to the PID AUV heading controller sea test, the H_∞ control approach has no overshoot, and the tracking accuracy is also improved. In figure 6-19, the unmeasured AUV angular velocity $\dot{x}_r$ is clearly estimated by the designed

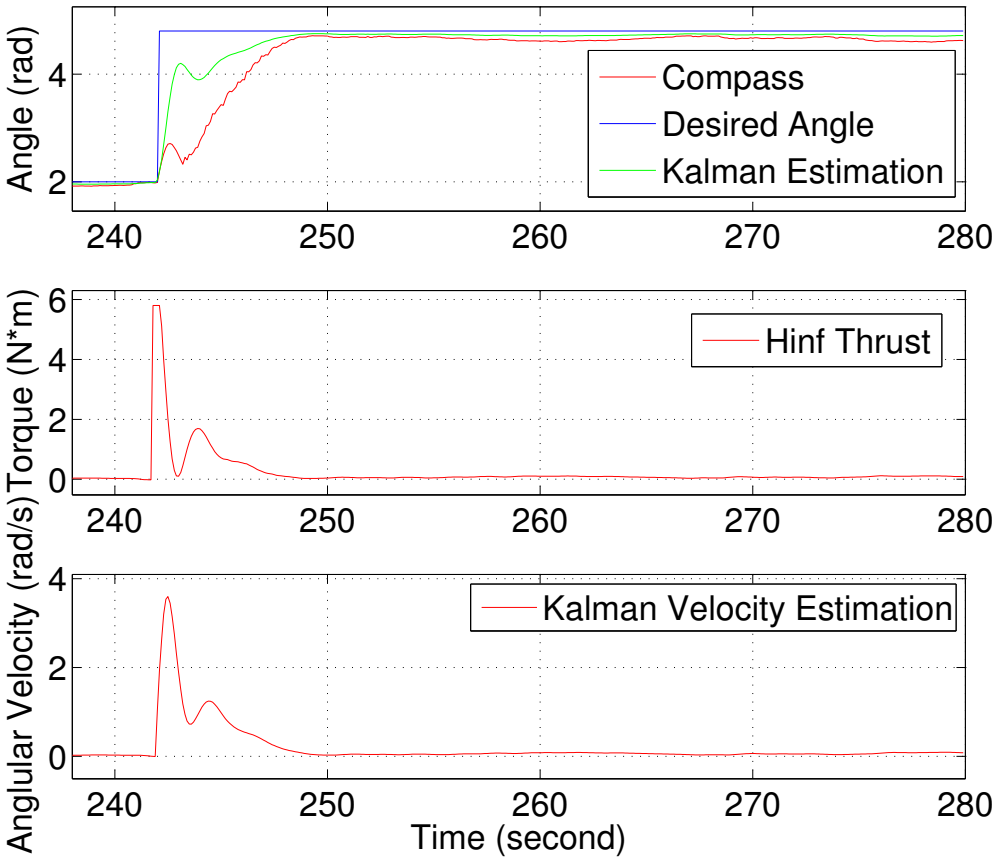

Figure 6-19: Experimental heading control results of the *CISCREA* AUV using the proposed fully compensated H_∞ control approach the near Brest harbour, France. The above and down subplots respectively show the robot yaw angle, the control output propulsions, and the Kalman estimation of the yaw angular velocity $\dot{x}_r$. During the selected time slot, the *CISCREA* AUV is of low battery. However, the robot is still shows good robust capability.

Kalman filter. Meanwhile, the AUV yaw angle x_r is well filtered by the Kalman design. There is notable noise attenuation on the magnetic compass output, which extend the AUV propeller lifespan and dramatically reduces the battery consumption. In the sea test, the H_∞ control approach has proved its optimal advantages. In summary, the experimental results of the *CISCREA* AUV heading control demonstrate that the improved H_∞ control approach can adapt to the real sea changes. Our approach can almost maintain the same robust performances comparing to the AUV simulations and pool tests. In this case, the improved H_∞ approach can dramatically improve

the AUV controller design efficiency. The H_∞ controller, that obtained from the numerical modeling and control synthesis, can directly validated in the pool test, and the same control design would have almost the same control performance in face of real sea uncertainties and disturbance. In short, the H_∞ AUV control design can be an one-shoot calculation procedure.

In order to show the long term performance of the improved H_∞ *CISCREA* AUV heading control approach, the long period sea test results are shown in figure 6-21. The proposed control approach demonstrated sufficient robust ability in presence of various real sea uncertainties and disturbances in a long peroid. Note that, for simplicity, we have not developed the obstacle avoidance program for the *CISCREA* AUV during the sea test. Moreover, there exist minor bugs in the compass reading function. Therefore, several inessential AUV behavior malfunctions can be seen in figure 6-21. Label A stands for the inconsiderable kayak collision with the *CISCREA* AUV. In addition, Label B denotes respectively the *CISCREA* AUV communication cable hooked by an underwater concrete structure, and at the same time, the program triggered a bug while the compass switches instantly between the maximum range and the minimum. As the magnetic compass output ranges from $0 \sim 6.28\ rad$, there is the instant jump when the robot cross the two limits. In summary, the irregular curves are caused by irrelevant issues, and our experimental goal to validate the AUV CFD modeling and H_∞ control design approach is achieved.

6.4 AUV Virtual Simulation Program

As mentioned before, the proposed CFD modeling and H_∞ control can be a fully numerical one-shoot design procedure on normal PC, therefore, a virtual environment is essential for the physical control validations and AUV display. Currently, there are many matured virtual simulation programs for the ocean vehicle designs, such as the open-source *Fossen*'s MSS for large vessels and oil platforms [117]. In fact, the physical AUV virtual visualization programs can facilitate many high level researches, such as: mission control program validation, artificial intelligence algorithm, and

even some AUV visual swarm approaches, etc. The visualization of the AUV control motions can provide intuitive perfromance information to avoid design failures. Moreover, the AUV Virtual Simulation Program can review and demonstrate some physical dynamic details that can be difficult to found in traditional experiments.

In figure 6-20, a virtual simulation environment was built using the Maltlab Simulink 3D package, and the dynamic and hydrodynamic AUV models that obtained in previous chapters. The bathymetry data in figure 6-20 comes from the open source sonar scan of a volcano (Geographic Information System, GIS, such as ArcGis software). The 3D environment is driven by the background running Matlab code of the proposed AUV controllers. As the virtual program topic is out of our academic scope, hence, the further program details are not covered.

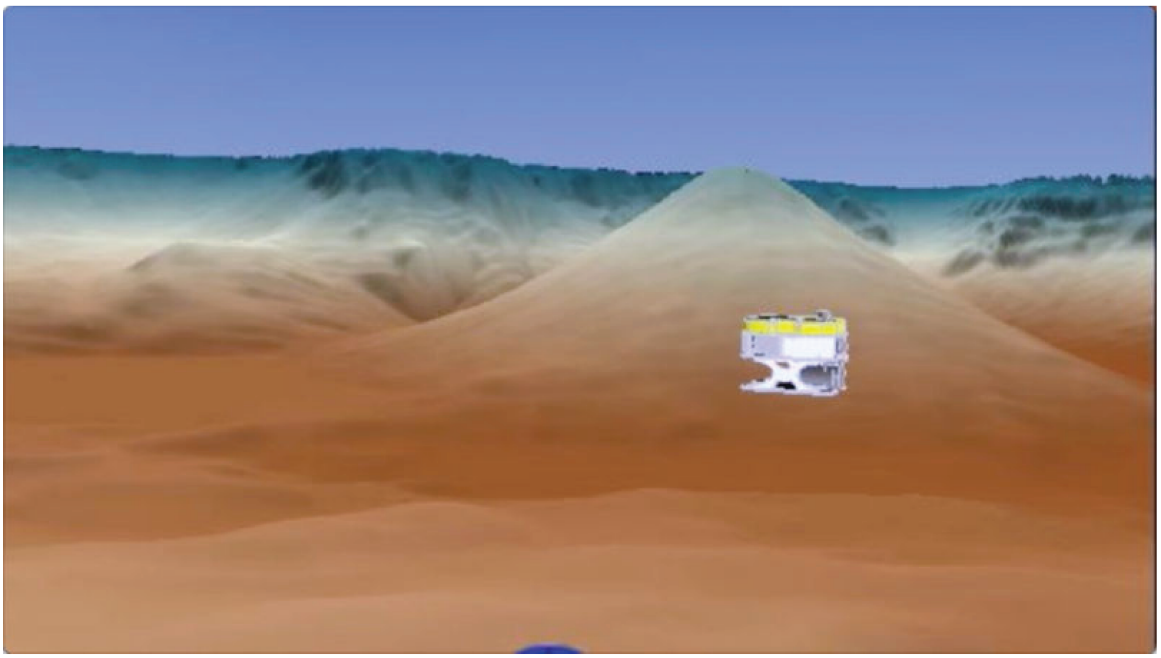

Figure 6-20: The 3D virtual dynamic and hydrodynamic simulation environment of the *CISCREA* AUV. The bathymetry data come from online sonar scan of a volcano.

6.5 Conclusion

In this chapter, a fully numerical improved applicable H_∞ control approach is proposed for the *CISCREA* AUV heading control and the other AUV control applications

in real sea environment. Only one magnetic compass is used as the feedback sensor for the *CISCREA* AUV heading control application.

The principles of the proposed improved H_∞ control approach are:

- A model based H_∞ controller handles the AUV dynamic nonlinearity and uncertainty issues with the aid of numerical CFD modeling prediction and the robust control design.

- Kalman filter estimates unmeasured yaw angular velocity $\dot{x}_r$ in order to provide nonlinear quadratic damping compensation input information. Meanwhile, the noisy magnetic compass yaw angle x_r measurement is efficiently filtered for control feedback. The numerical Kalman estimations avoid the need to add expensive sensors.

- A delay compensator is derived using the AUV model, which eliminates the $0.5s$ delay of the magnetic compass. Generally, excessive signal transmission delay can cause control performance decrease and even stability lost.

To validate the improved H_∞ control approach, heading control simulations, pool and sea tests are implemented for the *CISCREA* AUV. The simulations and experimental results demonstrate the adequacy of the robust ability using the proposed improved H_∞ AUV control approach in real sea environments.

In summary, the H_∞ control approach has fast response speed, and it is several times faster than the traditional PID control method. Rotating from 2 rad to 4.8 rad only needs 2$\sim$3 s (the response speed specification of the robust synthesis is 2 s). Comparing to the PID AUV heading controller, the H_∞ control approach has no overshoot, and the tracking accuracy is largely improved. Unmeasured AUV angular velocity $\dot{x}_r$ is clearly estimated by the designed Kalman filter, which provides the input information to eliminate the nonlinear quadratic damping terms. The AUV yaw angle x_r is also well filtered by the Kalman design, which provides notable noise attenuation on the magnetic compass output. Comparing to the PID control method, the H_∞ control approach is optimal, as a result, it improves the of propulsion efficiency and reduce battery power consumptions.

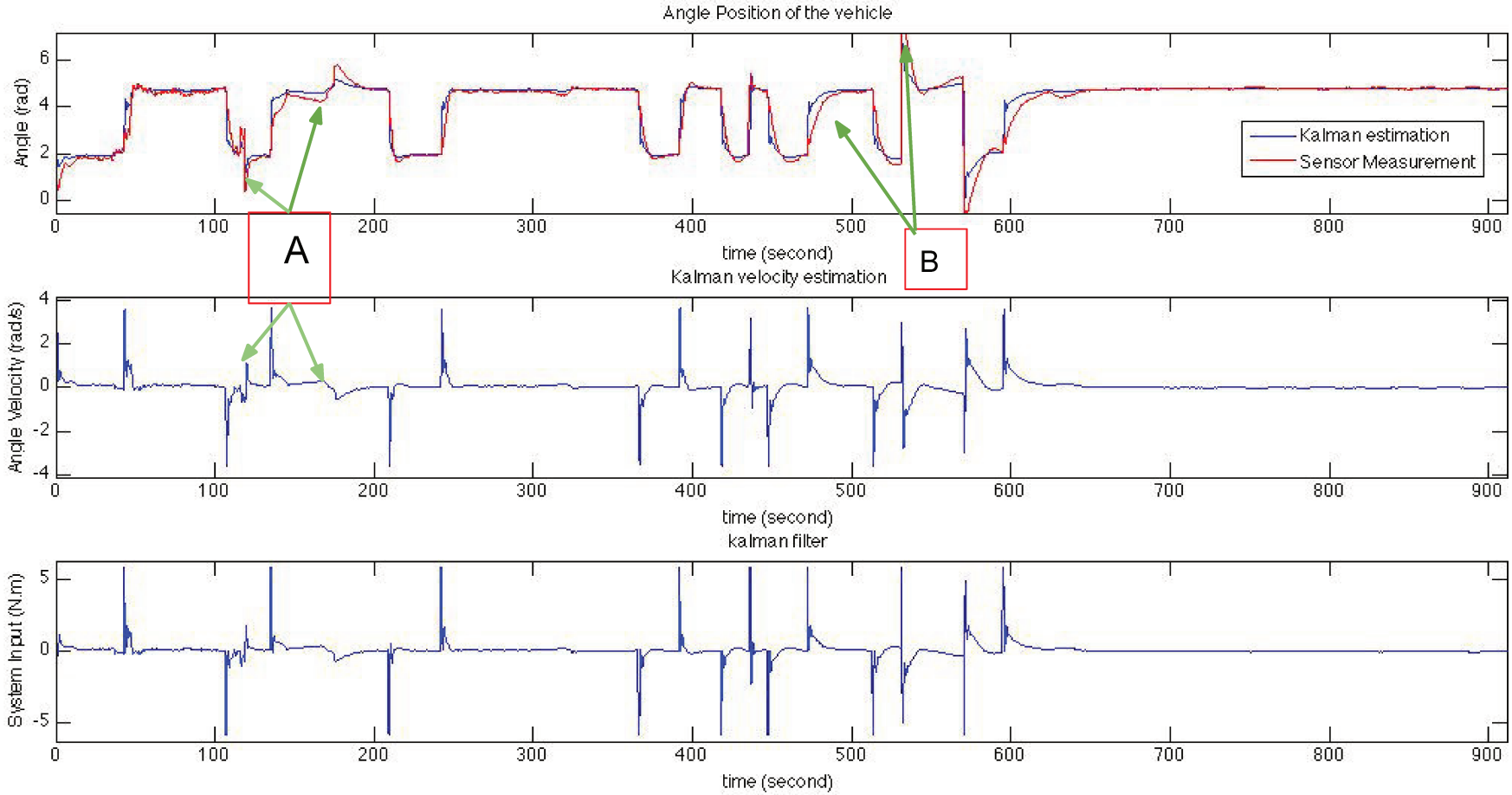

Figure 6-21: Full length experimental heading control results of the *CISCREA* AUV. The control algorithm is the proposed fully compensated H_∞ control approach, and the data was obtained in Brest harbour, France. The subplots show the yaw angle, the propulsion torques, and the yaw angular velocity $\dot{x}_r$ estimation using Kalman filter. Label A stands for the disturbances that induced by a kayak collision with the AUV. Label B denotes respectively the *CISCREA* AUV communication cable hooked by an underwater concrete structure, and at the same time, the program triggered a bug while the compass switch instantly between the maximum range and the minimum.

Part IV

General Conclusion and Perspectives

Chapter 7

General Conclusion and Perspectives

Contents

7.1 Summary of the work 186

7.2 Future Work 189

The scopes of this dissertation are the numerical AUV modeling and robust control approaches. The fundamental goal is to provide sufficient AUV robustness and control performance for the future intelligent, agile and reliable AUV or AUV group to work under the deep-sea for long periods. However, the traditional modeling methods are generally insufficient to reveal the hydrodynamic characteristics of the low mass and complex-shaped underwater vehicles. Moreover, the past AUV modeling results are not directly oriented for the robust control scheme. Generally, the underwater environment is complex, un-modeled or even unknown. AUV robustness becomes one of the key challenges for long term working AUVs in the presence of uncertainties. Due to complex and coupling AUV modeling and control issues, we address the numerical AUV dynamic modeling methods and the H_∞ robust control algorithms simultaneously. A low mass and complex-shaped *CISCREA* AUV is used to validate the proposed numerical modeling and H_∞ robust control approach in real sea test.

7.1 Summary of the work

The major contributions of the dissertation are concluded as follows:

1. After review currently available AUV modeling methods, our focus has been on the computational fluid dynamic method. The goal is to avoid implementing hydrodynamic experiments using expensive equipments. Meanwhile, sufficient modeling accuracy are necessarily required to reveal the robust control oriented AUV dynamic characteristics. For an AUV such as the *CISCREA*, the robot geometry is complex, and it becomes very difficult to identify its dynamic and hydrodynamic parameters. Therefore, we estimated the AUV models as follows:

   - Added mass matrix M_A is calculated using radiation/diffraction program WAMIT and MCC.
   - Hydrodynamic programs ANSYS-CFX and STAR-CCM+ are studied to predict damping behavior $D(|\upsilon|)$ on the surge, sway, and heave directions. Rotational damping effects are numerically built using moving reference and overset mesh techniques in STAR-CCM+.
   - Mass inertia matrix M_{RB} and the center of gravity CG are approximated using CAD program PRO/E.

   Based on these numerical estimations, a four degree-of-freedoms model is derived for the *CISCREA* AUV, which provides the foundations for the hydrodynamic experiment and control design simulations. WAMIT and MCC results show that the mass and inertia elements of the added mass matrix M_A are even larger than those in the mass inertia matrix M_{RB}. Therefore, the added mass matrix M_A is an inevitable hydrodynamic effects for the control design. The analysis of the *CISCREA* AUV damping matrix $D(|\upsilon|)$ shows that the quadratic damping components dominates the damping effects, and the linear damping component is negligible. Numerical results confirm the prediction of *Morison* equation, that the quadratic damping is the major nonlinearity in the underwater vehicle dynamics.

2. A 4 DOFs (Surge, Sway, Heave, and Yaw) experiment is designed to validate the CFD models and its hydrodynamic parameters. The numerical AUV modeling method is concluded efficient for the complex-shaped underwater vehicles (Using robust control scheme). The hydrodynamic experiment confirms the damping effect is nonlinear, and it is mainly caused by the quadratic damping. This nonlinear damping issue is essential and critical for the further control design.

3. A model based nonlinear compensated H_∞ control approach is proposed for the *CISCREA* AUV and others to solve the following issues:

   - Dynamic and hydrodynamic parametric uncertainties.
   - External disturbance from the ocean environment and sensor noise.
   - Nonlinear damping compensation errors.

   In general, the nonlinear damping and parametric uncertainty issues are the two critical problems that solved in the proposed approach. In the proposed approach, the thruster compensates the nonlinear quadratic damping behavior by calculating its propulsion value using equation 5.45 and the AUV angular velocity $\dot{x}_r$. From the controller perspective, the compensated AUV controlled-plant is a first order linear system with minor uncertainties. Finally, the parametric uncertainty issues can be conveniently solved by essential H_∞ controllers. The following conclusion can be draw after the heading control simulations:

   - The theoretical compensated H_∞ control approach is robust stable. It eliminates the control overshoot with the aid of CFD model based nonlinear compensation. The controller has good robust ability to handle the 30% inetria variations.
   - The proposed H_∞ control approach has the fast response speed, and it is generally several times faster than the PID controller.
   - The control commands of the proposed H_∞ approach is optimal, which can extend the propeller lifespan and reduce battery consumptions.

- H_∞ approach can achieve accurate tracking performance, for example, the *CISCREA* AUV heading control tracking errors is less than 1%.
- The proposed H_∞ approach is insensitive to the hydrodynamic estimation errors, such as the numerical AUV parameters of WAMIT, ANSYS-CFX, and STAR-CCM+ results.

4. To solve the applicable issues in real sea AUV control applications, we proposed an improved nonlinear compensated H_∞ control scheme. The proposed approach is validated as efficient in the *CISCREA* AUV heading control simulations, pool and sea tests. The principles of the proposed improved H_∞ control approach are:

   - A model based H_∞ controller handles the AUV dynamic nonlinearity and uncertainty issues with the aid of numerical CFD modeling prediction.
   - Kalman filter estimates unmeasured yaw angular velocity $\dot{x}_r$ in order to provide information for nonlinear quadratic damping compensation. Meanwhile, the noisy magnetic compass yaw angle x_r measurement is efficiently filtered for control feedback. The numerical Kalman estimations avoid the need to add expensive sensors.
   - A delay compensator is derived using the AUV model, which eliminates the $0.5s$ delay of the magnetic compass. Generally, signal transmission delay can cause control performance decrease and even stability lost.

   In summary, the *CISCREA* AUV heading control simulation, pool and sea tests all demonstrate that:

   - Unmeasured AUV angular velocity $\dot{x}_r$ is clearly estimated by the designed Kalman filter, which provides the input information to eliminate the nonlinear quadratic damping terms. The AUV yaw angle x_r is also well filtered by the Kalman design, which provides notable noise attenuation on the magnetic compass output.

- The H_∞ control approach has fast response speed. Rotating from 2 rad to 4.8 rad only needs 2$\sim$3 s .
- Comparing to the PID AUV heading controller, the H_∞ control approach eliminates the overshoot, and the tracking accuracy is largely improved. Moreover, the H_∞ control approach is optimal, as a result, it improves the AUV lifespan and its working range.

7.2 Future Work

This dissertation is actually a beginning of further AUV modeling and robust control research. A lot of work is still needed to solid the AUV robustness fundations. Therefore, some recommendations are given as follows:

1. The principals for weighting function selection in the H_∞ control synthesis is still empirical with the AUV control applications. However, it is a critical issue that decide the robust performance of the synthesized controller. Therefore, it is urgent to create the relationship between the AUV dynamic characteristics and the weighting function selections.

2. In this dissertation, the H_∞ control approach can generate high dimensional controllers. For example, three weighting functions are chosen for the H_∞ AUV heading control applications, and it results in a high dimensional controller of 5 states. Therefore, relevant dimension reduction robust control algorithm should be considered.

3. Current H_∞ control approach generally uses either the *Riccati* equations or the LMI approach for controller synthesize. The synthesize controller are usually suboptimal, and sometimes has no solution. Therefore, the interval analysis theory (un-convex theory) can be considered to improve the synthesize results.

Part V

Appendix

Appendix A

AUV Modeling

Contents

A.1 Euler Angles 191

A.2 Quaternion 195

A.3 Dynamics Essentials 197

A.4 Six DOFs AUV Model 198

A.5 Rigid Body Coriolis Force 199

A.6 Restoring Force 200

A.7 Added Mass Expression 201

A.8 Added Mass Coriolis Expression 202

A.9 Damping coefficients 203

A.1 Euler Angles

Generally, the AUV motion or flight path in the body-fixed frame (B-frame) is described relative to an inertial reference frame (NED-frame). Therefore, the Euler angle is necessary to represent the transformation.

According to [115], a simple rotation denotes that frame A relative to B (or B-frame and NED-frame), and there exists the axis of rotation $\lambda = [\lambda_1, \lambda_2, \lambda_3]^T$ ($|\lambda| = I$, unit vector), after the rotation of angle β, the orientation of λ to A and B remains unaltered.

Let a be a vector fixed in frame A, and its representation b in frame B. Hence, the rotation can be described by equation A.1:

$$b = cos\beta a + (1 - cos\beta)\lambda\lambda^T a - sin\beta \times a \tag{A.1}$$

Consequently, the rotation from a to b can be given in equation A.2:

$$b = Ca \tag{A.2}$$

where, C can be interpreted as a rotation matrix, see equation A.3.

$$C = cos\beta I + (1 - cos\beta)\lambda\lambda^T a - sin\beta S(\lambda) \tag{A.3}$$

$S(\lambda)$ is a skew-symmetric matrix defined such that $\lambda \times a \triangleq S(\lambda)a$, that is:

$$S(\lambda) = \begin{bmatrix} 0 & -\lambda_3 & \lambda_2 \\ \lambda_3 & 0 & -\lambda_1 \\ -\lambda_2 & \lambda_1 & 0 \end{bmatrix} \tag{A.4}$$

Expanding equation A.3 yields the rotation matrix elements C_{ij} in equation A.5:

$$
\begin{aligned}
C_{11} &= (1 - cos\beta)\lambda_1^2 + cos\beta \\
C_{22} &= (1 - cos\beta)\lambda_2^2 + cos\beta \\
C_{33} &= (1 - cos\beta)\lambda_3^2 + cos\beta \\
C_{12} &= (1 - cos\beta)\lambda_1\lambda_2 + \lambda_3 sin\beta \\
C_{21} &= (1 - cos\beta)\lambda_2\lambda_1 + \lambda_3 sin\beta \\
C_{23} &= (1 - cos\beta)\lambda_2\lambda_3 + \lambda_1 sin\beta \\
C_{32} &= (1 - cos\beta)\lambda_3\lambda_2 + \lambda_1 sin\beta \\
C_{31} &= (1 - cos\beta)\lambda_3\lambda_1 + \lambda_2 sin\beta \\
C_{13} &= (1 - cos\beta)\lambda_1\lambda_3 + \lambda_2 sin\beta
\end{aligned}
\tag{A.5}
$$

By setting $\lambda = [1, 0, 0]^T$, $\lambda = [0, 1, 0]^T$, $\lambda = [0, 0, 1]^T$, we can obtain the principal rotation matrix around the three axis x, y, z. The rotation angles are defined as ϕ, θ, ψ (Euler angle $\Theta = [\phi, \theta, \psi]^T$). The principal rotation around x axis is given in equation A.6:

$$
C_{x,\phi} = \begin{bmatrix} 1 & 0 & 0 \\ 0 & cos(\phi) & sin(\phi) \\ 0 & -sin(\phi) & cos(\phi) \end{bmatrix} \tag{A.6}
$$

around y axis in equation A.7:

$$
C_{y,\phi} = \begin{bmatrix} cos(\theta) & 0 & -sin(\theta) \\ 0 & 1 & 0 \\ sin(\theta) & 0 & cos(\theta) \end{bmatrix} \tag{A.7}
$$

around z axis in equation A.8:

$$
C_{z,\phi} = \begin{bmatrix} cos(\psi) & sin(\psi) & 0 \\ -sin(\psi) & cos(\psi) & 0 \\ 0 & 0 & 1 \end{bmatrix} \tag{A.8}
$$

Generally the linear velocity transformation $R(\Theta)$ is described by three rotations. Note that, the order in which these rotation is carried out is not arbitrary. It is common to use the xyz-convention specified in terms of Euler angles for the rotation. The rotation sequence is written in equation A.9 and A.10:

$$R(\Theta) = C_{z,\phi}^T C_{y,\phi}^T C_{x,\phi}^T \tag{A.9}$$

$$R^{-1}(\Theta) = C_{x,\phi}^T C_{y,\phi}^T C_{z,\phi}^T \tag{A.10}$$

The B-fixed angular velocity vector $\upsilon_2 = [p, q, r]^T$ and the Euler rate vector $\dot{\Theta} = [\dot{\phi}, \dot{\theta}, \dot{\psi}]$, are related through a transformation matrix $T(\Theta)$ according to equation A.11:

$$\upsilon_2 = T^{-1}(\Theta)\dot{\Theta} \tag{A.11}$$

$T(\Theta)$ is written in equation A.12:

$$T_\Theta^{-1} = \begin{bmatrix} 1 & 0 & 0 \\ 0 & 0 & 0 \\ 0 & 0 & 0 \end{bmatrix} + C_{x,\phi} \begin{bmatrix} 0 & 0 & 0 \\ 0 & 1 & 0 \\ 0 & 0 & 0 \end{bmatrix} + C_{x,\phi} C_{y,\theta} \begin{bmatrix} 0 & 0 & 0 \\ 0 & 0 & 0 \\ 0 & 0 & 1 \end{bmatrix} \tag{A.12}$$

Summarizing the Euler angle results, the kinematic equations can be expressed in vector form in equation A.13:

$$\upsilon = J(\Theta)\dot{\eta} = \begin{bmatrix} R(\Theta) & 0_{3\times3} \\ 0_{3\times3} & T(\Theta) \end{bmatrix} \dot{\eta} \tag{A.13}$$

Note that, as the $T(\Theta)$ matrix has the element of $\frac{1}{cos(\theta)}$, therefore, the singularity issue is encountered when $\theta = \pm 90°$. To solve this issue the Quaternion representation can be used.

A.2 Quaternion

An alternative to the Euler angle representation is a four-parameter method based on unit quaternions. The Quaternion representation do not has the singularity issue.

A quaternion q is defined as a complex number in equation A.14:

$$q = q_1 i + q_2 j + q_3 k + q_4 \tag{A.14}$$

where, i, j, k are three orthogonal unit vectors, $q_i (i = 1, 2, 3, 4)$ are the real parameters. In fact, a quaternion q can be seen as the linear combination of a scalar q_4 and a vector $q_0 = [q_1, q_2, q_3]^T$:

$$q = q_0 + q_4 \tag{A.15}$$

The Euler parameters or unit quaternions are defined as:

$$\begin{aligned} \epsilon = [\epsilon_1, \epsilon_2, \epsilon_3]^T = \lambda sin\frac{\beta}{2} \\ \eta = cos\frac{\beta}{2} \end{aligned} \tag{A.16}$$

where $\lambda = [\lambda_1, \lambda_2, \lambda_3]^T$ is:

$$\lambda = \pm \frac{\epsilon}{\sqrt{\epsilon^T \epsilon_1}} \quad \sqrt{\epsilon^T \epsilon_1} \neq 0 \tag{A.17}$$

Consequently, the Euler parameters can be expressed in the form:

$$e = \begin{bmatrix} \epsilon_1 \\ \epsilon_2 \\ \epsilon_3 \\ \eta \end{bmatrix} = \begin{bmatrix} \lambda sin\frac{\beta}{2} \\ cos\frac{\beta}{2} \end{bmatrix} \quad 0 \leqslant \beta \leqslant 2\pi \tag{A.18}$$

From A.18, A.16 and A.3, we obtain the following coordinate transformation matrix

for the Euler parameters:

$$C = (\eta^2 - \epsilon^T\epsilon)I + 2\epsilon\epsilon^T - 2\eta S(\epsilon)\eta = cos\frac{\beta}{2} \tag{A.19}$$

The transformation $E_1^{-1}(e) = E_1^T(e)$ relating the linear velocity vector in the NED-frame to the velocity in the B-frame can be expressed as equation A.20 and A.21:

$$\dot{\eta} = E_1(e)\upsilon_1 \tag{A.20}$$

$$E_1(e) = \begin{bmatrix} 1-2(\epsilon_2^2+\epsilon_3^2) & 2(\epsilon_1\epsilon_2-\epsilon_3\eta) & 2(\epsilon_1\epsilon_3+\epsilon_2\eta) \\ 2(\epsilon_1\epsilon_2+\epsilon_3\eta) & 1-2(\epsilon_1^2+\epsilon_3^2) & 2(\epsilon_2\epsilon_3-\epsilon_1\eta) \\ 2(\epsilon_1\epsilon_3-\epsilon_2\eta) & 2(\epsilon_2\epsilon_3+\epsilon_1\eta) & 1-2(\epsilon_1^2+\epsilon_2^2) \end{bmatrix} \tag{A.21}$$

The angular velocity kansformation can be derived in equation A.22 and A.23

$$\dot{e} = E_2(e)\upsilon_2 \tag{A.22}$$

$$E_2(e) = \frac{1}{2}\begin{bmatrix} \eta & -\epsilon_3 & \epsilon_2 \\ \epsilon_3 & \eta & -\epsilon_1 \\ -\epsilon_2 & \epsilon_1 & \eta \\ -\epsilon_1 & -\epsilon_2 & -\epsilon_3 \end{bmatrix} \tag{A.23}$$

Consequently, the kinematic equations of motion can be expressed as:

$$\dot{\eta}_E = \begin{bmatrix} \dot{\eta}_1 \\ \dot{e} \end{bmatrix} = E(\eta_E)\upsilon = \begin{bmatrix} E_1(e) & 0_{3\times3} \\ 0_{3\times3} & E_2(e) \end{bmatrix}\begin{bmatrix} \upsilon_1 \\ \upsilon_2 \end{bmatrix} \tag{A.24}$$

A.3 Dynamics Essentials

All the AUV dynamics follows the Newton's Second Law which relates mass m, acceleration $\dot{v}_c$ and force f_c, see equation A.25:

$$m\dot{v}_C = f_C \tag{A.25}$$

Meanwhile, Euler's First and Second Axioms, respectively describes the conservation of both linear P_C and angular momentum h_C.

$$\begin{aligned} \dot{p}_C &\triangleq f_C \qquad p_C \triangleq mv_C \\ \dot{h}_C &\triangleq m_C \qquad h_C \triangleq I_C\omega \end{aligned} \tag{A.26}$$

It will be assumed that the mass is constant in time ($\dot{m} = 0$). For a rigid body satisfying this the distance from the origin O of the body-fixed coordinate system to the vehicle's center of gravity can be defined as [115]:

$$r_G = \frac{1}{m}\int r\rho_A dV \tag{A.27}$$

AUV motion can be respectively described as translational motion and rotational motion. The translational motion of a marine vehicle is described as equation A.28:

$$m(\dot{v}_0 + \omega \times v_0 + \dot{\omega} \times r_G + \omega \times (\omega \times r_G)) = f_0 \tag{A.28}$$

where, ω is the angular velocity vector, v_0 is the velocity vector in B-frame. If the origin of the B-frame is chosen to coincide with the AUV center of gravity CG, we have $r_G = 0$. Hence, equation A.28 with $f_0 = f_C$, $v_0 = v_C$ yields equation A.29:

$$m(\dot{v}_C + \omega \times v_C) = f_C \tag{A.29}$$

Here, v_C is defined according to CG, and the mass is $m = \int_V \rho_A dV$. Rotational

motion has the similar representation in equation A.30:

$$I_0\dot{\omega} + \omega \times (I_0\omega) + mr_G \times (\dot{v}_0 + \omega \times v_0) = m_0 \tag{A.30}$$

where, m_0 is the input torque, I_0 is the inertia tensor in B-frame, and defined as follows (equation A.31 $\sim$ A.34):

$$I_0\omega = \int_V r \times (\omega \times r)\rho_A dV \tag{A.31}$$

$$I_x = \int_V (y^2 + z^2)\rho_A dV \qquad I_{xy} = \int_V xy\rho_A dV = \int_V yx\rho_A dV = I_{yx} \tag{A.32}$$

$$I_y = \int_V (x^2 + z^2)\rho_A dV \qquad I_{xz} = \int_V xz\rho_A dV = \int_V zx\rho_A dV = I_{zx} \tag{A.33}$$

$$I_z = \int_V (y^2 + z^2)\rho_A dV \qquad I_{yz} = \int_V yz\rho_A dV = \int_V zy\rho_A dV = I_{zy} \tag{A.34}$$

If the origin of the B-frame coincide with AUV center of gravity CG, equation A.30 is simplified as equation A.31:

$$I_C\dot{\omega} + \omega \times (I_C\omega) = m_C \tag{A.35}$$

A.4 Six DOFs AUV Model

The nonlinear equations of the translational and rotational motion are given in equation A.36 $\sim$ A.42:

$$m[\dot{u} - vr + wq - x_G(q^2 + r^2) + y_G(pq - \dot{r}) + z_G(pr + \dot{q})] = X \tag{A.36}$$

$$m[\dot{v} - wp + ur - y_G(r^2 + p^2) + z_G(qr - \dot{p}) + x_G(qp + \dot{r})] = Y \tag{A.37}$$

$$m[\dot{w} - uq + vp - z_G(p^2 + q^2) + x_G(rp - \dot{q}) + y_G(rq + \dot{p})] = Z \tag{A.38}$$

$$\begin{aligned} I_x\dot{p} + (I_z - I_y)qr - (\dot{r} + pq)I_{xz} + (r^2 - q^2)I_{yz} + (pr - \dot{q})I_{xy} \\ + m[y_G(\dot{w} - uq + vp) - z_G(\dot{v} - wp + ur)] = K \end{aligned} \tag{A.39}$$

$$\begin{aligned} I_y\dot{q} + (I_x - I_z)rp - (\dot{p} + qr)I_{xy} + (p^2 - r^2)I_{zx} + (qp - \dot{r})I_{yz} \\ + m[z_G(\dot{u} - vr + wq) - x_G(\dot{w} - uq + vp)] = M \end{aligned} \tag{A.40}$$

$$\begin{aligned} I_z\dot{r} + (I_y - I_x)pq - (\dot{q} + rp)I_{yz} + (q^2 - p^2)I_{xy} + (rq - \dot{p})I_{zx} \\ + m[x_G(\dot{v} - wp + ur) - y_G(\dot{u} - vr + wq)] = N \end{aligned} \tag{A.41}$$

The three first equations represent the translational motion while the three last equations represent the rotational motion.

A.5 Rigid Body Coriolis Force

For a rigid-body moving through an ideal fluid the hydrodynamic Coriolis and centripetal matrix $C_{RB}(\upsilon)$ can always be parameterized such that $C_{RB}(\upsilon)$ is skew-symmetrical [115], that is:

$$C_{RB}(\upsilon) \triangleq \begin{bmatrix} 0 & 0 & 0 \\ 0 & 0 & 0 \\ 0 & 0 & 0 \\ -m(y_G q + z_G r) & m(y_G p + w) & m(z_G p - v) \\ -m(x_G p - w) & -m(z_G r + x_G p) & m(z_G q + u) \\ m(x_G r + v) & m(y_G r - u) & -m(x_G p + y_G q) \end{bmatrix} \begin{bmatrix} m(y_G q + z_G r) & -m(x_G q - w) & -m(x_G r + v) \\ -m(y_G p + w) & m(z_G r + x_G p) & -m(y_G r - u) \\ -m(z_G p - v) & -m(z_G q + u) & m(x_G p + y_G q) \\ 0 & -I_{yz} q - I_{xz} p + I_z r & I_{yz} r + I_{xy} p - I_y q \\ I_{yz} q + I_{xz} p - I_z r & 0 & -I_{xz} r - I_{yz} q + I_x p \\ -I_{yz} r - I_{xy} p + I_y q & I_{xz} r + I_{xy} q - I_x p & 0 \end{bmatrix} \tag{A.42}$$

A.6 Restoring Force

The Euler angle representation of the hydrostatic forces and moments is given in equation A.43 (neutrally buoyant underwater vehicle):

$$g(\eta) = \begin{bmatrix} 0 \\ 0 \\ 0 \\ -BG_y W cos(\theta) cos(\phi) + BG_z W cos(\theta) sin(\phi) \\ -BG_z W sin(\theta) + BG_x W cos(\theta) sin(\phi) \\ -BG_x W cos(\theta) sin(\phi) - BG_y W sin(\theta) \end{bmatrix} \tag{A.43}$$

A.7 Added Mass Expression

The following equations A.44 $\sim$ A.48 shows the added mass terms (*Imlay* 1961) [115]:

$$\begin{aligned} X_A = X_{\dot{u}}\dot{u}+X_{\dot{w}}(\dot{w}+uq)+X_{\dot{q}}\dot{q}+Z_{\dot{w}}wq+Z_{\dot{q}}q^2+X_{\dot{v}}\dot{v}+X_{\dot{p}}\dot{p}+X_{\dot{r}}\dot{r}- \\ Y_{\dot{v}}\dot{v}r-Y_{\dot{p}}rp-Y_{\dot{r}}r^2-X_{\dot{v}}ur-Y_{\dot{w}}wr+Y_{\dot{w}}vq+Z_{\dot{p}}pq- \\ (Y_{\dot{q}}-Z_{\dot{r}})qr \end{aligned} \tag{A.44}$$

$$\begin{aligned} Y_A = X_{\dot{v}}\dot{u}+Y_{\dot{w}}\dot{w}+Y_{\dot{q}}\dot{q}+Y_{\dot{v}}\dot{v}+Y_{\dot{p}}\dot{p}+Y_{\dot{r}}\dot{r}+X_{\dot{v}}vr-Y_{\dot{w}}vp+X_{\dot{r}}r^2+ \\ (X_{\dot{p}}-Z_{\dot{r}})rp-Z_{\dot{p}}p^2-X_{\dot{w}}(up-wr)+X_{\dot{u}}ur-Z_{\dot{w}}wp- \\ Z_{\dot{q}}pq+X_{\dot{q}}qr \end{aligned} \tag{A.45}$$

$$\begin{aligned} Z_A = X_{\dot{w}}(\dot{u}-wq)+Z_{\dot{w}}\dot{w}+Z_{\dot{q}}\dot{q}-X_{\dot{u}}uq-X_{\dot{q}}q^2+Y_{\dot{w}}\dot{v}+Z_{\dot{p}}\dot{p}+Z_{\dot{r}}\dot{r}+ \\ Y_{\dot{v}}vp+Y_{\dot{r}}rp+Y_{\dot{p}}p^2+X_{\dot{v}}up+Y_{\dot{w}}wp-X_{\dot{v}}vq- \\ (X_{\dot{p}}-Y_{\dot{q}})pq-X_{\dot{r}}qr \end{aligned} \tag{A.46}$$

$$\begin{aligned} K_A = X_{\dot{p}}\dot{u}+Z_{\dot{p}}\dot{w}+K_{\dot{q}}\dot{q}-X_{\dot{v}}wu+X_{\dot{r}}uq-Y_{\dot{w}}w^2-(Y_{\dot{q}}-Z_{\dot{r}})wq+ \\ M_{\dot{r}}q^2+Y_{\dot{p}}v+K_{\dot{p}}\dot{p}+K_{\dot{r}}\dot{r}+Y_{\dot{w}}v^2-(Y_{\dot{q}}-Z_{\dot{r}})vr+ \\ Z_{\dot{p}}vp-M_{\dot{r}}r^2-K_{\dot{q}}rp+X_{\dot{w}}uv-(Y_{\dot{v}}-Z_{\dot{w}})vw- \\ (Y_{\dot{r}}+Z_{\dot{q}})wr-Y_{\dot{p}}wp-X_{\dot{q}}ur+(Y_{\dot{r}}+Z_{\dot{q}})vq+ \\ K_{\dot{r}}pq-(M_{\dot{q}}-N_{\dot{r}})qr \end{aligned} \tag{A.47}$$

$$
\begin{aligned}
M_A = {} & X_{\dot{q}}(\dot{u} + wq) + Z_{\dot{q}}(\dot{w} - uq) + M_{\dot{q}}\dot{q} - X_{\dot{w}}(u^2 - w^2) \\
& - (Z_{\dot{w}} - X_{\dot{u}})wu + Y_{\dot{q}}\dot{v} + K_{\dot{q}}\dot{p} + M_{\dot{r}}\dot{r} + Y_{\dot{p}}vr - Y_{\dot{r}}vp \\
& - K_{\dot{r}}(p^2 - r^2) + (K_{\dot{p}} - N_{\dot{r}})rp - Y_{\dot{w}}uv + X_{\dot{v}}vw \\
& - (X_{\dot{r}} + Z_{\dot{p}})(up - wr) + (X_{\dot{p}} - Z_{\dot{r}})(wp + ur) \\
& - M_{\dot{r}}pq + K_{\dot{q}}qr
\end{aligned}
\tag{A.48}
$$

$$
\begin{aligned}
N_A = {} & X_{\dot{r}}\dot{u} + Z_{\dot{r}}\dot{w} + M_{\dot{r}}\dot{q} + X_{\dot{v}}u^2 + Y_{\dot{w}}wu - (X_{\dot{p}} - Y_{\dot{q}})uq - Z_{\dot{p}}wq \\
& - K_{\dot{q}}q^2 + Y_{\dot{r}}\dot{v} + K_{\dot{r}}\dot{p} + N_{\dot{r}}\dot{r} - X_{\dot{v}}v^2 - X_{\dot{r}}vr \\
& - (X_{\dot{p}} - Y_{\dot{q}})vp + M_{\dot{r}}rp + K_{\dot{q}}p^2 - (X_{\dot{u}} - Y_{\dot{v}})uv - X_{\dot{w}}vw \\
& + (X_{\dot{q}} + Y_{\dot{p}})up + Y_{\dot{r}}ur + Z_{\dot{q}}wp - (X_{\dot{q}} + Y_{\dot{p}})vp \\
& - (K_{\dot{p}} - M_{\dot{q}})pq - K_{\dot{r}}qr
\end{aligned}
\tag{A.49}
$$

A.8 Added Mass Coriolis Expression

For a rigid-body moving through an ideal fluid the added mass hydrodynamic Coriolis and centripetal matrix $C_A(\upsilon)$ can always be parameterized such that $C_A(\upsilon)$ is skew-symmetrical, that is:

$$
C_A(\upsilon) = \begin{bmatrix}
0 & 0 & 0 & 0 & -a_3 & a_2 \\
0 & 0 & 0 & a_3 & 0 & -a_1 \\
0 & 0 & 0 & -a_2 & a_1 & 0 \\
0 & -a_3 & a_2 & 0 & -b_3 & b_2 \\
a_3 & 0 & -a_1 & b_3 & 0 & -b_1 \\
-a_2 & a_1 & 0 & -b_2 & b_1 & 0
\end{bmatrix}
\tag{A.50}
$$

where,

$$\begin{aligned}
a_1 =& X_{\dot{u}}u + X_{\dot{v}}v + X_{\dot{w}}w + X_{\dot{p}}p + X_{\dot{q}}q + X_{\dot{r}}r \\
a_2 =& X_{\dot{v}}u + Y_{\dot{v}}v + Y_{\dot{w}}w + Y_{\dot{p}}p + Y_{\dot{q}}q + Y_{\dot{r}}r \\
a_3 =& X_{\dot{w}}u + Y_{\dot{w}}v + Z_{\dot{w}}w + Z_{\dot{p}}p + Z_{\dot{q}}q + Z_{\dot{r}}r \\
b_1 =& X_{\dot{p}}u + Y_{\dot{p}}v + Z_{\dot{p}}w + K_{\dot{p}}p + K_{\dot{q}}q + K_{\dot{r}}r \\
b_2 =& X_{\dot{q}}u + Y_{\dot{q}}v + Z_{\dot{q}}w + K_{\dot{q}}p + M_{\dot{q}}q + M_{\dot{r}}r \\
b_3 =& X_{\dot{r}}u + Y_{\dot{r}}v + Z_{\dot{r}}w + K_{\dot{r}}p + M_{\dot{r}}q + N_{\dot{r}}r
\end{aligned} \tag{A.51}$$

A.9 Damping coefficients

The damping coefficient diagram of sphere and cylinder drag test are given in figure A-1 (*Polezhaev*'s experimental work).

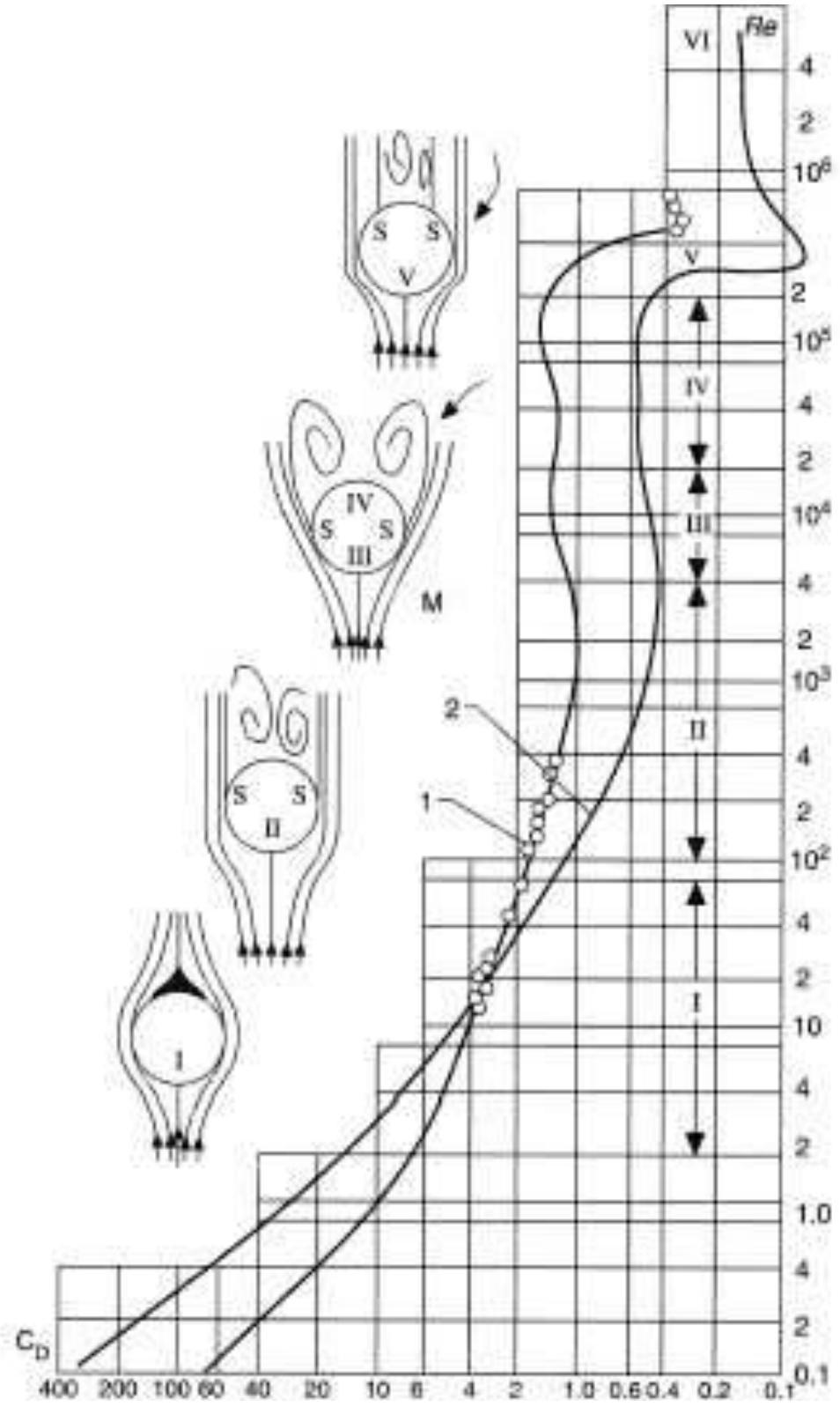

Figure A-1: The damping coefficient Cd of Cylinder and Sphere under different Reynold number Re scenarios

Appendix B

Parameter Identification

Contents

B.1 PRO/E Report of *CISCREA* AUV 205

B.2 CISCREA WAMIT Configuration and Output 209

B.1 PRO/E Report of *CISCREA* AUV

The rigid body mass matrix M_{RB} and the vehicle center of gravity CG are estimated by the PRO/E software, its estimation results are given as follows:

```
1
2  VOLUME = 1.7593886e+07 MM^3
3  SURFACE AREA = 2.4735707e+06 MM^2
4  AVERAGE DENSITY = 8.8913622e-04 GRAM / MM^3
5  MASS = 1.5643361e+04 GRAM
6
7  CENTER OF GRAVITY with respect to ORINGIN_NORM coordinate frame:
8  X Y Z 3.1029524e+01 -2.8276873e-02 -6.9961429e+00 MM
9
10 INERTIA with respect to ORINGIN_NORM coordinate frame: (GRAM * MM^2)
11
```

```
12 INERTIA TENSOR:
13 Ixx Ixy Ixz 2.4803007e+08 2.1257730e+04 -4.3343827e+05
14 Iyx Iyy Iyz 2.1257730e+04 3.8562086e+08 1.7392295e+04
15 Izx Izy Izz -4.3343827e+05 1.7392295e+04 3.7283113e+08
16
17 INERTIA at CENTER OF GRAVITY with respect to ORINGIN_NORM coordinate
       frame:   (GRAM * MM^2)
18
19 INERTIA TENSOR:
20 Ixx Ixy Ixz 2.4726438e+08 3.4983495e+04 2.9625318e+06
21 Iyx Iyy Iyz 3.4983495e+04 3.6979326e+08 2.0487006e+04
22 Izx Izy Izz 2.9625318e+06 2.0487006e+04 3.5776920e+08
23
24 PRINCIPAL MOMENTS OF INERTIA: (GRAM * MM^2)
25 I1   I2   I3   2.4718500e+08  3.5784853e+08  3.6979330e+08
26
27 ROTATION MATRIX from ORINGIN_NORM orientation to PRINCIPAL AXES:
28
29 0.99964 0.02678 -0.00033
30 -0.00028 -0.00179 -1.00000
31 -0.02678 0.99964 -0.00178
32
33
34 ROTATION ANGLES from ORINGIN_NORM orientation to PRINCIPAL AXES (
       degrees):
35 angles about x y z  90.102  0.000   -1.535
36
37 RADII OF GYRATION with respect to PRINCIPAL AXES:
38 R1  R2  R3   1.2570311e+02    1.5124624e+02   1.5374977e+02  MM
39
40 ------------------------------------------------
41
42 MASS PROPERTIES OF COMPONENTS OF THE ASSEMBLY
43 (in assembly units and the ORINGIN_NORM coordinate frame)
44 DENSITY MASS C.G.: X  Y  Z
45 VOLUME = 1.7593886e+07 MM^3
```

```
SURFACE AREA = 2.4735707e+06 MM^2
AVERAGE DENSITY = 8.8913622e-04 GRAM / MM^3
MASS = 1.5643361e+04 GRAM

CENTER OF GRAVITY with respect to ORINGIN_NORM coordinate frame:
X Y Z 3.1029524e+01 -2.8276873e-02 -6.9961429e+00 MM

INERTIA with respect to ORINGIN_NORM coordinate frame: (GRAM * MM^2)

INERTIA TENSOR:
Ixx Ixy Ixz  2.4803007e+08 2.1257730e+04 -4.3343827e+05
Iyx Iyy Iyz  2.1257730e+04 3.8562086e+08 1.7392295e+04
Izx Izy Izz  -4.3343827e+05 1.7392295e+04 3.7283113e+08

INERTIA at CENTER OF GRAVITY with respect to ORINGIN_NORM coordinate
    frame:  (GRAM * MM^2)

INERTIA TENSOR:
Ixx Ixy Ixz  2.4726438e+08 ă3.4983495e+04 ă2.9625318e+06
Iyx Iyy Iyz  3.4983495e+04 ă3.6979326e+08 ă2.0487006e+04
Izx Izy Izz  2.9625318e+06 ă2.0487006e+04 ă3.5776920e+08

PRINCIPAL MOMENTS OF INERTIA: ă(GRAM * MM^2)
I1  I2  I3   2.4718500e+08   3.5784853e+08   3.6979330e+08

ROTATION MATRIX from ORINGIN_NORM orientation to PRINCIPAL AXES:
        0.99964   0.02678   -0.00033
        -0.00028   -0.00179   -1.00000
        -0.02678   0.99964   -0.00178

ROTATION ANGLES from ORINGIN_NORM orientation to PRINCIPAL AXES (
    degrees):
angles about  x  y  z   90.102   0.000   -1.535

RADII OF GYRATION with respect to PRINCIPAL AXES:
R1   R2   R3  1.2570311e+02  1.5124624e+02  1.5374977e+02  MM
```

```
80
81 ------------------------------------------------
82
83 MASS PROPERTIES OF COMPONENTS OF THE ASSEMBLY
84 (in assembly units and the ORINGIN_NORM coordinate frame)
85
86 DENSITY MASS C.G.:   X   Y   Z
87
88 BATTERYFINI
89 1.79967e-03  3.63499e+03 -3.71642e+01 -2.58660e-02 -5.34932e+01
90 TUBE
91 6.08005e-04  2.48000e+03 -3.75000e+01 -3.33779e-03 ă2.07051e+00
92 TOPCASE
93 8.97370e-04  7.87744e+02 -3.77574e+01 -8.95838e-02 ă1.14168e+02
94 BOXFINI
95 1.02974e-03  3.42999e+03 -3.24817e+01 -6.65864e-02 ă8.94431e+01
96 LEDFINI
97 3.66046e-03  4.60000e+02 ă1.76496e+02 -3.73462e-01 -6.30027e+01
98 LOAD
99 1.00000e-10   2.40277e-04 ă1.37115e+02 ă0.00000e+00 -1.40000e+02
100 MIDCASEFINI
101 8.97370e-04  2.62059e+03 -4.34468e+01 ă6.12507e-02 ă1.22148e+01
102 LOWCASEFINI
103 8.97370e-04  1.63005e+03 -3.75311e+01 -1.07202e-02 -2.00591e+02
104 MOTOCORDIFINI
105 2.83108e-02  1.00000e+02 ă1.61137e+02 -9.94919e+01 ă0.00000e+00
106 MOTOCORDIFINI
107 2.83108e-02  1.00000e+02 -2.35707e+02 -9.97912e+01 ă0.00000e+00
108 MOTOCORDIFINI
109 2.83108e-02  1.00000e+02 ă1.61050e+02 ă9.94291e+01 ă0.00000e+00
110 MOTOCORDIFINI
111 2.83108e-02  1.00000e+02 -2.35623e+02 ă9.97306e+01 ă0.00000e+00
112 MOTOCORDIFINI
113 2.83108e-02  1.00000e+02 -3.70005e+01 -1.44998e+02 ă3.54481e+01
114 MOTOCORDIFINI
115 2.83108e-02  1.00000e+02 -3.69995e+01 ă1.44998e+02 ă3.54481e+01
```

B.2 CISCREA WAMIT Configuration and Output

WAMIT program is used to estimate the added mass matrix M_A of the *CISCREA* AUV, and its configuration and output files are given as follows:

1. pot file:

```
CISCREA.POT -- CISCREA R=1, ILOWHI=0, IRR=0
-1.                          HBOT
1   -1                       IRAD,IDIFF
CISCREA.POT -- CISCREA R=1, ILOWHI=0, IRR=0
-1.                          HBOT
1   -1                       IRAD,IDIFF
```

2. frc file

```
 CISCREA.FRC  CISCREA, ILOWHI=0, IRR=0
 1   0   0   0   0   0   0   0   0
 0.000000                                          VCG
 1.000000      0.0000000      0.0000000
 .0000000      1.000000       0.0000000
 0.0000000     0.0000000      1.000000         XPRDCT
 0                                            NBETAH
 0                                            NFIELD
```

3. cfg file

```
! CISCREA.CFG -- CISCREA R=1, T=0.5, ILOWHI=0, IRR=0
 ipltdat=5
 ISOR=1        (omit ISOR in POT file, include source formulation)
 ISOLVE=0      (use iterative solver)
 ISCATT=0      (solve for total diffraction potential, not scattering)
 ILOG=1        (omit ILOG in POT file, integrate log singularity)
 IRR=0         (omit IRR in POT file, no irregular-frequency removal)
 MONITR=0      (do not write FORCE output data to monitor)
 NUMHDR=1      (write headers to numeric output files)
```

4. output file

```
 1  ------------------------------------
 2              WAMIT  Version 7.023
 3      Copyright (c) 1999-2012 WAMIT Incorporated
 4      Copyright (c) 1998 Massachusetts Institute of Technology
 5  ------------------------------------
 6      The WAMIT software performs computations of wave interactions
 7      with floating or submerged vessels.  WAMIT is a registered
 8      trademark of  WAMIT, Incorporated.  This demonstration version
 9      of WAMIT and the User Manual may be downloaded from the
10      wamit.com website as shown  below. This is a complete
11      implementation of WAMIT V7PC, which may be used with any
12      of the standard geometry inputs used for the Test Runs described
13      in the User Manual.  The other inputs may be modified by the
14      user. This version may be used only for educational purposes, or
15      for demonstration of the WAMIT software. Please refer to the
16      website for a complete statement of these conditions and for
17      further information.  Email requests for end-user licenses
18      should be sent to  <info@wamit.com>
19
20
21      <http://www.wamit.com>                 Release date: 21 Mar 2012
22
23  ------------------------------------
24
25  Low-order panel method  (ILOWHI=0)
26
27  Input from Geometric Data File:         ciscrea.gdf
28  Model 3STL Ciscrea Real Model      06-Feb-2014  01:15:32
29
30  Input from Potential Control File:      ciscrea.pot
31  ciscrea.POT -- ciscrea R=1, ILOWHI=0, IRR=0
32
33
34  POTEN run date and starting time:        26-Feb-2014  --  21:16:26
35    Period       Time           RAD      DIFF  (max iterations)
```

```
   -1.0000    21:16:36         21 (24)
   0.0000    21:16:37         21 (24)

Gravity:     9.80665               Length scale:        1.00000
Water depth:        infinite
Logarithmic singularity index:              ILOG =     1
Source formulation index:                   ISOR =     1
Diffraction/scattering formulation index: ISCATT =     0
Number of blocks used in linear system:   ISOLVE =     0
Number of unknowns in linear system:        NEQN =  1468
Irregular frequency index: IRR = 0

BODY PARAMETERS:

Total panels: 1468  Waterline panels 0 Symmetries: none
Irregular frequency index: IRR = 0

XBODY = 0.0000  YBODY = 0.0000 ZBODY = -10.0000  PHIBODY = 0.0
Volumes (VOLX,VOLY,VOLZ):  0.258101E-01 0.258100E-01 0.258088E-01
Center of Buoyancy (Xb,Yb,Zb):  -0.037376     0.000221     0.023391
Hydrostatic and gravitational restoring coefficients:
C(3,3),C(3,4),C(3,5): -0.12706E-06 -0.28522E-08 -0.61273E-08
C(4,4),C(4,5),C(4,6): 0.30990E-03  0.29859E-03   0.0000
C(5,5),C(5,6):  0.61812E-03   0.0000
Center of Gravity  (Xg,Yg,Zg):   -0.037376     0.000221     0.000000
Radii of gyration:         1.000000     0.000000     0.000000
                        0.000000     1.000000     0.000000
                        0.000000     0.000000     1.000000


 ----------------------------------------
                          Output from  WAMIT
 ----------------------------------------
FORCE run date and starting time:               26-Feb-2014 --
   21:16:37
 ----------------------------------------
```

```
 I/O Filenames:  ciscrea.frc     ciscrea.p2f    ciscrea.out
  ciscrea.FRC  , ILOWHI=0, IRR=0

**************************
 Wave period = infinite                      Wavenumber = zero
  ------------------------------------

    ADDED-MASS COEFFICIENTS
     I     J         A(I,J)

     1     1   1.171528E-02
     1     2  -8.942108E-05
     1     3  -1.029174E-04
     1     4   3.796293E-05
     1     5   3.006848E-04
     1     6   1.212778E-05
     2     1   1.458955E-04
     2     2   1.980570E-02
     2     3  -1.433134E-04
     2     4   8.338600E-05
     2     5  -1.279987E-05
     2     6  -7.411116E-04
     3     1   1.086597E-04
     3     2  -1.263564E-04
     3     3   6.563238E-02
     3     4  -3.253423E-05
     3     5   2.473420E-03
     3     6   6.278550E-05
     4     1   1.192901E-04
     4     2   3.118029E-04
     4     3  -5.490492E-05
     4     4   3.764071E-04
     4     5   2.914943E-06
     4     6  -1.116816E-05
     5     1   3.976160E-04
     5     2  -1.363751E-06
     5     3   2.486089E-03
```

```
     5      4  −2.378708E−06
     5      5   7.736886E−04
     5      6   1.648271E−06
     6      1  −2.633395E−06
     6      2  −7.410161E−04
     6      3   6.288557E−05
     6      4  −3.072417E−06
     6      5   3.585445E−06
     6      6   1.352324E−04
**********************
 Wave period = zero               Wavenumber = infinite
 ————————————————————————————————

   ADDED−MASS COEFFICIENTS
     I      J         A(I,J)

     1      1   1.171527E−02
     1      2  −8.942225E−05
     1      3  −1.029206E−04
     1      4   3.796255E−05
     1      5   3.006848E−04
     1      6   1.212765E−05
     2      1   1.458927E−04
     2      2   1.980564E−02
     2      3  −1.433154E−04
     2      4   8.338643E−05
     2      5  −1.279964E−05
     2      6  −7.411097E−04
     3      1   1.086725E−04
     3      2  −1.263412E−04
     3      3   6.563196E−02
     3      4  −3.253357E−05
     3      5   2.473410E−03
     3      6   6.278532E−05
     4      1   1.192890E−04
     4      2   3.118026E−04
     4      3  −5.490580E−05
```

```
143       4       4    3.764074E-04
144       4       5    2.914843E-06
145       4       6   -1.116817E-05
146       5       1    3.976155E-04
147       5       2   -1.363049E-06
148       5       3    2.486073E-03
149       5       4   -2.378656E-06
150       5       5    7.736896E-04
151       5       6    1.648279E-06
152       6       1   -2.633213E-06
153       6       2   -7.410133E-04
154       6       3    6.288552E-05
155       6       4   -3.072432E-06
156       6       5    3.585429E-06
157       6       6    1.352323E-04
```

Appendix C

H_∞ Control Theory Essentials

Contents

C.1 Norms 215

C.2 Linear Fractional Transformation 220

The robust control theory can be found in *Zhou*'s book [76]. Here, we selected some important conception for this dissertation.

C.1 Norms

Let vector $x = [x_1, x_2, \cdots x_n]^T \in C$, then we can define the follows vector norms in equation C.1 $\sim$ C.3:

(1) 2- norm (Euclidean distance)

$$||x||_2 = \sqrt{x^T x} = (\sum_{i=1}^{n} x_i^2)^{\frac{1}{2}} \tag{C.1}$$

(2) ∞-norm

$$||x||_\infty = \max_{1 \leqslant i \leqslant n} |x_i| \tag{C.2}$$

(3) p-norm

$$||x||_p = (\sum_{i=1}^{n} x_i^p)^{\frac{1}{p}}, \quad 1 \leqslant i \leqslant n \tag{C.3}$$

Let matrix $A = (a_{ij}) \in C^{m\times n}$, then we can define the follows matrix norms in equation C.4 $\sim$ C.6:

(1) 1-norm

$$||A||_1 = \sum_{i,j=1}^{n} |a_{ij}| \tag{C.4}$$

(2) 2-norm (Frobenius)

$$||A||_2 = (\sum_{i,j=1}^{n} |a_{ij}|^2)^{\frac{1}{2}} \tag{C.5}$$

(3) ∞-norm

$$||A||_\infty = n \max_{i,j} |a_{ij}| \tag{C.6}$$

Let $A = (a_{ij}) \in C^{m\times n}$, and $A^T A$ should has n number of eigen values λ_i, and the singular value $\delta = \sqrt{\lambda_1}$. According to the singular value decomposition lemma, there exist unitary matrices:

$$\begin{aligned} U &= [u_1, u_2, \cdots, u_m] \in C^{m\times m} \\ V &= [v_1, v_2, \cdots, v_n] \in C^{n\times n} \end{aligned} \tag{C.7}$$

such that

$$A = UDV, \quad D = \begin{bmatrix} Si & 0 \\ 0 & 0 \end{bmatrix} \tag{C.8}$$

and $D \in R_{m\times n}$ should consist of all the singular values δ_i in the descending order, see equation C.9.

$$\begin{aligned} Si &= diag(\delta_1, \delta_2, \cdots, \delta_r, \cdots) \\ \delta_1 > \delta_2 > \cdots \delta_r > \cdots, r &= minm, n \end{aligned} \tag{C.9}$$

Let matrix $A \in C^{m\times n}$, vector $x \in C^n$, and sup is supremum, inf denotes infimum,

then, we have equation C.10 and C.20 stands:

$$\sup_{||x||_2=1} ||Ax||_2 = \sup_{x\neq 0} \frac{||Ax||_2}{||x||_2} = \delta_{max}(A) \tag{C.10}$$

$$\inf_{||x||_2=1} ||Ax||_2 = \inf_{x\neq 0} \frac{||Ax||_2}{||x||_2} = \delta_{min}(A) \tag{C.11}$$

In fact, the singular values denotes the maximum or minimum gain to the vector x in its length $||x||_2$ by the matrix A, see equation C.12. Therefore, the matrix norms induced by vector p-norms are sometimes called induced p-norms.

$$\delta_{min}(A)||x||_2 \leqslant ||Ax||_2 \leqslant \delta_{max}(A)||x||_2 \tag{C.12}$$

Consider a signal $f(t), t \in R$ space instead of vector (length) and matrix (gain). The system can be seen as a mathematical operator that transform the input signal to another output space. Define the linear signal space as the set of the signals $f(t), t \in R$ that meet the homogeneous and additive property.

Then, the regular signal space are given as follows:

1) L_p space

The set of signals $f : R^+ \to R, \quad R^+ \in [0, \infty)$ that satisfied:

$$\int_0^\infty |f(t)|^p dt < \infty, \quad p \in [1, \infty) \tag{C.13}$$

2) L_∞ space

The set of signals $f : R^+ \to R, \quad R^+ \in [0, \infty)$ that satisfied:

$$\sup_{t\in R^+} |f(t)| < \infty \tag{C.14}$$

3) H_2 space

The set of signals $f : C \to C$ (analytic on the right complex surface) that

satisfied:

$$\int_{-\infty}^{\infty} f^*(j\omega)f(j\omega)d\omega < \infty \tag{C.15}$$

4) H_∞ space

The set of signals $f : C \to C$ (analytic on the right complex surface) that satisfied:

$$\sup_{\omega} |f(j\omega)| < \infty \tag{C.16}$$

Define the norm for the above signal spaces N. If exist a real number function $||f|| : N \to R$ meets the homogeneous and additive property, then it can be call the norm of correspond space N.

The L_p-norm of the L_p space is :

$$||f||_p = (\int_0^{\infty} |f(t)|^p)^{\frac{1}{p}} \tag{C.17}$$

The L_∞-norm of the L_∞ space is :

$$||f||_\infty = \sup_{t \in R^+} |f(t)| \tag{C.18}$$

The H_2-norm of the H_2 space is :

$$||f||_2 = (\frac{1}{2}\int_{-\infty}^{\infty} f^*(j\omega)f(j\omega)d\omega)^{\frac{1}{2}} \tag{C.19}$$

The H_∞-norm of the H_∞ space is :

$$||f||_\infty = \sup_{\omega} |f(j\omega)|, \quad f(t) \in H_\infty \tag{C.20}$$

Specifically, the H_∞-norm of the function $T(s)$ in the H_∞ space is :

$$||T(s)||_\infty = \sup_{\omega} |\delta_{max}|T(j\omega)|, \quad T(s) \in H_\infty \tag{C.21}$$

Consider two signal f and g in the L_2 space, then define its interior product as $\langle f|g\rangle = \int_{-\infty}^{\infty} f^T(t)g(t)dt$, and the L_2 norm is $||f||_2 = (\langle f|f\rangle)^{\frac{1}{2}}$ (the energy of the

signal f).

Consider two signal F and G in the H_2 space, then define its interior product as $\langle F|G\rangle = \int_{-\infty}^{\infty} F^T(j\omega)G(\omega)d\omega$, and the H_2 norm is $||F||_2 = (\langle F|F\rangle)^{\frac{1}{2}}$.

As the L_2 space and H_2 space is relative Laplace transform (or inverse transform) $L(\dot{})$ and $L^{-1}(\dot{})$, hence, there is:

$$\forall f(t) \in L_2^n, \quad F(s) = L(f(t)) \in H_2^n \tag{C.22}$$

$$\forall F(s) \in H_2^n, \quad f(t) = L^{-1}(f(t)) \in L_2^n \tag{C.23}$$

As a result, there is the Parseval lemma stands:

$$\begin{aligned} ||f(t)||_2 &= ||F(s)||_2 \\ \forall f(t) \in L_2^n, \quad F(s) &= L(f(t)) \in H_2^n \end{aligned} \tag{C.24}$$

Consider a control system, it transforms the input signal from input signal space Ω to the output signal space $Gamma$, and we can define the norms as equation C.25:

$$||G|| = \sup_{u\in\Omega} \frac{||GU||}{||Y||} \tag{C.25}$$

If exist the transfer matrix $G(s) \in H_\infty$, input signal $U(s) \in H_2^n$, and output signal $Y(s) \in H_2^m$, then the H_∞ norm of $G(s)$ is:

$$||G(s)||_\infty = \sup_{U\neq 0} \frac{||Y(s)||_2}{||U(s)||_2} = \sup_{\omega} \delta_{max}(G(j\omega)) \tag{C.26}$$

The H_2 norm of $G(s)$ is

$$||G(s)||_2 = \sup_{U\neq 0} \frac{||Y(s)||_2}{||U(s)||_\infty} = (\frac{1}{2\pi}\int_{-\infty}^{\infty} Tr(G^*(j\omega)G(j\omega))d\omega)^{\frac{1}{2}} \tag{C.27}$$

In short, the signal norm is the energy property, and system norm is the gain of the signals during the transform from input to output.

C.2 Linear Fractional Transformation

LFT has two types, the lower LFT in equation C.28 and upper LFT in equation C.29.

If $(I - P_{22}K)^{-1}$ exists, then the lower LFT is given as:

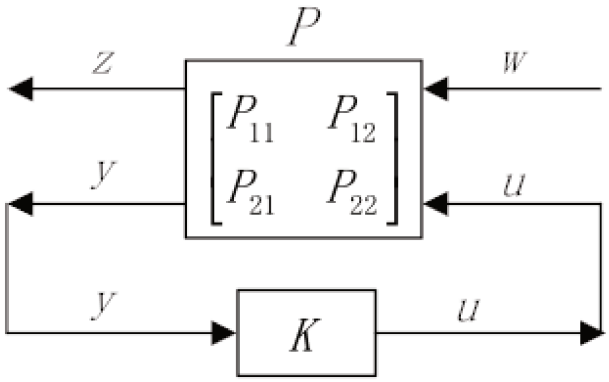

$$S(P, K) := P_{11} + P_{12}(I - P_{22}K)^{-1}P_{21} \tag{C.28}$$

If $(I - P_1\Delta)^{-1}$ exists, then the upper LFT is given as:

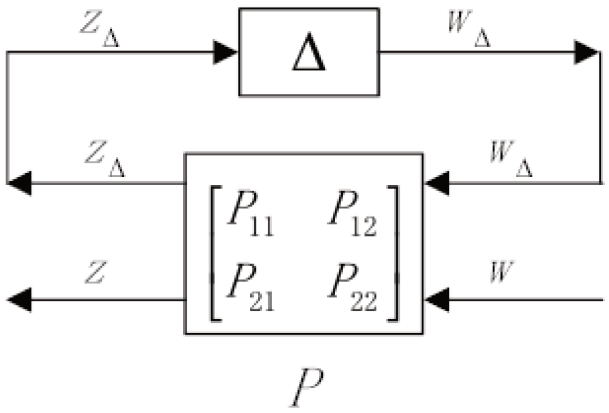

$$S(\Delta, P) := P_{22} + P_{21}\Delta(I - P_{11}\Delta)^{-1}P_{12} \tag{C.29}$$

Appendix D

Yaw Control Experiment

Contents

D.1 H_∞ Robust Control Synthesis 221

D.2 *CISCREA* AUV H_∞ Heading Controller 223

D.3 *CISCREA* AUV Control Code 224

D.1 H_∞ Robust Control Synthesis

The *CISCREA* AUV heading control H_∞ synthesis report is given as follows:

```
1
2  ----------------------------------------------------------------
3          Synthesis Hinf Controller
4  ----------------------------------------------------------------
5
6  Minimization of gamma:
7
8  Solver for linear objective minimization under LMI constraints
9
10 Iterations    :    Best objective value so far
11
```

```
     8                   13.778424
     9                    8.847459
    10                    7.144456
    11                    5.148941
    12                    5.148941
    13                    1.577334
    14                    1.577334
    15                    1.247157
    16                    1.247157
    17                    1.105779
    18                    1.105779
    19                    1.085374
    20                    1.085374
    21                    1.085374
    22                    1.076968
    23                    1.076968
    24                    1.075859
    25                    1.075859
    26                    1.075859
***                 new lower bound:     1.071807

 Result:  feasible solution of required accuracy
          best objective value:     1.075859
          guaranteed relative accuracy:  3.77e-03
          f-radius saturation:  0.980% of R =  1.00e+08

 Optimal Hinf performance:  1.074e+00


------------------------------------------------------------------------
Controller:
------------------------------------------------------------------------
system:   5 states     1 outputs     1 inputs
```

D.2 *CISCREA* AUV H_∞ Heading Controller

The continuous state space realization of the *CISCREA* AUV H_∞ heading controller is given in equation D.1 $\sim$ D.4:

$$K(s) = D_K + C_K(sI - A_K)^{-1}B_K \tag{D.1}$$

$$A_K = \begin{bmatrix} -34.2773 & 117.5721 & 359.5323 & -521.3096 & 33.8238 \\ 0.4552 & -5.3277 & -16.0319 & 20.431 & -1.3867 \\ 0.9887 & -5.6593 & -16.4799 & 16.8002 & -1.2409 \\ -0.0444 & -0.7728 & -0.8041 & -11.4784 & 0.4766 \\ 0.0114 & -0.0106 & -0.0646 & 0.5909 & -0.032 \end{bmatrix} \tag{D.2}$$

$$B_{ZK} = \begin{bmatrix} 0.0948 \\ 0.2193 \\ 2.711 \\ 1.9683 \\ -0.0281 \end{bmatrix} \tag{D.3}$$

$$C_{ZK} = \begin{bmatrix} -16.0063 & 58.3996 & 178.6582 & -258.9466 & 16.8046 \end{bmatrix} \tag{D.4}$$

$$D_K = 0 \tag{D.5}$$

D.3 *CISCREA* AUV Control Code

The python program of the PID and improved H_∞ *CISCREA* AUV heading controllers are given as follows:

```
#PID Controller
def psi_control(psi, target_psi):
    #global variable
    global P
    global D
    global I
    global yold
    global psilist
    #    psi: the yaw angle in rad
    #    target_psi: the expected orientation in rad
    # psilist.append(psi)
    y=psi
    r=target_psi
    psi_err=r-y
    # Pre compute PID controller parameters
    #gain
    kp=15
    ki=0.6
    kd=10
    N=2.59
    #interval 0.1s
    h=0.1
    bi=ki*h
    Tf=kd/(kp*N)
    ad=Tf/(Tf+h)
    bd=kd/(Tf+h)
    P=kp*psi_err
    D=ad*D-bd*(y-yold)
    v=P+I+D
    I=I+bi*(psi_err)
    yold=y
    moto_ref_psi =v
```

```
33      print("PID:",psi, target_psi, moto_ref_psi)
34      return moto_ref_psi
35
36  # Kalman filter: estimation of angular velocity
37  def kalmf_ang_vel(psi, moto_ctrler,comp_damp):
38      global ang_vel
39      global moto_limit
40      global kalxk
41      global kalmf_ang
42      global kalmfinput
43      # use compensation  and moto limit calculate the kalman input
44      moto_max=moto_limit
45      moto_min=-moto_limit
46      kalmfinput=moto_ctrler
47      Motoinput=moto_ctrler-comp_damp
48      if Motoinput>moto_max:
49          kalmfinput=moto_max+comp_damp
50      elif Motoinput<moto_min:
51          kalmfinput=moto_min+comp_damp
52      #kalman iteration
53      a=np.matrix(" 0.817434207010430 -0.0270295049541631;
            0.0905652303625428 0.917467766665371")
54      b=np.matrix(" 0.182565792989570 0.0270295049541631;
            0.00943476963745717 0.0825322333346289")
55      c=np.matrix("0 0.920462421552291; 1 -0.0330662758205544; 0
            0.920462421552291")
56      d=np.matrix(" 0 0.0795375784477090; 0 0.0330662758205544; 0
            0.0795375784477090")
57      uk=np.matrix([kalmfinput, psi])
58      uk=uk.transpose()
59      xkk=a*kalxk+b*uk
60      yk=c*kalxk+d*uk
61      kalxk=xkk
62      #write campass and control command
63      ang_vel=yk[1,0]
64      kalmf_ang=yk[0,0]
```

```
65      #print on screen
66      print("Input",kalmfinput,"Psi:",psi,"y", yk[0,0], "Ang_Vel:",yk
            [1,0],"x2:", yk[2,0])
67      return ang_vel
68
69  #   Nonlinear Compensator
70  def nonlin_compensator(ang_vel):
71      global comp_damp
72      global fedfwd
73      global DN
74      # make a feed back
75      comp_damp=fedfwd*ang_vel-DN*abs(ang_vel)*ang_vel
76      return comp_damp
77
78  # Hinfinity Controller
79  def psi_hinf_control(psi, target_psi):
80      global xk
81      global v
82      #    psi: the yaw angle in rad
83      #    target_psi: the expected orientation in rad
84      y=psi
85      r=target_psi
86      psi_err=r-y
87      uk=np.matrix(psi_err)
88      #hinf controller
89      a=np.matrix("0.197256482648792    1.59540314598849
            4.49798010253664    -3.71776829599392    0.300123924813506;
            -0.00621131141495130    0.759731533313859
            -0.685176910215340    0.547387817981330
            -0.0450683664607837; 0.0146347815053511    -0.170901816165014
                0.550453855157298    0.0406100731570936
            -0.0155990464674315; -0.00153580351247490
            -0.0362653741260259    -0.0211178973384089
            0.305283481543664    0.0296900874424064; 0.000293001798299378
                0.000255776045928881    0.000246755112570867
            0.0276890693987905    0.998376332616215")
```

```
90      b=np.matrix("0.273103219717465; -0.0179292130016475;
            0.206521330295216; 0.110601840954218; 0.000521323997792441")
91      c=np.matrix("-16.0062512802928    58.3996253615540
            178.658222489516    -258.946581201241    16.8045790623509")
92      xkk=a*xk+b*uk
93      yk=c*xk
94      xk=xkk
95      #write campass and control command
96      moto_ref_psi=yk[0,0]
97      print('psi:', psi, 'tar:', target_psi, 'ctrl:', moto_ref_psi*
            moto_cmd_limit/moto_limit)
98      return moto_ref_psi
99
100 # smith compensator
101 def smith_compensation(control_input,psi):
102     global smith_xk
103     global smithlist
104     a=np.matrix(" 0.8174 0;0.0906 1.0000")
105     b=np.matrix(" 0.1826; 0.0094")
106     c=np.matrix(" 0 1")
107     d=np.matrix(" 0")
108     uk=np.matrix(control_input)
109     xkk=a*smith_xk+b*uk
110     yk=c*smith_xk+d*uk
111     smith_xk=xkk
112     smithlist.append(yk)
113     comp_smith_psi=yk-smithlist.popleft()+psi
114     return comp_smith_psi
```

Bibliography

[1] National Oceanic and Atmospheric Administration, "Ocean," viewed 01/03/2015. [Online]. Available: http://www.noaa.gov/ocean.html

[2] L. Lapierre, "Underwater robots part i: current systems and problem pose," *Mobile Robotics Towards New Applications*, pp. 335–360, 2006.

[3] J. Yuh, "Design and control of autonomous underwater robots: A survey," *Autonomous Robots,*, vol. 8, pp. 7–24, 2000.

[4] A. Brandt, A. J. Gooday *et al.*, "The southern oceandeepsea: first insights into biodiversity and biogeography," *Nature*, vol. 447, no. 7142, pp. 307–311, 2007.

[5] K. Hardy, T. Bulman *et al.*, "Hadal landers: the deepsea chanllenge ocean trench free vehicles," *In Proceedings of the Oceans*, vol. 13, pp. 23–26, 2013.

[6] A. S. Brierley, P. G. Fernandes *et al.*, "Antarctic krill under sea ice: elevated abundance in a narrow band just south of ice edge," *Science*, vol. 295, no. 5561, pp. 1890–1892, 2002.

[7] A. Brandt, H. Griffiths *et al.*, "Challenges of deep-sea biodiversity assessments in the southern ocean," *Advances in Polar Science*, vol. 25, no. 3, pp. 204–212, 2014.

[8] M. Hildebrandt, J. Albiez *et al.*, "Design of an autonomous under-ice exploration system," *Oceans San Diego*, vol. 71, no. 2, pp. 151–185, 2013.

[9] S. R. Pezeshki, M. W. Hester *et al.*, "The effects of oil spill and clean-up on dominant us gulf coast marsh macrophytes: a review," *Environmental Pollution*, vol. 108, no. 2, pp. 129–139, 2000.

[10] F. Matsuno, N. Sato *et al.*, "Utilization of robot systems in disaster sites of the great eastern japan earthquake," *In Field and Service Robotics, Springer Berlin Heidelberg*, pp. 1–17, 2014.

[11] Y. Zhang, R. S. McEwen *et al.*, "A peak capture algorithm used on an autonomous underwater vehicle in the 2010 gulf of mexico oil spill response scientific survey," *Journal of Field Robotics*, vol. 28, no. 4, pp. 484–496, 2011.

[12] SAUC-E, "Student autonomous underwater challenge-europe," viewed 19/09/2014. [Online]. Available: http://sauc-europe.org

[13] euRathlon, "Outdoor robotics challenge for land, sea and air," viewed 15/09/2014. [Online]. Available: http://www.eurathlon.eu/site/

[14] A. Caiti, V. Calabro *et al.*, "Underwater robots: Past, present and future," *University of Pisa*, no. 422-437, 2013.

[15] T. W. Rochholz, "Wave-powered unmanned surface vehicle as a station-keeping gateway node for undersea distributed networks," Ph.D. dissertation, Naval Postgraduate School, Monterey, California., 2012.

[16] F. L. Bars and L. Jaulin, "An experimental validation of a robust controller with the vaimos autonomous sailboat," in *Proceedings of the 5th International Robotic Sailing Conference*, Cardiff, England, 2013, pp. 73–84.

[17] W. S. Chu, K. T. Lee *et al.*, "Review of biomimetic underwater robots using smart actuators," *International Journal of Precision Engineering and Manufacturing*, vol. 13, no. 7, pp. 1281–1292, 2012.

[18] D. Normile, "Lost at sea," *Science*, vol. 344, no. 6187, pp. 963–965, 2014.

[19] P. K. LeHardy and C. Moore, "Deep ocean search for malaysia airlines flight 370," in *Oceans-St. John's, IEEE.*, Sep. 2014, pp. 1–4.

[20] M. Hildebrandt and J. Hilljegerdes, "Design of a versatile auv for high precision visual mapping and algorithm evaluation," *Autonomous Underwater Vehicles, IEEE/OES*, pp. 1–6, 2010.

[21] M. Carreras, C. Candela, and D. Ribas, "Sparus ii, design of a lightweight hovering auv," *Martech 2013 5th International Workshop on Marine Technology, SARTI*, 2013.

[22] L. L. Whitcomb, "Underwater robotics: Out of the research laboratory and into the field," in *IEEE International Conference on robotics and Automation*, vol. 1, 2000, pp. 709–716.

[23] E. Bovio, "Autonomous underwater vehicles for scientific and naval operations," *Annual Reviews in Control,*, vol. 30, no. 2, pp. 117–130, 2006.

[24] U. S. Navy, *The Navy Unmanned Undersea Vehicle (UUV) Master Plan.* USA: Department of the Navy, 2004.

[25] D. Maalouf, "Contribution to nonlinear adaptive control of low inertia underwater robots," Ph.D. dissertation, University of Montpellier, Montpellier, France, 2014.

[26] R. Julio, S. Williams, and H. D. Whyte, "A behavior-based architecture for autonomous underwater exploration," *Information Sciences*, vol. 145, no. 1, pp. 69–87, 2002.

[27] R. McEwen and H. Thomas, "Performance of an auv navigation system at arctic latitudes," *IEEE Journal of Oceanic Engineering*, vol. 30, no. 2, pp. 443–454, 2003.

[28] B. Ferreira, M. Pinto *et al.*, "Hydrodynamic modeling and motion limits of auv mares." in *35th Annual Conference of IEEE on Industrial Electronics*, Porto, 2009, pp. 2241–2246.

[29] R. Yang, B. Clement *et al.*, "Modeling of a complex-shaped underwater vehicle." in *2014 IEEE International Conference on Autonomous Robot Systems and Competitions (ICARSC2014)*. Espinho, 2014, p. 36 41.

[30] H. Tan, R. Diamant *et al.*, "A survey of techniques and challenges in underwater localization," *Ocean Engineering*, vol. 38, pp. 1663–1676, 2011.

[31] A. Bahr, J. J. Leonard, and M. F. Fallon, "Cooperative localization for autonomous underwater vehicles," *International Journal of Robotics Research, Springer Berlin Heidelberg*, vol. 28, no. 6, pp. 714–728, 2009.

[32] L. Whitcomb, D. Yoerger *et al.*, "Advances in underwater robot vehicles for deep ocean exploration: Navigation, control, and survey operations." in *Navigation Control and Survery Operations in the Ninth International Symposium on Robotics Research*, 1999, pp. 346–353.

[33] S. Carreno, P. Wilson *et al.*, "A survey on terrain based navigation for auvs," in *OCEANS 2010 IEEE*, 2010, pp. 1–7.

[34] A. Pascoal, I. Kaminer, and P. Oliveira, "Navigation system design using time-varying complementary filters," *IEEE Transactions on Aerospace and Electronic System*, vol. 36, no. 4, pp. 1099–1114, 2000.

[35] R. G. Brown and Y. H. Patrick, *Introduction to random signals and applied Kalman filtering*. New York: Wiley, 1992, vol. 3.

[36] R. G. Brown, "Integrated navigation systems and kalman filtering: a perspective," *Journal of the Institute of Navigation*, vol. 19, no. 4, pp. 355–362, 1973.

[37] P. Oliveira, "Periodic and non-linear estimators with applications to the navigation of ocean vehicles," Ph.D. dissertation, Instituto Superior Tcnico Lisbon, Portugal, 2002.

[38] K. B. Anonsen and O. K. Hagen, "An analysis of real-time terrain aided navigation results from a hugin auv," in *Oceans, IEEE*, 2010, pp. 1–9.

[39] A. Caiti, V. Calabro *et al.*, "Underwater communication and distributed localization of auv teams," in *Oceans-bergen, MTS/IEEE*, 2013, pp. 1–8.

[40] M. F. Fallon, P. Georgios *et al.*, "Cooperative auv navigation using a single maneuvering surface craft," *International Journal of Robotics Research*, vol. 29, no. 12, pp. 1461–1474, 2010.

[41] L. Paull, S. Saeedi *et al.*, "Auv navigation and localization: A revie," in *IEEE Journal of Oceanic Engineering*, vol. 39, no. 1, 2014, pp. 131–149.

[42] J. Aulinas, Y. R. Petillot *et al.*, "The slam problem: a survey." in *CCIA2008*, 2008, pp. 363–371.

[43] A. M. Hasan, K. Samsudin *et al.*, "A review of navigation systems integration and algorithms," *Australian journal of basic and applied sciences*, vol. 3, no. 2, pp. 943–959, 2009.

[44] H. Kondo and T. Ura, "Navigation of an auv for investigation of underwater structures," *Control engineering practice*, vol. 12, no. 12, pp. 1551–1559, 2004.

[45] A. Mallios, P. Ridao *et al.*, "Navigating and mapping with the sparus auv in a natural and unstructured underwater environment," in *OCEANS IEEE*, no. 1-7, Sep. 2011.

[46] J. Aulinas, Y. R. Petillot *et al.*, "Vision-based underwater slam for the sparus auv," in *10th International Conference on Computer and IT Applications in the Maritime Industries*, Berlin, Germany, 2011, pp. 2–4.

[47] A. Bethencourt, "Interval analysis for swarm localization. application to underwater robotics." Ph.D. dissertation, Universite de Breatgne Occidental, Brest, France, 2014.

[48] W. Aeem, R. Sutton *et al.*, "A review of guidance laws applicable to unmanned underwater vehicles," *Journal of Navigation*, vol. 56, no. 1, pp. 15–29, 2003.

[49] C. Samson and K. Ait-Abderrahim, "Mobile robot control. part 1: Feedback control of nonholonomic wheeled cart in cartesian space," *INRIA report, France*, 1990.

[50] L. Lapierre, D. Soetanto, and A. Pascoal, "Non-singular path-following control of a unicycle in the presence of parametric modeling uncertainties," *International Journal on Robust and Nonlinear Control*, vol. 16, no. 10, pp. 485–503, 2006.

[51] M. R. Benjamin, J. J. Leonard *et al.*, "An overview of moos-ivp and a brief users guide to the ivp helm autonomy software." 2009.

[52] I. Yamamoto, "Robust and non-linear control of marine system," *International Journal of Robust and Nonlinear Control*, vol. 11, no. 13, pp. 1285–1341, Aug., 2001.

[53] B. M. Ferreira, A. C. Matos, and N. A. Cruz, "Modeling and control of trimares auv," in *12th International Conference on Autonomous Robot Systems and Competitions*, Portugal, April, 2012, pp. 57–62.

[54] M. Caccia, G. Indiveri, and G. Veruggio, "Modeling and identification of open-frame variable configuration unmanned underwater vehicles." *IEEE Journal of Oceanic Engineering*, vol. 25, no. 2, pp. 227–240, 2000.

[55] M. E. Rentschler, F. S. Hover, and C. Chryssostomidis, "Modeling and control of an odyssey iii auv through system identification tests," in *Unmanned Untethered Submersible Technology Conference*, Durham, USA, Aug, 2003.

[56] A. Ross, T. I. Fossen, and T. A. Johansen, "Identification of underwater vehicle hydrodynamic coefficients using free decay tests," in *IFAC Conference on Control Applications in Marine Systems*, Ancona, Italy, 2004, pp. 362–368.

[57] Y. H. Eng, M. Lau, and C. Chin, "Added mass computation for control of an open-frame remotely-operated vehicle: Application using wamit and matlab," *Journal of Marine Science and Technology*, vol. 22, no. 4, pp. 405–416, 2014.

[58] B. Ferreira, A. Matos, and N. Cruz, "Modeling and control of trimares auv," in *12th International Conference on Autonomous Robot Systems and Competitions*, Portugal, 2012, pp. 57–62.

[59] J. Newman, *Marine Hydrodynamics.* The MIT press, 1977.

[60] R. Yang, B. Clement *et al.*, "Modeling of a complex-shaped underwater vehicle for robust control scheme," *Journal of Intelligent and Robotic Systems*, pp. 1–16, 2015.

[61] MCC, "Marine craft characteristics," viewed 01.02.2014. [Online]. Available: https://moodle.ensta-bretagne.fr/course/view.php?id=18

[62] Y. H. Eng, W. S. Lau *et al.*, "Identification of the hydrodynamics coefficients of an underwater vehicle using free decay pendulum motion." in *International MultiConference of Engineers and Computer Scientists*, vol. 2, HongKong, pp. 423-430, Mar., 2008.

[63] T. A. Johansen and T. I. Fossen, "Control allocation: A survey," *Automatica*, vol. 49, no. 5, pp. 1087–1103, 2013.

[64] A. Budiyono, "Advances in unmanned underwater vehicles technologies: Modeling, control and guidance perspectives," in *Indian Journal of Marine Sciences*, vol. 38, no. 282-295, 2009, p. 3.

[65] S. D. McPhail and M. Pebody, "Autosub-1. a distributed approach to navigation and control of an autonomous underwater vehicle," in *7th International Conference on Electronic Engineering in Oceanography*, vol. 173, no. 19 21, Southampton, England: IET, 1997.

[66] R. Yang, I. Probst *et al.*, "Underwater vehicle modeling and control application to ciscrea robot," in *MOQESM'14 conference*, Brest, France, 2014.

[67] P. M. Ostafichuk, "Auv hydrodynamics and modelling for improved control," Ph.D. dissertation, University of British Columbia, Canada, 2004.

[68] M. Perrier and C. Canudas-De-Wit, "Experimental comparison of pid vs. pid plus nonlinear controller for subsea robots," *Autonomous robots*, vol. 3, no. 2-3, pp. 195–212, 1996.

[69] S. Y. Liu and D. Wang, "Nonlinear output feedback controller design for tracking control of odin in wave disturbance condition," in *Proceedings of OCEANS 2005 MTS/IEEE*, Washington, DC: IEEE, 2005, pp. 1–3.

[70] J. E. Refsnes, A. J. Sorensen, and K. Y. Pettersen, "Output feedback control of slender body underwater vehicles with current estimation," in *Internation Journal of Control*, vol. 80, no. 7, 2008, pp. 1136–1150.

[71] A. A. Mirhosseini, A. P. Aguiar, and M. J. Yazdanpanah, "Seabed tracking of an autonomous underwater vehicle with nonlinear output regulation," in *50th IEEE Conference on Decision and Control and Eurpean Control Conference*, Orlando, FL, USA, 2011, pp. 3928–3933.

[72] R. Sutton, W. Naeem, and S. M. Ahmad, "Lqg/ltr control of an autonomous underwater vehicle using a hybrid guidance law," in *1st IFAC Workshop on Guidance and Control of Underwater Vehicles*, Newport, Wales: IFAC, 2003, pp. 31–36.

[73] C. Silvestre, A. Pascoal, and I. Kaminer, "On the design of gain-scheduled trajectory tracking controllers," *International Journal of Robust and Nonlinear Control*, vol. 12, no. 9, pp. 797–839, 2002.

[74] C. Silvestre and A. Pascoal, "Control of the infante auv using gain scheduled static output feedback," *Control Engineering Practice*, vol. 12, no. 12, pp. 1501–1509, 2004.

[75] J. C. Doyle, "Guaranteed margins for lqg regulators," *IEEE Trans. Autom. Control*, vol. 23, pp. 756–757, 1978.

[76] K. M. Zhou and J. C. Doyle, *Essentials of robust control.* Upper Saddle River, Prentice hall, 1998, vol. 180.

[77] D. Gu, P. H. Petkov, and M. M. Konstantinov, *Robust Control Design with MATLAB.* Springer, 2005.

[78] H. J. Li, S. L. J. Hu, and C. Jakubiak, "H2 active vibration control for offshore platform subjected to wave loading,," *Journal of sound and vibration*, vol. 263, no. 4, pp. 709–724, 2003.

[79] H. J. Li, "Optimal active control of wave-induced vibration for offshore platforms," *Journal of China Ocean Engineering*, vol. 15, no. 1, pp. 1–14, 2001.

[80] H. J. Pan and M. Xin, "Depth control of autonomous underwater vehicles using indirect robust control method," *International Journal of Control*, vol. 85, no. 1, pp. 98–113, 2012.

[81] E. Roche, O. Sename *et al.*, "A hierarchical varying sampling h_∞ control of an auv," in *18th IFAC world congress*, Milano, Italy, 2011.

[82] E. Roche, O. Sename, and D. Simon, "Lpv/h_∞ varying sampling control for autonomous underwater vehicles," in *In 4th IFAC Symposium on System, Structure and Control*, Delle Marche, 2010, pp. 17–24.

[83] B. Clement, "Interval analysis and convex optimization to solve a robust constraint feasibility problem," *Eur. J. Autom. Syst.*, vol. 46, no. 4-5, pp. 381–395, 2012.

[84] Z. Feng and R. Allen, "Reduced order h_∞ control of an autonomous underwater vehicle," *Control. Eng. Pract.*, vol. 12, no. 12, pp. 1511–1520, 2004.

[85] B. Clement, "Synthese multiobjectifs et sequencement de gains: application au pilotage d'un lanceur spatial," Ph.D. dissertation, Université de Paris 11, Orsay, FRANCE, 2001.

[86] J. Slotine, *Applied Nonlinear Control*. London,UK: Prentice Hall, 1991.

[87] J. Vaganay, B. Jouvencel *et al.*, "Taipan an auv for very shallow water applications," in *Proceedings of World Automation Congress (WAC'98)*, San Diego, USA, 1998.

[88] T. I. Fossen and S. Sagatun, "Adaptive control of nonlinear underwater robotic systems," in *IEEE International Conference on Robotic and Automation ICRA'91*, Sacramento CA,USA, 1991, pp. 1687–1695.

[89] T. Salgado-Jimenez, J. M. Spiewak *et al.*, "A robust control algorithm for auv: based on a high order sliding mode," in *MTS/IEEE TECHNO-OCEAN04*, vol. 1, 2004, pp. 276–281.

[90] A. Pisano and E. Usai, "Output feedback control of an underwater vehicle prototype by higher-order sliding modes," *Automatica*, vol. 40, no. 9, pp. 1525–1531, 2004.

[91] G. Campa, M. Innocenti, and F. Nasuti, "Robust control of underwater vehicles: sliding mode control vs. mu synthesis," in *Proceedings of the IEEE Oceanic Engineering Society OCEANS'98*, Nice, France, 1998, pp. 1640–1644.

[92] L. Lapierre and J. Bruno, "Robust nonlinear path-following control of an auv," *IEEE Journal of Oceanic Engineering*, vol. 33, no. 2, pp. 89–102, 2008.

[93] H. Khalil, *Nonlinear systems third edition.* New Jersey, USA: Prentice Hall, 2002.

[94] M. Krstic and P. K. Kokotovic, *Nonlinear and Adaptive Control Design.* New York, US: Wiley, 1995.

[95] J. H. Li, P. M. Lee, and B. H. Jun, "An adaptive nonlinear controller for diving motion of an auv," in *Proceedings of MTTS/IEEE OCEANS'04*, 2004, pp. 282–286.

[96] D. Maalouf, I. Tamanaja *et al.*, "From pd to nonlinear adaptive depth-control of a tethered autonomous underwater vehicle," in *IFAC Joint conference'2013: 5th Symposium on System Structure and Control.*, Grenoble, France, 2013.

[97] S. Zhao and J. Yuh, "Experimental sutdy on advanced underwater robot control," *IEEE Transactions on Robotics*, vol. 21, no. 3, pp. 695–703, 2000.

[98] G. Antonelli, F. Cacciavale *et al.*, "A novel adaptive control law for autonomous underwater vehicle," in *Proceedings of IEEE International Conference on Robotics and Automation*, Seoul, Korea: IEEE, 2001, p. 447 452.

[99] T. I. Fossen and O. E. Fjellstad, "Robust adaptive control of underwater vehicles: A comparative study," in *IFAC Workshop on Control Applications in Marine Systems (CAMS'95)*, vol. 17, Trondheim, Norway, 1996, pp. 47–61.

[100] G. Antonelli, "On the use of adaptive/integral actions for six degrees of freedom control of autonomous underwater vehicles," *IEEE Journal of Oceanic Engineering*, vol. 32, no. 2, pp. 300–312, 2007.

[101] Y. Shi, W. Q. Qian *et al.*, "Adaptive depth control for autonomous underwater vehicles based on feedforward neural networks," *International Journal of Computer Science and Applications*, vol. 4, no. 3, pp. 107–118, 2007.

[102] P. Szymak and J. Malecki, "Control system of underwater vehicle based on artificial intelligence methods," *Automation and Robotics*, vol. 17, pp. 285–296, 2008.

[103] M. Chang, W. Chang, and H. H. Liu, "Model-based fuzzy modeling and control for autonomous underwater vehicles in the horizontal plane," *Journal of Marine Sciences and Technology*, vol. 11, pp. 155–163, 2003.

[104] A. El-Fakdi and M. Carreras, "Policy gradient based reinforcement learning for real autonomous underwater cable tracking," *IROS. IEEE/RSJ International Conference*, pp. 3635–3640, 2008.

[105] A. Lamas, F. L. Pez-Pe, and R. J. Duro, "A hybrid approach for designing the control system for underwater vehicles," in *4th International Conference on Hybrid Artificial Intelligent Systems*, Salamanca, Spain, 2009, pp. 88–95.

[106] M. B. Wallace, S. D. Max, and E. Kreuzer, "Depth control of remotely operated underwater vehicles using an adaptive fuzzy sliding mode controller," *Robotics and Autonomous Systems*, vol. 5, no. 8, pp. 670–677, 2008.

[107] A. R. Marzbanrad, M. Eghtesad, and R. Kamali, "A robust adaptive fuzzy sliding mode controller for trajectory tracking of rovs," in *50th IEEE Conference onf Decision and Control and European Control Conference*, Orlando, FL, USA, 2011, pp. 2863–2869.

[108] L. V. Steenson, A. B. Phillips *et al.*, "Experimental verification of a depth controller using model predictive control with contraints onboard a thruster actuated auv," in *IFAC Workshop on Navigation, Guidance and Control of Underwater Vehicles*, Ireland, 2012, pp. 275–280.

[109] F. Le-Bars and L. Jaulin, "An experimental validation of a robust controller with the vaimos autonomous sailboat," in *Proceedings of the 5th International Robotic Sailing Conference*, Cardiff, England, 2013, pp. 73–84.

[110] J. Newman and C. H. Lee, *WAMIT user manual*. WAMIT Inc, 2013.

[111] R. Yang, B. Clement *et al.*, "Modeling of a complex-shaped underwater vehicle for robust control scheme," *Journal of Intelligent and Robotic Systems*, Jan. 2015.

[112] J. Yuh, "Modeling and control of underwater robotic vehicles," *IEEE Transactions on Systems, Man, and Cybernetics*, vol. 20, no. 6, pp. 1475–1483, 1990.

[113] N. E. Leonard, "Stabilization of steady motions of an underwater vehicle," in *Proceedings of the 35th IEEE Conference on Decision and Control*, 1996, pp. 3980–3985.

[114] T. I. Fossen, *Marine control systems: Guidance, navigation and control of ships, rigs and underwater vehicles*. Marine Cybernetics Trondheim, 2002.

[115] ——, *Guidance and Control of Ocean Vehicles*. Wiley, New York, 1994.

[116] SNAME[1950], "Nomenclature for treating the motion of a submerged body through a fluid." *The Society of Naval Architects and Marine Engineers, Technical and Reserach Bulletin*, pp. 1–15, April 1950.

[117] MSS, "Marine systems simulator (2010)," viewed 01.02.2014. [Online]. Available: http://www.marinecontrol.org.

[118] O. M. Faltinsen, *Sea Loads on Ships and Offshore Structures*. Cambridge, UK: Cambridge University Press,, 1990.

[119] L. Lapierre, "Underwater robots part ii: Existing solutions and open issues," *Mobile Robotics Towards New Applications*, pp. 362–398, 2006.

[120] M. Blanke, K. P. Lindegaard, and T. I. Fossen, "Dynamic model for thrust generation of marine propellers." in *Proc. 5th IFAC Conference on Manoeuvring and Control of Marine Craft*, 2000, pp. 363–368.

[121] C. Chin and M. Lau, "Modeling and testing of hydrodynamic damping model for a complex-shaped remotely-operated vehicle for control," *Journal of Marine Science and Application*, vol. 11, no. 2, pp. 150–163, 2012.

[122] D. Perrault, N. Bose *et al.*, "Sensitivity of auv added mass coefficients to variations in hull and control plane geometry,," *Ocean Eng.*, vol. 30, no. 5, pp. 645–671, 2003.

[123] T. I. Fossen, "Description of mss vessel models: Configuration guidelines for hydrodynamic codes," 2008.

[124] T. Perez, O. N. Smogeli *et al.*, "An overview of the marine systems simulator (mss): A simulink toolbox for marine control systems." *Modeling, identification and Control*, vol. 27, no. 4, p. 259, 275 2006.

[125] STAR-CCM+, "Cd-adapco user guide, version 7.04," 2012.

[126] R. Comolet and J. BONNIN, *Mécanique expérimentale des fluides.* Tome I, Masson, Paris, 1979.

[127] F. Floc'H, "Prédiction de trajectoires d'objets immergés par couplage entre modèles d'écoulement et équations d'euler-newton," Ph.D. dissertation, Université de Bretagne occidentale, Brest, France, July, 2011.

[128] E. Schreck and M. Peric, "Overset grids in star-ccm+ methodology, applications and future developments," 2014. [Online]. Available: http://www.cd-adapco.com/presentation/overset-grids-technology-star-ccm-current-state-future-developments

[129] R. Yang, B. Clement *et al.*, "Modeling of a complex-shaped underwater vehicle," in *2014 IEEE International Conference on Autonomous Robot Systems and Competitions (ICARSC2014)*, Espinho, Portugal, May, 2014.

[130] P. Dorato, "A historical review of robust control," *IEEE Control Systems Magazine*, vol. 7, no. 2, pp. 44–47, 1987.

[131] S. Carsten, *Theory of robust control.* Delft University of Technology, 2001.

[132] G. Zames, "Feedback and optimal sensitivity: Model reference transformations, multiplicative seminorms and approximate inverses," *IEEE Transactions on Automatic Control*, vol. 26, pp. 301–320, 1981.

[133] G. Zames and B. Francis, "Feedback, minimax sensitivity, and optimal robustness," *IEEE Transactions on Automatic Control*, vol. 28, no. 585-600, 1983.

[134] B. A. Francis and G. Zames, "Design of h_∞-optimal multivariable feedback systems," in *Conference on Decision and Control*, vol. 22, 1983, pp. 103–108.

[135] B. Francis, J. Helton, and G. Zames, "h_∞-optimal feedback controllers for linear multivariable systems," *IEEE transactions on Automatic Control*, vol. 29, no. 10, pp. 888–900, 1984.

[136] B. Chang and J. Pearson, "Optimal disturbance reduction in linear multivariable systems," *IEEE Transactions on Automatic Control*, vol. 29, no. 10, pp. 880–887, 1984.

[137] R. Curtain and K. Glover, "Robust stabilization of infinite dimensional systems by finite dimensional controllers," *System and control letters*, vol. 7, no. 1, pp. 41–47, 1986.

[138] J. C. Doyle, K. Glover *et al.*, "State-space solutions to standard h_2 and h_∞ control problems," *IEEE Transactions on Automatic Control*, vol. 34, no. 8, pp. 831–847, 1989.

[139] K. Thomas, *Linear systems*. Englewood Cliffs, NJ: Prentice-Hall, 1980.

[140] S. Boyd, E. Ghaoui *et al.*, *Linear matrix inequalities in system and control theory,*. Society for industrial and applied mathematics, SIAM, Philadelphia, USA, 1994.

[141] L. E. Ghaoui and S. Niculescu, *Advances in Linear Matrix Inequality Methods in Control*. SIAM, 2000.

[142] P. Gahinet and P. Apkarian, "A linear matrix inequality approach to control," *Journal of robust and nonlinear control*, vol. 4, pp. 421–448, 1994.

[143] S. Carsten, "The riccati inequality and state space h_∞ optimal control," Ph.D. dissertation, University of Wnrzburg, Germany, 1990.

[144] K. Astrom and R. Murray, *Feedback systems: an introduction for scientists and engineers*. New Jersey: Princeton university press, 2010.

[145] Q. Zhong, *Robust control of time delay systems*. Berlin: Springer, 2006.

[146] A. Visioli, "Optimal tuning of pid controllers for integral and unstable processes," in *IEEE Proceedings Control Theory and Applications 2001*, vol. 148, no. 2, 2001, pp. 180–194.

[147] CISCREA Company, viewed 01.02.2015. [Online]. Available: http://www.ciscrea.fr

[148] ENSTA Bretagne, OSM, viewed in 01/02/2015. [Online]. Available: http://www.ensta-bretagne.fr/stic/index.php/ocean-sensing-and-mapping/

List of Figures

1-1 Thales USV 6
1-2 Ifremer Vaimos USV 6
1-3 Alive Ifremer 7
1-4 L2ROV *LIRMM* 7
1-5 Slocum Glider 7
1-6 Blue Fin 9 7
1-7 OCEAN Modules 9
1-8 CISSAU AUV 9
1-9 Avalon 9
1-10 Sparus II 9
1-11 CISCREA 24

2-1 B-frame and NED-frame of Underwater Vehicles 35

3-1 Measure the size and weight of main components on *CISCREA* AUV 53
3-2 Explode View of the *CISCREA* AUV 55
3-3 PRO/E Center of Gravity CG Estimation of the *CISCREA* AUV . . 55
3-4 Low Order Representation of *CISCREA* AUV in MULTISURF 59
3-5 WAMIT working chart 60
3-6 Neutral representation of *CISCREA* AUV in GAMBIT 62
3-7 Neutral representation of *CISCREA* AUV in MCC 63
3-8 *CISCREA* AUV in ANSYS 70

3-9 *CISCREA* AUV in ANSYS, constant speed boundary is on the left side with arrows pointing inside the water tank, and zero pressure boundary is on right side with arrows pointing out 71
3-10 The Mesh of *CISCREA* AUV in ANSYS 72
3-11 Streamline View of *CISCREA* AUV in ANSYS Surge Damping Analysis 74
3-12 *CISCREA* AUV fixed in Star-ccm+ for Heave Damping Analysis . . . 75
3-13 Star-ccm+ Meshing Result of *CISCREA* AUV for Surge Damping Analysis 76
3-14 Star-ccm+ Prsim Layer Meshing Result of *CISCREA* AUV 77
3-15 *CISCREA* AUV Fixed in the Cylinder Tank 79
3-16 Meshing Result of *CISCREA* AUV for Rotational Damping Analysis (STAR-CCM+) 80
3-17 Damping force and velocity of *CISCREA* AUV (CFX: solid line, STAR-CCM+: dash line) 81
3-18 CISCREA Surge 0.5m/s (CFX) 82
3-19 CISCREA Surge 0.5m/s (CCM+) 82
3-20 CISCREA Sway 0.5m/s (CFX) 83
3-21 CISCREA Sway 0.5m/s (CCM+) 83
3-22 CISCREA Heave 0.5m/s (CCM+) 83
3-23 CISCREA Heave 0.5m/s (CCM+) 83
3-24 Moving Reference Rotation (2.381 $N \cdot m$) 83
3-25 Overset Mesh Method (2.515 $N \cdot m$) 83

4-1 Propulsion Configuration of the *CISCREA* AUV 89
4-2 Force measurement using a dynamometer with an accuracy of 0.01 N 90
4-3 Measurement of the vertical propeller bollard thrust on *CISCREA* AUV 90
4-4 Bollard thrust measurement of the horizontal propellers 91
4-5 Torque measurement 91
4-6 Measurements of propulsion forces and torques of the *CISCREA* AUV 92
4-7 *CISCREA* AUV captured by a camera moving in the surge direction . 94

4-8 *CISCREA* AUV captured by a camera moving in the sway direction . 94
4-9 *CISCREA* AUV captured by an underwater camera moving in the heave direction 95
4-10 *CISCREA* AUV captured by a camera moving in the yaw direction . 95
4-11 Convergence of velocities after 10s for 10 constant bollard force points 98
4-12 Experimental and computational comparison of damping and velocity relationship in the surge direction of the *CISCREA* AUV 100
4-13 Experimental and computational comparison of damping and velocity relationship in the sway direction of the *CISCREA* AUV 100
4-14 Experimental and computational comparison of damping and velocity relationship in the heave direction of the *CISCREA* AUV 101
4-15 Experimental and computational comparison of damping and velocity relationship in the yaw direction of the *CISCREA* AUV 101

5-1 Robust control design diagram, where G matrix is the controlled plant, Δ matrix block describes the uncertainties, K matrix is the controller, d, w, u are elements of input vectors, e, z, y consist of output vectors. . 112
5-2 Nonlinear damping compensation 131
5-3 Robust controller & Nominal model of damping compensation 134
5-4 H_∞ control design with weighting functions connected 136
5-5 Bode Plot of Open-loop Perturbed Plants 140
5-6 Complementary sensitivity function T(s) is well covered by the inverse of weighting functions $1/W_p(s)$, $1/W_e(s)$ 141
5-7 Sensitivity function $T_k(s)$ is well covered by the inverse of weighting functions $1/W_u(s)$ 141
5-8 Step Response of three scenarios: PID control, damping compensated H_∞ approach and H_∞ control 143
5-9 Step Response and Propeller Output on Nominal Yaw Model 144
5-10 Step Response and Propeller Output with 30% of inertia variation . 145

6-1 *CISCREA* semi-AUV can work in the ROV mode with connected communication cable, or it can work in an AUV mode with autonomous devices. 152

6-2 An improved AUV version of the *CISCREA* robot that equipped with fully autonomous sensors, such as sonar, underwater cameras, INS/electro-gyros, depth meter and other self-navigate and control unit 154

6-3 *CISCREA* AUV founds the router on the bottom of shallow water one year after its lost. 155

6-4 *CISCREA* AUV discovers the underwater structures and its valve and o-ring for autonomous manipulations. 155

6-5 The hardware hierarchy diagram of the *CISCREA* AUV 155

6-6 The improved compensated H_∞ control approach for the *CISCREA* AUV and other AUVs. Only one magnetic compass is used as the feedback sensor. The H_∞ controller, nonlinear compensator, delay compensator, and Kalman filter are all numerical calculations. 157

6-7 Kalman filter 159

6-8 H_∞ heading control of the *CISCREA* AUV with the aid of Kalman filter that estimates the angular velocity $\dot{x}_r$. The above subplot shows the yaw angle control step response, and the down one shows the thruster propulsions. 162

6-9 Sensor signal transmission delay issue (magnetic compass) and its oscillation consequences about the H_∞ heading control during the water tank experiment of the *CISCREA* AUV. Subplot (a) shows the yaw angle control step response, subplot (b) shows the thruster propulsions, and subplot (c) shows the Kalman angular velocity estimations. A clear time delay of 0.5s can be seen between the yaw angle Kalman estimation and the magnetic compass measurements. 163

6-10 The simulation result of the *CISCREA* AUV H_∞ heading control method in face of a virtually adding delay of 0.5 s on the magnetic compass sensor. The above subplot shows the yaw angle control step response, the down one shows the thruster propulsions. A similar oscillation pattern can be drawn comparing to the *CISCREA* AUV heading control pool test. 164

6-11 Diagram of the Smith compensating technique 165

6-12 The simulation result of the improved *CISCREA* H_∞ heading controller (Smith Compensation). The above subplot shows the yaw angle control step response, the down one shows the thruster propulsions. Both Kalman filter and Smith compensators are used to eliminate the applicable issue for the original H_∞ control design. 167

6-13 The simulation result of the improved *CISCREA* H_∞ heading controller (Kalman Compensation). The above subplot shows the yaw angle control step response, the down one shows the thruster propulsions. 168

6-14 The pool experiment of the fully compensated H_∞ heading control approach as well as other control methods on the *CISCREA* AUV. The above subplot shows the *CISCREA* AUV rotating around the yaw axis in the testing pool, and the one below shows the real-time control monitor of the AUV camera and control parameters, such as the yaw angle. 172

6-15 Experimental heading control results of the *CISCREA* AUV using the PID control approach in the water pool of ENSTA Bretagne laboratory (CNRS 6285), the subplots respectively show the robot yaw angle and control output propulsions 173

6-16 Experimental heading control results of the *CISCREA* AUV using the proposed fully compensated H_∞ control approach in the water pool of ENSTA Bretagne laboratory (CNRS 6285) , the subplots show the robot yaw angle, the control output propulsions, and the Kalman estimation of the yaw angular velocity $\dot{x}_r$ 174

6-17 The sea experiment of the fully compensated H_∞ heading control approach as well as other control methods on the *CISCREA* AUV near the Brest harbour, France. 175

6-18 Experimental heading control results of the *CISCREA* AUV using the PID control approach near Brest harbour, France. The subplots respectively show the robot yaw angle and control output propulsions. . 177

6-19 Experimental heading control results of the *CISCREA* AUV using the proposed fully compensated H_∞ control approach the near Brest harbour, France. The above and down subplots respectively show the robot yaw angle, the control output propulsions, and the Kalman estimation of the yaw angular velocity $\dot{x}_r$. During the selected time slot, the *CISCREA* AUV is of low battery. However, the robot is still shows good robust capability. 178

6-20 The 3D virtual dynamic and hydrodynamic simulation environment of the *CISCREA* AUV. The bathymetry data come from online sonar scan of a volcano. 180

6-21 Full length experimental heading control results of the *CISCREA* AUV. The control algorithm is the proposed fully compensated H_∞ control approach, and the data was obtained in Brest harbour, France. The subplots show the yaw angle, the propulsion torques, and the yaw angular velocity $\dot{x}_r$ estimation using Kalman filter. Label A stands for the disturbances that induced by a kayak collision with the AUV. Label B denotes respectively the *CISCREA* AUV communication cable hooked by an underwater concrete structure, and at the same time, the program triggered a bug while the compass switch instantly between the maximum range and the minimum. 182

A-1 The damping coefficient Cd of Cylinder and Sphere under different Reynold number Re scenarios 204

List of Tables

1.1 CISCREA AUV Characteristics 25

2.1 The notation of SNAME for marine vessels 35
2.2 Nomenclature of the notations of rigid-body dynamics 38
2.3 Nomenclature of the notations of hydrodynamics 41

3.1 The mass distribution of the *CISCREA* AUV 54
3.2 Added Mass Results of Standard Sphere in the Surge Direction (Radius $1m$, density 1 kg/m^3, depth 10 m, Geometry: 1024 surfaces) 61
3.3 Configurations of ANSYS-CFX 73
3.4 Damping Forces of *CISCREA* AUV at Different Velocities 74
3.5 Configurations of STAR-CCM+ Estimating the Damping Effects of *CISCREA* AUV 77
3.6 Damping Forces and Moments of *CISCREA* AUV at Different Velocities 77
3.7 Configurations of STAR-CCM+ estimating the rotational damping effects of *CISCREA* AUV 80
3.8 Damping moments of *CISCREA* AUV at different Velocities 81
3.9 CFD results curve fitting 81

4.1 Bollard thrust measurement results, Heave direction using 2 vertical propellers 90
4.2 Bollard thrust measurement results, Surge direction using 2 front horizontal propellers 90

4.3 Bollard thrust measurement results, Sway direction using 4 horizontal propellers . . . 91
4.4 Bollard thrust measurement results, Torque on yaw direction using 4 horizontal propellers, around the center of the AUV body . . . 91
4.5 Surge direction using 2 front horizontal propellers . . . 99
4.6 Sway direction using 4 horizontal propellers . . . 99
4.7 Heave direction using 2 vertical propellers . . . 99
4.8 Yaw direction rotation both clockwise (CW) and counter-clockwise (CCW) using 4 horizontal propellers, around the center of the AUV body . . . 99
4.9 Experimental results of curves fitting (x: velocity m/s or angular velocity rad/s, y: propulsion force N or torque $N \cdot m$, CW: clockwise, CCW: Counter-clockwise) . . . 102
4.10 STAR-CCM+ results curve fitting (x: velocity m/s or angular velocity rad/s, y: propulsion force N or torque $N \cdot m$) . . . 102
4.11 ANSYS-CFX results curve fitting (x: velocity m/s or angular velocity rad/s, y: propulsion force N or torque $N \cdot m$) . . . 102
4.12 Assumed nominal model (x: velocity m/s or angular velocity rad/s, y: propulsion force N or torque $N \cdot m$) . . . 102
4.13 Rotational model notions of yaw direction . . . 106

5.1 Robust stable conditions under different types of uncertainties, given by the small gain theorem . . . 116
5.2 Rotational model notions of yaw direction . . . 129
5.3 Linear Damping Uncertainty Margin . . . 132

Abbreviations

ARE Algebraic *Riccati* Equation.

AUV Autonomous Underwater Vehicle.

B-frame Body Fixed Reference.

CAD Computer Aided Design.

CB Center of Buoyancy.

CFD Computational Fluid Dynamic.

CG Center of Gravity.

DOF Degree of Freedom.

DR Dead Reckoning.

DVL Doppler Velocity Log.

EKF Extended Kalman filter.

GPS Global Position System.

HOV Human Occupied Vehicle.

IAUV Intervention Autonomous Underwater Vehicles.

KF Kalman filter.

LBL Long Base-line.

LFT Linear Fractional Transformation.

LMI Linear Matrix Inequality.

LPV Linear Parameter Varying.

LQG Linear Quadratic Gaussian.

LTI Linear Time Invariant.

MCC Marine Craft Characteristics.

MIMO Multi Input Multi Output.

NED-frame North East Down Reference.

NOAA National Oceanic and Atmospheric Administration.

PDF Probability Density Function.

PID Proportional-Integral-Derivative.

PRO/E PRO/ENGINEER.

PWM Pulse Width Modulation.

ROV Remotely Operated Vehicle.

SISO Single Input Single Output.

SLAM Simultaneous Localization and Mapping.

SNAME Society of Naval Architects and Marine Engineers.

USBL Ultra Short Base-Line.

USV Unmanned Surface Vehicles.

UUV Unmanned Underwater Vehicle.

List of Publications

[1] R. YANG, B. Clement, A. Mansour, M. Li, N.L. Wu: Modeling of a complex-shaped underwater vehicle for Robust Control Scheme. Journal of Intelligent and Robotic Systems, online p. 1-16, Jan. 2015. (SCI, EI)

[2] R. YANG, B. Clement, A. Mansour, H.J. Li, M. Li: Robust Heading Control and its Application to CISCREA Underwater Vehicle. OCEANS 2015 MTS/IEEE Genova conference, Italy, May 2015. (EI, Selected Paper in Student Poster Competition)

[3] R. YANG, I. Probst, B. Clement, A. Mansour, M. Li: Underwater Vehicle Modeling and Control Application to CISCREA Robot. Quantitative Monitoring of Underwater Environment in SEA TECH Week 2014, MOQSEM'14, Brest, France, Oct. 2014. (In: Springer Series: Ocean Engineering & Oceanography)

[4] R. YANG, B. Clement, A. Mansour, H.J. Li, M. Li, N.L. Wu: Modeling of a complex-shaped underwater vehicle. 2014 IEEE International Conference on Autonomous Robot Systems and Competitions, ICARSC2014. p. 36-41 Esphino, Portugal, May 2014. (EI)

[5] R. YANG, J.G Wang, B. Clement, A. Mansour: FPGA Implementation of a Parameterized Fourier Synthesizer. IEEE International Conference on Electronics, Circuits, and Systems, ICECS 2013, p. 473-476 Abu Dhabi, UAE, Dec. 2013. (EI)

Résumé

L'utilisation des AUV pour une exploitation durable des ressources océaniques est pertinente. Un robot sous-marin peut être utilisé comme plateforme pour observer, recueillir des informations sur l'environnement marin. Afin d'améliorer la qualité des observation et d'augmenter la capacité de navigation, de nombreuses questions doivent être abordées et examinées simultanément. Nous abordons ici le problème du pilotage de ces robots autonomes.

Atteindre la maniabilité nécessaire dépend de deux facteurs clés: un modèle hydrodynamique précis et un système de contrôle performant. Cependant, le coût de développement d'un modèle précis est généralement très élevé. De plus, lorsque la géométrie du robot est complexe, il devient très difficile d'identifier de manière pertinente les paramètres dynamiques et hydrodynamiques. En outre, du point de vue de la commande, les modèles obtenus sont non linéaire, en particuliers pour les amortissements. De nombreux phénomènes dynamiques ne sont pas modélisés: dynamiques internes au robot, environnementales, liées aux bruits des capteurs, aux retards intrinsèques.

Dans les concours de robotique sous-marine, il est confirmé que le traditionnel régulateur Proportionnel-Intégral-Dérivé (PID) est peu efficace pour les robot légers. Dans ce cas, notre champ d'application est plus axé sur la combinaison des approches de modélisation numérique et la commande robuste.

Dans ce travail, nous proposons un schéma de régulation basé sur la commande robuste et la modélisation. La régulation robuste a été mise en place et validée en mer sur un AUV de la marque *CISCREA* et la solution proposée utilise Computational Fluid Dynamic (CFD) pour caractériser les deux paramètres hydrodynamiques (ma-

trice de masse ajoutée et matrice d'amortissement). Puis un modèle à quatre degrés de liberté est construit pour le *CISCREA*. Les résultats numériques et expérimentaux sont alors comparés.

La commande robuste proposée est basée sur une compensation non linéaire et de la commande H_∞. La validation de la robustesse a été testée par simulation en *Matlab* et finalement validée par des essais en mer à *Brest*. La simulation et l'expérience montrent que l'approche en plus d'être robuste est plus rapide que les régulateurs précédemment proposés.